Imperial College London

Investigation of low-temperature solution processed metal oxide for organic and perovskite photovoltaics

Jiaqi Zhang

Department of Materials

Imperial College London

June 2017

A thesis submitted in fulfilment of the requirements for the degree of

Doctor of Philosophy

Declaration of Originality

I declare that the work contained in this thesis is my own unless stated otherwise or referenced specifically in-text. Where work was done in collaboration with others, the contribution and the persons who carried it out are stated. The copyright of this thesis rests with the author and is made available under a Creative Commons Attribution Non-Commercial No Derivatives licence. Researchers are free to copy, distribute or transmit the thesis on the condition that they attribute it, that they do not use it for commercial purposes and that they do not alter, transform or build upon it. For any reuse or redistribution, researchers must make clear to others the licence terms of this work.

© Copyright by Jiaqi Zhang, 2017.

All rights reserved.

Foreword

This thesis is the work carried out in the period between October 2013 and October 2016, in the Department of Materials, Imperial College London. All work was carried out by the author with the exception of the following:

- The transient photovoltage and photocurrent were carried out by Jiaying Wu (Durrant group, Dept. of Chemistry)
- The transient absorption was carried out by Ching-Hong Tan (Durrant group, Dept. of Chemistry)
- TEM and Hall measurements were carried out by Dr. Claire Burgess (McLachlan group)
- XPS, FTIR and the majority of Kelvin probe measurements were carried out by Maurizio Morbidoni (McLachlan group)
- Thin film transistors were measured by Dr. Yoann Porte and Rebecca Kilmurray (McLachlan group)
- Polymer LEDs were fabricated and tested by Dr. Jorge Costa and Maurizio Morbidoni (McLachlan group)

The work shown in this thesis has been published in the following papers. Work that is under review is also included in this list.

- **J. Zhang**, J. C. D. Faria, M. Morbidoni, Y. Porte, C. H. Burgess, K. Harrabi, and M. A. McLachlan, "Low-Temperature Solution-Processed Electron Transport Layers for Inverted Polymer Solar Cells," *Adv. Electron. Mater.*, vol. 2, 1600008, 2016.
- **J. Zhang**, M. Morbidoni, C. H. Burgess, J. Wu, T. Du, K. Harrabi, J. R. Durrant, M. A. McLachlan, "Low Temperature Solution Processed Nanocrystalline ZnO Electron Transport Layers for Organic Photovoltaics," In review *(Scientific Report)*
- **J. Zhang**, C. H. Tan, T. Du, M. Morbidoni, J. R. Durrant, M. A. McLachlan, "Metal Oxide/Organic Bilayer as Electron Transport Layer for Low Temperature Processed, Thermal Stable and Hysteresis Free Regular Perovskite Solar Cells," In review *(Advanced Energy Materials)*
- **J. Zhang**, M. Morbidoni, C. H. Burgess, R. Kilmurray, J. R. Durrant, M. A. McLachlan, "Effect of Processing Temperature on Film Properties of ZnO by

Aqueous Method and Related Organic Photovoltaics and LEDs," In review *(Sustainable Energy Fuels)*

- **J. Zhang**, M. Morbidoni, M. A. McLachlan, "Environmental Friendly and Simple Processed ZnO as Electron Transport Layer for All-Step-Low-Temperature Processed Efficient Regular Perovskite Solar Cells," In review *(ACS nano)*

Furthermore, the following work is not included in this thesis, but was carried out during this period of research in collaboration with others:

- T. Du, C. Burgess, J. Kim, J. Durrant, **J. Zhang**, and M. McLachlan, "Formation, location and beneficial role of PbI_2 in lead halide perovskite solar cells," *Sustain. Energy Fuels*, vol. 1, 119–126, 2017.

- G. Berdiyorov, K. Harrabi, U. Mehmood, F. M. Peeters, N. Tabet, **J. Zhang**, I. A. Hussein, and M. A. McLachlan, "Derivatization and Diffusive Motion of Molecular Fullerenes: Ab Initio and Atomistic Simulations," *J. Appl. Phys*., vol. 118, 2, 2015.

- **J. Zhang**, J. Kim, S. Pont, J. R. Durrant, M. A. McLachlan, "Building on Soft Hybrid Perovskites: Highly Oriented Oxides as Electron Transport and Humidity Protect Layers," In review *(Advanced Functional Materials)*

- T. Wang*, **J. Zhang***, A. Cheetham, M. A. McLachlan, S. Smoukov, "Hybrid Perovskite Materials with Excellent Thermal Stability," In review *(Advanced Materials)*

Acknowledgement

First and foremost, I am eternally grateful to my supervisor Dr. Martyn McLachlan for his continued advice, patience and support over the last four years. His wisdom, enthusiasm and preciseness on science deeply influence me and make me to choose to continue on the way in science. I would also like to thank co-supervisor Prof. Neil Alford for his encouragement and giving me this precious opportunity to come to this wonderful place.

I am indebted to everyone who helped me in this research. Prof. James Durrant for kindly allowing me to use his lab for solar cell fabrication and providing fruitful discussions on solar cell device physics, Dr. David Payne for the fruitful discussion on photoelectron spectroscopy, Jiaying for TPV test, Ching-Hong for TAS test, Prof. John De Mello and Dr. James Bannock for kindly providing the P3HT materials. I would also like to thank Zhe, Xiaoe, Pabitra and Jinhyun who helped me in the cleanroom.

I am grateful to all the lovely people of the McLachlan group: Jorge for getting me set-up in the initial stage; Claire for TEM and Hall measurements; Maurizio for XPS, FTIR and majority of Kelvin probe measurements; Yoann and Becky for TFT tests. To everybody else in the McLachlan group: Joe, Rob Hewlett, Kirsty, Rob Maller, Tian, Bob, Jaspreet, Chien-Ting, David, Ahmed, Jonathan, Huda, Feichi and Yan, but also Xuemei, Tiesheng, Daniel, Heng and Xiangyu for useful discussions and all the fun times both in and out of the office.

I would also like to show my gratitude to my flatmates and long-term friends Bin, Dong and Zhaolong for all the hard times we went through together and the countless wine and beer bottles.

A special thanks go to my parents for their unconditional love and support, without which I would not be where I am. And also my grandma, who makes me look back now and then when I go forward.

Finally, I would like to acknowledge the China Scholarship Council and the Amrourers & Brassiers's Company for the financial support.

Abstract

In the solar energy arena, there is a considerable market for portable, lightweight, and flexible solutions for solar energy harvesting, in which organic and perovskite photovoltaics are two promising candidates. Cathode-bottom device architecture is commonly used in organic and perovskite photovoltaics due to its long-term stability. However, in this structure the electron transport layer (ETL) adjacent to the cathode commonly requires high temperature annealing, which limits the use of flexible substrates. In this thesis, low temperature processed ZnO thin films are applied as ETLs in organic and perovskite solar cells with two fabrication methods employed: i) sol-gel chemistry and ii) aqueous ammonia approach.

In terms of ZnO films by two methods, the relationship between the film composition and the film properties (optical, electrical, surface morphological) is elucidated. The low temperature processed ZnO by sol-gel chemistry, which was previously commonly considered as amorphous ZnO, has been confirmed consisting of ZnO nanoparticles embedded in an extended amorphous organic matrix in our study. The aqueous processed counterpart has been confirmed containing only ZnO nanoparticles. The distinct compositional difference of two low temperature processed films results in some interesting comparisons, not only in the film properties but also when applied in the organic and perovskite solar cells. In addition, the influence of film processing temperature, in a range from as-cast to 450 ˚C high temperature, is investigated.

We have proved that sol-gel and aqueous processed ZnO films both are effective ETLs in the application of OPVs. Specially, the work function of the ETLs shows significant impact on the device performance. In the application of perovskite solar cells, despite the intrinsic nature of the thermal instability of perovskite when fabricated on ZnO, the ZnO/PCBM bilayer ETLs with two ZnO processing routes both enable all-low-temperature, thermal stable, low hysteresis and high performance devices.

Abbreviations

AFM	Atomic force microscopy
B.E.	Binding energy
BHJ	Bulk heterojunction
CB	Conduction band
DMSO	Dimethyl sulfoxide
EA	Electron affinity
E_F	Fermi level
E_g	Energy bandgap
ETL	Electron transport layer
FF	Fill factor
FFT	Fast Fourier transform
FTIR	Fourier transform infrared spectroscopy
FWHM	Full width at half maximum
GBL	Gamma-butyrolactone
High-T	High temperature processing
HMT	Hexamethylenetetramine
HOMO	Highest occupied molecular orbital
HOPG	Highly oriented pyrolitic graphite
HTL	Hole transport layer
ICBA	Indene-C_{60}-bisadduct
IP	Ionisation potential
ITO	Indium tin oxide

J	Current density
J_{SC}	Short circuit current density
J-V	Current density – voltage
Low-T	Low temperature processing
LUMO	Lowest unoccupied molecular orbital
MEA	2-aminoethanol
M_n	Number average molecular weight
MoO_X	Molybdenum oxide
M_w	Weight average molecular weight
OPV	Organic photovoltaic
P3HT	Poly-(3-hexylthiophene)
$PC_{(61)}BM$	[6,6]-phenyl-C61-butyric acid methyl ester
$PC_{71}BM$	[6,6]-Phenyl-C71-butyric acid methyl ester
PCE	Power conversion efficiency
PDI	Polydispersity index
PEI	Polyethylenimine
PTB7	oly[[4,8-bis[(2-ethylhexyl)oxy]benzo[1,2-b:4,5-b']dithiophene-2,6-diyl][3-fluoro-2-[(2-ethylhexyl)carbonyl]thieno[3,4-b]thiophenediyl]]
PTFE	Polytetrafluoroethylene
Ref	Reference
RMS	Root mean square
R_s	Series resistance
R_{sh}	Shunt resistance
RT	Room temperature
SEM	Scanning electron microscopy

TA	Transient absorption
TCO	Transparent conducting oxide
TEM	Transmission electron spectroscopy
TFT	Thin film transistor
TMO	Transition metal oxide
TPC	Transient photocurrent
TPV	Transient photovoltage
TGA	Thermogravimetric analysis
UV	Ultraviolet
V	Voltage
VB	Valance band
Vis	Visible
V_{OC}	Open circuit voltage
XPS	X-ray photoelectron spectroscopy
XRD	X-ray diffraction
ZAD	Zinc acetate dihydrate
ZnO	Zinc oxide

Contents

Declaration of Originality 2
Foreword 3
Acknowledgement 5
Abstract 6
Abbreviations 7
Contents 10
List of Figures and Tables 14
Chapter 1 – Introduction 23
1.1 Photovoltaics 24
1.1.1 Silicon solar cells 24
1.1.2 Compound thin film solar cells 25
1.1.3 Dye sensitized solar cells 26
1.1.4 Organic and perovskite solar cells 26
1.1.5 Motivation for organic and perovskite photovoltaics 27
1.2 Organic photovoltaics 28
1.2.1 Materials 28
1.2.2 Device structure 32
1.2.3 Device operating principles 35
1.3 Perovskite photovoltaics 38
1.3.1 Materials 38
1.3.2 Device structure 43
1.3.3 Device operating principle 45
1.4 Interfacial layers in organic and perovskite solar cells 48
1.4.1 Functions of interfacial layers 48
1.4.2 Hole transport layer 53
1.4.3 Electron transport layer 56
1.5 ZnO properties and processing methods 62
1.5.1 ZnO properties 62
1.5.2 ZnO low temperature processing methods 63
1.5.3 ZnO films by sol-gel method 67
1.5.4 ZnO film by carbon-free chemistry 70
1.6 Summary 72
References 73
Chapter 2 - Characterisation Techniques 89
2.1 Structural characterisation 89

2.1.1 X-ray diffraction 89
2.1.2 Transmission electron microscopy 90
2.2 Chemical analysis 90
2.2.1 X-ray photoelectron spectroscopy 90
2.2.2 Fourier transform infrared spectroscopy 91
2.3 Surface morphology characterisation 91
2.3.1 Scanning electron microscopy 91
2.3.2 Atomic force microscopy 93
2.4 Optical techniques 94
2.4.1 Ultraviolet-visible spectrophotometry 94
2.4.2 Contact angle measurement 95
2.4.3 Line profilometry 95
2.5 Electrical characterisation 96
2.5.1 Kelvin probe measurement 96
2.5.2 Thin film transistor 97
2.5.3 Hall effect measurement 97
2.5.4 Four point probes 97
2.6 Solar cell characterisation 98
2.6.1 Current density – voltage characteristics 98
2.6.2 Transient photovoltage and photocurrent measurement 98
2.6.3 Transient absorption spectroscopy 99
References 99
Chapter 3 - Sol-gel derived ZnO Film Properties 101
3.1 Introduction 101
3.2 Experimental methods 101
3.2.1 Precursor solution 101
3.2.2 ZnO film formation 101
3.3 Results and discussion 102
3.3.1 Crystallinity 102
3.3.2 Chemical analysis 106
3.3.3 Optical properties 109
3.3.4 Surface morphology 113
3.3.5 Electrical properties 116
3.4 Conclusions 119
References 120
Chapter 4 - Sol-gel derived ZnO as Electron Transport Layers for Organic Solar cells 122
4.1 Introduction 122
4.2 Experimental methods 122
4.2.1 Solar cells fabrication 122

4.3 Results and discussion 123
4.3.1 Wetting 123
4.3.2 Device performance 123
4.3.3 Operating principles 126
4.3.4 OPV with other active layer materials 129
4.4 Conclusions 134
References 134
Chapter 5 - Sol-gel derived ZnO as Electron Transport Layers for Perovskite Solar Cells 136
5.1 Introduction 136
5.2 Experimental methods 136
5.2.1 Perovskite films 136
5.2.2 Perovskite solar cells 137
5.3 Results and discussion 137
5.3.1 ZnO/perovskite interface 137
5.3.2 Interfacial modification 141
5.4 Conclusions 149
References 149
Chapter 6 - Aqueous processed ZnO as Electron Transport Layers for Organic and Perovskite Solar Cells 151
6.1 Introduction 151
6.2 Experimental methods 151
6.2.1 Zinc precursor solution 151
6.2.2 ZnO film formation 152
6.2.3 OPV fabrication 152
6.3 Results and discussion 152
6.3.1 ZnO films 152
6.3.2 ZnO films for organic solar cells 163
6.3.3 ZnO films for perovskite solar cells 165
6.4 Conclusions 173
References 174
Chapter 7 - Conclusions and Future Work 176
References 179
Appendix A - Sol-gel derived ZnO Films Properties 180
A.1 Starting materials 180
A.2 Film thickness measurement 180
A.3 TGA results of zinc acetate dihydrate 182
A.4 ZnO nanostructures by hydrothermal growth 182
A.4.1 Experimental 184

A.4.2 Nanorods 185
A.4.3 Dense layer and nanowalls 190
Appendix B - Sol-gel derived ZnO as Electron Transport Layers for Organic Solar cells 193
B.1 Starting materials 193
B.2 ZnO thickness dependent OPVs 193
B.3 Statistical data of OPV performance 197
B.4 Sol-gel derived ZnO for OLED 198
B.4.1 Experimental 198
B.4.2 Results and discussion 198
Appendix C - Sol-gel derived ZnO as Electron Transport Layers for Perovskite Solar Cells 201
C.1 Starting materials 201
Appendix D - Aqueous processed ZnO as Electron Transport Layers for Organic and Perovskite Solar Cells 202
D.1 Starting materials 202
D.2 ZnO films by aqueous processing 202
D.3 Aqueous processed ZnO films for OLEDs 203
D.3.1 Experimental methods 203
D.3.2 Results and discussion 203
D.4 Extrinsic dopants 204
References 206

List of Figures and Tables

Chapter 1 Figures

Figure 1.1 Chemical structures of poly(3-hexylthiophene) (P3HT) and polythieno [3,4-b]-thiophene-co-benzodithiophene (PTB7). 29

Figure 1.2 Chemical structures of $PC_{61}BM$, $PC_{71}BM$ and $IC_{61}BA$, adapted from Ref[51]. 31

Figure 1.3 Active layer structures for conjugated polymer solar cells: a) single layer cell; b) bilayer cell; c) bulk heterojunction; d) ordered nanostructured cell, adapted from Ref[63]. 33

Figure 1.4 Conventional (left) and inverted (right) device structure of organic solar cells. 35

Figure 1.5 Representative current density vs. voltage of a solar cell. 36

Figure 1.6 Carrier dynamics of typical bulk heterojunction OPVs. 37

Figure 1.7 Left: Three-dimensional representation of basic perovskite structure AMX_3. Right: Extended network model, adapted from Ref[88]. 39

Figure 1.8 (a) Steady-state UV-visible absorption spectrum for a pure $CH_3NH_3PbI_3$ layer, adapted from Ref[91]; (b) Images of mesoporous $TiO_2/CH_3NH_3Pb(I_{1-x}Br_x)_3$ on FTO substrates, adapted from Ref[89]; (c) Variation of absorption of $TiO_2/CH_3NH_3Pb(I_{1-x}Br_x)_3$ layers, adapted from Ref[89]. 40

Figure 1.9 Effective absorption coefficient of a $CH_3NH_3PbI_3$ perovskite thin film via photothermal deflection spectroscopy compared with other typical photovoltaic materials, adapted from Ref[94]. 40

Figure 1.10 Scheme of 'toluene dripping' solvent engineering process, adapted from Ref[108]. 42

Figure 1.11 Active layer structures for perovskite solar cells: left) mesoporous cell; right) planar cell. 44

Figure 1.12 Conventional (n-i-p) (left) and inverted (p-i-n) (right) device structure of perovskite solar cells. 45

Figure 1.13 Carrier dynamics of typical perovskite solar cells. 46

Figure 1.14 Schematics of possible mechanisms for work function modification by interlayer, adapted from Ref[152]. 49

Figure 1.15 (a) energy level diagram of organic/electrode interfaces. EA: electron affinity, IE: ionisation energy; (b) energy alignment trend in week interacting interfaces, showing linear and pinning regimes; (c) energy level diagram in the case of OPV; (d) the dependence of V_{OC} on energy level alignment. All figures are adapted from Ref[154]. 50

Figure 1.16 Schematic energy level diagrams of charge selective interfacial layer in OPV, adapted from Ref[154]. 51

Figure 1.17 $CH_3NH_3PbI_3$ surface morphology by SEM with good (left) and bad (right) wetting of perovskite precursor solution on lower interlayer. 52

Figure 1.18 Chemical structures of (left) Spiro-OMeTAD, adapted from Ossila website; (right) PEDOT:PSS, adapted from Ref[171]. 53

Figure 1.19 Representative J-V curves with device structure ITO/HTL/$CH_3NH_3PbI_3$/PCBM/LiF/Al. 56

Figure 1.20 (a) perovskite inverted device structure with PCBM (b) J-V characteristic curves for devices with PCBM show reduced hysteresis. Both adapted from Ref[134]. 57

Figure 1.21 (a) chemical structures of PEIE and PEI; (b) Proposed model of molecular dipole (MD)–induced and interface dipole (ID)–induced WF reduction on ZnO surface. Photographs adapted from Ref[200]. 58

Figure 1.22 (a) Energy level alignment with CBs and VBs of TiO_2, ZnO and SnO_2; (b) the proton-transfer reaction at the perovskite (upside)/ZnO (downside) interface, red ball: O, white ball: H, adapted from Ref [222]. 60

Figure 1.23 Schematic energy-level diagram of representative materials: ITO[44], ZnO[224], $PC_{61}BM$[54], $PC_{71}BM$[54], $IC_{61}BA$[44], P3HT[44], PTB7[228], $MAPbI_3$[151], $FAPbI_3$[151], $MAPbBr_3$[151], Spiro-OMeTAD[166] and MoO_X[175]. 61

Figure 1.24 Stick and ball representation of ZnO crystal structure: yellow ball Zn, red ball O. Adapted from Ref [241]. 62

Figure 1.25 (a) TEM image showing ZnO deposited on P3HT by PLD, adapted from Ref[260]; (b) SEM image showing ZnO deposited on $CH_3NH_3PbI_3$ by PLD. 64

Figure 1.26 SEM images of different ZnO morphologies by hydrothermal synthesis: (a) nanorods; (b) nanowalls; (c) compact layer. 66

Figure 1.27 Various ways to form metal oxide films by sol-gel methods, adapted from Ref[209]. 68

Figure 1.28 Description of the chemical equilibria in the initial solution (precursor: zinc acetate dihydrate; additive: MEA; solvent: ethanol), adapted from Ref[284]. 70

Chapter 1 Tables

Table 1.1 Comparisons between TiO_2, SnO_2 and ZnO as electron extraction layer for OPV and perovskite solar cells (positive ✓; negative ×) 61

Chapter 2 Figures

Figure 2.1 A typical XRD pattern of ZnO powders. 89

Figure 2.2 SEM images: (a) a working distance of 5.6 mm showing low depth of field; (b) low magnification (10k) showing large area film uniformity; (c) high magnification (100k) showing film morphology details. 92

Figure 2.3 left) Schematic of the relationship among laser, cantilever and photodiode, adapted from Ref[4]; right) An example of AFM image showing high resolution on height, measured on an ITO substrate surface. 93

Figure 2.4 Transmission spectrum and corresponding Tauc plots of ZnO films on quartz substrates. 95

Figure 2.5 Original pictures of precursor droplets on film surfaces: (a) relatively poor wetting; (b) relatively good wetting. 95

Chapter 2 Tables

Table 2.1 The grain sizes calculated from XRD patterns by the Scherrer formula 90

Chapter 3 Figures

Figure 3.1 XRD patterns for ITO and ITO/ZnO stacks with the same thickness under different heating conditions (ITO diffraction Peaks).* 103

Figure 3.2 XRD patterns for ITO and ITO/ZnO stacks with different thicknesses under the same heating conditions (preheated at 300 ˚C and postannealed at 450 ˚C). (ITO diffraction Peaks)* 103

Figure 3.3 XRD patterns for glass/ZnO stacks with different preheating temperatures. 104

Figure 3.4 TEM image showing the 110 °C annealed ZnO layer between the ITO (left) and PTB7:PC71BM (right) layers within the device. 105

Figure 3.5 STEM dark field image of full device showing, from left to right, the ITO, ZnO (110 °C), PTB7:$PC_{71}BM$, MoO_3 and Ag layers. 106

Figure 3.6 ZnO XPS spectra of C 1s, with different processing temperatures. 107

Figure 3.7 ZnO XPS spectra of O 1s, with different processing temperatures. 107

Figure 3.8 ZnO XPS spectra of Zn 2p, with different processing temperatures. 108

Figure 3.9 ZnO XPS spectra of N 1s, with different processing temperatures. 108

Figure 3.10 FTIR spectra of ZnO with different processing temperatures. 109

Figure 3.11 UV-vis spectra for Glass/ITO/ZnO stacks with different processing temperatures. 110

Figure 3.12 Tauc plots calculated from ZnO on quartz substrates. 111

Figure 3.13 Room temperature PL spectra of ZnO films with different processing temperatures, all normalised to the peak intensity in the NBE region. 112

Figure 3.14 UV-vis spectra for Glass/ITO/ZnO stacks with different thicknesses. 113

Figure 3.15 SEM images of ZnO layers with different processing temperatures. 114

Figure 3.16 AFM image of ZnO films on ITO substrates, inset is the RMS of the films. 115

Figure 3.17 SEM images of ZnO layers prepared from concentrations indicated, measured thicknesses (a) 58 nm; (b) 90 nm; (c) 158 nm. 116

Figure 3.18 Transfer curves of TFT with ZnO films in saturation region, V_d = 45 V. 117

Figure 3.19 The field effect mobility of ZnO films calculated from the transfer curves of TFTs. 117

Figure 3.20 Work functions of the ITO and ITO/ZnO films by Kelvin probe. 119

Chapter 3 Tables

Table 3.1 The $d_{(002)}$ crystallite sizes calculated from XRD patterns for seed layers preheated at 300 ˚C and postannealed at 450 ˚C, refers to Figure 3.2. 104

Table 3.2 The grain size calculated by SEM images for films at 450 ℃ _____ *116*

Table 3.3 Resistivity, mobility and carrier concentration of ZnO films by Hall measurement _____ *118*

Chapter 4 Figures

Figure 4.1 Representative J-V curves for devices prepared using ZnO electron transport layers (ETLs) deposited at the temperatures indicated. Inset shows a schematic illustration of the devices. _____ *124*

Figure 4.2 Measured device performance characteristics for P3HT:ICBA based photovoltaic devices fabricated with ZnO ETLs processed at the temperatures indicated. a) Open circuit voltage (V_{OC}) and short circuit current density (J_{SC}). b) Fill factor (FF) and power conversion efficiency (PCE). c) Series resistance (R_s) and shunt resistance (R_{sh}). _____ *125*

Figure 4.3 Flat band energy diagram showing the energy levels of the various materials contained in our device stacks[2–4]. The measured change in work function of the ETLs is highlighted which falls below the work function of the ITO cathode when processed at 450 ℃. _____ *126*

Figure 4.4 Sheet resistances of ITO substrates with and without 450˚C annealing. _____ *127*

Figure 4.5 Representative current density - voltage plots of ITO/ZnO/Ca/Ag stacks. _____ *127*

Figure 4.6 Dark J–V characteristics shown for all devices, a clear increase in leakage current is observed as the ETL processing temperature is increased (semi-log scale). _____ *128*

Figure 4.7 Representative J-V curves for devices prepared using ZnO electron transport layers (ETLs) deposited at the temperatures indicated. Inset shows a schematic illustration of the devices. _____ *129*

Figure 4.8 Measured device performance characteristics for PTB7:PC_{71}BM based photovoltaic devices fabricated with ZnO ETLs processed at the temperatures indicated. a) Open circuit voltage (V_{OC}) and short circuit current density (J_{SC}). b) Fill factor (FF) and power conversion efficiency (PCE). c) Series resistance (R_s) and shunt resistance (R_{sh}). _____ *130*

Figure 4.9 Representative dark J-V curves for devices prepared using ZnO ETLs deposited at the temperatures indicated. _____ *131*

Figure 4.10 The device charge carrier density and lifetime were measured by (a) transient photocurrent (TPC) and (b) transient photovoltage (TPV) of PTB7:PC_{71}BM solar cells with ZnO at 110 and 450 ℃. _____ *132*

Figure 4.11 (a) Representative J-V curves of PTB7:PC_{71}BM solar cells with 110 and 450 ℃ ZnO ETLs under dark and illumination; (b) open circuit voltage V_{OC} measured value and reconstruction from charge density n and charge carrier lifetime τ for 110 and 450 ℃ processed devices as a function of light intensities. _____ *133*

Chapter 4 Tables

Table 4.1 Contact angles of P3HT:ICBA blend solution droplet on top of the surface of ZnO layers.123

Chapter 5 Figures

Figure 5.1 XRD patterns of glass/ITO/ZnO/$CH_3NH_3PbI_3$ stacks annealed at 100 °C in a N_2 filled glovebox for (a) 60 s; (b) 10 min. _____ *138*

Figure 5.2 (a) Normalised and (b) original XRD patterns of glass/ITO/ZnO (200 °C)/$CH_3NH_3PbI_3$ stacks annealed at 100 °C; (c) original XRD patterns of glass/ITO/ZnO (450 °C)/ $CH_3NH_3PbI_3$ stacks annealed at 100 °C. _____ *139*

Figure 5.3 XRD pattern of $CH_3NH_3PbI_3$ on ZnO (110 °C), by controlling the perovskite annealing time we confirm the co-existence of diffraction peaks of MAI-PbI_2-DMSO and PbI_2 (001), indicating that the perovskite degradation has begun before the complete transformation of MAI-PbI_2-DMSO. __ *139*

Figure 5.4 SEM images of $CH_3NH_3PbI_3$ on top of ZnO films, annealed at 100 °C for 60 s. _____ *140*

Figure 5.5 SEM images of $CH_3NH_3PbI_3$ on top of ZnO (200 °C) films, annealed at 100 °C. _____ *141*

*Figure 5.6 XRD patterns of glass/ITO/ZnO (450 °C)/$CH_3NH_3PbI_3$ (left) and glass/ITO/ZnO (110 °C)/ PCBM/ $CH_3NH_3PbI_3$ (right) stacks annealed at 100 °C in a N_2 filled glovebox for 20 min.*_____ *142*

Figure 5.7 (a) Representative J-V curves for perovskite devices prepared using ZnO (110 °C) and ZnO (110 °C)/PCBM as ETLs; (b) J-V curves for perovskite devices using ZnO (110 °C)/PCBM bilayer as ETLs measured by forward and reverse scans, with 0.2 V/s scan rate. _____ *143*

Figure 5.8 Representative J-V curves of illuminated devices with PCBM-only as ETLs, the thickness of PCBM: (a) 0 nm; (b) 30 nm; (c) 35 nm; (d) 50 nm; (e) 100 nm. _____ *144*

Figure 5.9 UV-visible transmission spectra of glass/ITO/PCBM and glass/ITO/ZnO (110 °C)/PCBM stacks. _____ *145*

Figure 5.10 XRD patterns of (a) ITO/PCBM/$CH_3NH_3PbI_3$ and (b) ITO/ZnO(110 °C)/PCBM/ $CH_3NH_3PbI_3$, both showing pure $CH_3NH_3PbI_3$ phases without precursor or PbI_2 peaks. _____ *145*

*Figure 5.11 Representative AFM images of PCBM-only and ZnO (110 °C)/PCBM films on ITO substrates.*_____ *146*

Figure 5.12 SEM images of (a) PCBM, (b) ZnO (110 °C)/PCBM, (c) $CH_3NH_3PbI_3$ on PCBM and (d) $CH_3NH_3PbI_3$ on ZnO (110 °C)/PCBM films. _____ *146*

*Figure 5.13 Flat band energy diagram showing the energy levels of the various materials contained in our device stacks. The measured change in work function of the ETLs is highlighted.*_____ *148*

*Figure 5.14 (a) Transient absorption kinetics of glass/PCBM/$CH_3NH_3PbI_3$ and glass/PCBM/ZnO (110 °C)/$CH_3NH_3PbI_3$ excited at 500 nm (7 uJ/cm^2) and probed at 750 nm in N_2 atmosphere; (b) Transient absorption spectra of PCBM/$CH_3NH_3PbI_3$ excited at 500 nm (15 uJ/cm^2) in N_2 atmosphere.*_____ *148*

Chapter 5 Tables

Table 5.1 Contact angles of $CH_3NH_3PbI_3$ precursor solution droplet on top of ZnO films. _____ *138*

Table 5.2 The grain size measured by SEM images for $CH_3NH_3PbI_3$ films on top of PCBM layer and ZnO (110 °C)/PCBM bilayers. _____ *147*

Table 5.3 Work functions of ETLs on ITO substrates, measured by Kelvin Probe _____ *147*

Chapter 6 Figures

Figure 6.1 XRD patterns of ZnO films processed by the aqueous method on glass, with different processing temperatures. _____ *153*

Figure 6.2 HRTEM image showing the 100 °C annealed ZnO layer deposited on ITO substrate (lower dark area), indicating the nanocrystalline nature of ZnO (100 °C) films. A selection of fringe spacings and corresponding wurtzite ZnO planes are annotated and the inset shows a fast Fourier transform (FFT). _____ *154*

Figure 6.3 FTIR spectra of ZnO with different processing temperatures. _____ *155*

Figure 6.4 ZnO XPS spectra of O 1s, with different processing temperatures. _____ *155*

Figure 6.5 ZnO XPS spectra of C 1s, N 1s and Zn 2p, with different processing temperatures. _____ *156*

Figure 6.6 Left: UV-vis spectra for glass/ITO/ZnO stacks with different processing temperatures; Right: An optical photo of a glass/ITO/ZnO (100 °C) substrate. _____ *157*

Figure 6.7 Tauc plots calculated from ZnO films on quartz substrates. _____ *158*

Figure 6.8 AFM image of ZnO films on ITO substrates, inset is the rms roughness of the films. ____ *159*

Figure 6.9 SEM images of ZnO layers with different processing temperatures. _____ *160*

Figure 6.10 Transfer curves of TFT with ZnO films in saturation region, V_D = 35 V. _____ *161*

Figure 6.11 Field effect mobilities of ZnO films calculated from transfer curves in saturation region. _____ *161*

Figure 6.12 (a) Schematic illustration of OPVs with inverted device architecture; (b) Energy level diagram of devices; (c) Molecular structure of electron donor (PCDTBT) and acceptor ($PC_{71}BM$) active layer materials and (d) representative J-V curves for devices prepared using ZnO ETLs deposited at the temperatures indicated. _____ *164*

Figure 6.13 Representative dark J-V curves for PCDTBT:$PC_{71}BM$ solar cells prepared using ZnO ETLs deposited at the temperatures indicated. _____ *165*

Figure 6.14 XRD patterns of glass/ITO/ZnO/$CH_3NH_3PbI_3$ stacks annealed at 100 °C in a N_2 filled glovebox, normalised data with different ZnO films under 1 min thermal stability test. _____ *166*

Figure 6.15 SEM images of $CH_3NH_3PbI_3$ on top of ZnO films, annealed at 100 °C in a N_2 filled glovebox for 60 s. _____ *167*

Figure 6.16 Representative J-V curves for perovskite devices prepared using (a) ZnO (100 °C) and (b) ZnO (450 °C) as ETLs, measured by forward and reverse scans with a 0.2 V/s scan rate. _____ *169*

Figure 6.17 XRD patterns of glass/ITO/ZnO (450 °C)/$CH_3NH_3PbI_3$ (left) and glass/ITO/ZnO (100 °C)/ PCBM/$CH_3NH_3PbI_3$ (right) stacks annealed at 100 °C in a N_2 filled glovebox for 20 min. _____ *170*

Figure 6.18 Representative J-V curves for perovskite devices prepared using ZnO (100 °C)/PCBM as ETLs, measured by forward and reverse scans with 0.2 V/s scan rate. _____ *170*

Figure 6.19 UV-visible transmission of glass/ITO/ZnO (100 ℃) and glass/ITO/ZnO (100 ℃)/PCBM stacks. _____ *171*

Figure 6.20 AFM images of ZnO (100 ℃) and ZnO (100 ℃)/PCBM on ITO substrates. _____ *172*

Figure 6.21 Flat band energy diagram showing the energy levels of the various materials contained in our device stacks. The measured change in work function of the aqueous processed ZnO (100 ℃) and ZnO (100 ℃)/PCBM is highlighted. _____ *172*

Chapter 6 Tables

Table 6.1 The grain sizes calculated from XRD patterns for ZnO layers with different temperatures _____ *153*

Table 6.2 The granular size calculated by SEM images for ZnO films with annealing temperatures _ *160*

Table 6.3 Work functions of ZnO prepared on ITO substrates, measured by Kelvin probe _____ *162*

*Table 6.4 Statistical data of PCDTBT:$PC_{71}BM$ based OPV devices*_____ *164*

*Table 6.5 Contact angles of $CH_3NH_3PbI_3$ precursor droplet on ZnO and ZnO/PCBM surfaces*_____ *165*

Table 6.6 The grain size measured by SEM images for perovskite films on ZnO films, annealed at 100 °C in a N_2 filled glovebox for 60 s. _____ *168*

Table 6.7 Work functions of ZnO (100 ℃) and ZnO (100 ℃)/PCBM on ITO substrates, measured by Kelvin Probe. _____ *172*

Table 6.8 Work functions of sol-gel derived ZnO (450 ℃) and ZnO (450 ℃)/PCBM on ITO substrates, measured by Kelvin Probe. _____ *173*

Appendix A Figures

Figure A.1 The relationship between the thickness of ZnO planar films and the solution concentration. The average values are plotted and standard deviations are shown as error bars. *181*

Figure A.2 TGA curve of ZnO formation from zinc acetate dihydrate. _____ *182*

Figure A.3 Schematic diagram illustrating the variation of nanorod growth with KCl addition, a) 0 mM, b) <100 mM, c) >>100 mM. Adapted from Ref[2]. _____ *183*

*Figure A.4 Pictures of water bath apparatus.*_____ *184*

Figure A.5 Hydrothermal growth on bare ITO substrates, no nanorod arrays are found. _____ *185*

*Figure A.6 UV-vis spectra for Glass/ITO/ZnO seed layers with different heat treatment conditions/ZnO nanorods in the range of 300-1100nm.*_____ *185*

Figure A.7 XRD patterns of ITO/ZnO seed layers with varying processing temperatures/ZnO nanorod stacks. (ITO diffraction Peaks)* _____ *186*

*Figure A.8 SEM images of nanorods on the seed layers with different thicknesses, (a) 0.1 M, (b) 0.3 M, (c) 0.5 M, (d) 0.75 M.*_____ *187*

*Figure A.9 SEM image of nanorods on the seed layers of different heating conditions, (a) 110 ˚C, (b) 200˚C, (c) 300˚C, (d) 450˚C.*_____ *189*

Figure A.10 SEM images of nanorods on 60nm-thick seed layers by pulsed laser deposition (PLD). _____ *190*

*Figure A.11 SEM images of dense layer, (a) top-view and (b) cross section.*_____ *191*

Figure A.12 ZnO nanowalls obtained by etching dense layer in KOH for 15 min, (a) nanowall morphology from top-view; (b) enlarged image shows the wall thickness around 50 nm; (c) uniform morphology is confirmed in large area. _____ *191*

Figure A.13 Etching in KOH for 30 min, (a) nanowall morphology from top-view shows wall width is decreased; (b) enlarged image shows no change of wall thickness. _____ *192*

*Figure A.14 Etching after 1h shows no ZnO nanostructure left.*_____ *192*

Appendix A Tables

Table A.1 Starting materials _____ *180*

Table A.2 Thickness of ZnO planar films at 3000 rpm spinning speed _____ *181*

Table A.3 Thickness of ZnO planar films at 2000 rpm spinning speed _____ *182*

Table A.4 The FWHM and (002) peak intensity obtained from XRD patterns of ZnO nanorods with seed layers of different heating conditions. _____ *186*

Table A.5 The diameter, length and areal density of nanorods by variation of seed layer thickness _____ *188*

*Table A.6 The diameter, length and areal density of nanorods by variation of the seed layer heating conditions.*_____ *190*

*Table A.7 Nanorod parameters of nanorods on seed layers by PLD.*_____ *190*

Appendix B Figures

Figure B.1 Open-circuit voltage (V_{OC}) changing with ZnO film thickness (controlled by precursor concentration) under different ZnO processing temperatures. _____ *194*

Figure B.2 Short-circuit current density (J_{SC}) changing with ZnO film thickness under different ZnO processing temperatures. _____ *195*

*Figure B.3 Fill factor (FF) changing with ZnO film thickness under different ZnO processing temperatures.*_____ *196*

Figure B.4 Power conversion efficiency (PCE) changing with ZnO film thickness under different ZnO processing temperatures. _____ *197*

*Figure B.5 Light turn-on voltage (V) of PLEDs with different ZnO processing temperatures.*_____ *199*

*Figure B.6 Current density and current efficiency at 1000 cd/m^2 with different ZnO processing temperatures.*_____ *199*

Figure B.7 Voltage and power efficiency at 1000 cd/m^2 with different ZnO processing temperatures. _____ *200*

Appendix B Tables

Table B.1 Starting materials ____ *193*

Table B.2 Statistical data of P3HT:ICBA based OPV devices ____ *197*

Table B.3 Statistical data of PTB7:$PC_{71}BM$ based OPV devices ____ *198*

Appendix D Figures

Figure D.1 ZnO XPS spectra of O 1s (O-Zn) and Zn $2p_{3/2}$, with different processing temperatures, indicating the E_F shift of ZnO films. ____ *202*

Figure D.2 Large area SEM images of ZnO films by ammonia methods. ____ *203*

Figure D.3 J-V-L data of representative OLED devices with various ZnO layers. ____ *204*

Figure D.4 SEM images of Ga-doped ZnO films by aqueous processing with 3 at% doping: (a) $Ga(NO_3)_3xH_2O$ as dopant; (b) $Ga(OH)_3$ as dopant. ____ *205*

Appendix D Tables

Table D.1 Starting materials ____ *202*

Table D.2 OLED performance with various ZnO layers ____ *204*

Table D.3 Field effect mobilities of ZnO films calculated from transfer curves in saturation region. ____ *205*

Chapter 1 – Introduction

Since the industrial revolution of the 18th century the rapid development of modern industrial society has been driven by fossil fuels, however the demand for these finate resources coupled with their environmental impact has led to a search for supplies of clean, renewable energy.

In 1972, the report 'The Limits to Growth' by the Club of Rome simulated the consequence of interactions between human and Earth's systems[1]. It led society and governments beginning to sustainable development from a global perspective. One major challenge of the sustainable development is the utilisation of renewable energy sources.

Nowadays, the exploitation of renewable energy sources is driven not only by the deceasing fossil fuel resources, but by increasing global populations and attempts to moderate the anthropogenic global warming effect. There are numerous complimentary solutions to deliver clean, renewable power including; wind, water, solar and arguable nuclear power. In many cases the local environment dictates the optimum solution for a given location. Whilst some solutions *e.g.* water based technologies (hydro/tidal) may be suited to mountainous or coastal regions others, particularly those based on harnessing solar energy are well suited in most locations and indeed have established a market share in numerous global locations. In this thesis the research described is focused on the development of new materials aimed at improving efficiency and lifetime in two exiting areas of photovoltaics, namely organic photovoltaics (OPVs) and the emerging perovskite photovoltaics.

In the following pages a background to photovoltaics is given, primarily to describe the motivation for studying OPV and perovskite photovoltaics. In the latter sections, a comprehensive literature review of organic and perovskite photovoltaics is given which develops into tackling the research problem addressed during this research *i.e.* the requirement for charge selective interlayers in both technologies. This develops into a focused review of ZnO as an electron transport layer (ETL), where the specific material properties and fabrication methods are described. The chapter concludes with a brief outline of the thesis and an overview of the individual chapter contents.

1.1 Photovoltaics

The photoelectric effect, first observed by Becquerel in 1839[2] and later described in greater detail by Einstein in 1905[3], suggested a new area of science whereby energy can be created by converting light into electricity. The first report of a photovoltaic cell by Fritts in 1883, described selenium being inserted between two gold electrodes – however this attracted little attention at the time.

What we may consider as the modern solar cell was first developed at Bell Labs during the 1950's based on the silicon p-n junction[4]. However, at the time the costs associated with producing high quality silicon were prohibitively high, which hindered development and subsequent commercialising. Since then, new photovoltaic materials and fabrication techniques have been continuously investigated, with the aim to decreasing the system cost until be competitive with other resources of electricity. Now the cost of PV-produced electricity is commercially competitive although further cost reduction and other challenges still remain.

Here a brief introduction of the widely studied photovoltaic materials is given. The technological merits and relative disadvantages of each material will be discussed. In order to facilitate a comparison between power conversion efficiency (PCE) here only single junction devices are discussed.

1.1.1 Silicon solar cells

Silicon photovoltaics are the most mature technology, with their development extending over some 30 years. Crystalline Si has an ideal bandgap (1.12 eV) based on the terrestrial solar spectrum. The fundamental disadvantage is its indirect bandgap, such that the absorption coefficient is relatively low, meaning layers (100-200 μm) are required to absorb sufficient light. Owing to the high carrier mobilities in crystalline Si, (electron/hole mobilities are 1200 and 400 $cm^2V^{-1}s^{-1}$ [5] respectively) the thick absorbing layers do not cause significant bulk recombination.

In typical monocrystalline Si solar cells, n-type doped and p-type doped regions form a homojunction, at which interface an electric field is generated. When light illuminates devices photon absorption generates electron-hole pairs. Due to the low exciton binding energy, charge carriers freely mobile in the crystal. When the charge carriers reach the region of the junction they are separated into free electrons and holes, the built-in field then moves electrons towards the n-type region and holes to the p-type region. Thus, when connected to an external load, photogenerated current can be extracted to do work. Today monocrystalline Si has already demonstrated operational efficiencies of 25.6%[6], which is still somewhat lower than the 29.4% theoretical limit based on the Shockley-Queisser model[7].

In addition to monocrystalline Si solar cells, multicrystalline Si cells have also been widely investigated, primarily due to their reduced manufacturing costs. At the time of writing the record reported PCE of multicrystalline Si photovoltaics was 21.3% [8] .This is mainly attributed to grain boundary effects that result in increased recombination and ultimately reduced charge carrier collection.

Considering more recent silicon technologies the emergence of microcrystalline and nanocrystalline devices, fabricated by chemical vapor deposition (CVD), have record PCEs of 11.8%[9]. This is significantly lower than the other silicon technologies, owing to the combination of lower film thickness and increased grain boundary losses; these must however be offset over the reduced fabrication costs. Amorphous silicon (a-Si) can also be made in thin film geometry, this is an interesting material as the optical absorption is greater than crystalline Si. The bandgap of a-Si is somewhat higher than the ideal value, typically 1.7 – 1.8 eV, nonetheless record PCE values of 10.2%[6] have been reported.

As a consequence of the achievable performances, the established infrastructure and more recently the declining raw materials and processing costs the global PV market is dominated by crystalline silicon devices, some 90% of the total market share, where multicrystalline and monocrystalline Si represent 65% and 35% respectively[10]. Furthermore the high reliability and limited degradation – with lifetime guarantees of 25 years offered by manufacturers, it's easy to see why silicon technology currently dominates.

Whilst silicon leads in the photovoltaic marketplace the ability to prepare thin film devices is challenging for silicon-based technologies. It is in the realm of thin film devices where the development of numerous technologies has accelerated over the past few decades and where significant advancements can still be made.

1.1.2 Compound thin film solar cells

Compound thin film solar cells consist of a variety of inorganic, non-silicon, materials where subtle changes in composition are made to achieve optimum performance. Thin film devices require lower quantities of active materials, which impacts cost. Among these devices GaAs has the highest PCE, with the record reported at 28.8%. This can be partially attributed to the materials possessing a direct bandgap with an ideal bandgap energy of 1.42 eV[6]. The greatest limitation to this technology is the fabrication costs, where CVD is routinely employed. These devices have however found applications in space-limited, high-performance applications including terrestrial satellites.

Two other widely used III-V compound absorbers are InP (E_g=1.35 eV) and GaInP (E_g=1.81 eV), the record PCEs of these materials are 22.1%[6] and 20.8%[6], respectively.

Here the presence of indium, which is an element that has become increasing scarce, limits large scale production and implementation.

$Cu(In,Ga)(Se,S)_2$ (CIGS) have a tunable bandgap from 1.0 - 2.4 eV, achieved by varying the composition, specifically the In/Ga and Se/S ratios; the record PCE is 21.7%[6]. CIGS films are normally deposited by evaporation or sputtering. However, similar to InP and GaInP the presence of In presents a problem to long term development. $Cu(Zn,Sn)(S,Se)_2$ (CZTS) cells were developed as an In free alternative where In/Ga are replaced by Zn/Sn. The band gap of CZTS is also tunable, from 1.0 - 1.6 eV with a record PCE of 12.6%[6], supporting similar fabrication methods as CIGS. As an environment friendly and low cost material, CZTS is expected to have an impact in the marketplace, particularly if the PCE can be further improved.

Another chalcogenide based material is CdTe, with a nearly ideal band gap of 1.43 eV. The maximum reported PCE is 21.5%[6], very close to that of CIGS. Polycrystalline CdTe films are commonly fabricated by evaporation from CdTe powder at around 300 °C[11]. Today CdTe dominates the thin film solar modules that appear in the commercial market, however continuous development of recycling systems are needed owing to the presence of toxic cadmium and the scarce element tellurium.

1.1.3 Dye sensitized solar cells

Dye sensitized solar cells (DSSCs) were first reported by O'Regan and Grätzel in 1991[12]. In DSSCs, a strongly absorbing dye is coated on a highly porous nanostructured semiconducting scaffold (typically TiO_2). Under illumination, electrons are photogenerated from dye molecules and then are rapidly transferred to the oxide. The dye is regenerated by redox couples in a surrounding electrolyte. The circuit is completed by the diffusion of redox active species to the counter electrode.

The current PCE record for DSSCs is 11.9%[6]. Although there is still room for efficiency improvements DSSCs have already reached the commercial market as the first generation of low-cost solar cells[13]. There are further considerations that make DSSCs attractive, including simple fabrication processes and tunable colour and opacities, the latter two parameters being particularly suitable for building integration. In addition, flexible devices can now be fabricated, where conventional porous TiO_2 is prepared at reduced temperatures[14]. Further development of this technology is required, for both efficiency and stability improvement that can be achieved by optimizing the dye species, electrolytes, metal oxides and electrodes.

1.1.4 Organic and perovskite solar cells

Organic photovoltaics (OPV) consist of a variety of combinations of organic small molecules, conjugated polymers and fullerene derivatives. These technologies support

large-area, high-throughput and low-cost fabrication on flexible substrates and aesthetically can obtain colour tunability and variable opacity. The record PCE for OPVs is currently 11.5%[15]. In a typical OPV device there exists a complex multilayer structure, where the core active layer is sandwiched between charge selective electrodes in contact with each of the electrodes. Typically the thickness of the whole device (excluding substrate) is less than 500 nm. New processing routes for the active materials, for example droplet-based microfluidic reactors[16] and the development of non-fullerene acceptor materials will significantly drive down device costs as OPV technologies continue to develop. Issues associated with stability and lifetime remain but in certain *niche* applications OPVs are having a commercial impact.

The emergence of so-called perovskite photovoltaics has had a tremendous impact on the field of photovoltaics. The device structure is derived from DSSCs, where initially the perovskite material was suggested as a replacement sensitizer, making these devices true hybrid inorganic:organic systems. The active material adopts the perovskite crystal structure (AMX_3) in which A is an organic cation (typically CH_3NH_3), M is an inorganic cation (typically Pb) and X is a halide. The highest reported PCE at present is 22.1%[17][18]. Besides the remarkable efficiencies demonstrated in these novel systems their synthesis by low-temperature routes is remarkably simple and colour tunability is possible through compositional changes whilst solution processing supports large volume processing. Further improvements in efficiency are predicted however the issue of device instability following exposure to ultraviolet light, oxygen, heat and humidity remain. Another challenge is to replace the toxic element Pb, where metals such as Bi and Cs are some of the common candidates.

1.1.5 Motivation for organic and perovskite photovoltaics

Photovoltaic materials mainly have two aspects of application. One is large-area photovoltaic system, to compete in electricity markets with other technologies. To achieve this goal and become disruptive device, processing and materials cost require to be addressed. Currently fabrication costs make only a partial contribution to overall cost with component and installation making up some 50% of the total cost, a value that is still increasing [19]. Therefore efficiency remains a key target as potentially smaller cells can be prepared, reducing material and installation costs.

Another important application of photovoltaic materials is flexible electronics, including wearable devices, remote/isolated power generation systems, *etc*. Unlike large-area photovoltaic system, the fabrication cost of solar cells themselves is the key factor in flexible electronics. As a result, to decrease the cost, roll-to-roll, low processing temperature, small material quantities and solution processing are expected during the solar cell fabrication. In addition, device availability in a variety of transparencies and

colours is important for a range of emerging applications. Therefore DSSCs, OPV and perovskite photovoltaics are three promising systems to achieve these objectives. In contrast to the rapid development of organic and perovskite cells, DSSCs have not reported record PCE improvement since 2012. A key advantage to OPV and perovskite cells is that simple device architectures can be implemented where remarkably thin devices deliver comparable performances to many of the established inorganic systems which provides a pathway for flexible devices that can be prepared by numerous high volume processing techniques. For these reasons the emphasis of the research carried out in this thesis is placed on OPV and perovskite photovoltaics.

1.2 Organic photovoltaics

1.2.1 Materials

There has been a tremendous emphasis on developing novel organic semiconducting materials, including small molecules and conjugated polymers during the last decade. Here, some of the more common p-/n-type materials are introduced and a detailed description of the organic materials investigated during this research is given.

1.2.1.1 P-type small molecules

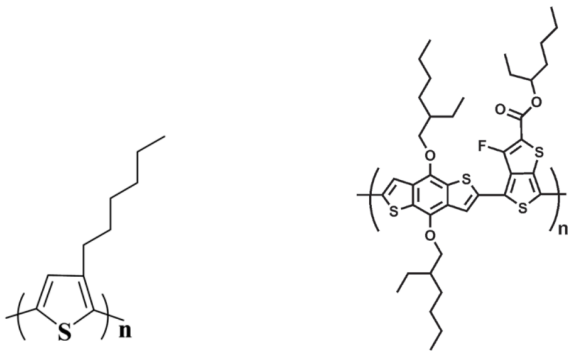
The first observation of utilising organic materials in solar cells was in 1975, where small molecules using chlorophyll pigments were shown in single layer solar cells[20]. Although operational devices were demonstrated there was slow progress until some 10 years afterwards, where in 1986 Tang *et al* reached a breakthrough in devices using a bilayer of copper phthalocyanine (CuPc) and a perylene tetracarboxylic derivative as electron donors and acceptors, respectively[21].

These early demonstrator devices relied on thermal evaporation to deposit the organic active materials. More recently, and in this thesis also, the emphasis has shifted towards solution deposition routes for active layer preparation hence more emphasis is placed here on soluble small molecules. Among the solution processed small molecules, a series of oligothiophenes have been investigated in detail[22][23][24]. The donor-acceptor type small molecules containing solubilising substituents have been intensely developed that are considered as promising materials for organic solar cells. Many structures have been developed to date, including fused acenes, triphenylamine derivatives, merocyanine, isoindigo, subphthalocyanine, diketopyrrolopyrroles, borondipyrromethene, perylene diimides and oligothiophenes[25][26]. Nowadays, OPVs based on soluble small molecules have achieved high performances[27], comparable with conjugated polymer systems.

1.2.1.2 P-type polymers

Solution processed conjugated polymers are the best-studied electron donor materials for OPVs. For conjugated polymers, if the repeat units enable π-orbital delocalisation, electrons can move along the backbone of the chain. And if organized regions can be formed as the polymer solidifies charge hopping between chains may happen by inter-chain electronic coupling. The electric properties of conjugated polymers are highly influenced by the inter-chain charge transport *i.e.* crystal packing is important[28].

Among all the candidate materials, poly(3-hexylthiophene) (P3HT) is one of the most commonly used semiconducting polymers and it was also used extensively in this work, Figure 1.1. P3HT has a high hole mobility (up to 0.1 $cm^2V^{-1}s^{-1}$)[29]. In addition, P3HT is easily synthesised and is commercially available in a range of molecular weights. Bannock *et al*. reported the continuous synthesis of P3HT in droplet-based microreactors, which significantly decreases the synthesis cost and dispersity[16]. P3HT is not only applied as active layer material in OPVs but also applied to organic field effect transistors[30] and as hole transport layer in solid-state dye-sensitized solar cells[31] and perovskite solar cells[32].



P3HT PTB7

Figure 1.1 Chemical structures of poly(3-hexylthiophene) (P3HT) and polythieno [3,4-b]-thiophene-co-benzodithiophene (PTB7).

Crystalline P3HT films show absorption with onset at 650 nm, band gap of 1.9 eV[33]. While for amorphous P3HT, the absorption onset is blue-shifted, caused by exciton localisation which enhances absorption energy.

The properties of P3HT are highly influenced by the molecular structure. Because of the asymmetry of the 3-hexylthiophene monomer, different dimer units can form with different monomer couplings[33][34]. Some combinations tend to form non-planar conformations, which have a negative influence on charge transport. P3HT with higher regioregularity shows better electronic properties due to improved film packing[35], and also shows better OPV performance[36].

The molecular weight also influences the properties of P3HT, including melting point, morphology, mechanical and electronic properties. For solar cell applications, P3HT with higher molecular weight (> 30 kg/mol) shows higher charge carrier mobility, originating from improved carrier transport between crystal domains by being interconnected through chain entanglement[37].

Processing is important to the morphology control of P3HT and therefore has great influence on electronic properties. There are many ways to deposit P3HT, including spin coating, wire bar coating[38], inkjet printing[39], electrodeposition[40], melt pressing[37] *etc*. In solution based P3HT fabrication methods *i.e.* those commonly used for OPVs in research laboratories, precise control of the interaction between P3HT and solvents is important. In general, slower solvent evaporation enables higher portion of crystalline P3HT, which may enhance the charge transport[41]. Post annealing is another method to control the morphology. When the polymer film is heated above its glass transition temperature ~140 °C the alkyl chains can move which has a positive impact on the packing in crystallites[42].

Although P3HT has been well studied and shown good performance in OPV (efficiency above 7%[43]), P3HT still has intrinsic drawbacks. Importantly its relatively large bandgap (1.9 eV) results in insufficient absorption in the near infrared (NIR) region and therefore relatively low photocurrent is achievable. Another issues is the relatively large highest occupied molecular orbital (HOMO), at around -5.2 eV which tends to result in low open circuit voltage (V_{OC}) as this parameter typically depends on the energetic offset between the donor HOMO and the lowest occupied molecular orbital (LUMO) of the electron acceptor[44]. To address these limitations, many new p-type polymers have been developed. Polythieno[3,4-b]-thiophene-co-benzodithiophene (PTB7) is one of the most promising candidates, Figure 1.1.

PTB7 has a bandgap of 1.8 eV and a HOMO level of -5.15 eV[45]. The hole mobility of PTB7 neat films is also high, around 1×10^{-3} $cm^2V^{-1}s^{-1}$[46]. In addition, a strong absorption from 550 nm to 750 nm is recorded for PTB7[47]. Although PTB7 exhibits relatively weak absorption from 300 nm to 500 nm, when combined with $PC_{71}BM$ as an electron acceptor ($PC_{71}BM$ has strong absorption in the visible region) the resulting blend films show strong absorption from 300 - 800 nm[45].

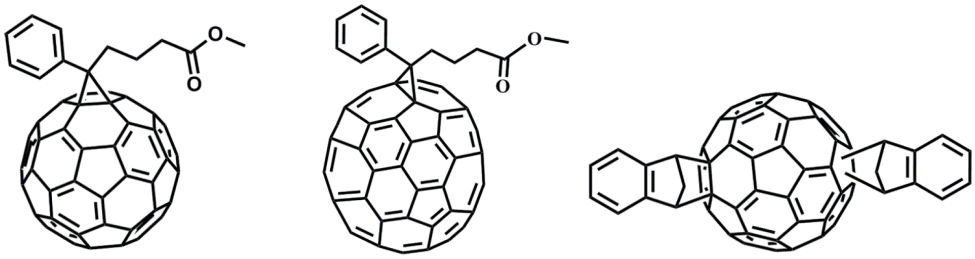
Morphology control plays an important role in PTB7 based solar cells. For depositing a PTB7:$PC_{71}BM$ bulk heterojunction film by spin coating, chlorobenzene (CB) is a typical solvent. The morphology of the blend film can be effectively optimised by adding a small amount of diiodooctane (DIO), a high boiling point solvent. The addition of DIO achieves smaller $PC_{71}BM$ domains and therefore allows $PC_{71}BM$ to more easily penetrate into

PTB7 domains. PTB7 only shows a small fraction (about 20%) of crystalline regions while the majority of PTB7 is amorphous[48].

The molecular weight of PTB7 is also another a key factor in the OPV performance. By increasing the molecular weight of PTB7 from 18 to 128 kg/mol, the efficiencies of PTB7:$PC_{71}BM$ cells were enhanced from 5.41% to 8.50%[49]. The boosted performance results from strengthened absorption, increased hole mobility of PTB7 and optimised PTB7:$PC_{71}BM$ intercalating network with higher PTB7 molecular weight.

1.2.1.3 N-type materials

The n-type semiconductor plays an equally important role in OPVs. Fullerene based acceptor materials are the most widely used in bulk heterojunction (BHJ) organic solar cells. Although recently non-fullerene acceptors have attracted research attention for both small molecule and polymer devices[50], fullerenes remain the best choices when matched with most donor materials. Three commonly used fullerene derivatives, $PC_{61}BM$, $PC_{71}BM$ and $IC_{61}BA$, are shown in Figure 1.2.



$PC_{61}BM$ $PC_{71}BM$ $IC_{61}BA$

Figure 1.2 Chemical structures of $PC_{61}BM$, $PC_{71}BM$ and $IC_{61}BA$, adapted from Ref[51].

$PC_{61}BM$ ([6,6]-phenyl-C_{61}-butyric acid methyl ester), a soluble C_{60} derivative, was the first acceptor material used in BHJ OPVs in 1995 by Heeger *et al.*[52]. The electron mobility of $PC_{61}BM$ is relatively high, about 2×10^{-3} $cm^2V^{-1}s^{-1}$[53]. The HOMO and LUMO energy levels of $PC_{61}BM$ are -5.93 eV and -3.91 eV, respectively[54]. In addition to the low-lying LUMO level which tends to decrease V_{OC}, another drawback of $PC_{61}BM$ is its very weak absorption in visible region[54]. P3HT:$PC_{61}BM$ is the most widely studied BHJ OPVs, achieving PCEs > 4%[55]. The off-set of the LUMO levels of donor and acceptor normally only needs about 0.3 eV to dissociate the excitons at the donor/acceptor interface, while for P3HT:$PC_{61}BM$, this difference is larger than 1 eV, this energy loss decreases the V_{OC}. Furthermore, the absorption of P3HT and $PC_{61}BM$ does not match very well for BHJ active layer because of the P3HT absorption onset at 650 nm and $PC_{61}BM$ weak visible absorption.

Compared to its corresponding C_{60} analogue, $PC_{71}BM$ ([6,6]-phenyl-C_{71}-butyric acid methyl ester)[56] exhibits much stronger absorption in visible range (400 - 700 nm), which makes it widely applied in solar cells with low bandgap polymer donors[54]. However, $PC_{71}BM$ adopts similar electronic energy levels to $PC_{61}BM$, the HOMO and LUMO levels of $PC_{71}BM$ are -5.87 eV and -3.91 eV, respectively[54]. The electron mobility of $PC_{71}BM$ is around 1×10^{-3} $cm^2V^{-1}s^{-1}$[46], which is similar as that of $PC_{61}BM$. One drawback of $PC_{71}BM$ compared with $PC_{61}BM$ is that with the increase of the fullerene cage size the solubility in organic solvents and the miscibility with polymer donors both decrease, which has been observed among $PC_{61}BM$, $PC_{71}BM$ and $PC_{85}BM$[57].

$IC_{61}BA$ (indene-C_{60} biadduct) was initially designed for improving the performance of OPVs reliant on P3HT as a donor[58]. Compared with $PC_{61}BM$, the LUMO of $IC_{61}BA$ is upshifted by 0.17 eV. Consequently, the V_{OC} of P3HT based OPVs with $IC_{61}BA$ reached 0.84 V[58], while those with $PC_{61}BM$ show 0.58 V. In addition, the synthesis of $IC_{61}BA$ is easier than that of $PC_{61}BM$. $IC_{61}BA$ also has excellent solubility, even better than $PC_{61}BM$. For carrier transport, $IC_{61}BA$ exhibits high electron mobility, around 1×10^{-2} $cm^2V^{-1}s^{-1}$ in pure films[59]. One drawback of $IC_{61}BA$ is its weak light absorption in visible region, as also with $PC_{61}BM$[60]. Another limitation is that although $IC_{61}BA$ devices show excellent performance (PCE < 6.5%[61]) in P3HT based OPVs, the attempts to apply $IC_{61}BA$ to other low bandgap polymers have not been very successful. Further studies on high performance polymer donor materials which energy levels are well matched with $IC_{61}BA$ (sufficient LUMO offset) are anticipated.

1.2.2 Device structure

In organic semiconductors, the binding energy of photoexcited excitons is typically too high to allow excitons dissociate into free holes and electrons by thermal excitation[62]. However, the exciton dissociation can occur at an interface owing to the energetic offset. This interface can be between donor/acceptor species or organic semiconductor/metal. Hence, several device structures have been invented, as shown in Figure 1.3.

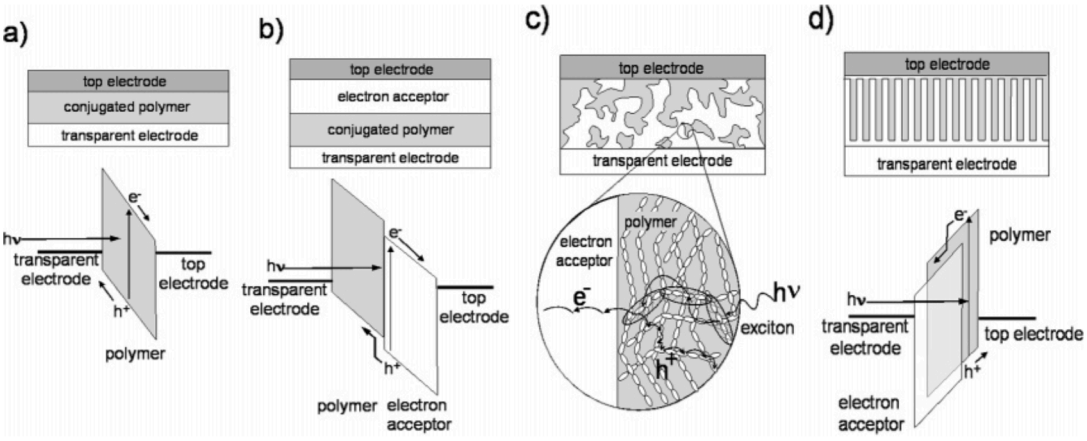


Figure 1.3 Active layer structures for conjugated polymer solar cells: a) single layer cell; b) bilayer cell; c) bulk heterojunction; d) ordered nanostructured cell, adapted from Ref[63].

1.2.2.1 Active layer structure

The first OPVs were prepared as single layer structures, sandwiching a thermally evaporated organic layer between two electrodes with varying work functions[64][65]. For conjugated polymer based cells with single layer structures, the V_{oc} is modest but the photocurrent is typically quite low[66]. The difference between the effective photon absorption (>50%) and the low PCE (1%) indicates the strong tendency of the recombination of photoexcited carriers in the conjugated polymer layer[66].

Bilayer structures were then introduced by inserting an electron acceptor layer onto the donor species[21]. The objective of this work was to facilitate exciton dissociation at donor/acceptor interface, due to the energy offset, then allow free charge to move towards the opposing electrodes[63]. This strategy reduced the possibility of recombination of the free carriers once they moved away from the interfaces because almost no minority carriers are in the intrinsic organic semiconductors. Although bilayer structure modifies the free carrier recombination in single layer structure, the performance of bilayer OPVs is poor. This is because the exciton diffusion length of typical conjugated polymers is only tens of nanometers[22][67] therefore only excitons generated within the exciton length of the donor/acceptor interface have the chance to create free carriers.

One primary way to promote more excitons to transfer into free carriers is to increase the donor/acceptor interface area. Bulk heterojunction (BHJ) OPVs were designed to achieve this goal, by intimately intermixing conjugated polymer donors with polymer[68][69], fullerene[52] or inorganic nanocrystal[70] acceptors. Undoubtedly, this morphology was critical in the development of OPVs. The self-assembly of BHJ nanomaterials is driven by spontaneous phase separation[71]. One goal of tuning the blend morphology is to allow every absorbing site in the active layer to be within its

carrier photoexcitation recombination lengths to the donor/acceptor interface, which means the length scale for phase separation should be in order of 10-20 nm. Another goal is that the separated holes and electrons have fully percolated pathways to their opposite electrodes, which means bicontinuous interpenetrating networks are needed. To achieve these goals, the BHJ film morphology can be controlled by tuning the phase separation during the film formation or by the subsequent annealing of solid films[71]. Specifically, the following parameters are typically fine-tuned: solvent, solution concentration, chemical additives, donor/acceptor ratio, molecular structure of materials and thermal/solvent treatment. Today, the organic solar cell with highest efficiency (11.5%) still relies on the BHJ structure[17][72].

In BHJ devices, the donor and acceptor species are randomly interdispersed. In some cases, some acceptors may be isolated, which leads to electron trapping[63]. To overcome this issue, ordered nanostructured solar cells have evolved. One advantage of ordered nanostructured cells is that there are few isolated donors and acceptors. Another advantage is that the sequential depositions of acceptors and polymers allow the fine interfacial modification between donor/acceptor interfaces, which decreases the recombination at the interfaces[73]. Inorganic materials are typically used to form the nanostructured scaffold due to the established synthesis techniques[74–77]. Two nanostructures are of great interest. One is the mesoporous scaffold (derived from DSSCs), with pore sizes typically around 10s of nanometers, *i.e.* matching the diffusion length of the conjugated polymers[77]. The problem of such structures is that the polymers are hard to fully penetrate into the mesopores[78]. The other is that conjugated polymers and electron acceptors can hold straight pathways to opposite electrodes, which minimises the charge mobile time thus reduces the recombination related to back carrier transport[74–76][79]. But the limitation is that the interspace of scaffold is hard to be as small as that of polymer diffusion length thus leads to insufficient exciton dissociation[75][76]. The contradiction between polymer infiltration and exciton diffusion length hinders the development of ordered nanostructured cells. Breakthroughs on longer exciton diffusion length polymers, interfacial modification, balanced holes/electrons transport are expected.

1.2.2.2 Complete device structure

OPVs are multilayered structures, typically containing transparent substrates (glass or plastic), transparent bottom electrode (transparent conducting oxide), active layer and top electrode (typically a metal). Charge selective layers normally are also needed, inserted between the active layer and electrodes. Due to different functions, they are usually called electron transport layer (ETL) and hole transport layer (HTL). There are two types of device structures according to the electrode positions, as shown in Figure

1.4. In a conventional structure, the bottom electrode acts as anode with top cathode, whist in inverted structure, the top electrode acts as anode with bottom cathode.

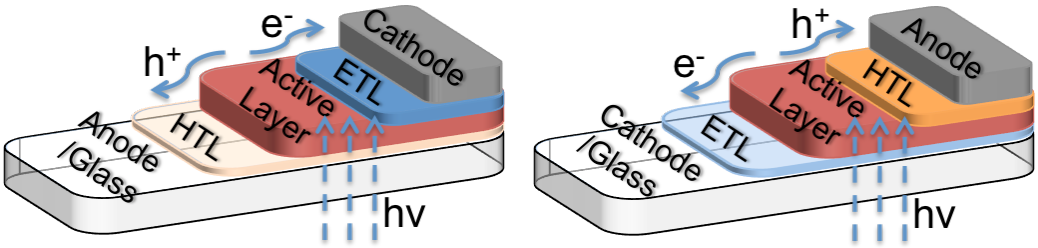


Figure 1.4 Conventional (left) and inverted (right) device structures of organic solar cells.

The early studies of OPVs mainly focused on the devices with the conventional structure due to the popular use of high work function indium tin oxide (ITO) as transparent bottom anode[65]. One drawback of conventional structure is that the top cathode is typically low work function metal such as Ca, Ba or Al which tends to oxidise when exposed to the air. With the development of bulk heterojunction cells, inverted device structures achieved more attention due to their long-term stability. High work function top anodes (Au, Ag etc.) in inverted structure show improved chemical stability. In addition, although high work function ITO changes the role to bottom cathode in inverted structures, the energy alignment can be modified by interfacial modification[80] or the insertion of ETL[44]. Hence, in the OPV part of this study, the inverted architecture was investigated.

1.2.3 Device operating principles

In this subsection, a brief description of the device operating principles of BHJ OPVs is provided, where three primary processes are required for converting sunlight directly into electrical power: a) absorption of photons by the active layer; b) photogenerated charge separation and the generation of mobile carriers; c) charge collection. The absorption by typical photoactive organic materials has been briefly introduced in subsection 1.2.1. Hence, here we give more discussion about the latter two steps. Before that, an introduction of major device parameters is given.

1.2.3.1 Current density – voltage characteristics

A typical current density (J) – voltage (V) curve of solar cells is shown in Figure 1.5.

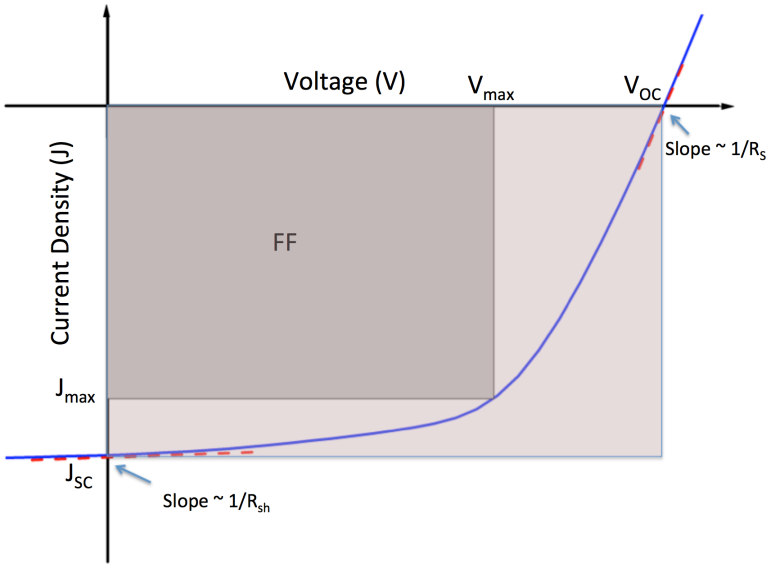


Figure 1.5 Representative current density vs. voltage of a solar cell.

The short circuit current density (J_{SC}) is the current density when no external field is applied. At this time, the driving force of charge drifting is the built-in internal field. J_{SC} is influenced by photon absorption, charge separation and collection.

The open circuit voltage (V_{OC}) is the voltage when the current is zero, which is the maximum voltage output provided by the solar cell. In BHJ OPVs, V_{OC} is related to the offset between the LUMO of the acceptor and the HOMO of the donor[81]. V_{OC} also can be influenced by the carrier recombination, work function of electrodes, interfacial dipoles *etc*.

The fill factor (FF) is the ratio between the actual maximum obtainable power and the product of J_{SC} and V_{OC}. FF reflects the competition between the carrier recombination and sweep-out of the photoinduced carriers. FF can be tuned by both series resistance (R_s) and shunt resistance (R_{sh}) that is introduced in the following sections. It is also influenced by the balanced mobilities of electrons and holes in the active layer.

The power conversion efficiency (PCE) can be calculated from the equation, PCE = $J_{SC}V_{OC}FF$/Power (solar in), in which $J_{SC}V_{OC}FF$ is the maximum power created in the external circuit.

The series resistance (R_s) is associated with the bulk resistance of the active layer, functional layers and electrodes, contact resistance of every interface and the probe resistance[82]. The shunt resistance (R_{sh}) comes from the carrier recombination and the

consequent leakage current in the device. The values of R_s and R_{sh} can be roughly estimated by the reciprocal of the slope of J-V curves when J = 0 and V = 0, respectively.

1.2.3.2 Photogenerated charge separation and the generation of mobile carriers

The mobile carrier generation of bulk heterojunction OPVs comes from two pathways, shown in Figure 1.6: one is the ultrafast electron transfer over distances of ~10 nm between the polymer electron donor and the fullerene acceptor; the other is the exciton diffusion and the subsequent dissociation at the donor/acceptor interface[71].

Ultrafast electron transfer is considered to result from the fundamental quantum uncertainty principle[83]. The photoexcited state is a delocalized coherent state, which lifetime is sufficiently long for participating in electron transfer from electron donor to fullerene acceptor before the collapse of the coherent state[71]. The phenomenon of ultrafast electron transfer has been observed by different measurements, with timescale less than 100 fs[84][85].

The other pathway, with slower dynamics (50-500 ps), originates from the diffusion of the localised excitons which remain after the collapse of the initial delocalised coherent state[83]. The excitons diffuse to the interface of the heterojunction and are split due to the interface energy offset, leaving holes on the donor side and electrons on the acceptor side.

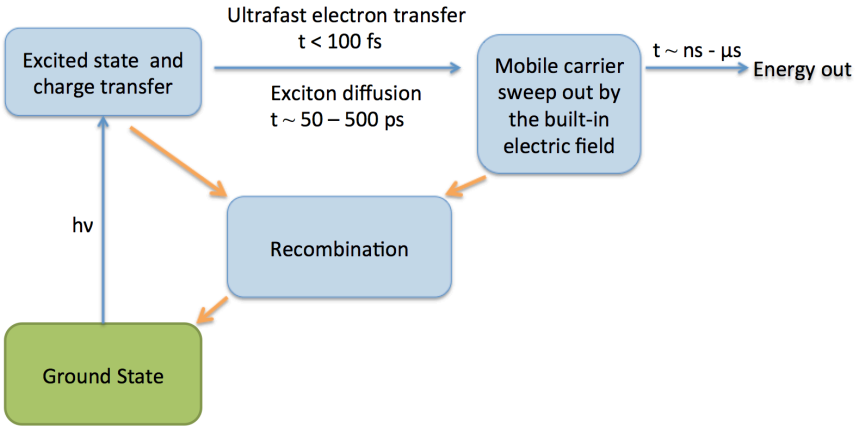


Figure 1.6 Carrier dynamics of typical bulk heterojunction OPVs.

1.2.3.3 Carrier collection at electrodes

Charge carrier collection at the electrodes is a competition between sweep-out by the internal field and recombination losses before and after mobile carrier generation[71], as shown in Figure 1.6. For sweep-out, it is proportional to the magnitude of the built-in electric field. It is also influenced by the mobility and therefore by the intrinsic material properties and the morphology in the heterojunction. The estimated timescale of sweep-out is less than 1 µs[86].

Recombination can occur both during the generation and the sweep-out processes of the mobile carriers. It mainly has four kinds[87]:

i) Diffusing excitons recombine before they reach the donor/acceptor interface. The recombination can be by an Auger process, *i.e.* an exciton in polymer can recombine with a hole and similarly an exciton in fullerenes can recombine with an electron. This is a bimolecular recombination.

ii) When the exciton reaches the donor/acceptor interface, it splits into a hole in the polymer and an electron in the fullerene, which are considered to be bound geminate electron-hole pairs. The built-in electric field reduces the barrier for separation of the electron-hole pair. So the mobile carrier collection decreases with forward bias, which is a monomolecular recombination process caused by the reduced field ionisation of geminate electron-hole pairs with the reduced internal field.

iii) Now the electrons and holes are already separated by ultrafast electron transfer or exciton diffusion and they are mobile in acceptor and donor domains, respectively. However, there is still a possibility that a mobile electron and a hole will meet at the interface and recombine. This is a non-geminate and bimolecular recombination.

iv) Recombination also can occur through interface defect states. In this case, it supposes that there are defects or impurity states energetically within the interface gap and physically near the interface so that can trap electrons and holes and consequently lead to recombination.

1.3 Perovskite photovoltaics

1.3.1 Materials

1.3.1.1 Crystalline structure

The perovskite crystal structure can be described as an AMX_3 unit cell, where A is a large cation, M a metal cation and X an oxide or halide series anion[88]. They form a MX_6 octahedral structure where M is in the centre and X is located in the corner (Figure 1.7). The extended MX_6 three-dimensional structure is also shown in Figure 1.7. The component A fills the space surrounded by the adjacent octahedron. To make sure a closed packed perovskite network, the size of cation A is of great importance as it should be smaller than the interstitial space. It will also have great influence on the modulation of material's physical properties such as electronic and optical aspects. In the case of hybrid perovskite photovoltaic materials, cations A are normally methylammonium (MA), formamidinium (FA) or Cs[89]. Cation M is typically a divalent metal ion such as Pb^{2+}, Sn^{2+} *etc*. Halogen X anions are Cl^-, Br^- or I^-. Indeed as the field rapidly develops

so-called mixed perovskites are emerging where one or more metal, halogen and cation are incorporated into the same structure.

The organic/inorganic perovskites tend to form a two-dimensional layered structure by continuously alternating the inorganic and organic layers. This can be obtained by cutting the 3D structure along <100> direction. The so-called "perovskite sheet", which is the inorganic layer containing corner-sharing MX_6 octahedra, is subsequently sandwiched by organic molecules layers[88]. This inorganic framework now is considered as highly dynamic, flexible and 'alive' (can respond to external stimuli) that is responsible for the ion migration in perovskites.

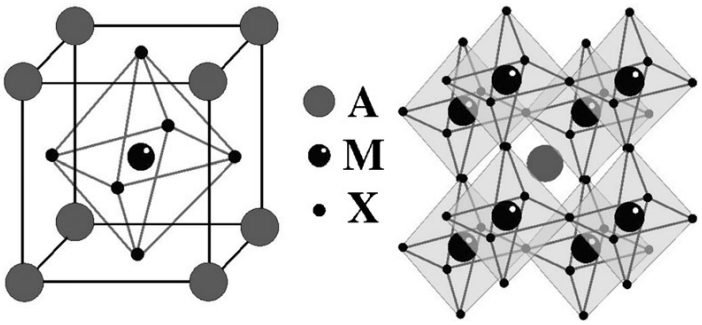


Figure 1.7 Left: Three-dimensional representation of basic perovskite structure AMX_3. Right: Extended network model, adapted from Ref[88].

The lattice parameters of typical perovskite materials have been measured. For $CH_3NH_3PbI_3$, a tetragonal perovskite structure is formed (a = 8.855 Å and c = 12.659 Å). In such structures typical laboratory X-ray diffraction (XRD) peaks, using a Cu K_α source, appear at 14.00° and 28.36° degrees 2θ for the (110) and (220) planes, respectively. For $CH_3NH_3PbBr_3$, a cubic structure is formed with a lattice constant of 5.9 Å. Diffraction peaks are seen at 14.77, 20.97, 29.95, 42.9, and 45.74°, assigned as the (100), (110), (200), (220), and (300) planes, respectively[90].

1.3.1.2 Optical properties

Perovskite materials have shown a broad (panchromatic) absorption window in the solar spectrum. Figure 1.8a[91] illustrates the absorption spectrum of $CH_3NH_3PbI_3$ from the ultraviolet to near infrared region via steady-state UV-visible spectroscopy. There are two distinct maxima, at 480 and 760 nm[91–93]. Figure 1.9 shows the effective absorption coefficient of a $CH_3NH_3PbI_3$ perovskite thin film by photothermal deflection spectroscopy (PDS), which also has two similar peaks[94]. A high absorption coefficient with particularly sharp onset is obtained when compared to other typical photovoltaic materials. Besides, $CH_3NH_3PbI_3$ is inferred to be a semiconductor with a direct bandgap according to both the experiments (Tauc plot)[95] and the calculation[96].

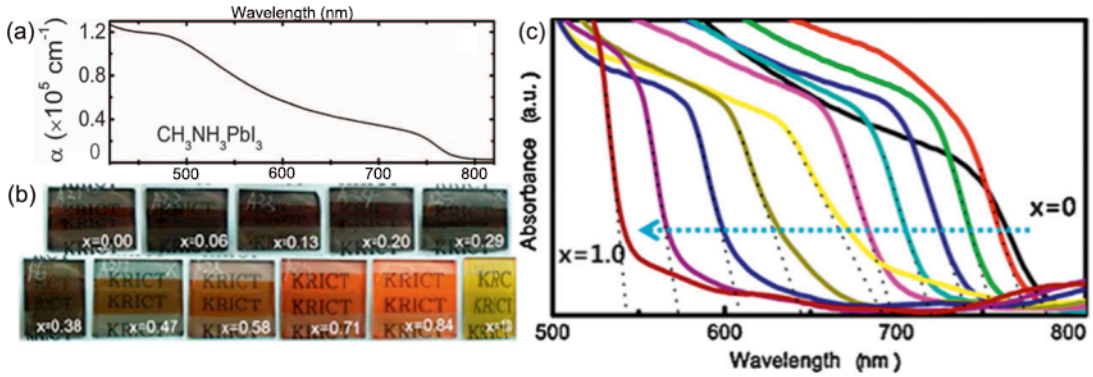


Figure 1.8 (a) Steady-state UV-visible absorption spectrum for a pure $CH_3NH_3PbI_3$ layer, adapted from Ref[91]; (b) Images of mesoporous $TiO_2/CH_3NH_3Pb(I_{1-x}Br_x)_3$ on FTO substrates, adapted from Ref[89]; (c) Variation of absorption of $TiO_2/CH_3NH_3Pb(I_{1-x}Br_x)_3$ layers, adapted from Ref[89].

Continuous tuning of the bandgap is achieved in alloyed perovskite materials where two halide species are incorporated[88]. The corresponding variation of UV-vis absorption spectra is shown in Figure 1.8c in the case of mesoporous $TiO_2/CH_3NH_3Pb(I_{1-x}Br_x)_3$. The colour of the devices can be modified by tuning the composition of the alloy, as shown in Figure 1.8b. The absorption band edge shifts from longer wavelength (x=0, 1.58 eV) to shorter wavelength (x=1, 2.28 eV). This corresponds to the previous papers that the band gaps of $CH_3NH_3PbI_3$ and $CH_3NH_3PbBr_3$ were 1.5 and 2.3 eV, respectively[90][97].

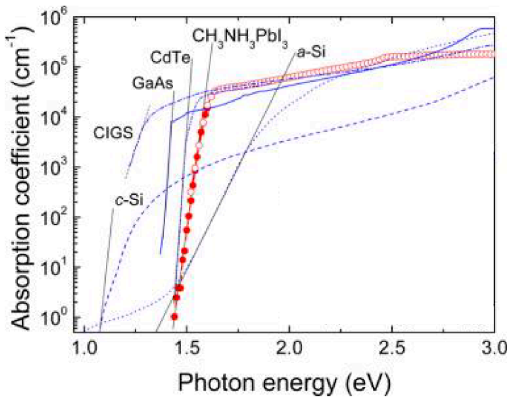


Figure 1.9 Effective absorption coefficient of a $CH_3NH_3PbI_3$ perovskite thin film by photothermal deflection spectroscopy compared with other typical photovoltaic materials, adapted from Ref[94].

1.3.1.3 Electronic properties

The exciton binding energy of $CH_3NH_3PbI_3$ is determined to be only 16 meV at low temperature and even smaller at room temperature[98]. This leads to spontaneous free carrier generation after light absorption. The typical organic/inorganic halide perovskite materials such as $CH_3NH_3PbI_3$ show ambipolar charge transport properties.

In the early stages of perovskite development excellent electron-transport properties were demonstrated and efficient PV devices were fabricated by introducing an insulating alumina (Al_2O_3) scaffold instead of the TiO_2 mesoporous structure[92]. The conduction band of Al_2O_3 is much higher than the LUMO of perovskites, which means no electron injection from the absorber to the scaffold happens. Meanwhile, good hole-transport properties were demonstrated in an efficient perovskite solar cell with 5.5% PCE which has a simple $TiO_2/CH_3NH_3PbI_3$/Au configuration without any hole transport layer[93].

Now the electrical properties, especially the carrier mobility, are much better understood, although new works continue to appear describing transport properties in these fascinating materials. The electron and hole mobilities of perovskites are nearly balanced and extremely high, although the fabrication methods show great influence on the values measured[99]. Carrier mobilities of perovskite are estimated to be 12.5 $cm^2V^{-1}s^{-1}$ for polycrystalline thin films[100] and as high as 164 $cm^2V^{-1}s^{-1}$ for single crystals[101]. In addition, balanced long-range electron and hole diffusion lengths are observed above 100 nm for $CH_3NH_3PbI_3$ films and above 1 μm for '$CH_3NH_3PbI_{3-x}Cl_x$' films[102][103]. While for single crystals, the carrier diffusion length is considered to be as large as 175 μm although further corroboration is expected[101]. This indicates the perovskite materials break the bottleneck of short diffusion length that limits the typical solution-processed active layer materials for example polymers.

Lead based halide perovskites always behave as intrinsic semiconductors[99], with trap densities as low as 10^{10} cm^{-3}[104]. Also, the carrier concentration in perovskites is remarkably low, around 10^9 – 10^{14} cm^{-3}[105]. As for the defect chemistry, ion migration is considered as an important issue for perovskites. However, there is still a controversy: some believe charged point defects are available in the lattice[105][106] while some think only the whole formula units are removed (MAX, PbX_2 or $MAPbX_3$) and leave a partially hollow lattice[99].

1.3.1.4 Processing methods

The traditional deposition method for perovskite films is a single-step spin-coating process[92][93]. For example, in the case of $CH_3NH_3PbI_3$, a precursor solution of equimolar CH_3NH_3I and PbI_2 in γ-butyrolactone (GBL) is spin-coated onto the substrates, typically pre-deposited oxide films. Then the films are dried at room temperature to form solid state $CH_3NH_3PbI_3$, and subsequently annealed in argon at 100 °C. However, this method causes uncontrolled precipitation of the perovskite leading to a variation in morphology. This finally leads to a wide variation in the performance of solar cells.

Later a two-step sequential deposition technique has been developed, which improved the PCE of the devices consisting of perovskite and mp-TiO_2 films to above 14% with good reproducibility[107]. Specifically, PbI_2 was initially spin-coated on mp-TiO_2 films, subsequently dipped into a solution of CH_3NH_3I causing the formation of $CH_3NH_3PbI_3$ when two components are mixed. This raises better control over the morphology and higher stability compared to conventional methods. However, this method is not suitable for the situation of planar surface, as larger PbI_2 crystallites will cause incomplete conversion to $CH_3NH_3PbI_3$.

Solvent engineering has also been developed for solution-process fabrication. For example, the use of a mixed solvent of dimethylsulphoxide (DMSO) and GBL followed by toluene dripping forms an extremely uniform and dense $CH_3NH_3PbI_3$ layer, as shown in Figure 1.10[108]. The precursor solution is prepared by mixing MAI and PbI_2 in DMSO:GBL co-solvent. During the spin coating, first GBL, which has a higher evaporation rate than DMSO, is evaporated. Then toluene, that does not dissolve perovskite but is miscible with GBL and DMSO, is drop cast on the film during the substrate spinning. The toluene dripping quickly removes the residue DMSO solvent and forms an intermediate phase MAI-PbI_2-DMSO. Finally, the complex turns into crystalline perovskite by annealing at 80-100 °C, with a device efficiency above 16%[108].

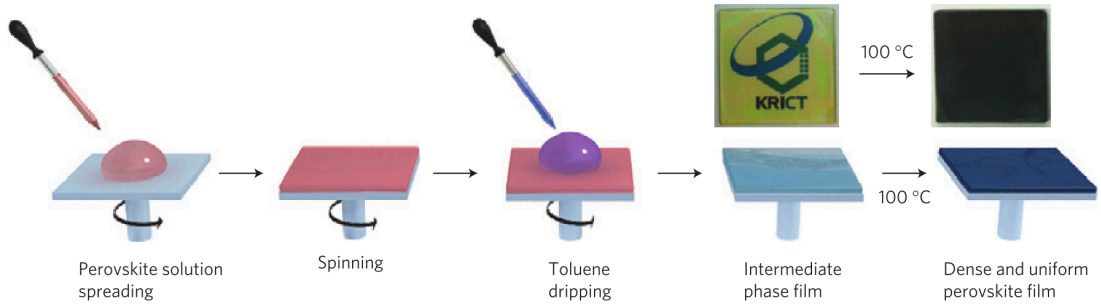


Figure 1.10 Scheme of 'toluene dripping' solvent engineering process, adapted from Ref[108].

Using vacuum techniques a dual-source vapour deposition method was also utilised for simple planar heterojunction perovskite solar cells resulting in PCE values < 15%[109]. Here the perovskite absorbers were deposited from the evaporation of $PbCl_2$ and CH_3NH_3I at the same time, onto the TiO_2-deposited FTO films within a high-vacuum chamber.

1.3.1.5 Exploration of new perovskite materials

Until now, much attention is still directed to the archetypal perovskite $CH_3NH_3PbI_3$. However, efforts have also been made on other perovskite materials. AMX_3 perovskite structure is proven that all three lattice positions could be fully replaced thus forming a solid solution. For the X site, researchers now believe that a solid solution can be formed

only from halides adjacent in the periodic table[99]. The previously reported $CH_3NH_3PbI_{3-x}Cl_x$ perovskite[92] now are considered as two-phase composites[99] although the reason of enhanced device performance by involving Cl is still under debate[110][111].

In the case of the A site, in addition to methylammonium ($MAPbX_3$)[112], other cations has also been introduced to form solid solutions such as caesium ($CsPbX_3$)[113] and formamidinium ($FAPbX_3$)[114]. In the case of M site, Sn was investigated to replace Pb because Sn is somewhat more environmentally friendly[115][116]. Researchers also synthesised solid solutions $CH_3NH_3Sn_{1-x}PbxI_3$[117]. However, the compound is likely to form Sn^{4+} due to oxidation and thus displays metal-like conductivity, which decreases the performance of the devices.

Although to date the highest certified efficiency (20.1%) is achieved by $FAPbI_3$[118], blends of mixed cations and mixed halides are considered as promising materials[119]. New perovskite materials with a combination of excellent device performance, more eco-friendly and good environmental stability, are still to be pursued.

1.3.2 Device structure

1.3.2.1 Active layer structure

There are two typical active layer morphologies of perovskite solar cells: mesoporous and planar structures, as shown in Figure 1.11. The mesoporous structure initially came from that using perovskite as sensitiser for mesoporous TiO_2 in DSSCs[90]. Then by increasing the degree of pore filling the morphologies changed from perovskite-sensitised[90] to perovskite-filled[92], and finally to completely perovskite filled with a perovskite capping layer[120]. The mesoporous scaffold materials originally are semiconducting TiO_2 that transport electrons from perovskite even though perovskite itself have the ability to do it[121][122]. Insulating Al_2O_3 has also been developed as the scaffold, at present perovskite needs to transport electrons itself[92]. In addition to mesoporous structure, other nanostructures have also been investigated, such as nanosheets[93], nanofiber[123] and nanorods[124][125].

The planar structure refers to the structure without nanostructured scaffold. In this structure the perovskite functions in a manner similar to that in the early Al_2O_3 based devices, not only as the light absorber, but also as electron and hole transporters. Crystal size is one important difference between mesoporous and planar perovskite films varying from 60 nm of mesoporous structure to above 500 nm of planar structure[126]. The relative contribution of surface influence increases with the decrease of crystal size. D'Innocenzo *et al* infer the optoelectronic properties of the perovskite may be tuned by the crystal size[127]. To date high efficiency devices have been achieved by both planar[128] and mesoporous structures[118]. However, the mesoporous scaffolds typically need high

temperature annealing[118], which deviates from our aim in this thesis *i.e.* to prepare low temperature processed solar cells. In addition, the mesoporous electron transport layer is more necessary for photoactive materials with too short carrier diffusion length but here we utilise $MAPbI_3$ that has long diffusion length. Hence the planar structure was identified as the candidate architecture for the work in this thesis.

Recently, the BHJ has also been used in perovskite solar cells, by mixing PCBM in perovskite active layer[129]. PCBM plays an important role in improving the active layer quality by filling vacancies and pinholes among perovskite grains, forming a film with large grain and fewer grain boundaries.

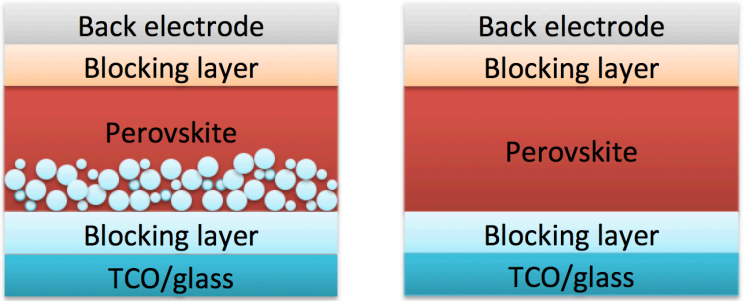


Figure 1.11 Active layer structures for perovskite solar cells: left) mesoporous cell; right) planar cell.

1.3.2.2 Whole device structure

Because the perovskite initially comes from the device with mesoporous TiO_2 as bottom electrode, the so-called conventional (n-i-p) perovskite device structure is the structure with the bottom electrode acts as cathode with top anode, which is opposite to the organic solar cells, as shown in Figure 1.12. The first conventional perovskite cell with planar structure was reported using FTO/compact TiO_2/perovskite/spiro-OMeTAD /Au[120]. Later doped TiO_2[130] and other oxides such as ZnO[131] and SnO_2[132] were also involved in this structure. However, a hysteretic response between reverse and forward scans during J-V characterization was observed[133].

Interestingly, the J-V hysteresis in planar structured devices can be largely suppressed by inverting (p-i-n) the structure, as shown in Figure 1.12, where the fullerene layer is typically on top of perovskite[134]. Fullerene deposited on perovskite is considered to passivate the charge trap states on the surface and grain boundary of the perovskite layer that is an important origin of the J-V hysteresis.

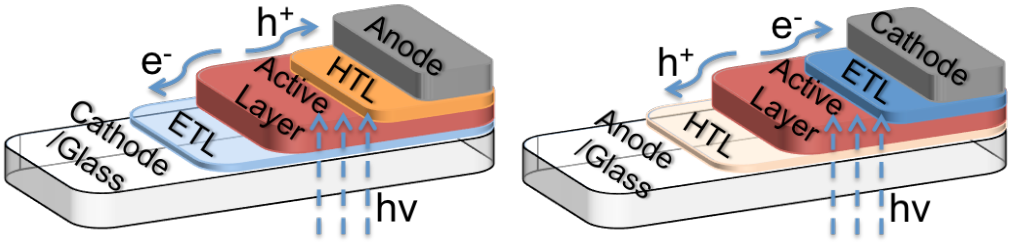


Figure 1.12 Conventional (n-i-p) (left) and inverted (p-i-n) (right) device structure of perovskite solar cells.

The conventional device architecture provides easy access to solution processed devices and facilitates the investigation of the role of low-temperature processed ETLs. The solution-based oxides typically require a polar solvent in the oxide precursor solution. The polar solvent may dissolve the perovskite film hence we cannot deposit the solution with polar solvent on top of perovskite, as in an inverted structure. While oxide nanoparticles can be deposited on top of the perovskite by dispersing nanoparticles in non-polar solvent and use in inverted perovskite structure[135], the complicated synthesis of oxide nanoparticles violates the aim of this thesis. In addition, considering typical planar conventional perovskite device faces the J-V hysteresis problem, we also seek to reduce the J-V hysteresis by tuning ETL in conventional structure.

1.3.3 Device operating principle

In this subsection, a brief description of the device operating principles of perovskite solar cells will be introduced. The operating principle of perovskite planar heterojunction cells has been proven similar to thin-film p-i-n heterojunction cells with a high electronic quality 'i' layer, achieved from the electron beam induced current (EBIC) mapping[136]. Although OPVs have a typical p-n heterojunction that differs from that of p-i-n of perovskite cells, the perovskite device working principle still can be described in a similar manner to OPVs: a) absorption of photons by the active layer; b) photogenerated charge separation and the generation of mobile carriers; c) collection of holes at anode and electrons at cathode. The absorption of typical perovskite materials has been briefly introduced in subsection 1.3.1. Hence, here we will give more discussion about the latter two steps.

1.3.3.1 Photogenerated charge separation and the generation of mobile carriers

Under light illumination, the perovskite absorbs light and subsequently electron-hole pairs are created nearly instantaneously[137]. There has been some controversy over whether bound excitons are created, transported to the heterojunction and then dissociate at the interface, or free carrier charges are spontaneously produced in the bulk of the perovskite materials. Now it is clear that the exciton binding energy

$E_B << k_BT$ at operating temperature[98]. It is demonstrated that equilibrium exists between free charge carriers and excitonic species under illumination. The ratio of free charges to excitons nearly reaches 100% under device operating condition and the exciton population only becomes dominant when the temperature is reduced to below 120 K[127]. Here we only use 3D $CH_3NH_3PbI_3$ as an example. The situation may be changed in lower dimensional perovskite networks due to enhanced exciton binding.

The generation of free electrons and holes by exciton dissociation happens around 2 ps after photoexcitation[100][138]. After the generation of free charge carriers in the perovskite region, they move towards opposite electrodes. This movement in bulk perovskite is very fast, with the timescale around 1 fs[106]. This may benefit from the high carrier mobilities and long carrier diffusion length of both electrons and holes in perovskites. When the carriers arrive the interfaces between $CH_3NH_3PbI_3$ and ETL/HTL, the time for carriers to pass the interfaces depends on the ETL/HTL materials. For instance, electron injection from $CH_3NH_3PbI_3$ to TiO_2 is on the sub-ps timescale while the injection from $CH_3NH_3PbI_3$ to PCBM is slower, typically ~100s ps. The hole injection from $CH_3NH_3PbI_3$ to Spiro-OMeTAD is also ultrafast, on the sub-ps timescale. Thus, the electron and hole transport in bulk perovskites and at the carrier injection interface are both very fast.

In addition to the electron and hole transport, in perovskite there is still the issue of ion transport. The ion transport in perovskites is much slower, with a timescale of around 1 ps[106]. Now ion transport can be considered the most likely origin of the slow part of the J-V hysteresis[106]. Although the ion migration results in defects, fortunately these defects do not lead to deep electronic states in the band gap so that Shockley-Read-Hall type nonradiative recombination is avoided[106].

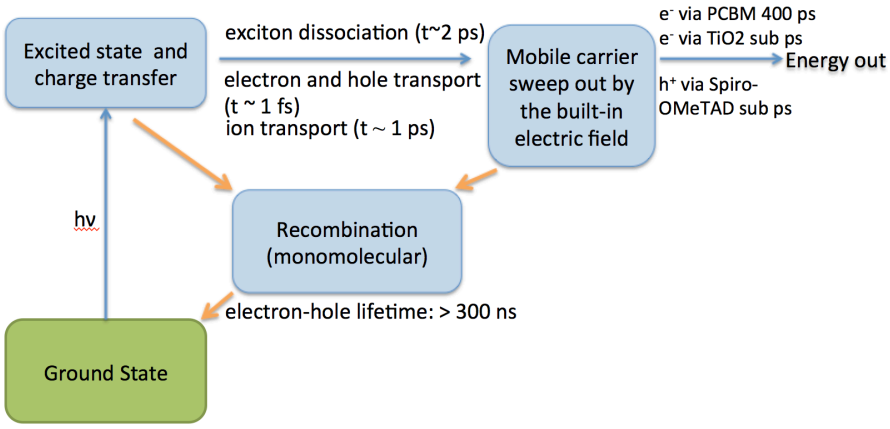


Figure 1.13 Carrier dynamics of typical perovskite solar cells.

1.3.3.2 Carrier collection at electrodes

As mentioned in the OPV discussion, here we focus on the carrier recombination losses before being swept to the external circuit. Compared with BHJ OPVs, the recombination pathways of perovskite should be less. One reason is that the active layer in an OPV is the bulk blend of donor/acceptor two materials while that in latter situation is typically only one perovskite bulk layer. Another reason is that both excitons and free charge carriers play important roles in OPV, while in perovskite, such as $CH_3NH_3PbI_3$, we could only consider free carriers.

Typically, carrier generation and recombination can be simulated in parallel *via* $dn/dt = G-k_1n-k_2n^2-k_3n^3$, where n is the total carrier concentration dependent on time, G is the carrier generation term, k_1, k_2, k_3 are the monomolecular (first order), bimolecular (second order) and three-body Auger (third order) recombination rate constants, respectively[139]. The monomolecular part is related to trap-assisted or geminate/ excitonic recombination; the bimolecular part is related to nongeminate or exciton-exciton annihilation; the Auger part is related to nonradiative three-carrier interactions.

There remains some controversy as to which term dominates the recombination process in perovskite cells. Some believe that bimolecular recombination is dominant in free electron-hole recombination, measured at excitation fluence among 0.2 - 10 μJ/cm^2 (or corresponding to carrier densities of $10^{16\text{-}18}$ cm^{-3})[140][141]. While some others believe that monomolecular recombination dominates the recombination in operational perovskite cells[139][142–144]. The monomolecular term dominates for $n < 10^{16}$ cm^{-3}, bimolecular term dominates for n in the range of $10^{17\text{-}19}$ cm^{-3}, Auger term dominates for $n > 10^{19}$ cm^{-3}[144]. Characteristic charge density in $CH_3NH_3PbI_3$ solar cells at one sun intensity is around $10^{13\text{-}15}$ cm^{-3}[139] so that monomolecular process is dominant under normal situations.

The electron-hole lifetime in perovskites is long, in the order of 300 ns to microseconds[102]. The low recombination rate in perovskite may originate from several aspects: i) the structure of octahedral distortions and molecular dipoles leads to fluctuations in electrostatic potential, which separates electrons and holes in real space[145]; ii) relativistic splitting of the conduction band suppresses the recombination at the valance and conduction band edges because of momentum selection rules in reciprocal space[146]; iii) efficient carrier extraction via electron and hole selective layers[140]; iv) extremely low intergrain potential barrier (< 45 meV) in polycrystalline $CH_3NH_3PbI_3$ films[103].

1.3.3.3 J-V hysteresis

An anomalous phenomenon of current-voltage hysteresis in perovskite solar cells was first reported by Snaith *et al* in 2014[147]. Many potential origins of the hysteresis have been developed however it is not yet completely understood. Until now, among all candidates of causes, mobile ionic species is most likely responsible for the phenomenon. When an electric field is applied, positive and negative ionic species will move towards opposite directions[148]. This leads to the p-type and n-type doping of perovskite near two carrier extraction layers. Thus, one direction of electric field possesses favourable electronic contact while the other direction possesses unfavourable electronic contact, which results in hysteresis.

The J-V hysteresis has been found more obvious at lower temperature, which may be caused by ion migration rate reducing with temperature[149]. In addition, the contact between the perovskite and carrier extraction layers shows significant influence on the hysteresis. Mesoporous TiO_2 based n-i-p perovskite cells possess negligible hysteresis at room temperature as the pathways for unimpeded electron extraction are enhanced[108]. PCBM is also found to alleviate hysteresis in both n-i-p and p-i-n device structures, by passivating perovskite defect sites[134][150].

1.4 Interfacial layers in organic and perovskite solar cells

The utilisation of interfacial layers has been identified as an essential method for optimising the performance of OPV and perovskite solar cells. In this section, first the roles of interfacial layers will be discussed. Then the hole and electron transport layers will be separately introduced, especially those utilised in this project. Those materials which can be solution processed will also be emphasised, based on the aim of this thesis.

1.4.1 Functions of interfacial layers

1.4.1.1 Tuning energy level at the active layer/electrode interface

Suitable energy level alignment at the active layer/electrode interface has been proven important to enhance charge collection and V_{OC} of devices in OPV and perovskite solar cells[151]. The intrinsic V_{OC} is mainly determined by the material properties and morphology of the active layer. However, the actual V_{OC} obtained is usually lower than the ideal situation. A reduced barrier on contact with the electrodes, typically Ohmic contact, is expected to get the maximum V_{OC}. One effective way is modifying the work function of electrode by inserting interfacial layers. The underlying mechanisms of inserting work function modification layer (WML) are shown in Figure 1.14[152].

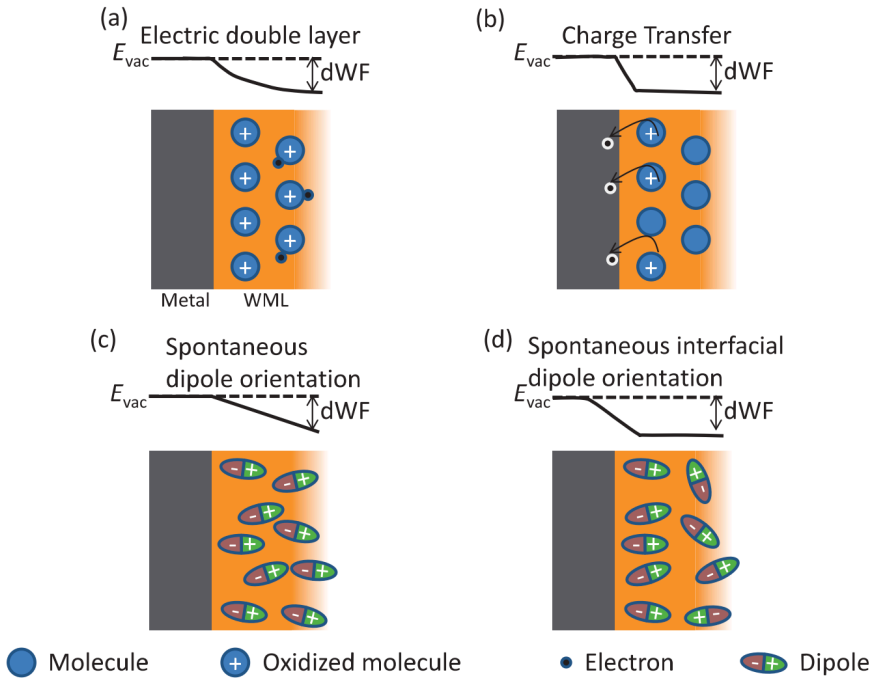


Figure 1.14 Schematics of possible mechanisms for work function modification by interlayer, adapted from Ref[152].

Figure 1.14a describes the formation of electrical double layer between metal and a doped semiconductor. A bias-dependent carrier depletion region is formed in the doped semiconductor at the interface. Figure 1.14b shows the work function tuning can also happen *via* dipole formation by charge transfer between the electrode and the interlayer. Another mechanism to modify the work function is the spontaneous orientation of dipoles in the interfacial layer deposited on the electrode, either be throughout the whole layer as Figure 1.14c or only at the interface as Figure 1.14d. The distinction of these two situations is whether the work function is continuously dependent on the interlayer thickness or just an abrupt change at the initial stage.

After modifying the work function of electrodes, another important issue is how this influences the adjacent photoactive layer. For weakly interacting interfaces, which is suitable for many metal oxide/organic interfaces[153], the energy alignment trend is shown in Figure 1.15. The figure illustrates that the electron-injection and hole-injection barriers are linearly dependent on the electrode work function within the middle region. However, the alignment between the HOMO and the E_F remains constant with further increase of electrode work function (called 'pinning') when the electrode work function exceeds a certain threshold value. This threshold value depends on the organic molecules. The same pinning behaviour is also shown between Fermi level and LUMO levels.

The origin of pinning is considered to be the combined effects of the molecular ionisation at the organic/electrode interface and capacitive charge redistribution in the electrode[154]. The pinning effect has been observed in organic small molecules[153], polymers[155] and also hybrid perovskite materials[156].

Fermi level pinning is important to designing solar cells to get maximum V_{OC}. For OPVs, the way to achieve maximum V_{OC} is to tune the work function of the electrodes to enable the HOMO level of the donor and LUMO level of the acceptor pinned to the corresponding electrodes, as shown in Figure 1.15. In this case, the V_{OC} mainly depends on the intrinsic properties of photoactive layer, without loss from the electrode energy level mismatch. Thus, the ideal situation is low work function cathode and high work function anode.

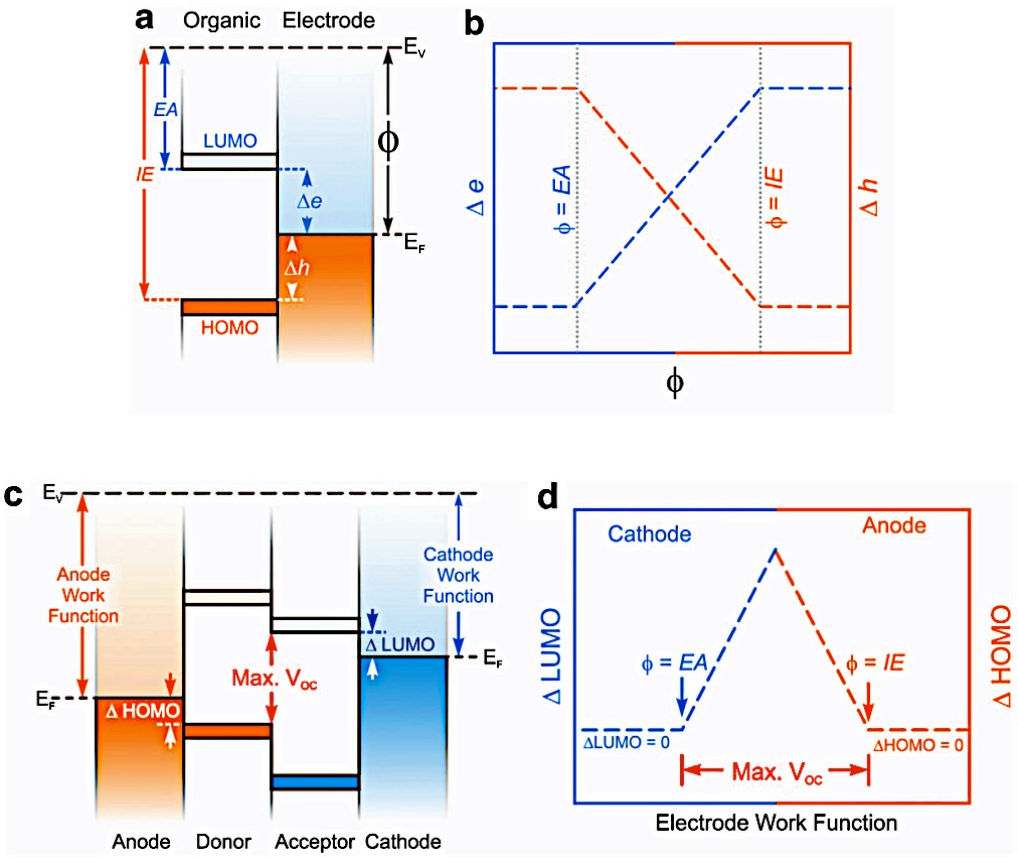


Figure 1.15 (a) energy level diagram of organic/electrode interfaces. EA: electron affinity, IE: ionisation energy; (b) energy alignment trend in week interacting interfaces, showing linear and pinning regimes; (c) energy level diagram in the case of OPV; (d) the dependence of V_{OC} on energy level alignment. All figures are adapted from Ref[154].

1.4.1.2 Charge carrier selectivity

Another role of interfacial layers is to improve the charge carrier selectivity of corresponding electrodes thus impeding unfavourable charge recombination or exciton

quenching at the active layer/electrode interfaces, which enhances the fill factor and the rectifying behaviour of the solar cells.

We use organic solar cells as an example to explain the energetic requirement of the charge selective layer, as shown in Figure 1.16[154]. The situation in perovskite solar cells is easy to deduce from it. The interlayers can be classified as hole transport layer (HTL) and electron transport layer (ETL) based on the nature of the collected charges. For an ideal HTL (the orange region in Figure 1.16), it should be a p-type semiconductor with its HOMO level near the HOMO level of donor; meanwhile its LUMO level should sit above the LUMO level of donor. In such way, this interlayer can only collect the holes and also block the electrons. The same rule should be applied to the ETL, an n-type semiconductor with its LUMO level aligning with the LUMO level of acceptor and its HOMO level below the HOMO level of acceptor.

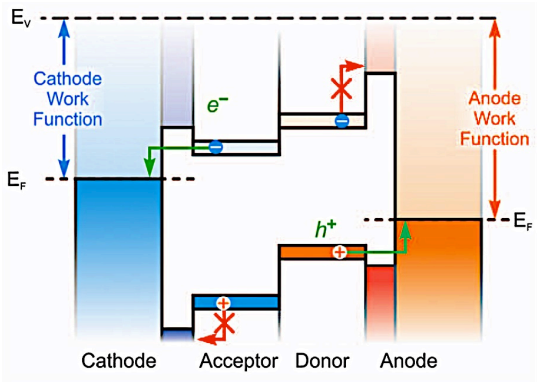


Figure 1.16 Schematic energy level diagrams of charge selective interfacial layer in OPV, adapted from Ref[154].

1.4.1.3 Other interlayer functions

Modifying the photoactive layer morphology is another important function of carrier transport layers. The degree of wetting of the active layer precursor solution on beneath interlayer has significant influence on active layer surface morphology. Insufficient wetting may cause the formation of pinholes, which is detrimental to the device performance. An example of $CH_3NH_3PbI_3$ surface morphology by SEM with different wetting is shown in Figure 1.17.

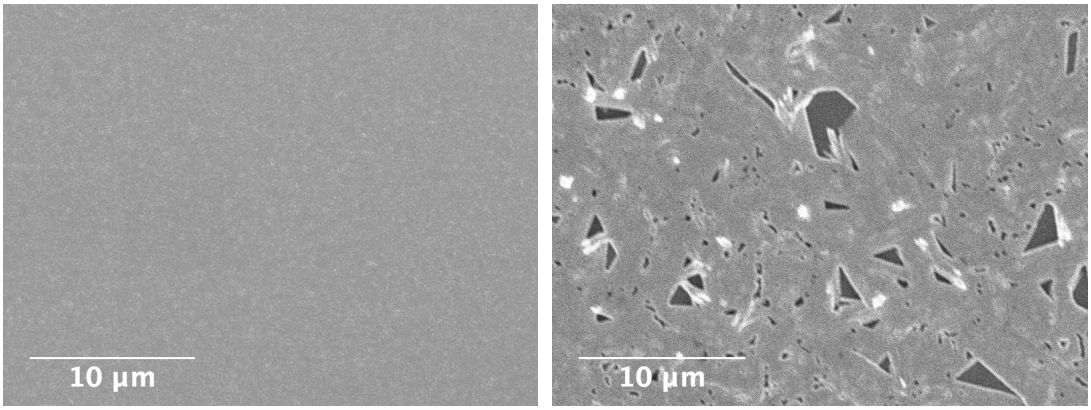


Figure 1.17 $CH_3NH_3PbI_3$ surface morphology by SEM with good (left) and bad (right) wetting of perovskite precursor solution on lower interlayer.

Some interlayer materials also play the role of surface trap state suppression of active layers. The trap states at the surface may cause carrier recombination, thus lead to carrier losses. Surface passivation has been shown to remarkably increase the device performance for perovskite solar cells[134][157].

Enhancing device stability is another expected function of the interlayer. The modification of the adhesion between active layer and electrodes can improve the durability and stability of devices[158][159]. The interlayer can also protect the active layer from the permeation of oxygen and water as organic and perovskite photoactive materials are typically sensitive to them[151][160]. In addition, some interfacial layers attached to the light-incident electrode side can absorb the UV light and enable visible light pass, thus protecting the active layer from the exposure of UV light.

Optical effects are also introduced by interlayers to improve light harvesting in photoactive layers. An interlayer can be utilised as an optical spacer to tune the optical and electrical field distribution in solar cells[27] and LEDs[161]. The intensity of the optical field within the active layer can be reinforced because of the optical interference effects by the insertion of interlayers. Surface plasmon resonance effect is another origin of light absorption enhancement within a device brought about by incorporating interlayers, *i.e.* by placing metal nanoparticles into the interlayer[162]. Luminescent materials, functioning as spectral converters (upconversion, quantum-cutting and down-shifting), are also placed in interlayer in solar cells[163]. The aim is to minimise the absorption losses derived from the intrinsic absorption wavelength limit of photoactive material compared with the broad solar spectrum.

1.4.2 Hole transport layer

1.4.2.1 Organic materials

Organic small molecules and polymers can act as efficient HTLs. Spiro-OMeTAD [2,2',7,7'-tetrakis(*N,N*-di-p-methoxyphenylamine)-9,9'-spiro-bifuorene] is a well known organic small molecule HTL , initially used in dye-sensitised solar cells to replace the ionic liquid[164]. The chemical structure is depicted in Figure 1.18. The solubility of spiro-OMeTAD in chlorobenzene is moderate, around 30 vol %[165]. This enables spiro-OMeTAD can be deposit on top of perovskite films by solution process because perovskite material typically cannot be dissolved in chlorobenzene. The glass transition temperature (T_g) is 125 °C and the melting point (T_m) is 248 °C[166]. The HOMO and LUMO energy levels of spiro-OMeTAD are -5.12 eV and -2.05 eV, respectively[166]. Pure spiro-OMeTAD shows low conductivity (about 4.4×10^{-5} S cm^{-1}) and low hole mobility (4×10^{-5} cm^2 V^{-1} s^{-1}), which impedes the carrier collection in the device[167]. Doping with ionic additives has been investigated as an effective way to increase the conductivity of spiro-OMeTAD. Bis(trifluoromethylsulfonyl) amine lithium salt (Li-TFSI) and 4-tert-butylpyridine (TBP) are typical dopant[168], enhancing the conductivity by around two orders of magnitude[169] and accelerating the oxidation of spiro-OMeTAD under O_2[167]. The hole concentration in spiro-OMeTAD can be further increased by the insertion of cobalt-based co-dopant whose role is to promote the spiro-OMeTAD one-electron oxidation reaction[167].

One downside of Spiro-OMeTAD is its high cost derived from the complicated synthesis and purification process[167]. Also, the ionic additive in Spiro-OMeTAD, Li-TFSI, shows hygroscopic nature, which limits the device long term stability when exposed in air[170]. Despite these disadvantages, spiro-OMeTAD with Li-TFSI and TBP as additives has still been chosen as hole transport material in perovskite devices in this work because it is well studied and provides a frame of reference for us to compare our ETL behaviour with published work.

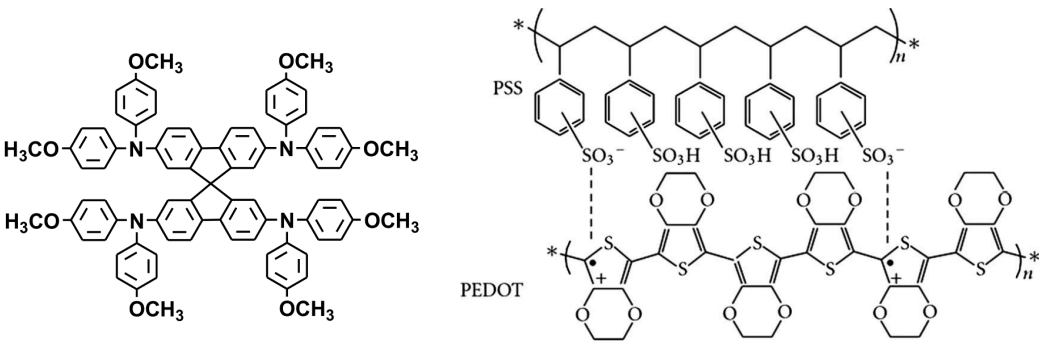


Figure 1.18 Chemical structures of (left) Spiro-OMeTAD, adapted from Ossila website; (right) PEDOT:PSS, adapted from Ref[171].

Poly(3,4-ethylenedioxythiophene):poly(styrene sulfonate) (PEDOT:PSS) is perhaps the most widely used polymer hole transport material, it has been widely applied in DSSCs, OPVs, perovskite PVs, supercapacitors, fuel cells, *etc*.[171] The chemical structure of PEDOT:PSS is shown in Figure 1.18. PEDOT:PSS possesses high conductivity, ranging from 10^{-2} to 10^{3} S cm^{-1}, varied by the synthesis process and additives[171]. The high conductivity results from the efficient p-type doping of PEDOT by PSS, forming $PEDOT^{+}$:PSS^{-}[151]. PSS also acts as polymer surfactant, to promote the dispersion of PEDOT in solvents, typically water. The work function of PEDOT:PSS is around 5.0-5.2 eV[171]. The carrier mobility of pristine PEDOT:PSS is moderate (0.045 $cm^2 V^{-1} s^{-1}$), while boost to 1.7 $cm^2 V^{-1} s^{-1}$ owing to the increased crystallinity and ordering of PEDOT nanocrystals by adding co-solvents[172].

One disadvantage of PEDOT:PSS is that the PSS component is acidic and hygroscopic in nature, which tends to show a negative influence on the device stability[173]. In addition, the solvent of PEDOT:PSS is normally polar solvent, such as water, limiting its application on top of organic and perovskite photoactive layer by solution process. To avoid the utilisation of polar solvent, the polymerisation of the EDOT (3,4-ethylene-dioxythiophene) monomers directly into PEDOT is an alternative pathway, including electrochemical, oxidative, reverse micro-emulsion and vapor phase polymerisation[171]. However, high performance solar cells with PEDOT by this pathway is still lacking to date.

1.4.2.2 Inorganic materials

Inorganic materials have also been well developed as interfacial layers due to their good environmental stability and ability to precisely control their electronic structure, particularly when compared with the organic counterparts. Transition metal oxides are the most widely used among inorganic interlayer materials. For hole extraction metal oxides, they are divided into p-type and n-type based on their distinct energy alignments. N-type hole extraction oxides show large work function with deep-lying conduction and valence bands. Fermi-level pinning occurs when the LUMO of n-type HTL matches the HOMO of photoactive layers. Typical n-type hole extraction oxides include MoO_X, CuO_X, VO_X and WO_3. P-type hole extraction oxides possess upshifting energy levels compared to n-type counterparts. Fermi-level pinning happens when the HOMO of p-type HTL matches the HOMO of photoactive layers. NiO_X and CrO_X are typical p-type HTLs.

Molybdenum oxide (MoO_X) is well studied as hole extraction layer due to its high transparency with optical bandgap around 3.0 eV[174]. The work function of MoO_3, about 7 eV[153][175][176], is sufficiently large for hole injection. MoO_3 is an n-type semiconductor, with HOMO level at -6.7 eV and LUMO level at -9.7 eV[175]. The fabrication methods of

MoO_X are numerous, including thermal evaporation[174], atomic layer deposition[177] and solution processing from precursor solutions[178] or nanoparticle suspension solutions[179]. In this project MoO_X was selected and deposition carried out by thermal evaporation. This is particularly suitable as the evaporation temperature of MoO_X is low (melting point 795 °C). And the precise control of evaporation process, including chamber pressure, deposition rate, in-situ film thickness monitoring, *etc*., enable good reproducibility, allowing the focus of the research to be on how the ETL impacts device performance. In addition, *in-situ* deposition of MoO_X and subsequent metal electrode in vacuum avoids contamination of freshly evaporated MoO_X films by ambient atmosphere that could influence the MoO_X film work function and energy alignment[180]. Evaporated MoO_X films possess mainly Mo^{6+} with very little Mo^{5+}, detected by XPS, which is close to the stoichiometric MoO_3[174].

Apart from transition metal oxides, there are other promising inorganic hole extraction materials. One, graphene oxide (GO), is investigated owing to the two-dimensional structures[181]. The work function of pristine GO is around 5 eV, which is suitable as hole extraction layer[181][182]. However, pristine GO is insulating in nature, which limits the thickness in devices to around 1-2 nm[183]. The challenge of uniformly depositing such layers hinders the development of GO in large-scale production. Reduced GO (rGO), achieved by thermal or chemical reduction methods, show improved conductivity compared with pristine GO[184]. Blending GO with conductive materials is another effective way to increase the electrical conductivity. PEDOT:PSS[185], Au nanoparticles[185], single walled carbon nanotubes (SWCNT)[186] *etc*. have been investigated as fillers. Solution processed graphene oxide nanoribbon has also been applied in hole extraction layer, showing good electrical properties with proper energy alignment[187].

Copper thiocyanate (CuSCN), a p-type semiconductor, is another promising HTL material. It has been applied in OPV[188], OLED[189] and perovskite PVs[190][191]. CuSCN is transparent within the entire visible region, with an absorption onset at 3.8 eV[189]. In addition, the raw material cost of CuSCN is low and the film fabrication can be achieved by the low temperature solution process in air[189]. However, the evaporation rate of CuSCN in typical solvent, such as dipropyl sulfide, is relatively fast, which influences the film morphology control. Copper selenocyanate (CuSeCN), analogous to CuSCN, is also considered as HTLs. Recently, we developed initial work using PEDOT:PSS/CuSeCN bilayer as HTL in perovskite solar cells, showing improved V_{OC} (1.00 V) compared with pristine PEDOT:PSS (0.91 V), Figure 1.19.

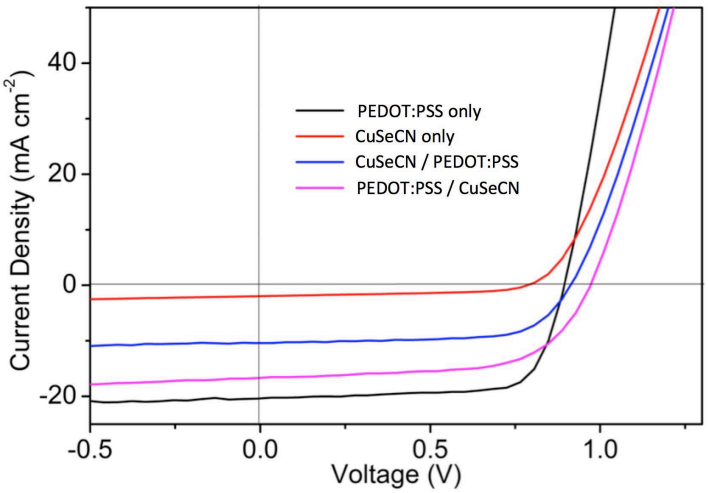


Figure 1.19 Representative J-V curves with device structure ITO/HTL/$CH_3NH_3PbI_3$/PCBM/LiF/Al.

1.4.3 Electron transport layer

1.4.3.1 Organic materials

Organic small molecules and polymers can also act as ETLs. For small molecules, they can be divided into fullerene derivatives and non-fullerene oligomers. PCBM is a typical fullerene derivative material, utilised not only as electron acceptor in OPV (see subsection 1.2.1.3) but also as an excellent electron extraction material in perovskite solar cells. When PCBM is deposited on top of perovskite films in inverted device structures, the perovskite trap density at surface and grain boundaries is reduced by some two orders of magnitude, Figure 1.20[134]. The J-V hysteresis is significantly reduced by the trap passivation. PCBM is reported to fill traps and macroscopic cracks between perovskite grains thus analogous bulk heterojunction perovskite-PCBM devices are created, resulting in high FF and high J_{SC} with little hysteresis[129]. Apart from inverted device structures, PCBM is also applied in conventional device structures, beneath perovskite films[192][150]. High efficiency with little hysteresis are also achieved. However, in this structure, the thin PCBM (~10's nm) compared with thick perovskite layers (~100's nm) illustrates trap passivation in perovskite grain boundary is not the only origin for the enhanced performance. The involvement of PCBM is believed to cause efficient charge extraction, which enables the device less sensitive to the device polarisation[150].

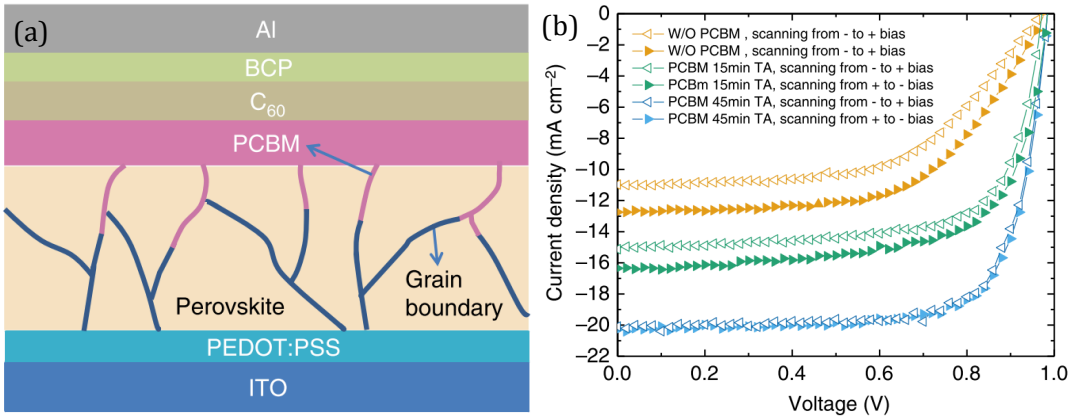


Figure 1.20 (a) Perovskite inverted device structure with PCBM (b) J-V characteristic curves for devices with PCBM show reduced hysteresis. Both adapted from Ref[134].

Besides typical fullerene derivatives that use nonpolar solvents, water/alcohol soluble fullerene derivatives have also attracted much attention. Water/alcohol soluble fullerene derivatives are generally modified C_{60}/C_{70} species[193] or fulleropyrrolidines[194], and can be applied on top of the active layer of polymer solar cells or on the bottom of perovskite layer of perovskite solar cells.

Another important small molecule electron extraction material is non-fullerene oligomers, containing non-conjugated oligomers, perylene-diimide (PDI) based salts and other polycyclic aromatic compounds[151]. The purpose of introducing these materials is mainly to tune the interface energy alignment between the active layer and the electrode. For the amino-containing non-conjugated oligomers, the density of amino groups can influence the interfacial dipole formation at BHJ/Al interface, which leads to work function shifting[195]. For the PDI based salt, PDINO also can tune the work function from its ionic feature, with relatively high intrinsic conductivity owing to PDI units self-organised π-stacking. Other polycyclic aromatic compounds, for example a conjugated zwitterion Rhodamine 101 material, formed strong dipoles at the active layer/electrode interface due to the zwitterionic moiety[196].

For polymers acting as electron extraction materials, they can be mainly divided into two categories: polyelectrolytes (PEs) and neutral polymers. There are three main kinds of polyelectrolytes for electron extraction, including polythiophene (PT) - based conjugated PEs (CPEs)[197], poly [(9,9-bis(3'-(*N*,*N*-dimethylamino) propyl)-2,7-fluorene) -alt-2,7-(9,9–dioctylfluorene)] (PFN)-based CPEs[198] and non-conjugated PEs[199]. Most PE electron extraction materials can be easily dissolved in alcohol-based solvents.

For neutral polymers, the typical materials include polyethylenimine ethoxylated / branched polyethylenimine (PEIE/PEI), polycarbazole (PC)-based and PFN-based

compounds. Most neutral polymer electron extraction materials can be dissolved in alcohol with acetic acid (AcOH) as an additive to increase the solubility. PEIE/PEI have been widely utilised to reduce the work function of metals, metal oxide, conjugated polymers and graphene[200]. The chemical structure of PEIE/PEI is shown in Figure 1.21. These polymers are insulators with large bandgaps so they should be considered as surface modifiers rather than charge injection species. The mechanism of work function shift by PEIE/PEI comprising of two parts: i) the ethylamine molecular dipole along the direction vertical to the substrate; ii) the interface dipole due to a slight electron transfer from the amine-containing polymers to the electrode surface. In particular, PEIE/PEI is widely used as surface modifiers of ZnO, both in organic solar cells[201] and perovskite solar cells[202].

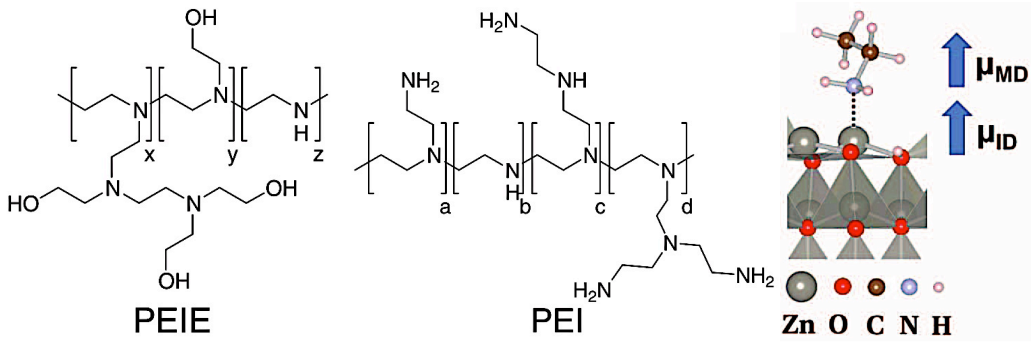


Figure 1.21 (a) chemical structures of PEIE and PEI; (b) Proposed model of molecular dipole (MD)–induced and interface dipole (ID)–induced WF reduction on ZnO surface. Photographs adapted from Ref[200].

PC-based derivatives have also been investigated as ETLs. Phosphonate side chains are typically used to decorate PC homopolymers and copolymers. These hydrophilic side chains can supply a sub-gap state for electron transport and change the ITO work function by introducing interfacial dipoles[203]. For PFN-based ETLs, intrinsic PFN can tune the work function of ITO to facilitate Ohmic contact at the interface between ITO and the active layer[204]. The PFN derivative PFN-OX shows good solvent resistance due to the crosslinking and it also can modify ZnO as electron extraction layer for better device performance[205].

1.4.3.2 Inorganic materials

Inorganic electron extraction materials have been widely investigated due to the excellent environmental stability and electrical properties. Apart from the most frequently studied transition metal oxides, reduced graphene oxide (rGO) based materials have also shown the potential as ETLs. Unlike the aforementioned pristine GO with a large work function (~ 5.0 eV) that is suitable for hole extraction layer, Caesium-neutralised GO (GO-Cs) possesses a much lower work function (4.0 eV),

making it suitable as an ETL[206]. Hybrid electron extraction layers have also been developed by mixing r-GO with other materials, such as rGO-TiO_2, rGO-ZnO and rGO-pyrene-PCBM[151]. Cs_2CO_3 is another promising electron extraction material, with tunable work function by annealing temperature[207]. Cs_2CO_3 has been utilised both in OPV[207] and perovskite solar cells[208]. However, the poor hole blocking ability of Cs_2CO_3 limits its wide application.

Metal oxides are still the most popular electron extraction materials when compared with organic and other inorganic counterparts, owing to their superior air stability, visible transparency, low synthesis cost and suitable energy level alignment with active layer materials. Most studies on metal oxide electron transport layer are centred around three materials: TiO_2, SnO_2 and ZnO. These three materials all fulfil the requirements of ETLs for organic and perovskite solar cells defined in this project: low costs of raw material and synthesis, low temperature fabrication and solution processing.

TiO_2 is transparent in the visible region, with band gap 3.2 eV for the anatase phase[209]. TiO_2 possesses a conduction band minimum (CBM) and valence band maximum (VBM) levels at -4.2 eV and -7.4 eV, respectively[210]. Although typical TiO_2 requires high annealing temperature (above 500 ˚C), low temperature processed titanium oxide has been successfully applied in both OPV[211] and perovskite solar cells[212][213]. For OPV, the device performance with TiO_2 and ZnO are comparable[214]. For perovskite cells, TiO_2 is the most widely used ETL. Perovskite films show good chemical stability when deposited onto TiO_2. Although the mobility of nanoporous TiO_2 is comparable with those of nanoporous ZnO and SnO_2[215], the oxides in this project will have a planar morphology, here it should be noted that the electron mobility of TiO_2 (bulk single crystal) is about 10^2 times lower than that of ZnO and SnO_2[215]. In addition, the atomic orbitals which contribute to the CB in TiO_2 differ from ZnO and SnO_2. Where the CB of TiO_2 purely comes from Ti 3*d* orbitals[209] in ZnO and SnO_2 the CB is made up of Zn and Sn *s* states[216]. The CB minima of ZnO and SnO_2 localised on the metal *s* states are free-electron-like states. Because of the spherical symmetry of s states, the interaction between two metal *s* states is only influenced by the metal-metal distance and is not influenced by any angular disorder. Thus, the effect of disorder on the s-states dominating CB minimum is very small. So even amorphous ZnO and SnO_2 are expected to possess considerable electrical properties, compared to TiO_2. One more limitation of TiO_2 is that perovskite solar cells with mesoporous TiO_2 suffer from instability induced by UV light when cells are encapsulated[217]. Surface adsorbed oxygen can be desorbed under UV illumination, which exposes the deep trap states. These electronic trap states then facilitate the recombination of photogenerated electrons, which decreases the carrier collection at the electrodes.

SnO_2 is also a promising n-type semiconductor, with large bandgap (3.8 eV)[215]. Apart from its high bulk electron mobility (240 $cm^2V^{-1}s^{-1}$) and s-like CB minimum, the advantages of SnO_2 include chemical compatability with perovskites and UV stability. Low temperature, solution processed SnO_2 as an ETL has resulted in perovskite solar cells with high efficiencies[218][219]. Albeit perovskite planar devices with SnO_2 by atomic layer deposition (ALD) showed negligible J-V hysteresis[220], planar perovskite cells using solution processed SnO_2 without surface modifier still faces the problem of hysteresis, the same as those with planar TiO_2 and ZnO. In addition, the CB minimum of SnO_2 is no less than 300 mV deeper than those of TiO_2 and ZnO[215][216][221], as shown in Figure 1.22a, which makes it unsuitable for many polymer solar cells – causing considerable V_{OC} loss and consequent low efficiency.

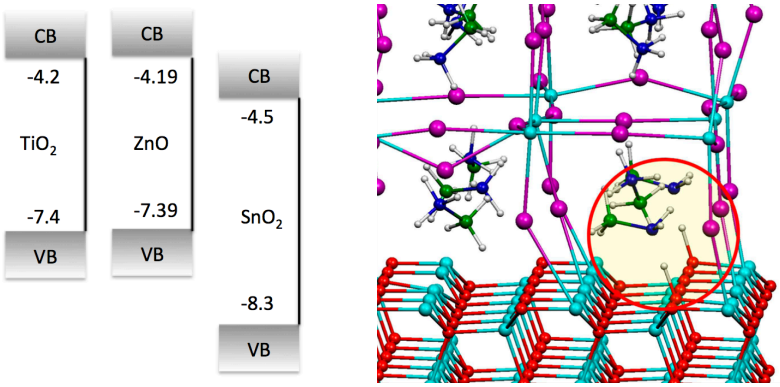


Figure 1.22 (a) Energy level alignment with CBs and VBs of TiO_2, ZnO and SnO_2; (b) the proton-transfer reaction at the perovskite (upside)/ZnO (downside) interface, red ball: O, white ball: H, adapted from Ref [222].

As for ZnO, this widely studied material combines excellent electron mobility (205 $cm^2V^{-1}s^{-1}$)[223] and s-like CB minimum. The CBM and VBM of ZnO are -4.19 eV and –7.39 eV, respectively[224], similar to those of TiO_2, suitable energy level alignment for electron extraction with most polymer and perovskite active layers, as illustrated in Figure 1.22. Low temperature, solution processed ZnO planar layers have also been applied both in OPV[225][226] and perovskite solar cells[192][131]. However, ZnO has been shown to cause perovskite thermal instability when perovskite directly contact with ZnO[222]. The origin of this perovskite thermal instability is the proton-transfer reaction at the perovskite/ZnO interface due to the basic nature of the ZnO surface, as shown in Figure 1.22b.

The merits and limitations of TiO_2, SnO_2 and ZnO as ETLs for OPV and perovskite cells are summarised in Table 1.1. Energy alignment, electron mobility and s-like CBM are more likely intrinsic properties of bulk materials, which is not easy to modify provided no deliberate doping were involved. However, the problem of active layer chemical

instability caused by the direct contact between oxide and active layer may be solved by the interfacial modification. In addition, the decomposition of perovskite on ZnO has been proven reversible and it can be prevented provided a limited volume solvent annealing process is employed[227]. Thus, we chose ZnO as the research object in this project. More details of ZnO will be introduced in the next section.

Table 1.1 Comparisons between TiO_2, SnO_2 and ZnO as electron extraction layer for OPV and perovskite solar cells (positive ✓; negative ×)

	Energy alignment with most active layer materials	Active layer chemical stability	Electron mobility	s-like CBM
TiO_2	✓	✓	×	×
SnO_2	×	✓	✓	✓
ZnO	✓	×	✓	✓

We introduced the interfacial layer in organic and perovskite solar cells in this section. A summarised energy-level diagram of representative materials discussed above is shown in Figure 1.23.

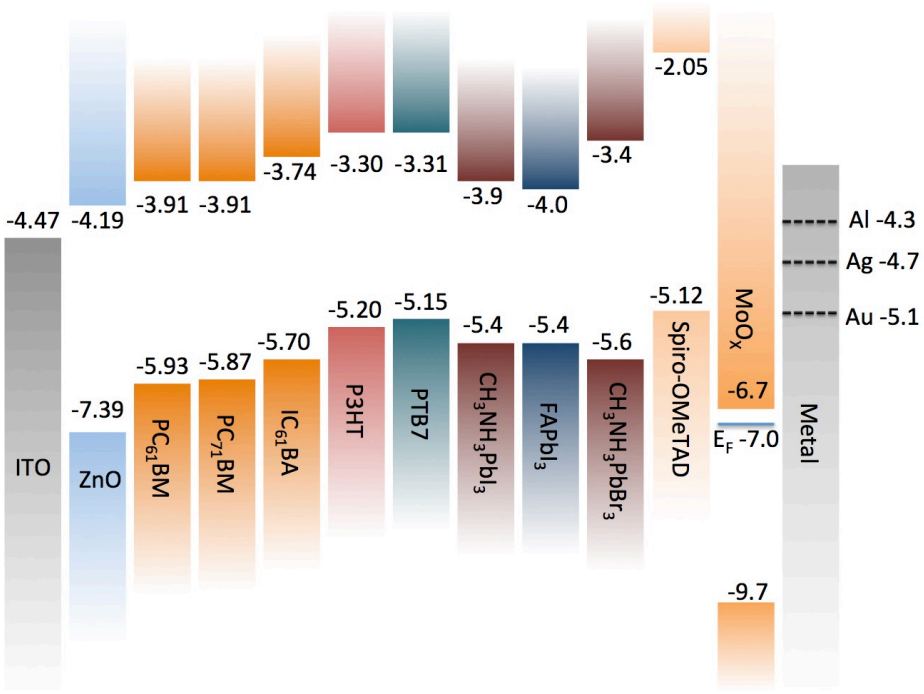


Figure 1.23 Schematic energy-level diagram of representative materials: ITO[44], ZnO[224], $PC_{61}BM$[54], $PC_{71}BM$[54], $IC_{61}BA$[44], P3HT[44], PTB7[228], $MAPbI_3$[151], $FAPbI_3$[151], $MAPbBr_3$[151], Spiro-OMeTAD[166] and MoO_X[175].

1.5 ZnO properties and processing methods

1.5.1 ZnO properties

1.5.1.1 Crystalline structure

The thermodynamically stable crystal structure of zinc oxide at ambient conditions is hexagonal wurtzite[229]. Other ZnO crystalline structures include cubic zinc-blende, obtained by growth on cubic substrates, and rock salt which is obtained at high pressures; both are metastable[229]. In the wurtzite structure, each zinc ion is surrounded by four oxide ions at the corners of a tetrahedron, and vice visa. The lattice constants at room temperature are measured and calculated (a= 3.2475 ~ 3.2501 Å, c= 5.2042 ~ 5.2075 Å)[229] and the density is 5.605 g cm^{-3}[230]. The crystal structure is shown in Figure 1.24. The alternating distance between closed packed O^{2-} and Zn^{2+} faces is 0.69 Å and 1.99 Å respectively[231]. The asymmetry in the c-direction results in polarity, the plane perpendicular to the c-axis is composed fully of either oxygen or zinc ions[230]. This polar plane also has the highest surface energy[232]. Thus the growth of ZnO tends to proceed in the <001> direction in order to minimise the area of high-energy surface, which results in the self-assembly of ZnO nanorods. Other ZnO nanostructures include nanowires[233], nanotubes[234], nanoflowers[235], mesoporous films[236], nanosheets[237], honeycomb[238], nanorings[239], nanopropeller arrays[240] *etc.*

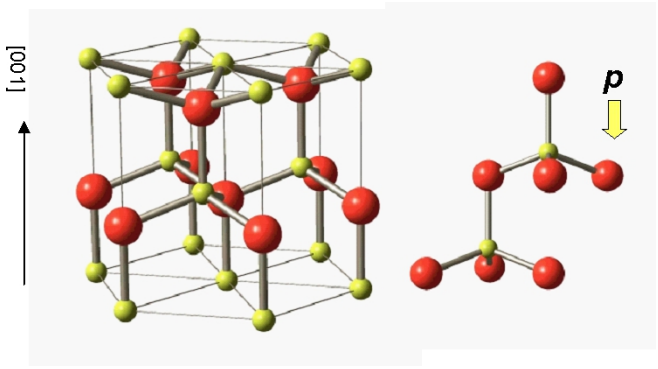


Figure 1.24 Stick and ball representation of ZnO crystal structure: yellow ball Zn, red ball O. Adapted from Ref [241].

1.5.1.2 Optoelectronic properties

ZnO is a wide band-gap semiconductor whose E_g is about 3.2 eV at room temperature[242]. This value corresponds to a wavelength of 387 nm, which means the optical absorption of ZnO is in the UV spectrum. In other words, ZnO is transparent to visible light and can thus be the charge transport layer at the transparent electrode. Bandgap engineering is also widely used in ZnO. For a wider band gap, $Mg_xZn_{1-x}O$ alloy is a candidate due to the introduction of MgO (Eg 7.7 eV) [229][243]. For a narrower band

gap, $Cd_xZn_{1-x}O$ is widely studied (E_g of CdO 2.3 eV) to adapt the optical absorption to the visible spectrum[244].

ZnO is an intrinsic n-type semiconductor. In general, unintentionally incorporated impurities are of two kinds: one from intrinsic crystalline defects and the other from extrinsic dopants. The position of defects in the energy level diagram plays an important role in the contribution to conductivity. The defects near the CB are called shallow donors which are likely to produce free charges and the ones far from CB are called deep donors which are less likely to increase conductivity. For intrinsic defects, two types are shown to be prevalent in ZnO: zinc interstitials and oxygen vacancies[230]. Both kinds of defects are influenced by the amount of oxygen, which is observed in experiments that growth and annealing conditions can tune the conductivity[245]. For extrinsic dopants, the most prevalent kind is hydrogen that forms hydroxyl type acting as shallow donors[246]. Nitrogen atoms are also inadvertently introduced as a complex[247]. In another aspect, intentional impurities are investigated in order to change the electrical properties of ZnO. On one hand, conductivity can be enhanced with donor elements (Group III, like Al[248], Ga[249] or halogen species like F[250] and Cl[251]). Transparent conducting oxide AZO is derived from this[252]. On the other hand, acceptor elements (Group V, like N[253], P[254] or monovalent metal like Li[255] and Na[256]) is doped into ZnO to try to invert it into p-type semiconductors. This still remains a challenge due to the compensation with intrinsic n-type donors[257]. In this project, deliberate doping will not be involved, but the influence of chemical composition on ZnO electrical properties and related solar cell performance will be investigated.

1.5.2 ZnO low temperature processing methods

1.5.2.1 Vacuum techniques

There are many methods to deposit ZnO planar films at relatively low temperatures. Vacuum deposition techniques include atomic layer deposition (ALD)[258], chemical vapour deposition (CVD)[259] and pulsed laser deposition (PLD)[260] . One advantage of these vacuum techniques is the ability to precisely control the film properties by tuning reaction conditions, such as processing temperature and oxygen partial pressure. Also, vacuum techniques allow ZnO films to be deposited on environmentally sensitive photoactive layers. Our group has successfully deposited ZnO on P3HT films by PLD, as shown in Figure 1.25a[260]. Recently, we also deposited ZnO on perovskite films, shown in Figure 1.25b. By careful control of ZnO deposition condition, no structural damage of underlying perovskite film is seen.

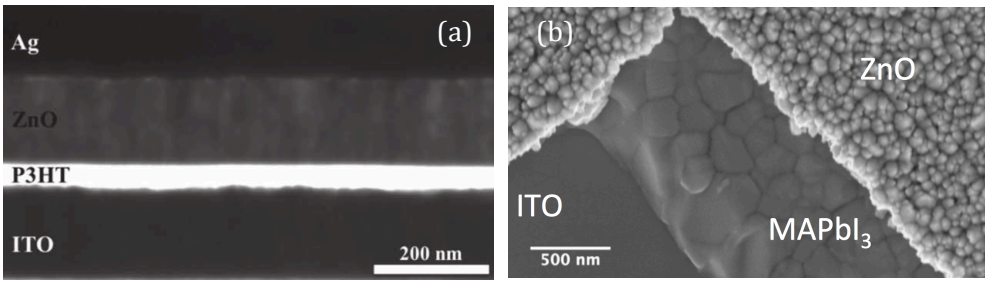


Figure 1.25 (a) TEM image showing ZnO deposited on P3HT by PLD, adapted from Ref[260]; (b) SEM image showing ZnO deposited on $CH_3NH_3PbI_3$ by PLD.

However, the fabrication costs when using vacuum techniques is high. In addition, the film area of uniform deposition is typically small in vacuum techniques, which limits the application of large-area solar cells. Thus, ZnO with low-temperature and solution processing methods are pursued. These methods mainly include colloidal nanoparticles, hydrothermal synthesis, electrodepositon, sol-gel processing and ammine-hydroxo zinc solutions, which will be separately introduced below.

1.5.2.2 Colloidal nanoparticles

The fabrication of ZnO planar layers can be achieved through spin casting using dispersed ZnO nanoparticle solution. The ZnO colloids are synthesised through the hydrolysis and the subsequent dehydration of thermodynamically unstable $Zn(OH)_2$. The reaction is as following:

$$Zn^{2+} + 2OH^- \rightleftharpoons Zn(OH)_2 \rightleftharpoons ZnO + H_2O \qquad \textbf{Eqn 1.1}$$

The precursors of ZnO nanoparticle solutions typically contain zinc acetate dihydrate with a strong base and tetramethyl-ammonium hydroxide[151]. The colloidal solution also can be achieved using alcoholic solutions, without strong base and other additives[261]. For the morphology, the crystalline orientation of ZnO nanoparticle film is random, similar to ZnO powder diffraction pattern. ZnO films by colloidal ZnO nanoparticles now have been successfully employed to both OPV[226] and perovskite solar cells[131].

One advantage of colloidal nanoparticles is that the small crystallite size (< 5 nm) enables closely packed nanoparticle films with low film thickness (< 20 nm). In addition, the film processing temperature when using colloidal nanoparticles can be as low as room temperature[131]. However, the synthesis route of dispersed ZnO nanoparticle solution is relatively complex, including long reaction duration, precipitation, washing and dilution procedures, which will increase the fabrication cost of whole solar cells. Moreover, ligand-linked nanoparticles typically need high temperature annealing

procedure, while ligand-free nanoparticles usually have the problem of poor dispersion stability[262][263].

1.5.2.3 Hydrothermal synthesis

Hydrothermal growth, also called chemical bath deposition, is an aqueous method leading to the formation of solid colloidal metal oxide or hydroxide *via* the forced hydrolysis process of metal salts at a proper temperature. Hydrothermal deposition can be applied to different substrates, including conducting and non-conducting, rigid and flexible substrates[264]. This technique is suitable for various oxides, such as ZnO[75], TiO_2[265] and other transition metal oxides[266]. For ZnO, the typical synthesis is based on the following reactions, using zinc nitrate as a zinc precursor and hexamethylene triamine (HMT) as an oxygen precursor to slowly provide OH^- ions to the solution[267]. The synthesis temperature is around 70-95 ˚C.

$$(CH_2)_6N_4 + 6H_2O \rightleftharpoons 4NH_3 + 6HCHO \qquad \textbf{Eqn 1.2}$$

$$NH_3 + H_2O \rightleftharpoons NH_3{\cdot}H_2O \rightleftharpoons NH_4^+ + OH^- \qquad \textbf{Eqn 1.3}$$

$$Zn(NO_3)_2 \rightarrow Zn^{2+} + 2NO_3^- \qquad \textbf{Eqn 1.4}$$

$$Zn^{2+} + 2OH^- \rightleftharpoons Zn(OH)_2 \rightleftharpoons ZnO + H_2O \qquad \textbf{Eqn 1.5}$$

By adjusting the synthesis conditions, we can tune the ZnO morphology from 1-D nanorods to 2-D nanowalls and even the compact layer, as shown in Figure 1.26. All three structures possess preferred c-axis orientation. However, the compact layer by hydrothermal growth is not very suitable for organic and perovskite PV applications. First, uniform films with low thickness (< 100 nm) are not easy to achieve due to the fast reaction rate. The film thickness by hydrothermal growth is typically several hundreds nm. Second, the hydrothermal growth needs nucleation sites, which makes it hard to directly proceed on bare ITO/FTO substrates. A seed layer is typically needed.

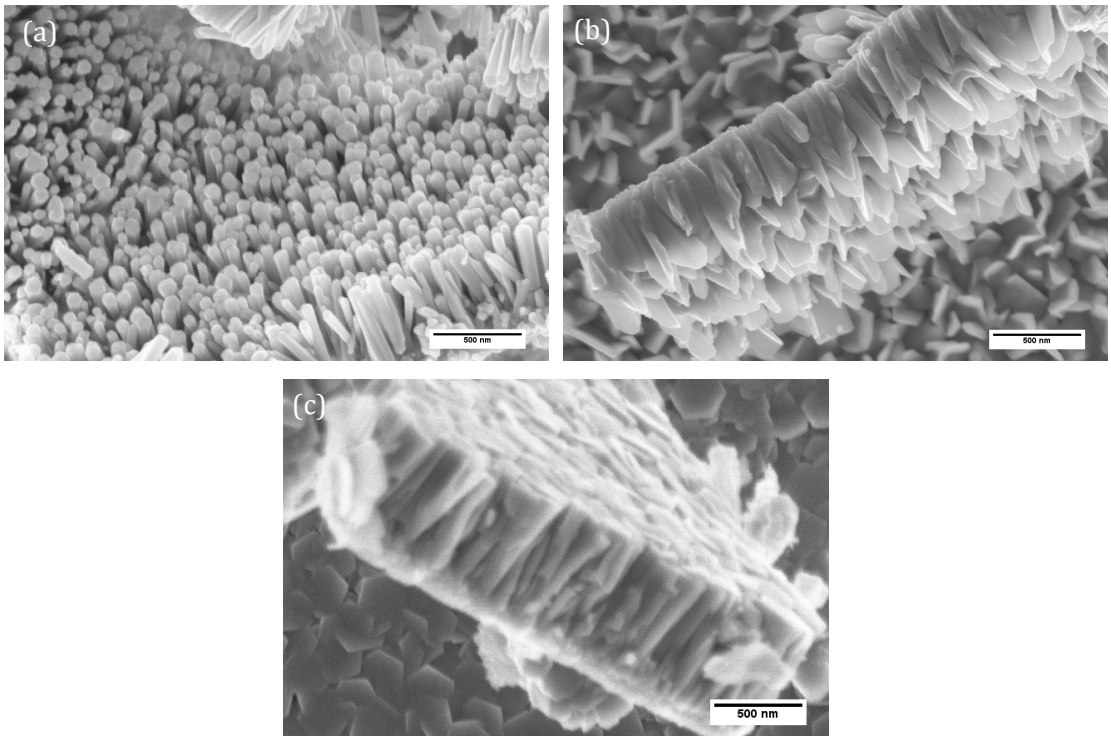


Figure 1.26 SEM images of different ZnO morphologies by hydrothermal synthesis: (a) nanorods; (b) nanowalls; (c) compact layer.

1.5.2.4 Electrodeposition

Electrodeposition typically employs a three-electrode geometry: a working electrode that ZnO will deposit on, a counter electrode to apply current and a reference electrode to monitor the process. The current between the two submerged working and counter electrodes drives the formation of ZnO from Zn^{2+}. An example is given with a simple aqueous zinc nitrate electrolyte, with the reaction equation shown below[268]. The reaction temperature is 80 ˚C.

$$Zn(NO_3)_2 \rightarrow Zn^{2+} + 2NO_3^- \qquad \textbf{Eqn 1.6}$$

$$NO_3^- + H_2O + 2e^- \rightarrow NO_2^- + 2OH^- \qquad \textbf{Eqn 1.7}$$

$$Zn^{2+} + 2OH^- \rightarrow Zn\,(OH)_2 \qquad \textbf{Eqn 1.8}$$

$$Zn(OH)_2 \rightarrow ZnO + H_2O \qquad \textbf{Eqn 1.9}$$

Similar to hydrothermal growth, ZnO film by electrodeposition also exhibits a preferred c-axis orientation. Although ZnO electrodeposition has the advantage of low temperature solution processing, it is also not an ideal method for this project. Electrodeposited ZnO films require an electrically uniform conducting substrate so that the nucleation and crystallite growth proceed simultaneously at all positions over the film. However, ITO cannot fulfil this requirement very well because it has been shown

that electron transfer only happens at around half of the ITO active sites[269]. It is therefore difficult to obtain uniform ZnO films on ITO substrates by electrodeposition, which limits the application of this method on organic and perovskite solar cells. As a result, perovskite solar cells with ZnO by electrodeposition only showed a relatively low PCEs of 5.54%[270].

The following two subsections separately introduce ZnO film formation by sol-gel processing and ammine-hydroxo zinc solutions. These two methods are both low temperature and solution processes. In addition, compared with colloidal nanoparticles, their precursor solutions for film casting are one-step prepared. Also, compared with hydrothermal synthesis and electrodeposition, they can deposit compact and thin films on ITO substrates. The combination of these advantages makes them ideal methods for fabricating ZnO electron transport layers in organic and perovskite solar cells. Thus, these two methods are chosen to be used in this project.

1.5.3 ZnO films by sol-gel method

Here a sol-gel process is a method to produce solid materials from solutions *via* sols or gels as intermediates. The process often involves the conversion of molecular precursors into an oxide network. Sol-gel methods can be divided into two kinds: the classical sol-gel method and the non-hydrolytic sol-gel method[209].

The sol-gel method for ZnO films in this thesis is the classical method, therefore the non-hydrolytic method are not discussed in much detail. In general, the non-hydrolytic sol-gel process involves the transformation of the precursor dissolved in an organic solvent excluding water or a base[271][272][273]. Non-hydrolytic hydroxylation reactions and aprotic condensation reactions are the important reaction paths for this method. The non-hydrolytic sol-gel methods have two advantages: one is the precise control of the particle size and shape; the second is the slow reaction rate due to the moderate reactivity of the precursors.

Compared with the non-hydrolytic methods, the classical sol-gel process was developed much earlier but is still under intense study because of the complicated interaction principles due to the formation of various oligomeric species[274]. The classical sol-gel process is the transformation of a precursor into an inorganic solid *via* hydrolysis and condensation reactions[275][276]. There are different routes to fabricate metal oxide films, as shown in Figure 1.27. For ZnO film formation by the classical sol-gel methods, the route can be summarized in three processes: (1) the preparation of the precursor solution; (2) the xerogel film deposition of the prepared sol on substrates; (3) transformation into dense film by annealing.

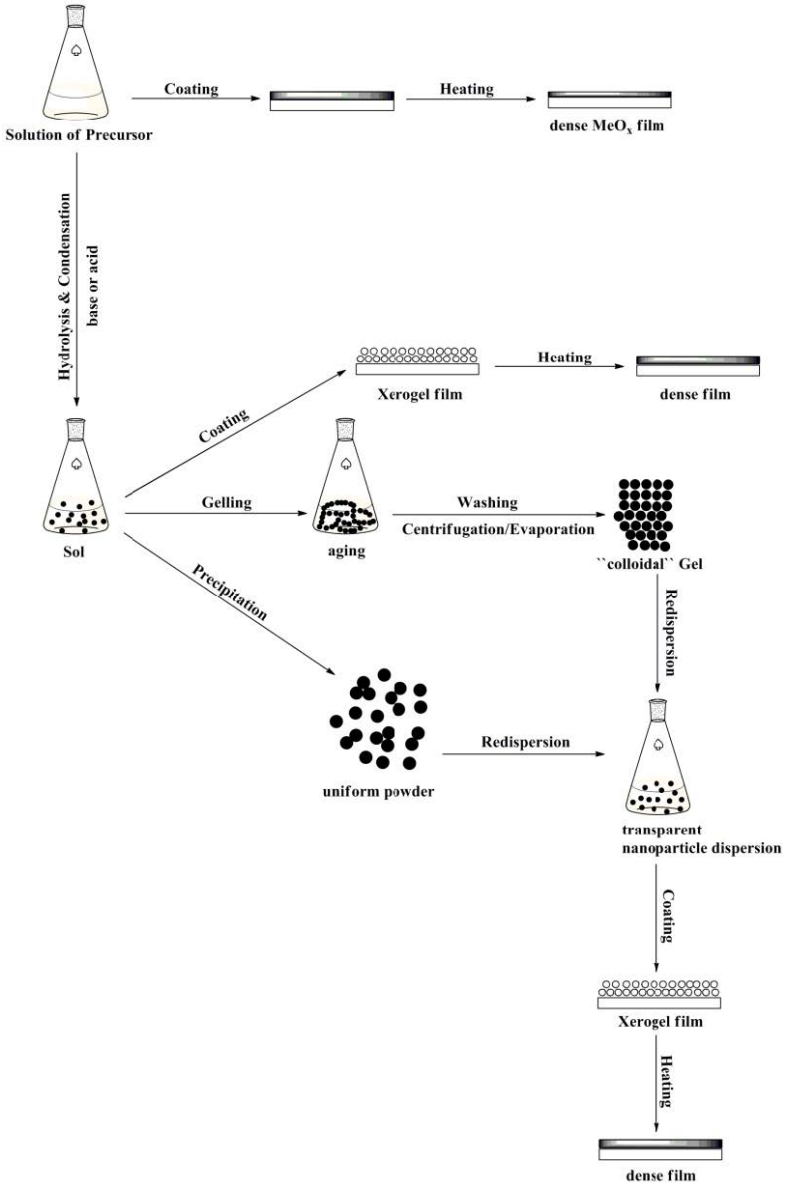


Figure 1.27 Various ways to form metal oxide films by sol-gel methods, adapted from Ref[209].

First, we summarise the nature of precursor in ZnO films by sol-gel methods. In a general sol-gel process, a molecular precursor goes through the following processes in the solution: (1) hydrolysis of the molecular precursor; (2) polymerization with a suitable reagent, forming oxo-, hydroxyl, or aqua bridge; (3) condensation by dehydration; (4) nucleation and growth[277][278]. From the ZnO sol-gel literatures, the starting materials are normally zinc salts in alcoholic solutions.

The anion in zinc salts has been reported to be very important for the preparation of the precursor solution[279][280]. Several zinc salts have been investigated as precursor: nitrate, chloride, perchlorate and acetate. Among them zinc acetate dihydrate is the most frequently used. The acetate can act as the stabiliser of the colloidal sol so that the system with acetate is more reproducible under a large range of experimental

conditions when compared with other anions[280]. In the sol formation, complexes are made with acetate and zinc cations, forming as basic zinc acetate $Zn_4O(Ac)_6$, ethoxy acetate $(EtOZnAc)_n$ and hydroxyl double salt $Zn_5(OH)_8(Ac)_2 \bullet 2H_2O$ (Zn-HDS) etc., dependent on the synthesis conditions[281][282]. Whatever their formation is, these complexes go through hydrolysis and polymerization, which forms the sol containing zinc oxide nanoparticles.

For the solvent to dissolve the zinc salts, alcohols are normally used, such as methanol[283], ethanol[280][284], 1-propanol[285], 2-propanol[286], and 2-methoxyethanol[287–289]. Additives are often used in the classical ZnO sol-gel process, playing the roles of facilitating the zinc salt dissolution and/or stabilizing the dispersions of colloids. Alkali metal hydroxides[290], alkanolamines[287–289], alkylamines[291], acetyacetone[292] etc. are reported to be used. The additives can avoid the fast precipitation of zinc hydroxide by chelating and stabilizing ligands.

Here the combination of zinc acetate dihydrate (ZAD), monoethanolamine (MEA) and ethanol are used as an example. ZAD has a limited solubility in ethanol without additives or heating. MEA as the additive can help ZAD to be completely dissolved[293]. In addition, the amino groups and the hydroxyl groups in MEA can coordinate the zinc atoms, enhancing the solubility and stability against hydrolysis[287]. The proposed reaction mechanism of this combination is shown in Figure 1.28[284]. Because of the very little water that only comes from the zinc acetate dihydrate, the reaction rate of forced hydrolysis and condensation is relatively low. The acetate group can complex Zn^{2+}. MEA also plays the role of a complexing agent and slows down Zn^{2+} condensation. But the addition of MEA also increases the pH, which may boost the ZnO formation. HO^- wants to combine with Zn^{2+} and form ZnO by hydrolysis and condensation. Hence, actually these three species (Ac^-, MEA, HO^-) compete for the Zn^{2+}. Small zinc-oxo-acetate oligomers tend to form in the initial stage, from gradual forced hydrolysis of Zn-Ac or Zn-MEA complexes during aging[284]. Then the condensation of the hydrolyzed products forms colloids or precipitates. Acetate-capped nanometric particles probably are formed in dilute solutions, which is deduced from the SEM and FTIR information[280][284].

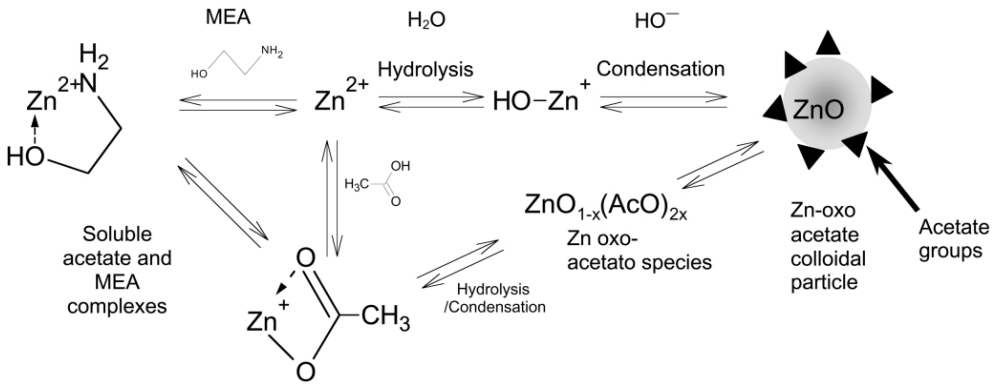


Figure 1.28 Description of the chemical equilibria in the initial solution (precursor: zinc acetate dihydrate; additive: MEA; solvent: ethanol), adapted from Ref[284].

After solution preparation, the films are fabricated by different ways, such as spin coating, dip coating and spray pyrolysis. Spin coating is the most widely used technique due to the low consumption of raw materials and uniform film surface.

The deposited films normally require heat treatment to thermally convert the precursors and ensure full functionality. To obtain polycrystalline oxide films, the heat treatment usually contains two steps. First, a preheating process is applied for solvent evaporation and organic residue decomposition. Second, a postheating process is applied for the crystallisation of oxide films and the complete removal of organic residues. The processing temperatures of two steps are critical to the film composition and the crystalline orientation. We use the combination of ZAD+MEA+2-methoxyethanol as an example. The boiling points of 2-methoxyethanol and MEA, are 125 ˚C and 171 ˚C, respectively[294]. The decomposition of zinc acetate is around 240 ˚C[294]. However, due to the complexation of zinc cation with MEA and acetate, MEA and acetate group have been proved to remain in the films up to 300 ˚C[295]. The decomposition starts at 300 ˚C by breaking the bonds in the complexes containing MEA and acetate. Zinc complex with MEA is reported to be completely decomposed at around 400 ˚C[295]. The nucleation and crystal growth occur accompanying with the decomposition. However, it is difficult to separate these processes because the nucleation and crystal growth has begun before the complete decomposition at 300 ˚C. The crystallization of ZnO is observed to be complete between 400-500 ˚C[295].

1.5.4 ZnO film by carbon-free chemistry

Unlike the sol-gel approach that has been developed for many years[277], ZnO carbon-free chemistry is relatively new[296]. The ZnO carbon-free method is a method based on ammine-hydroxo zinc solutions as precursors. This method enables the ZnO crystallisation at low temperature (< 150 ˚C) by the metal-ammine decomposition and hydroxide condensation/dehydration processes. The fast and low-energy kinetics of

these reactions provide superior film morphologies: low surface roughness and high film continuity by preventing long-range anisotropic particle growth[296]. Although the thickness of ZnO films by this method is limited by the low solubility of precursor at room temperature, this approach can fabricate ultra-thin and compact layers, which is very suitable for thin film transistor[296–299] and thin film polymer/perovskite solar cells[300][301]. And ammine-hydroxo zinc solutions now can form films either by inkjet printing[296] or spin-coating[298].

There are two typical synthesis routes of ZnO formation by carbon-free chemistry. One is two-step process: synthesising $Zn(OH)_2$ precipitate at first and then adding it into aqueous ammonia to form ammine-hydroxo zinc solutions[296]. The $Zn(OH)_2$ precipitate can be prepared by the reaction between $Zn(NO_3)_2$ and NaOH. The reactions can be expressed as follows[296]:

$$Zn(NO_3)_{2(aq)} + 2NaOH_{(aq)} \rightarrow Zn(OH)_{2(s)} + 2NaNO_{3(aq)} \quad \textbf{Eqn 1.10}$$

$$Zn(OH)_{2(s)} + xNH_{3(aq)} \rightarrow Zn(OH)_2(NH_3)_{x(aq)} \rightarrow ZnO_{(s)} + xNH_{3(g)} + H_2O_{(g)} \quad \textbf{Eqn 1.11}$$

Unlike the aforementioned first method that requires precipitation, washing and dilution procedures to prepare precursor solution, similar to nanoparticle preparation, the other one is one-step process: dissolving ZnO powders directly into aqueous ammonia at temperatures below 15 ˚C. The reaction of this minimalist approach can be expressed as following[297]:

$$NH_3 + H_2O \rightarrow NH_4^+ + OH^-,\ NH_4^+{}_{(aq)} \rightleftharpoons NH_{3(aq)} + H^+{}_{(aq)} \quad \textbf{Eqn 1.12}$$

$$ZnO_{(s)} + 4NH_{3(aq)} + 2H^+{}_{(aq)} \rightarrow Zn(NH_3)_4^{2+}{}_{(aq)} + H_2O \quad \textbf{Eqn 1.13}$$

$$Zn(NH_3)_4^{2+} + nOH^- \rightarrow [Zn(NH_3)_{4-n}(OH)_n]^{2-n} + nNH_3 \ (n=1\sim4,\ n \text{ is close to 4 at high PH}) \quad \textbf{Eqn 1.14}$$

$$Zn(OH)_4^{2-} \rightarrow ZnO + H_2O + 2OH^- \ (\text{when } n=4) \quad \textbf{Eqn 1.15}$$

The candidates of the complex with zinc ions are NH_3 and OH^- ions. When the pH of the zinc solution is 11~12, NH_3 is replaced by OH^- ions. As a result, $Zn(OH)_4^{2-}$ is formed and then easily decomposed into ZnO at low process temperature[297].

As stated above, although both are simple, low-cost, low-temperature and solution processes, ZnO sol-gel and carbon-free chemistries are different. The most significant difference is the reaction kinetics. For sol-gel method, the reaction is slow and energy intensive. Thus during the formation of polycrystalline films, the particles have enough time to move to the positions to allow lowest surface energy, normally resulting in

highly (002) oriented films. While for carbon-free chemistry, the reaction is rapid and low-energy. The consequential polycrystalline films processed at low temperature although also present hexagonal wurtzite structure, the orientation is relatively random, similar to the powder patterns[296].

1.6 Summary

Flexible electronics is an important application of photovoltaic materials. The fabrication cost of solar cells, rather than power conversion efficiency, is the key factor in flexible electronics. Organic and hybrid perovskite solar cells are two promising systems for low fabrication cost due to their advantages including roll-to-roll, low processing temperature, small material quantities and solution processing. In organic and perovskite solar cells, charge carrier transport layers are commonly needed to enhance the carrier extraction and therefore improve the power conversion efficiency. Metal oxides are widely studied as electron transport layers owing to their superior air stability, low synthesis cost and visible transparency. In this project, zinc oxide is chosen as the ETL material because it combines suitable energy alignment, excellent electron mobility and s-like CB minimum. Two ZnO film fabrication methods, *i.e.* sol-gel processing and carbon-free ammine-hydroxo zinc solutions, are investigated due to their low temperature solution processing, easy preparation of precursor solution and compact thin film morphology.

In summary, low temperature, solution processed ZnO thin films are investigated as ETLs for organic and perovskite solar cells in this thesis. Two ZnO film fabrication methods are employed: sol-gel chemistry and carbon-free approach. The aim is to investigate the influence of ZnO ETLs on organic and perovskite solar cell properties and to make high performance devices with ZnO ETL optimisation.

Chapter 3 investigates the sol-gel derived ZnO thin film. The influences of processing temperature on the film properties, including crystallinity, chemical analysis, surface morphology and optical/electrical properties, are explored.

Chapter 4 investigates organic solar cells with sol-gel derived ZnO as ETLs. Two types of OPVs are employed, one is prototype P3HT:$IC_{61}BA$ system and the other is high-performance PTB7:$PC_{71}BM$ system.

Chapter 5 investigates perovskite solar cells with sol-gel derived ZnO as ETLs. The influence of sol-gel ZnO with different processing temperatures on thermal stability of adjacent perovskite is studied. In addition, an interfacial modification is introduced between perovskite and sol-gel ZnO, showing improvement on both perovskite thermal stability and device performance.

In Chapter 6, first the thin film properties of ZnO by carbon-free chemistry are investigated. Although both processed at low temperature, ZnO films using sol-gel and carbon-free chemistry show distinct properties. Then the ZnO films are employed to organic and perovskite solar cells, with similar interfacial modification for perovskite works as that in previous chapter.

References

[1] D. H. Meadows, D. L. Meadows, J. Randers, W. W. Behrens, *The Limits to Growth : A Report to The Club of Rome*, **1972**.

[2] R. Williams, *J. Chem. Phys.* **1960**, *32*, 1505.

[3] A. B. Arons, M. B. Peppard, *Am. J. Phys.* **1965**, *33*, 367.

[4] D. M. Chapin, C. S. Fuller, G. L. Pearson, *J. Appl. Phys.* **1954**, *25*, 676.

[5] N. D. Arora, J. R. Hauser, D. J. Roulston, *IEEE Trans. Electron Devices* **1982**, *29*, 292.

[6] M. A. Green, K. Emery, Y. Hishikawa, W. Warta, E. D. Dunlop, *Prog. Photovoltaics Res. Appl.* **2016**, *24*, 3.

[7] A. Richter, M. Hermle, S. W. Glunz, *IEEE J. Photovoltaics* **2013**, *3*, 1184.

[8] W. Deng, D. Chen, Z. Xiong, P. J. Verlinden, J. Dong, F. Ye, H. Li, H. Zhu, M. Zhong, Y. Yang, Y. Chen, Z. Feng, P. Altermatt, *IEEE J. Photovoltaics* **2016**, *6*, 3.

[9] H. Sai, K. Maejima, T. Matsui, T. Koida, M. Kondo, S. Nakao, Y. Takeuchi, H. Katayama, I. Yoshida, *Jpn. J. Appl. Phys.* **2015**, *54*, 08KB05.

[10] D. D. Smith, P. J. Cousins, A. Masad, A. Waldhauer, S. Westerberg, M. Johnson, X. Tu, T. Dennis, G. Harley, G. Solomon, S. Rim, M. Shepherd, S. Harrington, M. Defensor, A. Leygo, P. Tomada, J. Wu, T. Pass, L. Ann, L. Smith, N. Bergstrom, C. Nicdao, P. Tipones, D. Vicente, in *2012 38th IEEE Photovolt. Spec. Conf.*, IEEE, **2012**, pp. 001594–001597.

[11] S. N. Alamri, *Phys. status solidi* **2003**, *200*, 352.

[12] B. O'Regan, M. Grätzel, *Nature* **1991**, *353*, 737.

[13] Mohammad K. Nazeeruddin, *Nature* **2016**, *538*, 463.

[14] H. C. Weerasinghe, F. Huang, Y.-B. Cheng, *Nano Energy* **2013**, *2*, 174.

[15] A. Polman, M. Knight, E. C. Garnett, B. Ehrler, W. C. Sinke, *Science* **2016**, *352*, 307.

[16] J. H. Bannock, S. H. Krishnadasan, A. M. Nightingale, C. P. Yau, K. Khaw, D. Burkitt, J. J. M. Halls, M. Heeney, J. C. de Mello, *Adv. Funct. Mater.* **2013**, *23*, 2123.

[17] M. A. Green, K. Emery, Y. Hishikawa, W. Warta, E. D. Dunlop, *Prog. Photovoltaics Res. Appl.* **2016**, *24*, 905.

[18] W. S. Yang, J. H. Noh, N. J. Jeon, Y. C. Kim, S. Ryu, J. Seo, S. Il Seok, *Science* **2015**, *348*, 1234.

[19] International Energy Agency, *Technology Roadmap Solar Photovoltaic Energy*, **2014**.

[20] C. W. Tang, A. C. Albrecht, *J. Chem. Phys.* **1975**, *62*, 2139.

[21] C. W. Tang, *Appl. Phys. Lett.* **1986**, *48*, 183.

[22] H. Hoppe, N. S. Sariciftci, *J. Mater. Res.* **2004**, *19*, 1924.

[23] L. Bormann, F. Nehm, L. Sonntag, F.-Y. Chen, F. Selzer, L. Müller-Meskamp, A. Eychmüller, K. Leo, *ACS Appl. Mater. Interfaces* **2016**, *8*, 14709.

[24] T. L. Chen, Y. Zhang, P. Smith, A. Tamayo, Y. Liu, B. Ma, *ACS Appl. Mater. Interfaces* **2011**, *3*, 2275.

[25] W. Tang, J. Hai, Y. Dai, Z. Huang, B. Lu, F. Yuan, J. Tang, F. Zhang, *Sol. Energy Mater. Sol. Cells* **2010**, *94*, 1963.

[26] Y. Lin, Y. Li, X. Zhan, *Chem. Soc. Rev.* **2012**, *41*, 4245.

[27] A. K. K. Kyaw, D. H. Wang, D. Wynands, J. Zhang, T. Q. Nguyen, G. C. Bazan, A. J. Heeger, *Nano Lett.* **2013**, *13*, 3796.

[28] A. Salleo, *Mater. Today* **2007**, *10*, 38.

[29] H. Sirringhaus, N. Tessler, R. H. L. B.-Ep.-O.-S. Friend, *Science* **1998**, *280*, 1741.

[30] Z. Bao, A. Dodabalapur, A. J. Lovinger, *Appl. Phys. Lett.* **1996**, *69*, 4108.

[31] W. Zhang, R. Zhu, F. Li, Q. Wang, B. Liu, *J. Phys. Chem. C* **2011**, *115*, 7038.

[32] A. Abrusci, S. D. Stranks, P. Docampo, H.-L. Yip, A. K.-Y. Jen, H. J. Snaith, *Nano Lett.* **2013**, *13*, 3124.

[33] E. Bundgaard, F. C. Krebs, *Sol. Energy Mater. Sol. Cells* **2007**, *91*, 954.

[34] M. Jaiswal, R. Menon, *Polym. Int.* **2006**, *55*, 1371.

[35] H. Sirringhaus, P. J. Brown, R. H. Friend, M. M. Nielsen, K. Bechgaard, B. M. W. Langeveld-Voss, A. J. H. Spiering, R. a. J. Janssen, E. W. Meijer, P. Herwig, D. M. de Leeuw, *Nature* **1999**, *401*, 685.

[36] Y. Kim, S. Cook, S. M. Tuladhar, S. A. Choulis, J. Nelson, J. R. Durrant, D. D. C. Bradley, M. Giles, I. McCulloch, C. S. Ha, M. Ree, *Nat. Mater.* **2006**, *5*, 197.

[37] F. P. V. Koch, J. Rivnay, S. Foster, C. Müller, J. M. Downing, E. Buchaca-Domingo, P. Westacott, L. Yu, M. Yuan, M. Baklar, Z. Fei, C. Luscombe, M. A. McLachlan, M. Heeney, G. Rumbles, C. Silva, A. Salleo, J. Nelson, P. Smith, N. Stingelin, *Prog. Polym. Sci.* **2013**, *38*, 1978.

[38] C. E. Murphy, L. Yang, S. Ray, L. Yu, S. Knox, N. Stingelin, *J. Appl. Phys.* **2011**, *110*, 93523.

[39] S. P. Speakman, G. G. Rozenberg, K. J. Clay, W. I. Milne, A. Ille, I. A. Gardner, E. Bresler, J. H. G. Steinke, *Org. Electron.* **2001**, *2*, 65.

[40] E. L. Ratcliff, J. L. Jenkins, K. Nebesny, N. R. Armstrong, *Chem. Mater.* **2008**, *20*, 5796.

[41] J. F. Chang, B. Sun, D. W. Breiby, M. M. Nielsen, T. I. Sölling, M. Giles, I. McCulloch, H. Sirringhaus, *Chem. Mater.* **2004**, *16*, 4772.

[42] T. T. Ngo, D. N. Nguyen, V. T. Nguyen, *Adv. Nat. Sci. Nanosci. Nanotechnol.* **2012**, *3*, 45001.

[43] X. Guo, C. Cui, M. Zhang, L. Huo, Y. Huang, J. Hou, Y. Li, *Energy Environ. Sci.* **2012**, *5*, 7943.

[44] J. Zhang, J. C. D. Faria, M. Morbidoni, Y. Porte, C. H. Burgess, K. Harrabi, M. A. McLachlan, *Adv. Electron. Mater.* **2016**, *2*, 1600008.

[45] Y. Liang, Z. Xu, J. Xia, S. T. Tsai, Y. Wu, G. Li, C. Ray, L. Yu, *Adv. Mater.* **2010**, *22*, 135.

[46] B. Ebenhoch, S. A. J. Thomson, K. Genevičius, G. Juška, I. D. W. Samuel, *Org. Electron.* **2015**, *22*, 62.

[47] L. Lu, L. Yu, *Adv. Mater.* **2014**, *26*, 4413.

[48] M. R. Hammond, R. J. Kline, A. A. Herzing, L. J. Richter, D. S. Germack, H. W. Ro, C. L. Soles, D. A. Fischer, T. Xu, L. Yu, M. F. Toney, D. M. DeLongchamp, *ACS Nano* **2011**, *5*, 8248.

[49] C. Liu, K. Wang, X. Hu, Y. Yang, C. H. Hsu, W. Zhang, S. Xiao, X. Gong, Y. Cao, *ACS Appl. Mater. Interfaces* **2013**, *5*, 12163.

[50] P. Sonar, J. P. Fong Lim, K. L. Chan, *Energy Environ. Sci.* **2011**, *4*, 1558.

[51] L. Dou, J. You, Z. Hong, Z. Xu, G. Li, R. a Street, Y. Yang, *Adv. Mater.* **2013**, *25*, 6642.

[52] G. Yu, J. Gao, J. C. Hummelen, F. Wudl, A. J. Heeger, *Science* **1995**, *270*, 1789.

[53] V. D. Mihailetchi, J. K. J. van Duren, P. W. M. Blom, J. C. Hummelen, R. A. J. Janssen, J. M. Kroon, M. T. Rispens, W. J. H. Verhees, M. M. Wienk, *Adv. Funct. Mater.* **2003**, *13*, 43.

[54] Y. He, Y. Li, *Phys. Chem. Chem. Phys.* **2011**, *13*, 1970.

[55] G. Li, V. Shrotriya, J. Huang, Y. Yao, T. Moriarty, K. Emery, Y. Yang, *Nat. Mater.* **2005**, *4*, 864.

[56] M. M. Wienk, J. M. Kroon, W. J. H. Verhees, J. Knol, J. C. Hummelen, P. A. van Hal, R. A. J. Janssen, *Angew. Chem. Int. Ed. Engl.* **2003**, *115*, 3493.

[57] F. B. Kooistra, V. D. Mihailetchi, L. M. Popescu, D. Kronholm, P. W. M. Blom, J. C. Hummelen, *Chem. Mater.* **2006**, *18*, 3068.

[58] Y. He, H.-Y. Chen, J. Hou, Y. Li, *J. Am. Chem. Soc.* **2010**, *132*, 1377.

[59] E. Orgiu, M. a Squillaci, W. Rekab, K. Börjesson, F. Liscio, L. Zhang, P. Samorì, *Chem. Commun.* **2015**, *51*, 5414.

[60] T. Zhuang, X. F. Wang, T. Sano, Z. Hong, Y. Yang, J. Kido, *Appl. Phys. Lett.* **2013**, *103*, 203301.

[61] G. Zhao, Y. He, Y. Li, *Adv. Mater.* **2010**, *22*, 4355.

[62] B. J. Briidas, J. Cornil, A. J. Heeger, *Adv. Mater.* **1996**, *8*, 447.

[63] K. M. Coakley, M. D. Mcgehee, *Chem. Mater.* **2004**, *16*, 4533.

[64] G. A. Chamberlain, *Sol. Cells* **1983**, *8*, 47.

[65] D. Wöhrle, D. Meissner, *Adv. Mater.* **1991**, *3*, 129.

[66] R. N. Marks, J. J. M. Halls, D. D. C. Bradley, R. H. Friend, A. B. Holmes, *J. Phys. Condens. Matter* **1994**, *6*, 1379.

[67] J. J. M. Halls, K. Pichler, R. H. Friend, S. C. Moratti, A. B. Holmes, *Appl. Phys. Lett.* **1996**, *68*, 3120.

[68] J. J. M. Halls, C. A. Walsh, N. C. Greenham, E. A. Marseglia, R. H. Friend, S. C. Moratti, A. B. Holmes, *Nature* **1995**, *376*, 498.

[69] G. Yu, A. J. Heeger, *J. Appl. Phys.* **1995**, *78*, 4510.

[70] N. C. Greenham, X. Peng, A. P. Alivisatos, *Phys. Rev. B* **1996**, *54*, 17628.

[71] A. J. Heeger, *Adv. Mater.* **2014**, *26*, 10.

[72] R. F. Service, *Science* **2011**, *332*, 293.

[73] J. Yu, T. L. Shen, W. H. Weng, Y. C. Huang, C. I. Huang, W. F. Su, S. P. Rwei, K. C. Ho, L. Wang, *Adv. Energy Mater.* **2012**, *2*, 245.

[74] J. Downing, M. P. Ryan, N. Stingelin, M. A. McLachlan, *J. Photonics Energy* **2011**, *1*, 11117.

[75] J. M. Downing, M. P. Ryan, M. A. McLachlan, *Thin Solid Films* **2013**, *539*, 18.

[76] J. Costa, D. Faria, M. A. Mclachlan, A. Campbell, Optimisation of Zinc Oxide as a Charge Injection Layer for Hybrid Organic-Inorganic Light Emitting Diodes, Imperial College London, **2013**.

[77] A. C. Arango, S. A. Carter, P. J. Brock, *Appl. Phys. Lett.* **1999**, *74*, 1698.

[78] A. Abrusci, I. K. Ding, M. Al Hashimi, T. Segal Peretz, M. D. McGehee, M. Heeney, G. L. Frey, H. J. Snaith, *Energy Environ. Sci.* **2011**, *4*, 3051.

[79] W. U. Huynh, J. J. Dittmer, A. P. Alivisatos, P. Alivisatos, *Science* **2002**, *295*, 2425.

[80] T. H. Lee, H. Choi, B. Walker, T. Kim, H.-B. Kim, J. Y. Kim, *RSC Adv.* **2014**, *4*, 4791.

[81] M. C. Scharber, D. Mühlbacher, M. Koppe, P. Denk, C. Waldauf, A. J. Heeger, C. J. Brabec, *Adv. Mater.* **2006**, *18*, 789.

[82] D. Gupta, S. Mukhopadhyay, K. S. Narayan, *Sol. Energy Mater. Sol. Cells* **2010**, *94*, 1309.

[83] L. G. Kaake, D. Moses, A. J. Heeger, *J. Phys. Chem. Lett.* **2013**, *4*, 2264.

[84] C. J. Brabec, G. Zerza, G. Cerullo, S. De Silvestri, S. Luzzati, J. C. Hummelen, S. Sariciftci, *Chem. Phys. Lett.* **2001**, *340*, 232.

[85] B. Kraabel, C. H. Lee, D. McBranch, D. Moses, N. S. Sariciftci, A. J. Heeger, *Chem. Phys. Lett.* **2013**, *589*, 63.

[86] S. R. Cowan, R. A. Street, S. Cho, A. J. Heeger, *Phys. Rev. B - Condens. Matter Mater. Phys.* **2011**, *83*, 35205.

[87] R. A. Street, S. Cowan, A. J. Heeger, *Phys. Rev. B* **2010**, *82*, 121301.

[88] S. Kazim, M. K. Nazeeruddin, M. Grätzel, S. Ahmad, *Angew. Chem. Int. Ed. Engl.* **2014**, *53*, 2812.

[89] P. P. Boix, K. Nonomura, N. Mathews, S. G. Mhaisalkar, *Mater. Today* **2014**, *17*, 16.

[90] A. Kojima, K. Teshima, Y. Shirai, T. Miyasaka, *J. Am. Chem. Soc.* **2009**, *131*, 6050.

[91] G. Xing, N. Mathews, S. Sun, S. S. Lim, Y. M. Lam, M. Grätzel, S. Mhaisalkar, T. C. Sum, *Science* **2013**, *342*, 344.

[92] M. M. Lee, J. Teuscher, T. Miyasaka, T. N. Murakami, H. J. Snaith, *Science* **2012**, *338*, 643.

[93] L. Etgar, P. Gao, Z. Xue, *J. Am. Chem. Soc.* **2012**, *134*, 17396.

[94] S. De Wolf, J. Holovsky, S. J. Moon, P. Löper, B. Niesen, M. Ledinsky, F. J. Haug, J. H. Yum, C. Ballif, *J. Phys. Chem. Lett.* **2014**, *5*, 1035.

[95] F. De Angelis, *Chem. Mater.* **2014**, *25*, 4613−4618.

[96] F. Brivio, A. B. Walker, A. Walsh, *APL Mater.* **2013**, *1*, 42111.

[97] H. S. Kim, C. R. Lee, J. H. Im, K. B. Lee, T. Moehl, A. Marchioro, S. J. Moon, R. Humphry-Baker, J. H. Yum, J. E. Moser, M. Grätzel, N. G. Park, *Sci. Rep.* **2012**, *2*, 591.

[98] A. Miyata, A. Mitioglu, P. Plochocka, O. Portugall, J. T. W. Wang, S. D. Stranks, H. J. Snaith, R. J. Nicholas, *Nat. Phys.* **2015**, *11*, 582.

[99] C. C. Stoumpos, M. G. Kanatzidis, *Adv. Mater.* **2016**, *28*, 5778.

[100] C. S. Ponseca, T. J. Savenije, M. Abdellah, K. Zheng, A. Yartsev, T. Pascher, T. Harlang, P. Chabera, T. Pullerits, A. Stepanov, J. P. Wolf, V. Sundstrom, *J. Am. Chem. Soc.* **2014**, *136*, 5189.

[101] Q. Dong, Y. Fang, Y. Shao, P. Mulligan, J. Qiu, L. Cao, J. Huang, *Science* **2015**, *347*, 967.

[102] S. D. Stranks, G. E. Eperon, G. Grancini, C. Menelaou, M. J. P. Alcocer, T. Leijtens, L. M. Herz, A. Petrozza, H. J. Snaith, *Science* **2013**, *342*, 341.

[103] E. Edri, S. Kirmayer, A. Henning, S. Mukhopadhyay, K. Gartsman, Y. Rosenwaks, G. Hodes, D. Cahen, *Nano Lett.* **2014**, *14*, 1000.

[104] D. Shi, V. Adinolfi, R. Comin, M. Yuan, E. Alarousu, A. Buin, Y. Chen, S. Hoogland, A. Rothenberger, K. Katsiev, Y. Losovyj, X. Zhang, P. A. Dowben, O. F. Mohammed, E. H. Sargent, O. M. Bakr, *Science* **2015**, *347*, 519.

[105] A. Walsh, D. O. Scanlon, S. Chen, X. G. Gong, S. H. Wei, *Angew. Chemie - Int. Ed.* **2015**, *54*, 1791.

[106] J. M. Frost, A. Walsh, *Acc. Chem. Res.* **2016**, *49*, 528.

[107] J. Burschka, N. Pellet, S. J. Moon, R. Humphry-Baker, P. Gao, M. K. Nazeeruddin, M. Grätzel, *Nature* **2013**, *499*, 316.

[108] N. J. Jeon, J. H. Noh, Y. C. Kim, W. S. Yang, S. Ryu, S. Il Seok, *Nat. Mater.* **2014**, *13*, 1.

[109] M. Liu, M. B. Johnston, H. J. Snaith, *Nature* **2013**, *501*, 395.

[110] Q. Chen, H. Zhou, Y. Fang, A. Z. Stieg, T. Bin Song, H. H. Wang, X. Xu, Y. Liu, S. Lu, J. You, P. Sun, J. McKay, M. S. Goorsky, Y. Yang, *Nat. Commun.* **2015**, *6*, 1.

[111] M. I. Dar, N. Arora, P. Gao, S. Ahmad, M. Grätzel, M. K. Nazeeruddin, *Nano Lett.* **2014**, *14*, 6991.

[112] J. H. Noh, S. H. Im, J. H. Heo, T. N. Mandal, S. Il Seok, *Nano Lett.* **2013**, *13*, 1764.

[113] L. Protesescu, S. Yakunin, M. I. Bodnarchuk, F. Krieg, R. Caputo, C. H. Hendon, R. X. Yang, A. Walsh, M. V. Kovalenko, *Nano Lett.* **2015**, *15*, 3692.

[114] G. E. Eperon, S. D. Stranks, C. Menelaou, M. B. Johnston, L. M. Herz, H. J. Snaith, *Energy Environ. Sci.* **2014**, *7*, 982.

[115] C. C. Stoumpos, C. D. Malliakas, M. G. Kanatzidis, *Inorg. Chem.* **2013**, *52*, 9019.

[116] F. Hao, C. C. Stoumpos, D. H. Cao, R. P. H. Chang, M. G. Kanatzidis, *Nat. Photonics* **2014**, *8*, 489.

[117] F. Hao, C. C. Stoumpos, R. P. H. Chang, M. G. Kanatzidis, *J. Am. Chem. Soc.* **2014**, *136*, 8094.

[118] W. S. Yang, J. H. Noh, N. J. Jeon, Y. C. Kim, S. Ryu, J. Seo, S. Il Seok, *Science* **2015**, *348*, 1234.

[119] N. J. Jeon, J. H. Noh, W. S. Yang, Y. C. Kim, S. Ryu, J. Seo, S. Il Seok, *Nature* **2015**, *517*, 476.

[120] J. M. Ball, M. M. Lee, A. Hey, H. J. Snaith, *Energy Environ. Sci.* **2013**, *6*, 1739.

[121] T. Leijtens, B. Lauber, *J. Phys. Chem. Lett.* **2014**, *5*, 1096.

[122] A. Abrusci, S. D. Stranks, P. Docampo, H. L. Yip, A. K. Y. Jen, H. J. Snaith, *Nano Lett.* **2013**, *13*, 3124.

[123] S. Dharani, H. K. Mulmudi, N. Yantara, P. T. Thu Trang, N. G. Park, M. Graetzel, S. Mhaisalkar, N. Mathews, P. P. Boix, *Nanoscale* **2014**, *6*, 1675.

[124] J. Qiu, Y. Qiu, K. Yan, M. Zhong, C. Mu, H. Yan, S. Yang, *Nanoscale* **2013**, *5*, 3245.

[125] H. S. Kim, J. W. Lee, N. Yantara, P. P. Boix, S. a Kulkarni, S. Mhaisalkar, M. Grätzel, N. G. Park, *Nano Lett.* **2013**, *13*, 2412.

[126] T. Leijtens, S. Stranks, G. Eperon, R. Lindblad, E. M. J. Johansson, I. McPherson, H. Rensmo, J. M. Ball, M. M. Lee, H. J. Snaith, *ACS Nano* **2014**.

[127] V. D'Innocenzo, G. Grancini, M. J. P. Alcocer, A. R. S. Kandada, S. D. Stranks, M. M. Lee, G. Lanzani, H. J. Snaith, A. Petrozza, *Nat. Commun.* **2014**, *5*, 3586.

[128] W. Nie, H. Tsai, R. Asadpour, J. C. Blancon, A. J. Neukirch, G. Gupta, J. J. Crochet, M. Chhowalla, S. Tretiak, M. A. Alam, H. L. Wang, A. D. Mohite, *Science* **2015**, *347*, 522.

[129] C. Chiang, C. Wu, *Nat. Photonics* **2016**, *10*, 196.

[130] H. Zhou, Q. Chen, G. Li, S. Luo, T. B. Song, H. S. Duan, Z. Hong, J. You, Y. Liu, Y. Yang, *Science* **2014**, *345*, 542.

[131] D. Liu, T. L. Kelly, *Nat. Photonics* **2013**, *8*, 133.

[132] J. P. C. Baena, L. Steier, W. Tress, M. Saliba, S. Neutzner, T. Matsui, F. Giordano, T. J. Jacobsson, A. R. S. Kandada, S. M. Zakeeruddin, A. Petrozza, A. Abate, M. K. Nazeeruddin, M. Grätzel, A. Hagfeldt, *Energy Environ. Sci.* **2015**, *8*, 2928.

[133] E. L. Unger, E. T. Hoke, C. D. Bailie, W. H. Nguyen, A. R. Bowring, T. Heumüller, M. G. Christoforo, M. D. McGehee, *Energy Environ. Sci.* **2014**, *7*, 3690.

[134] Y. Shao, Z. Xiao, C. Bi, Y. Yuan, J. Huang, *Nat. Commun.* **2014**, *5*, 1.

[135] J. You, L. Meng, T. Bin Song, T. F. Guo, Y. (Michael) Yang, W. H. Chang, Z. Hong, H. Chen, H. Zhou, Q. Chen, Y. Liu, N. De Marco, Y. Yang, *Nat. Nanotechnol.* **2015**, 1.

[136] E. Edri, S. Kirmayer, S. Mukhopadhyay, K. Gartsman, G. Hodes, D. Cahen, *Nat. Commun.* **2014**, *5*, 3461.

[137] C. S. Ponseca, T. J. Savenije, M. Abdellah, K. Zheng, A. Yartsev, T. Pascher, T. Harlang, P. Chabera, T. Pullerits, A. Stepanov, J. P. Wolf, V. Sundstrom, *J. Am. Chem. Soc.* **2014**, *136*, 5189.

[138] F. Deschler, M. Price, S. Pathak, L. E. Klintberg, D.-D. Jarausch, R. Higler, S. Hüttner, T. Leijtens, S. D. Stranks, H. J. Snaith, M. Atatüre, R. T. Phillips, R. H. Friend, *J. Phys. Chem. Lett.* **2014**, *5*, 1421.

[139] J. S. Manser, J. A. Christians, P. V. Kamat, *Chem. Rev.* **2016**, *116*, 12956.

[140] A. Paulke, S. D. Stranks, J. Kniepert, J. Kurpiers, C. M. Wolff, N. Schön, H. J. Snaith, T. J. K. Brenner, D. Neher, *Appl. Phys. Lett.* **2016**, *108*, 113505.

[141] Y. Yamada, T. Nakamura, M. Endo, A. Wakamiya, Y. Kanemitsu, *J. Am. Chem. Soc.* **2014**, *136*, 11610.

[142] S. D. Stranks, H. J. Snaith, *Nat. Nanotechnol.* **2015**, *10*, 391.

[143] T. C. Sum, S. Chen, G. Xing, X. Liu, B. Wu, *Nanotechnology* **2015**, *26*, 342001.

[144] C. Wehrenfennig, G. E. Eperon, M. B. Johnston, H. J. Snaith, L. M. Herz, *Adv. Mater.* **2014**, *26*, 1584.

[145] J. M. Frost, K. T. Butler, F. Brivio, C. H. Hendon, M. Van Schilfgaarde, A. Walsh, *Nano Lett.* **2014**, *14*, 2584.

[146] M. Kepenekian, R. Robles, C. Katan, D. Sapori, L. Pedesseau, J. Even, *ACS Nano* **2015**, *9*, 11557.

[147] H. J. Snaith, A. Abate, J. M. Ball, G. E. Eperon, T. Leijtens, N. K. Noel, S. D. Stranks, J. T. W. Wang, K. Wojciechowski, W. Zhang, *J. Phys. Chem. Lett.* **2014**, *5*, 1511.

[148] W. Tress, N. Marinova, T. Moehl, S. M. Zakeeruddin, N. Mohammad K., M. Grätzel, *Energy Environ. Sci.* **2015**, *8*, 995.

[149] D. Bryant, S. Wheeler, B. C. O'Regan, T. Watson, P. R. F. Barnes, D. a. Worsley, J. Durrant, *J. Phys. Chem. Lett.* **2015**, 150721102758007.

[150] C. Tao, S. Neutzner, L. Colella, S. Marras, A. Ram, S. Kandada, M. Gandini, M. De Bastiani, G. Pace, L. Manna, M. Caironi, C. Bertarelli, A. Petrozza, *Energy Environ. Sci.* **2015**, *8*, 2365.

[151] C. Chueh, C. Li, A. K. Jen, *Energy Environ. Sci.* **2015**, *8*, 1160.

[152] S. Van Reenen, S. Kouijzer, R. A. J. Janssen, M. M. Wienk, M. Kemerink, *Adv. Mater. Interfaces* **2014**, *1*, 1.

[153] M. T. Greiner, M. G. Helander, W. M. Tang, Z. Bin Wang, J. Qiu, Z. H. Lu, *Nat. Mater.* **2012**, *11*, 76.

[154] M. T. Greiner, Z. H. Lu, *NPG Asia Mater.* **2013**, *5*, e55.

[155] C. Tengstedt, W. Osikowicz, W. R. Salaneck, I. D. Parker, C. H. Hsu, M. Fahlman, *Appl. Phys. Lett.* **2006**, *88*, 1.

[156] E. M. Miller, Y. Zhao, C. C. Mercado, S. K. Saha, J. M. Luther, K. Zhu, V. Stevanović, C. L. Perkins, J. van de Lagemaat, *Phys. Chem. Chem. Phys.* **2014**, *16*, 22122.

[157] D. Song, D. Wei, P. Cui, M. Li, Z. Duan, T. Wang, J. Ji, Y. Li, J. M. Mbengue, Y. Li, Y. He, M. Trevor, N. G. Park, *J. Mater. Chem. A* **2016**, *4*, 6091.

[158] J. Huang, G. Li, Y. Yang, *Adv. Mater.* **2008**, *20*, 415.

[159] V. C. Tung, J. Kim, L. J. Cote, J. Huang, *J. Am. Chem. Soc.* **2011**, *133*, 9262.

[160] X. Dong, X. Fang, M. Lv, B. Lin, S. Zhang, J. Ding, N. Yuan, *J. Mater. Chem. A* **2015**, *3*, 5360.

[161] J. Costa Dantas Faria, A. J. Campbell, M. A. McLachlan, *J. Mater. Chem. C* **2015**, *3*, 4945.

[162] J. Yang, J. You, C. C. Chen, W. C. Hsu, H. R. Tan, X. W. Zhang, Z. Hong, Y. Yang, *ACS Nano* **2011**, *5*, 6210.

[163] X. Huang, S. Han, W. Huang, X. Liu, *Chem. Soc. Rev.* **2013**, *42*, 173.

[164] U. Bach, D. Lupo, P. Comte, J. E. Moser, F. Weissörtel, J. Salbeck, H. Spreitzer, M. Grätzel, *Nature* **1998**, *395*, 583.

[165] H. J. Snaith, R. Humphry-Baker, P. Chen, I. Cesar, S. M. Zakeeruddin, M. Grätzel, *Nanotechnology* **2008**, *19*, 424003.

[166] T. Leijtens, I. K. Ding, T. Giovenzana, J. T. Bloking, M. D. McGehee, A. Sellinger, *ACS Nano* **2012**, *6*, 1455.

[167] C. H. Teh, R. Daik, E. L. Lim, C. C. Yap, M. A. Ibrahim, N. A. Ludin, K. Sopian, M. A. Mat Teridi, *J. Mater. Chem. A* **2016**, *4*, 15788.

[168] J. H. Noh, N. J. Jeon, Y. C. Choi, M. K. Nazeeruddin, M. Gratzel, S. Il Seok, *J. Mater. Chem. A* **2013**, *1*, 11842.

[169] A. Abate, T. Leijtens, S. Pathak, J. Teuscher, R. Avolio, M. E. Errico, J. Kirkpatrik, J. M. Ball, P. Docampo, I. McPherson, H. J. Snaith, *Phys. Chem. Chem. Phys.* **2013**, *15*, 2572.

[170] S. N. Habisreutinger, T. Leijtens, G. E. Eperon, S. D. Stranks, R. J. Nicholas, H. J. Snaith, *Nano Lett.* **2014**, *14*, 5561.

[171] K. Sun, S. Zhang, P. Li, Y. Xia, X. Zhang, D. Du, F. H. Isikgor, J. Ouyang, *J. Mater. Sci. Mater. Electron.* **2015**, *26*, 4438.

[172] Q. Wei, M. Mukaida, Y. Naitoh, T. Ishida, *Adv. Mater.* **2013**, *25*, 2831.

[173] Y. Hyun Kim, C. Sachse, M. Hermenau, K. Fehse, M. Riede, L. Müller-Meskamp, K. Leo, *Appl. Phys. Lett.* **2011**, *99*, 113305.

[174] Y. Sun, C. J. Takacs, S. R. Cowan, J. H. Seo, X. Gong, A. Roy, A. J. Heeger, *Adv. Mater.* **2011**, *23*, 2226.

[175] M. Kröger, S. Hamwi, J. Meyer, T. Riedl, W. Kowalsky, A. Kahn, *Org. Electron.* **2009**, *10*, 932.

[176] M. Kröger, S. Hamwi, J. Meyer, T. Riedl, W. Kowalsky, A. Kahn, *Appl. Phys. Lett.* **2009**, *95*, 2007.

[177] Y. C. Tseng, A. U. Mane, J. W. Elam, S. B. Darling, *Sol. Energy Mater. Sol. Cells* **2012**, *99*, 235.

[178] S. Murase, Y. Yang, *Adv. Mater.* **2012**, *24*, 2459.

[179] Y. J. Lee, J. Yi, G. F. Gao, H. Koerner, K. Park, J. Wang, K. Luo, R. A. Vaia, J. W. P. Hsu, *Adv. Energy Mater.* **2012**, *2*, 1193.

[180] J. Meyer, A. Shu, M. Kröger, A. Kahn, *Appl. Phys. Lett.* **2010**, *96*, 133308.

[181] S. S. Li, K. H. Tu, C. C. Lin, C. W. Chen, M. Chhowalla, *ACS Nano* **2010**, *4*, 3169.

[182] D. Yang, L. Zhou, L. Chen, B. Zhao, J. Zhang, C. Li, *Chem. Commun.* **2012**, *48*, 8078.

[183] D. R. Dreyer, S. Park, C. W. Bielawski, R. S. Ruoff, *Chem. Soc. Rev.* **2010**, *39*, 228.

[184] S. Mao, H. Pu, J. Chen, *RSC Adv.* **2012**, *2*, 2643.

[185] G. Q. Fan, Q. Q. Zhuo, J. Zhu, Z. Q. Xu, P. P. Cheng, Y. Q. Li, X. H. Sun, S. T. Lee, J. X. Tang, *J. Mater. Chem.* **2012**, *22*, 15614.

[186] J. Kim, V. C. Tung, J. Huang, *Adv. Energy Mater.* **2011**, *1*, 1052.

[187] J. Liu, G. H. Kim, Y. Xue, J. Y. Kim, J. B. Baek, M. Durstock, L. Dai, *Adv. Mater.* **2014**, *26*, 786.

[188] N. Yaacobi-Gross, N. D. Treat, P. Pattanasattayavong, H. Faber, A. K. Perumal, N. Stingelin, D. D. C. Bradley, P. N. Stavrinou, M. Heeney, T. D. Anthopoulos, *Adv. Energy Mater.* **2015**, *5*, 1.

[189] A. Perumal, H. Faber, N. Yaacobi-Gross, P. Pattanasattayavong, C. Burgess, S. Jha, M. A. McLachlan, P. N. Stavrinou, T. D. Anthopoulos, D. D. C. Bradley, *Adv. Mater.* **2015**, *27*, 93.

[190] P. Qin, S. Tanaka, S. Ito, N. Tetreault, K. Manabe, H. Nishino, M. K. Nazeeruddin, M. G. A. Tzel, M. Grätzel, *Nat Commun* **2014**, *5*, 1.

[191] Jiewei Liu, S. Pathak, T. Leijtens, T. Stergiopoulos, K. Wojciechowski, S. Schumann, N. Kausch-Busies, H. J. Snaith, *2015 IEEE 42nd Photovolt. Spec. Conf.* **2015**, 1.

[192] J. Kim, G. Kim, T. K. Kim, S. Kwon, H. Back, J. Lee, S. H. Lee, H. Kang, K. Lee, *J. Mater. Chem. A* **2014**, *2*, 17291.

[193] C. Duan, W. Cai, B. B. Y. Hsu, C. Zhong, K. Zhang, C. Liu, Z. Hu, F. Huang, G. C. Bazan, A. J. Heeger, Y. Cao, *Energy Environ. Sci.* **2013**, *6*, 3022.

[194] Z. A. Page, Y. Liu, V. V. Duzhko, T. P. Russell, T. Emrick, *Science* **2014**, *346*, 441.

[195] X. Zhao, C. Xu, H. Wang, F. Chen, W. Zhang, Z. Zhao, L. Chen, S. Yang, *ACS Appl. Mater. Interfaces* **2014**, *6*, 4329.

[196] K. Sun, B. Zhao, V. Murugesan, A. Kumar, K. Zeng, J. Subbiah, W. W. H. Wong, D. J. Jones, J. Ouyang, *J. Mater. Chem.* **2012**, *22*, 24155.

[197] F. Liu, Z. A. Page, V. V. Duzhko, T. P. Russell, T. Emrick, *Adv. Mater.* **2013**, *25*, 6868.

[198] T. Yang, M. Wang, C. Duan, X. Hu, L. Huang, J. Peng, F. Huang, X. Gong, *Energy Environ. Sci.* **2012**, *5*, 8208.

[199] E. Puodziukynaite, H. W. Wang, J. Lawrence, A. J. Wise, T. P. Russell, M. D. Barnes, T. Emrick, *J. Am. Chem. Soc.* **2014**, *136*, 11043.

[200] Y. Zhou, C. Fuentes-hernandez, J. Shim, J. Meyer, A. J. Giordano, H. Li, P. Winget, T. Papadopoulos, H. Cheun, J. Kim, M. Fenoll, A. Dindar, W. Haske, E. Najafabadi, T. M. Khan, H. Sojoudi, S. Barlow, S. Graham, J. Brédas, S. R. Marder, A. Kahn, B. Kippelen, *Science* **2012**, *873*, 327.

[201] S. Woo, W. Hyun Kim, H. Kim, Y. Yi, H. K. Lyu, Y. Kim, *Adv. Energy Mater.* **2014**, *4*, 1301692.

[202] Y. Cheng, Q. D. Yang, J. Xiao, Q. Xue, H. W. Li, Z. Guan, H. L. Yip, S. W. Tsang, *ACS Appl. Mater. Interfaces* **2015**, *7*, 19986.

[203] J. Sun, Y. Zhu, X. Xu, L. Lan, L. Zhang, P. Cai, J. Chen, J. Peng, Y. Cao, *J. Phys. Chem. C* **2012**, *116*, 14188.

[204] Z. He, C. Zhong, S. Su, M. Xu, H. Wu, Y. Cao, *Nat. Photonics* **2012**, *6*, 593.

[205] K. Zhang, C. Zhong, S. Liu, C. Mu, Z. Li, H. Yan, F. Huang, Y. Cao, *ACS Appl. Mater. Interfaces* **2014**, *6*, 1.

[206] J. Liu, Y. Xue, Y. Gao, D. Yu, M. Durstock, L. Dai, *Adv. Mater.* **2012**, *24*, 2228.

[207] H. H. Liao, L. M. Chen, Z. Xu, G. Li, Y. Yang, *Appl. Phys. Lett.* **2008**, *92*, 173303.

[208] H. Dong, X. Guo, W. Li, L. Wang, *RSC Adv.* **2014**, *4*, 60131.

[209] I. Litzov, C. Brabec, *Materials (Basel).* **2013**, *6*, 5796.

[210] A. C. Arango, S. A. Carter, P. J. Brock, *Appl. Phys. Lett.* **1999**, *74*, 1698.

[211] A. Hadipour, R. Müller, P. Heremans, *Org. Electron.* **2013**, *14*, 2379.

[212] J. T. W. Wang, J. M. Ball, E. M. Barea, A. Abate, J. A. Alexander-Webber, J. Huang, M. Saliba, I. Mora-Sero, J. Bisquert, H. J. Snaith, R. J. Nicholas, *Nano Lett.* **2014**, *14*, 724.

[213] A. Yella, L. P. Heiniger, P. Gao, M. K. Nazeeruddin, M. Grätzel, *Nano Lett.* **2014**, *14*, 2591.

[214] S. Lattante, *Electronics* **2014**, *3*, 132.

[215] P. Tiwana, P. Docampo, M. B. Johnston, H. J. Snaith, L. M. Herz, *ACS Nano* **2011**, *5*, 5158.

[216] D. S. Ginley, J. D. Perkins, *Handbook of Transparent Conductors*, **2011**.

[217] T. Leijtens, G. E. Eperon, N. K. Noel, S. N. Habisreutinger, A. Petrozza, H. J. Snaith, *Adv. Energy Mater.* **2015**, *5*, 1500963.

[218] J. Song, E. Zheng, J. Bian, X. F. Wang, W. Tian, Y. Sanehira, T. Miyasaka, *J. Mater. Chem. A* **2015**, *3*, 10837.

[219] W. Ke, G. Fang, Q. Liu, L. Xiong, P. Qin, H. Tao, J. Wang, H. Lei, B. Li, J. Wan, G. Yang, Y. Yan, *J. Am. Chem. Soc.* **2015**, *137*, 6730.

[220] J. P. C. Baena, L. Steier, W. Tress, M. Saliba, S. Neutzner, T. Matsui, F. Giordano, T. J. Jacobsson, A. R. S. Kandada, S. M. Zakeeruddin, A. Petrozza, A. Abate, M. K. Nazeeruddin, M. Grätzel, A. Hagfeldt, *Energy Environ. Sci.* **2015**, *8*, 2928.

[221] G. Yang, H. Tao, P. Qin, W. Ke, G. Fang, *J. Mater. Chem. A* **2016**, *4*, 3970.

[222] J. Yang, B. D. Siempelkamp, E. Mosconi, F. De Angelis, T. L. Kelly, *Chem. Mater.* **2015**, 4229.

[223] D. C. Look, D. C. Reynolds, J. R. Sizelove, R. L. Jones, C. W. Litton, G. Cantwell, W. C. Harsch, *Solid State Commun.* **1998**, *105*, 399.

[224] P. Ravirajan, A. M. Peiró, M. K. Nazeeruddin, M. Grätzel, D. D. C. Bradley, J. R. Durrant, J. Nelson, *J. Phys. Chem. B* **2006**, *110*, 7635.

[225] Y. Sun, J. H. Seo, C. J. Takacs, J. Seifter, A. J. Heeger, *Adv. Mater.* **2011**, *23*, 1679.

[226] J. You, C. C. Chen, L. Dou, S. Murase, H. S. Duan, S. A. Hawks, T. Xu, H. J. Son, L. Yu, G. Li, Y. Yang, *Adv. Mater.* **2012**, *24*, 5267.

[227] C. Manspeaker, P. Scruggs, J. Preiss, D. A. Lyashenko, A. A. Zakhidov, *J. Phys. Chem. C* **2016**, *120*, 6377.

[228] X. Ouyang, R. Peng, L. Ai, X. Zhang, Z. Ge, *Nat. Photonics* **2015**, *9*, 520.

[229] U. Özgür, Y. I. Alivov, C. Liu, A. Teke, M. a. Reshchikov, S. Doğan, V. Avrutin, S. J. Cho, H. Morkoç, *J. Appl. Phys.* **2005**, *98*, 41301.

[230] J. M. Downing, Control and Characterisation of Metal Oxide / Polymer Morphologies for Hybrid Photovoltaic Devices, Imperial College London, **2013**.

[231] O. Dulub, U. Diebold, G. Kresse, *Phys. Rev. Lett.* **2003**, *90*, 16102.

[232] A. Wander, N. M. Harrison, *Surf. Sci.* **2000**, *468*, L851.

[233] M. Law, L. E. Greene, J. C. Johnson, R. Saykally, P. Yang, *Nat. Mater.* **2005**, *4*, 455.

[234] J. H. Yang, J. H. Zheng, H. J. Zhai, L. L. Yang, Y. J. Zhang, J. H. Lang, M. Gao, *J. Alloys Compd.* **2009**, *475*, 741.

[235] C. Y. Jiang, X. W. Sun, G. Q. Lo, D. L. Kwong, J. X. Wang, *Appl. Phys. Lett.* **2007**, *90*, 263501.

[236] J. Tian, Q. Zhang, E. Uchaker, R. Gao, X. Qu, S. Zhang, G. Cao, *Energy Environ. Sci.* **2013**, *6*, 3542.

[237] M. Zi, M. Zhu, L. Chen, H. Wei, X. Yang, B. Cao, *Ceram. Int.* **2014**, *40*, 7965.

[238] C. Li, Z. S. Yu, S. M. Fang, H. X. Wang, Y. H. Gui, J. Q. Xu, R. F. Chen, *Chinese Chem. Lett.* **2008**, *19*, 599.

[239] X. Y. Kong, Y. Ding, R. Yang, Z. L. Wang, *Science* **2004**, *303*, 1348.

[240] P. X. Gao, Z. L. Wang, *Appl. Phys. Lett.* **2004**, *84*, 2883.

[241] A. O. and M. Takesada, *Advances in Ferroelectrics*, InTech, **2012**.

[242] V. Srikant, D. R. Clarke, *J. Appl. Phys.* **1998**, *83*, 5447.

[243] A. Ohtomo, K. Tamura, M. Kawasaki, T. Makino, Y. Segawa, Z. K. Tang, G. K. L. Wong, Y. Matsumoto, H. Koinuma, *Appl. Phys. Lett.* **2000**, *77*, 2204.

[244] F. Koffyberg, *Phys. Rev. B* **1976**, *13*, 4470.

[245] O. Hamad, G. Braunstein, H. Patil, N. Dhere, *Thin Solid Films* **2005**, *489*, 303.

[246] C. G. Van de Walle, *Phys. Rev. Lett.* **2000**, *85*, 1012.

[247] D. Look, G. Farlow, P. Reunchan, S. Limpijumnong, S. Zhang, K. Nordlund, *Phys. Rev. Lett.* **2005**, *95*, 225502.

[248] B. Sernelius, K. F. Berggren, Z. C. Jin, I. Hamberg, C. Granqvist, *Phys. Rev. B* **1988**, *37*, 10244.

[249] C. Y. Tsay, C. W. Wu, C. M. Lei, F. S. Chen, C. K. Lin, *Thin Solid Films* **2010**, *519*, 1516.

[250] S. Ilican, Y. Caglar, M. Caglar, F. Yakuphanoglu, *Appl. Surf. Sci.* **2008**, *255*, 2353.

[251] E. Chikoidze, M. Nolan, M. Modreanu, V. Sallet, P. Galtier, *Thin Solid Films* **2008**, *516*, 8146.

[252] Chen Zhao-Quan, Liu Ming-Hai, Liu Yu-Ping, Chen Wei, Luo Zhi-Qing, Hu Xi-Wei, *ACTA Phys. Sin.* **2009**, *58*, 4260.

[253] J. Karamdel, C. F. Dee, B. Y. Majlis, *Appl. Surf. Sci.* **2010**, *256*, 6164.

[254] Y. Y. Kim, W. S. Han, H. K. Cho, *Appl. Surf. Sci.* **2010**, *256*, 4438.

[255] S. H. Jeong, B. N. Park, S. B. Lee, J. H. Boo, *Thin Solid Films* **2008**, *516*, 5586.

[256] S. S. Lin, J. G. Lu, Z. Z. Ye, H. P. He, X. Q. Gu, L. X. Chen, J. Y. Huang, B. H. Zhao, *Solid State Commun.* **2008**, *148*, 25.

[257] V. Avrutin, D. J. Silversmith, H. Morkoç, *Proc. IEEE* **2010**, *98*, 1269.

[258] R. L. Z. Hoye, D. Muñoz-Rojas, D. C. Iza, K. P. Musselman, J. L. MacManus-Driscoll, *Sol. Energy Mater. Sol. Cells* **2013**, *116*, 197.

[259] S. Faÿ, U. Kroll, C. Bucher, E. Vallat-Sauvain, A. Shah, *Sol. Energy Mater. Sol. Cells* **2005**, *86*, 385.

[260] J. B. Franklin, J. M. Downing, F. Giuliani, M. P. Ryan, M. A. McLachlan, *Adv. Energy Mater.* **2012**, *2*, 528.

[261] E. Hosono, S. Fujihara, T. Kimura, H. Imai, *J. Sol-Gel Sci. Technol.* **2004**, *29*, 71.

[262] Z. E. Allouni, M. R. Cimpan, P. J. Høl, T. Skodvin, N. R. Gjerdet, *Colloids Surfaces B Biointerfaces* **2009**, *68*, 83.

[263] M. R. Arefi, S. Rezaei-Zarchi, *Int. J. Mol. Sci.* **2012**, *13*, 4340.

[264] C. C. Lin, S. Y. Chen, S. Y. Cheng, *J. Cryst. Growth* **2005**, *283*, 141.

[265] D. V. Bavykin, J. M. Friedrich, F. C. Walsh, *Adv. Mater.* **2006**, *18*, 2807.

[266] L. Yuan, K. Huang, C. Hou, W. Feng, S. Wang, C. Zhou, S. Feng, *New J. Chem.* **2014**, *38*, 1168.

[267] J. H. Tian, J. Hu, S. S. Li, F. Zhang, J. Liu, J. Shi, X. Li, Z. Q. Tian, Y. Chen, *Nanotechnology* **2011**, *22*, 245601.

[268] T. Mahalingam, V. S. John, M. Raja, Y. K. Su, P. J. Sebastian, *Sol. Energy Mater. Sol. Cells* **2005**, *88*, 227.

[269] N. R. Armstrong, C. Carter, C. Donley, A. Simmonds, P. Lee, M. Brumbach, B. Kippelen, B. Domercq, S. Yoo, *Thin Solid Films* **2003**, *445*, 342.

[270] M. H. Kumar, N. Yantara, S. Dharani, M. Graetzel, S. Mhaisalkar, P. P. Boix, N. Mathews, *Chem. Commun.* **2013**, *49*, 11089.

[271] B. Cheng, W. Shi, J. M. Russell-Tanner, L. Zhang, E. T. Samulski, N. Carolina, C. Hill, N. Carolina, *Inorg. Chem.* **2006**, *45*, 1208.

[272] G. Clavel, M. G. Willinger, D. Zitoun, N. Pinna, *Adv. Funct. Mater.* **2007**, *17*, 3159.

[273] M. Niederberger, *Acc. Chem. Res.* **2007**, *40*, 793.

[274] M. Niederberger, N. Pinna, *Metal Oxide Nanoparticles in Organic Solvents*, Springer London, London, **2009**.

[275] J. Livage, *Curr. Opin. Solid State Mater. Sci.* **1997**, *2*, 132.

[276] M. Guglielmi, G. Carturan, *J. Non. Cryst. Solids* **1988**, *100*, 16.

[277] L. Znaidi, *Mater. Sci. Eng. B* **2010**, *174*, 18.

[278] M. Hu, E. A. Payzant, C. Byers, *J. Colloid Interface Sci.* **2000**, *222*, 20.

[279] D. W. Bahnemann, C. Kormann, M. R. Hoffmann, *J. Phys. Chem.* **1987**, *91*, 3789.

[280] L. Znaidi, G. J. A. A. Soler Illia, R. Le Guennic, C. Sanchez, A. Kanaev, *J. Sol-Gel Sci. Technol.* **2003**, *26*, 817.

[281] L. Spanhel, *J. Sol-Gel Sci. Technol.* **2006**, *39*, 7.

[282] V. Briois, C. Giorgetti, F. Baudelet, S. Blanchandin, M. S. Tokumoto, S. H. Pulcinelli, C. V. Santilli, *J. Phys. Chem. C* **2007**, *111*, 3253.

[283] P. Sagar, P. K. Shishodia, R. M. Mehra, *Appl. Surf. Sci.* **2007**, *253*, 5419.

[284] L. Znaidi, G. J. A. A. S. Illia, S. Benyahia, C. Sanchez, A. V Kanaev, *Thin Solid Films* **2003**, *428*, 257.

[285] D. Raoufi, T. Raoufi, *Appl. Surf. Sci.* **2009**, *255*, 5812.

[286] Y. S. Kim, W. P. Tai, S. J. Shu, *Thin Solid Films* **2005**, *491*, 153.

[287] M. Ohyama, H. Kozuka, T. Yoko, S. Sakka, *J. Ceram. Soc. Japan* **1996**, *104*, 296.

[288] M. Ohyama, H. Kouzuka, T. Yoko, *Thin Solid Films* **1997**, *306*, 78.

[289] T. Nagase, T. Ooie, J. Sakakibara, *Thin Solid Films* **1999**, *357*, 151.

[290] B. Pal, M. Sharon, *Mater. Chem. Phys.* **2002**, *76*, 82.

[291] R. Ghosh, D. Basak, S. Fujihara, *J. Appl. Phys.* **2004**, *96*, 2689.

[292] T. Okamura, Y. Seki, S. Nagakari, H. Okushi, *Jpn. J. Appl. Phys.* **1992**, *31*, L762.

[293] S. Chakrabarti, D. Ganguli, S. Chaudhuri, *Mater. Lett.* **2004**, *58*, 3952.

[294] T. Y. Masashi Ohyama, Hiromitsu Kozuka, *Thin Solid Films* **1997**, *306*, 78.

[295] S. Fujihara, C. Sasaki, T. Kimura, *Appl. Surf. Sci.* **2001**, *180*, 341.

[296] S. Meyers, J. Anderson, *J. Am. Chem. Soc.* **2008**, 17603.

[297] S. Y. Park, B. J. Kim, K. Kim, M. S. Kang, K. H. Lim, T. Il Lee, J. M. Myoung, H. K. Baik, J. H. Cho, Y. S. Kim, *Adv. Mater.* **2012**, *24*, 834.

[298] Y. H. Lin, H. Faber, K. Zhao, Q. Wang, A. Amassian, M. A. McLachlan, T. D. Anthopoulos, *Adv. Mater.* **2013**, *25*, 4340.

[299] S. Y. Cho, Y. H. Kang, J. Y. Jung, S. Y. Nam, J. Lim, S. C. Yoon, D. H. Choi, C. Lee, *Chem. Mater.* **2012**, *24*, 3517.

[300] S. Bai, Z. Wu, X. Xu, Y. Jin, B. Sun, X. Guo, S. He, X. Wang, Z. Ye, H. Wei, X. Han, W. Ma, *Appl. Phys. Lett.* **2012**, *100*, 203906.

[301] J. Zhou, X. Meng, X. Zhang, X. Tao, Z. Zhang, J. Hu, C. Wang, Y. Li, S. Yang, *Mater. Chem. Front.* **2017**, *131*, 6050.

Chapter 2 - Characterisation Techniques

2.1 Structural characterisation

2.1.1 X-ray diffraction

X-ray diffraction (XRD) was utilised to investigate the crystallinity (crystallite size, orientation and texture) of ZnO planar films. It was also used to study the crystallisation of perovskite films and decomposition of perovskite films influenced by the ZnO layer.

Data were collected using a Panalytical X'Pert Pro diffractometer equipped with a monochromated Cu K_α source (K→L, wavelength 0.15406 nm). K_β (K→M, 0.13923 nm) radiation was removed using a nickel filter. The accelerating voltage and beam current were set at 40 kV and 40 mA, respectively. Diffraction was carried out in the °2θ configuration.

A typical XRD pattern for crystalline ZnO is shown in Figure 2.1. Orientations of all diffraction peaks are illustrated. From the data, peak intensity, position and width are used to analyse the crystal structure.

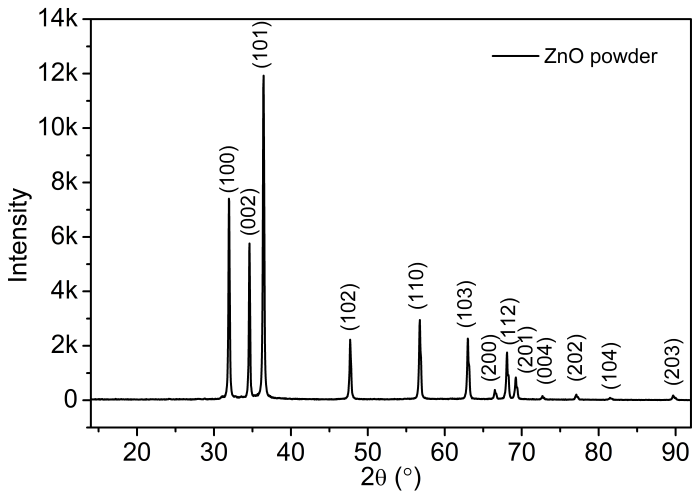


Figure 2.1 A typical XRD pattern of ZnO powders.

The mean crystallite size, D, is determined by the Scherrer formula:

$$D = \frac{K\lambda}{[\beta(2\theta)]\cos(\theta)} = \frac{K\lambda}{[\beta_0(2\theta) - \beta_i(2\theta)]\cos(\theta)} \qquad \textbf{Eqn 2.1}$$

where D is the mean crystallite size, λ the X-ray wavelength (0.15406 nm), θ the Bragg angle, β(2θ) the full width half maximum (FWHM) in radians. Considering the

instrumental broadening, $\beta(2\theta)$ equals to the difference between original FWHM β_0 (2θ) and the instrumental broadening $\beta_i(2\theta)$. In our case, $\beta_i(2\theta)$ = 0.09°, measured from Si (111) single crystal at diffraction peak at 28.5°. K is a shape factor, typically 0.9 for an assumption of spherical crystallites. From Figure 2.1 the extracted data of three typical peaks are shown below.

Table 2.1 The grain sizes calculated from XRD patterns by the Scherrer formula

Peak Position (°2θ)	β_0 (2θ)	hkl	D (nm)
31.96	0.19	100	82.6
34.61	0.18	002	92.5
36.44	0.21	101	69.7

2.1.2 Transmission electron microscopy

Transmission electron microscopy (TEM) was used to investigate the crystallinity of ZnO films on the nanoscale. Similar to SEM, TEM uses an electron beam to analyse the sample, but the accelerating voltage used is higher and images are formed using electrons transmitted through the sample, leading to a thickness limit of generally less than 200 nm. To comply with this requirement, ZnO films were first deposited on glass/ITO substrates. Cross-sections were then cut from the substrates using a Helios NanoLab DualBeam. The subsequent cross-section thinning was carried out using ion beam accelerating voltages of 30, 5 and 2 kV. TEM and Scanning TEM (STEM) imaging was carried out using JEOL 2100F at 200 kV. Lattice fringes and fast Fourier transforms were used to investigate the amorphous/nanocrystalline nature of the films. Great care was taken to minimise the sample exposure to the electron beam.

2.2 Chemical analysis

2.2.1 X-ray photoelectron spectroscopy

X-ray photoelectron spectroscopy (XPS) was performed to understand the composition and bonding of ZnO films fabricated by both sol-gel and carbon-free methods.

A typical XPS system is composed of a monochromated X-ray source, a cylindrical mirror analyser (CMA) and a detector[1]. First, the sample is irradiated by the X-ray. Then, photoelectrons are emitted with a kinetic energy (KE) from the sample surface (typically within 1-10 nm). Next, the emitted photoelectrons need to pass through the CMA. The CMA can be tuned to select photoelectrons with specific KE to pass through. Finally, the passed photoelectrons are collected by the detector.

ZnO films for XPS measurement were deposited on conductive ITO substrates. All spectra were recorded on a Thermo Scientific K-Alpha+ X-ray photoelectron

spectrometer operating at $2x10^{-9}$ mbar base pressure. This system incorporates a monochromated Al K_α X-Ray source ($h\nu$ = 1486.6 eV) and a 180° double focusing hemispherical analyser with a 2D detector. The X-ray source was set to 72 W, operated at 6 mA emission current and 12 kV anode bias. Data were acquired at 200 eV pass energy for survey scan, 20 eV pass energy for core level using an X-ray spot size of 400 μm^2. A flood gun was applied to minimise sample charging. All data were analysed using the Avantage software package.

2.2.2 Fourier transform infrared spectroscopy

Fourier transform infrared spectroscopy (FTIR) was used to investigate the composition of ZnO films, especially the residues from precursor solution, as a further confirmation of XPS results.

In this work, the specific chemical bonds were studied to infer the existence of precursor residues by investigating the absorption at characteristic resonant frequencies of chemical bonds. The FTIR measurement was conducted in ATR mode (Attenuated Total Reflectance). Compared to the traditional FTIR in transmission mode, ATR-FTIR is more sensitive to the sample surface, which is suitable for our smooth film sample. ZnO films were deposited on Si substrate for FTIR measurement. The test was conducted in air, with an instrument (NICOLET iS10) from Thermo Scientific.

2.3 Surface morphology characterisation

2.3.1 Scanning electron microscopy

The morphologies of ZnO and perovskite films were investigated using scanning electron microscopy (SEM). A Leo Gemini 1525 Field Emission Scanning Electron Microscope (FESEM) was used with accelerating voltage fixed at 5 kV. The field emission gun was held at high vacuum at all times, ~ 10^{-7} Pa. And the sample chamber was held at ~10^{-3} Pa during imaging.

Before characterisation, 5 nm chromium thin films were coated onto the samples by sputtering to increase surface conductivity for better image quality. To reduce the electron charging effect under electron beam irradiation, the edge of the substrate surface was coated by conductive carbon tape that the other side was connected to the aluminum sample holder. During characterisation, secondary electrons (SE) were recorded for imaging. Secondary electrons are produced within only several nanometers of the sample surface, with typical energies < 50 eV[2]. There are two secondary electron detectors in this SEM machine: one is mounted at a low angle to the sample surface; the other is positioned in-lens. The in-lens detector can capture more secondary electrons

created at the sample surface, which enables higher image resolution. Thus, we used in-lens detector for imaging.

Image contrast is related to the sample surface morphology. Greater exposed surfaces receive more electron irradiation and subsequently generate more secondary electrons, which shows brighter pixels in the images. Working distance can influence the depth of field and resolution. A large working distance results in a large depth of field and a reduced resolution, which is suitable for complex nanostructure imaging. A small working distance increases the resolution because closer distance between sample and detector allows for more secondary electrons to be captured, which is more suitable for samples with low roughness. In our project, we only detected ZnO and perovskite film surface so that the working distance was set as low as 5-7 mm. For magnification, low magnification enables large area to be detected, although resolution is reduced, which was used to confirm the uniformity of large area films for the application in solar cells. High magnification was used to observe fine surface detail, such as estimating grain size and surface roughness.

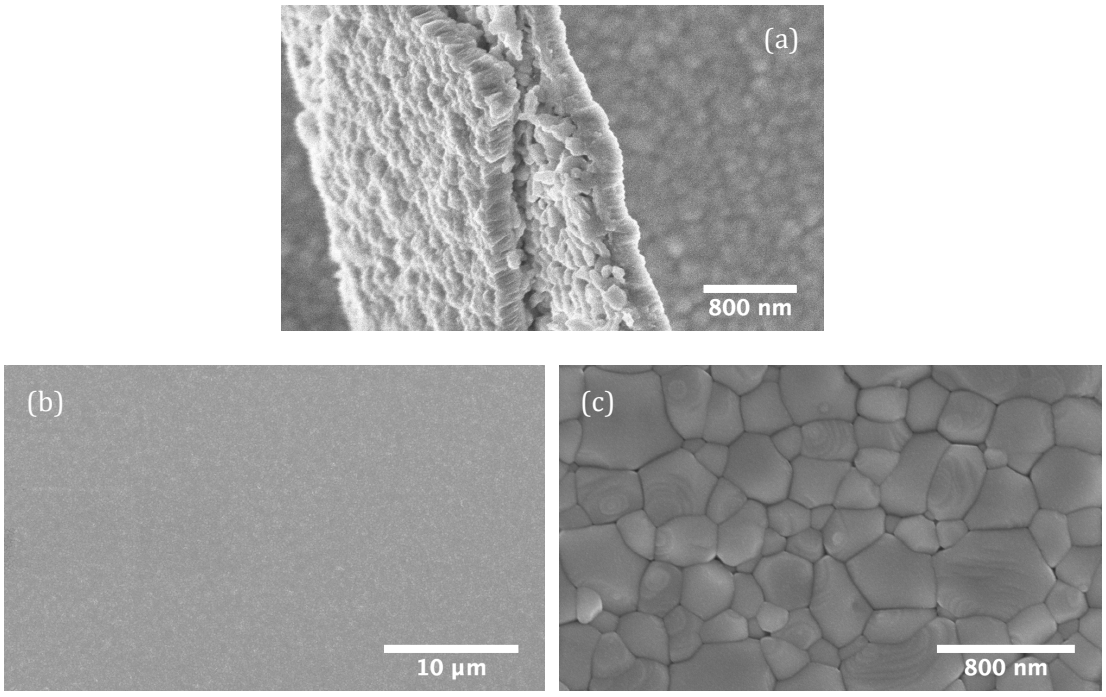


Figure 2.2 SEM images: (a) a working distance of 5.6 mm showing low depth of field; (b) low magnification (10k) showing large area film uniformity; (c) high magnification (100k) showing film morphology details.

Data analysis of estimating the average granular size of films was conducted using the program ImageJ. At least three areas were characterised for each sample to make generalisation among entire sample.

2.3.2 Atomic force microscopy

Atomic force microscopy (AFM) was used to investigate the surface morphology of a variety of films used in this work. Compared with SEM, AFM provides more detailed height information and related surface roughness. In addition, it is not necessary for the sample films to be conductive in AFM measurement. In principle, AFM comes from how the sample surface interacts a tip. The tip is attached to a cantilever and scans over the sample. A laser is incident on the cantilever and then is reflected onto a photodiode detector. The cantilever is bent with different sample surface heights thus the incident plot of laser on the photodiode is moved, which in turn builds the image of the sample[3].

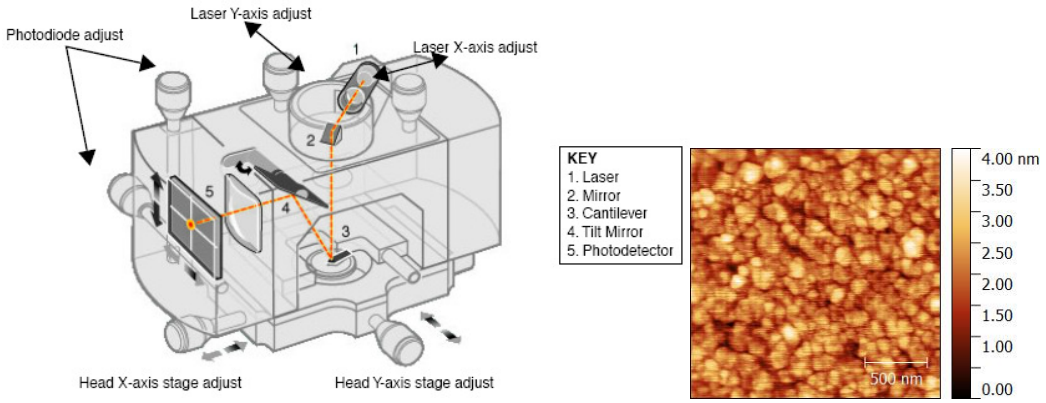


Figure 2.3 left) Schematic of the relationship among laser, cantilever and photodiode, adapted from Ref[4]; right) An example of AFM image showing high resolution on height, measured on an ITO substrate surface.

The AFM measurement (Bruker Multimode Nanoscope) was conducted under tapping mode that minimised the tip contamination and sample surface damage. The measurement parameters were set identically for the same sample materials. And the scanning areas for all images were 2×2 μm^2. The image processing was carried out with a Gwyddion software suite. In this work, the homogeneity and surface roughness were investigated by AFM. For homogeneity, pin-holes in carrier transporting layers and photoactive layers can result in leakage current in solar cells. For surface roughness, a highly rough film can lead to incomplete interface contact and thus influence charge carrier extraction.

The surface roughness can be quantified by AFM, typically using the root-mean-squared (RMS) roughness:

$$RMS = \sqrt{\frac{1}{n}\sum_{i=1}^{n} z_i^2}, \qquad \textbf{Eqn 2.2}$$

where n is the number of points and z_i the height of the i^{th} point.

2.4 Optical techniques

2.4.1 Ultraviolet-visible spectrophotometry

Ultraviolet-visible spectrophotometry (UV-Vis) (Agilent Technologies Cary 5000 UV-Vis-NIR Spectrophotometer) was used for measuring optical transmission of electron extraction layers and estimating optical bandgaps of ZnO films.

A monochromator composed of white light lamp and diffraction gratings is used to provide a monochromated beam with tunable wavelength. After passing a sample, the intensity of incident light is recorded by a photodiode. By comparing the obtained pristine signal with a reference of 100% transmission and a light-blocked reference (0% transmission) as background signals, the light transmittance at a certain wavelength is achieved. By changing the beam wavelength, a transmission spectrum is collected in an interested wavelength region.

For investigating the transmission of electron transport layers of solar cells, the layers were deposited on glass/ITO substrates. An air reference was used for 100% transmission. While for investigating the optical bandgap of ZnO films, the layers were deposited on quartz substrates. A quartz substrate was used for 100% transmission. The scan range was typically 200 – 1100 nm for this research, with a 1 nm step width. The diameter of the spot that the light was passing through samples was 5 mm.

If we ignore the loss of reflectance and scattering, which is suitable for planar thin films, the absorption coefficient α can be described from Beer-Lambert law:

$$\alpha = -\frac{1}{t}\ln(T) \qquad \textbf{Eqn 2.3}$$

where t is the film thickness and T is the transmission. A direct bandgap (direct allowed transition) semiconductor satisfies the following relationship[5]:

$$[\alpha(h\nu)]^2 \propto (h\nu - E_g) \qquad \textbf{Eqn 2.4}$$

where α is the absorption coefficient, h is the Planck's constant, ν is the frequency of light and E_g is the optical bandgap. By plotting $(\alpha h\nu)^2$ against hν, the value of optical bandgap can be estimated by extrapolating the linear portion of a curve with the hν axis, which is called Tauc plot. An example of transmission spectrum and related Tauc plot of ZnO film is shown in Figure 2.4.

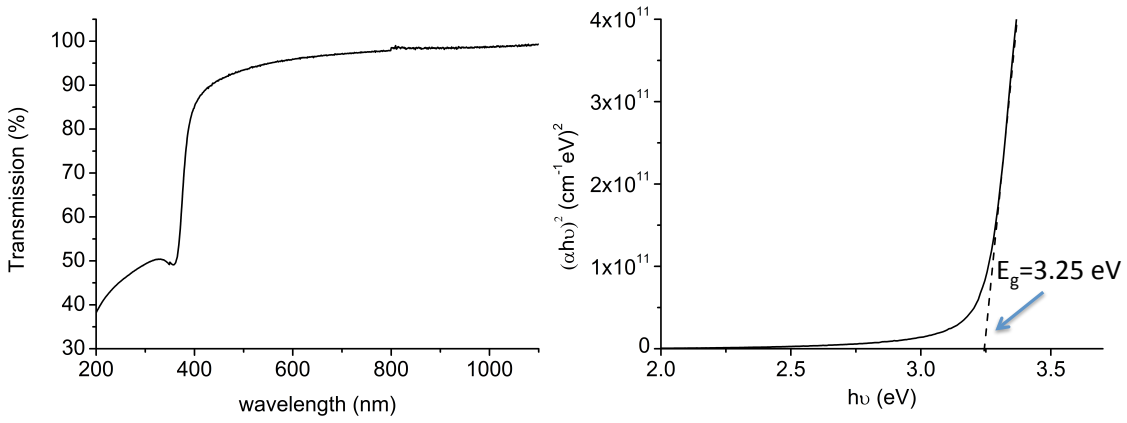


Figure 2.4 Transmission spectrum and corresponding Tauc plots of ZnO films on quartz substrates.

2.4.2 Contact angle measurement

Contact angle analysis was conducted to investigate the wetting of polymer blend or hybrid perovskite precursor solution droplets on electron extraction layers. Low contact angle and thus good wetting are desirable, as shown in Figure 2.5b.

The contact angles were obtained utilising an optical microscope (Veho Discovery VMS-004), by dropping solution droplets (fixing at 5 μL) on film surface. Considering the rapid evaporation rate of organic solvents, the processes of dropping solution droplets were recorded as videos. All images with different substrates were captured at the same time after the droplet dropping. Data analysis was made by the ImageJ software, with the 'contact angle' plugin.

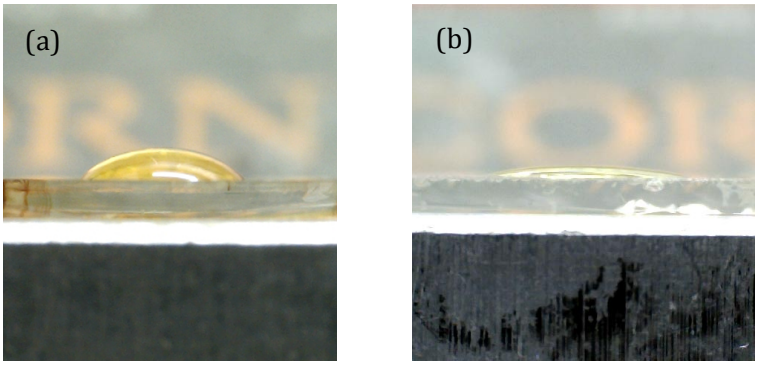


Figure 2.5 Original pictures of precursor droplets on film surfaces: (a) relatively poor wetting; (b) relatively good wetting.

2.4.3 Line profilometry

The thickness of thin films was obtained using a Dektak 150 stylus profilometer. The working mechanism is similar to that of the AFM. A tip was put in contact mode with a sample and then moved as a line across the film surface. The topographic variation of

the film surface induces a vertical displacement of the tip, recorded as a function of distance[6].

The topographic variation of the film sample was obtained by exposing a step between the substrate and the film. For ZnO, a diluted nitrate acid was used to remove the ZnO. Then DI water and isopropanol were used to rinse the film surface. For active layer, the step was obtained by carefully scratching with a scalpel. Each sample was measured as least 10 times to give an average value of the sample thickness.

2.5 Electrical characterisation

2.5.1 Kelvin probe measurement

Kelvin probe measurement was used to investigate the work function of electron transport layers in this work.

When a metal tip is electrically contacted with a sample (metal/semiconductor) with a different Fermi level (E_F), charges move towards the material with larger work function, until Fermi level keeps the same across the two materials. If the tip and the sample are fabricated into a parallel plate capacitor, equal and opposite charges form at two surfaces. This generates a contact potential difference (V_{CPD}) between two materials. The measurement of V_{CPD} can be done by applying an external DC bias V_b on the metal tip with the same value as V_{CPD} but opposite direction, at which point the surface charges disappear.

In actual measurement, the tip is forced to vibrate to generate varying capacitance by changing the distance of plates. Because the charge of the capacitor remains constant at a certain V_b, based on equation C=Q/V, the voltage between the tip and the sample plates is varied during tip vibration, resulting in the peak-to-peak output voltage (V_{ptp}). V_b is set to a range of potentials and when V_{ptp} = 0, V_b equals to - V_{CPD}. Hence, the E_F difference of tip/sample is extracted. By measuring a calibrated reference with known work function, provided the work function of the tip is constant, the work function of the sample can be acquired.

To avoid the charging effect and to show the same condition in actual solar cells, all ETLs for Kelvin probe measurement were deposited on ITO substrates. The measurement was conducted in air, with a Kelvin probe instrument (KP technologies, SKP 5050). A stainless steel tip (tip diameter: 2 mm) approaches the sample surface to get electrical contact (0.2-2 mm). The values were calibrated using a highly ordered pyrolytic graphite (HOPG) as a reference, with known work function value (4.48 eV)[7].

2.5.2 Thin film transistor

Thin film transistor (TFT) was involved in this work only for investigating the electron mobility of ZnO films. From the transfer characteristics, the mobility in the saturation region ($V_D \geq V_G$-V_T) can be extracted as follows[8]:

$$I_D = \frac{W}{2L} C_i \mu (V_G - V_{TH})^2 \qquad \textbf{Eqn 2.5}$$

$$\text{so that } \mu_{sat} = \frac{2L}{WC_i} \left(\frac{d\sqrt{I_{Dsat}}}{dV_G}\right)^2 \qquad \textbf{Eqn 2.6}$$

Where μ_{sat} is the saturation mobility, L the channel length, W the channel width, C_i the capacitance per unit area of gate oxide, I_{Dsat} the saturated drain current, V_G the gate voltage and V_{TH} the threshold voltage.

Coplanar bottom-gate structure thin film transistors (TFT) were fabricated on end-of-line test substrates (Fraunhofer, IPMS 5). The substrate (gate) was n-doped silicon and the gate oxide was 230 nm SiO_2. Contacts (Drain/Source) were 30 nm Au with 10 nm high work function adhesion layer (ITO). The channel length was 5 or 20 µm and the channel width was 2 mm. ZnO films were spin casted directly on the substrates in the air, no encapsulation layer or any type of protective layer. The TFT devices were measured at ambient atmosphere using a probe station (MMR Technologies, LTMP-4) and a semiconductor parameter analyzer (Agilent, 4155C) with a software Desktop Easy Expert.

2.5.3 Hall effect measurement

Hall measurement system was used to investigate the resistivity, carrier concentration and Hall mobility of ZnO films. First, the resistivity was obtained using the Van der Pauw method. Then a 1.2 T (RMS) AC magnetic field was applied and the measured Hall voltage was used to calculate carrier concentration and Hall mobility[1].

The films for Hall effect measurement were deposited on 1×1 cm^2 quartz substrates and indium was used for contacts on the four corners. The Hall measurement (Lakeshore 8400 system) was conducted in AC mode to eliminate systematic voltage errors that otherwise dominate signals from low mobility samples.

2.5.4 Four point probes

The sheet resistance of ITO films under different annealing conditions was characterised by a four-probe method. Four probes are arranged linearly with equal distance from each other (probe diameter 0.3 mm, spacing 0.6 mm). A constant current (I) supplied by a Keithley 2400 Source Unit is passed through the outer two probes and the potential

drop (V) across the inner two probes is measured. The sheet resistance can be presented as

$$R = \rho/t = k \times V/I \qquad \textbf{Eqn 2.7}$$

Where ρ is the resistivity of the sample, t is the film thickness, $k = \pi/\ln 2 \approx 4.532$ is a geometric factor[9][10]. Normally 10 (V, I) values in the current range of 0.01 – 1 mA were measured for each sample.

2.6 Solar cell characterisation

2.6.1 Current density – voltage characteristics

Current density – voltage (J-V) characteristics were measured using a xenon lamp at AM1.5 G solar illumination (Oriel Instruments). The measurement distance was adjusted to obtain an irradiation of 100 mW/cm^{-2} (1 sun), which used a silicon reference cell to calibrate. The testing was in the range between -1.5 V to 1.5 V with a Keithley 2400 source meter. Power conversion efficiency (PCE), open circuit voltage (V_{OC}), short circuit current density (J_{SC}), fill factor (FF), series resistance (R_S) and shunt resistance (R_{SH}) were calculated using the J-V results. The values of series resistance and shunt resistance are estimated by the reciprocal of the slope of J-V curves when J = 0 and V = 0, respectively. Generally, at least 5 devices were applied for each set of conditions.

2.6.2 Transient photovoltage and photocurrent measurement

Transient photovoltage (TPV) and transient photocurrent (TPC) measurements were used to determine the charge carrier density and lifetime in OPV devices employing different ZnO films. For TPV, white-light illumination was provided by a ring of 12 white LEDs capable of a power up to 7 suns, calibrated to device performance to 1 sun equivalent as measured under simulated AM1.5 illumination. An optical small perturbation (keep same pulse intensity for all light bias conditions) was then applied to the device on top of the illumination background using a pumped Nd:YAG laser (532 nm, 5 Hz, pulse duration < 1 ns). Voltage transients were measured on a Tektronix TDS 3032B oscilloscope.

Because the TPV process was held in open-circuit condition, the charges generated by the small perturbation were forced to recombine. Through measuring the lifetime of extra carriers photogenerated by the laser pulse, the total lifetime of charge carrier within the device were able to be determined[11].

The steady-state carrier density was determined by differential charging[11]. Through measuring the small perturbation charge (ΔQ) and voltage change (ΔV_0), the

differential capacitance can be determined as $C = \Delta Q/\Delta V_0$. Then charge density can be integrated:

$$n = \frac{1}{Aed}\int_0^{V_0} C(V)dV, \qquad \textbf{Eqn 2.8}$$

where A is the device area, e electronic charge and d the device thickness.

TPC was used to determine the ΔQ, measured at relatively low light intensity to minimise the influence of recombination[11]. The experimental setup of TPC is the same as TPV, except an additional resistor with small load (R_L = 50 Ω). The voltage (V_L) across this additional resistor was also monitored with the oscilloscope. ΔQ was calculated by integrating the current transient ($I = V_L/ R_L$) with respect to time.

2.6.3 Transient absorption spectroscopy

Transient absorption spectroscopy (TAS) was used in this work to investigate the charge carrier extraction ability of ETLs from perovskite active layer.

TAS is a pump / probe optical technique to study the decay dynamics of the photogenerated charges which in turn to understand the photophysical processes in a system[12]. A short excitation pulse is used to excite the electrons depending on the wavelength of interest and a continuous beam is employed to probe the decay of the excited electrons. Electrons in perovskite are mainly excited from its VB and the excited electrons become charges in only around several ps[13]. However, the response time of our TAS machine is in microsecond timescale. Hence, the recombination of the charges is mainly probed within our instrument respond time. In this work that ETL/perovskite bilayer stacks are investigated, there are two pathways of the recombination of charges: one is in the bulk perovskite material; the other is the electron transfer from perovskite to ETLs. Provided the perovskite films are the same, TAS allows a comparison of the extraction of electrons in perovskite of different ETLs.

For experiment setup, the excitation wavelength of pumped Nd:YAG laser (Lambda Photometrics) was set at 500 nm, with a pump intensity of 7 μJ cm^{-2}, a pump duration of 5 ns and a repetition frequency of 20 Hz. A 100 W quartz halogen lamp (Bentham, IL 1) was used as the probe light source. The probe light passing through the sample film was detected by a silicon photodiode (Hamamatsu Photonics, S1722-01). After amplification (Costronics Electronics), the signal was collected with an oscilloscope (Tektronics, TDS220). For all tests, samples were put in a N_2 atmosphere.

References

[1] D. K. Schroder, *Semiconductor Material and Device Characterization*, Wiley, **2006**.

[2] C. R. Brundle, C. A. Evans, S. Wilson, *Encyclopedia of Materials Characterization : Surfaces, Interfaces, Thin Films, Materials Characterization Series*, Butterworth-Heinemann, **1992**.

[3] P. Eaton, P. West, *Atomic Force Microscopy*, Oxford University Press, **2010**.

[4] Bruker, *Handbook: Instruction for Tapping Mode AFM*, **2006**.

[5] K. Morigaki, *Physics of Amorphous Semiconductors*, Imperial College Press, **1999**.

[6] Bruker, *Dektak 150 Surface Profiler Specifications Tachnical Report*, **2010**.

[7] W. N. Hansen, G. J. Hansen, *Surf. Sci.* **2001**, *481*, 172.

[8] A. Bashir, High-Performance Zinc Oxide Thin-Film Transistors For Large Area Electronics, Imperial College London, **2011**.

[9] R. Ellingson, M. Heben, "Sheet Resistance: Measurement and Significance," can be found under http://astro1.panet.utoledo.edu/~relling2/teach/archives/4580.6280.2011/20111025_lecture_4.2_phys4580.6280.pdf, **2011**.

[10] "Sheet Resistance," can be found under http://en.wikipedia.org/wiki/Sheet_resistance**.**

[11] C. G. Shuttle, Recombination Dynamics in Polythiophene : Fullerene Solar Cells, **2008**.

[12] X. Wu, Time-Resolved Spectroscopy Study on Carrier and Exciton Dynamics in Organo-Lead Iodide Perovskites, Columbia University, **2015**.

[13] C. S. Ponseca, T. J. Savenije, M. Abdellah, K. Zheng, A. Yartsev, T. Pascher, T. Harlang, P. Chabera, T. Pullerits, A. Stepanov, J. P. Wolf, V. Sundstrom, *J. Am. Chem. Soc.* **2014**, *136*, 5189.

Chapter 3 - Sol-gel derived ZnO Film Properties

3.1 Introduction

This chapter shows a systematic investigation on ZnO films by sol-gel methods. First we carried out an assessment of the crystallinity, macroscopic view by X-ray diffraction and microscopic view by transmission electron microscopy. Then the chemical analysis on ZnO films is made to confirm the presence of unreacted precursor/solvent dependent on the annealing temperature, using both X-ray photoelectron spectroscopy and Fourier transform infrared spectroscopy. Subsequently, the optical properties are presented *via* UV-vis spectroscopy and room temperature photoluminescence, to figure out the film transmittance. The estimated optical band gaps from optical analysis are combined with the previous microscopic structural characterisation and chemical to reveal what the low temperature processed film by sol-gel method exactly consists of.

Next, the film surface morphology, containing surface roughness, uniformity and granular size, is figured out by scanning electron microscopy and atomic force microscope. In the end we investigate the electrical properties. Bottom gate, bottom contact thin film transistors with ZnO films are utilised for revealing the ZnO electron field effect transport behaviour. AC Hall measurement is also conducted to obtain the resistivity, mobility and carrier concentration of the ZnO films. The Fermi levels of ZnO films on ITO substrates are also calculated from the contact potential difference measured by Kelvin Probe in air.

3.2 Experimental methods

3.2.1 Precursor solution

Sol-gel solutions were prepared by mixing zinc acetate dihydrate (ZAD) and 2-amino ethanol (MEA) in 2-methoxyethanol as the solvent. Equimolar ZAD and MEA were weighed and subsequently added with 20 ml 2-methoxyethanol to make solutions with a range of concentrations. The solutions were stirred overnight in dark, air, at room temperature. To ensure ageing effects do not cause any variation, solutions were used for spin coating only on the day following preparation. Before spin coating, the solutions were filtered through a 0.45 μm PTFE filter.

3.2.2 ZnO film formation

ZnO films were formed by spin coating using a static loading method. The spin coating parameters included a 500 rpm loading for 12 s and a 3000 rpm spinning for 30 s with an acceleration rate of 500 rpm/s. Three coatings were applied to achieve a dense layer

for the studies in Chapter 3 and 4[1]. The back of substrate was cleaned using isopropanol after every deposition to ensure optical properties were not compromised. The films were also preheated at a given temperature for 10 min on a hotplate (VWR) after each coating. Some samples were also treated with postannealing (Carbolite 5L RWF) at 450 ˚C for 1 hour in air with a cooling gradient of 5 ˚C/min to 300 ˚C, then left to cool to room temperature. Dense and planar ZnO layers were formed with a thickness corresponding to the solution concentration used.

All subsequent tests were conducted in ambient air and at room temperature unless specified.

3.3 Results and discussion

3.3.1 Crystallinity

A range of complementary measurements were carried out on the ZnO layers beginning with an assessment of the crystallinity by X-ray diffraction (XRD). The influence of processing temperature on the crystallinity of ZnO films was investigated, as shown in Figure 3.1. The precursor solution concentration was fixed at 0.75 M, which resulted in films with thickness > 100 nm[2] i.e. sufficient for XRD signal detection. The ITO diffraction peaks are indicated by asterisks. No peaks corresponding to crystalline ZnO are seen in the XRD patterns of the films deposited < 300 ˚C. Films deposited at 300 ˚C and those with additional postannealing at 300 ˚C show similar behavior, only very weak (002) peaks of ZnO are observed. In contrast, a strong ZnO (002) peak is shown in the film deposited at 300 ˚C and postannealed at 450 ˚C, consistent with the reference pattern (ICSD 01-076-0704). The results are consistent with the literature which suggests that the conversion from amorphous to the crystalline state starts within the temperatures range of 200-300 ˚C and is completed within the range of 400-500 ˚C[3]. Thus, from the XRD results the ZnO films at 110 ˚C appear to be macroscopically amorphous.

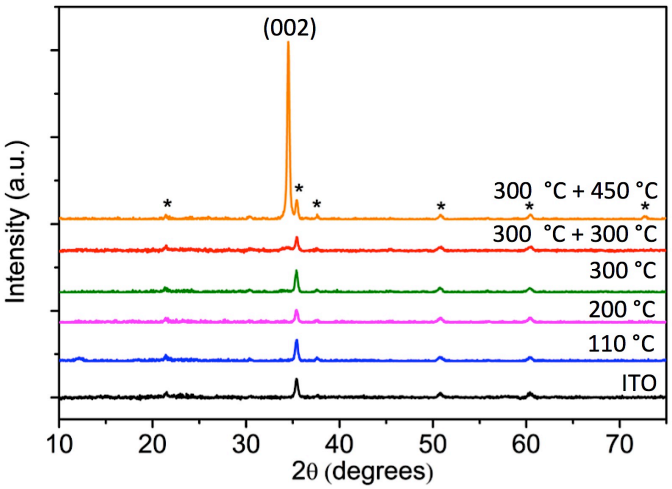


Figure 3.1 XRD patterns for ITO and ITO/ZnO stacks with the same thickness under different heating conditions (* ITO diffraction Peaks).

The influence of film thickness of ZnO 450 ˚C (preheat at 300 ˚C and postheat at 450 ˚C) was also investigated by changing the concentration of precursor solution, as shown in Figure 3.2. The details of film thickness measurement are presented in Appendix A. The films with Zn concentrations of 0.3 M, 0.5 M and 0.75 M all show strong ZnO (002) peaks and the XRD features of the films with a Zn concentration of 0.11 M are difficult to detect. The grain size of ZnO layers was calculated by the Scherrer equation, Eqn 2.1. A slight increase in the $d_{(002)}$ crystallite size from 37.8 nm (0.3 M) to 46.2 nm (0.75 M) could be observed from Table 3.1.

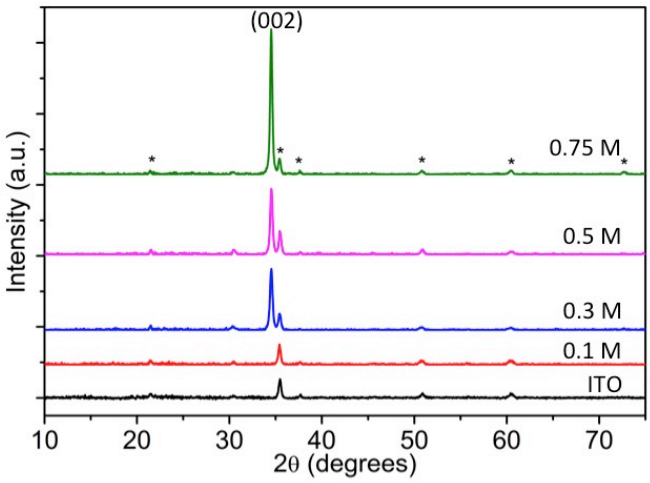


Figure 3.2 XRD patterns for ITO and ITO/ZnO stacks with different thicknesses under the same heating conditions (preheated at 300 ˚C and postannealed at 450 ˚C). (* ITO diffraction Peaks)

Table 3.1 The $d_{(002)}$ crystallite sizes calculated from XRD patterns for seed layers preheated at 300 ˚C and postannealed at 450 ˚C, refers to Figure 3.2.

Concentration of sol solution	0.1 M	0.3 M	0.5 M	0.75 M
Thickness of seed layers (nm)	33.0	61.0	88.2	158.7
FWHM (°2θ)	---	0.31	0.29	0.27
Grain size (nm, from (002) peak)	---	37.8	41.6	46.2

From the above figures, the ZnO (100) and (101) peaks are indiscernible for all ZnO films due to the optimisation by precisely adjusting the preheating temperature to 300 ˚C. Instead, for the films preheated at 350 ˚C, the peaks of ZnO (100) and (101) can be observed, as shown in Figure 3.3. The higher preheating temperature (>300 ˚C) may disturb the preferential (002) growth as the evaporation of the solvents and the thermal decomposition of the zinc acetate may happen abruptly and simultaneously with the crystallisation[1]. This comparison proves that the preheating process is a crucial step to govern the orientation of the crystallites[2]. The most appropriate temperature of preheating should be higher than the boiling points of additives and solvents and near the crystallization temperature. In the case of combination of ZAD + MEA + 2-methoxyethanol, around 300 ˚C is the optimal preheating temperature[1][2][4].

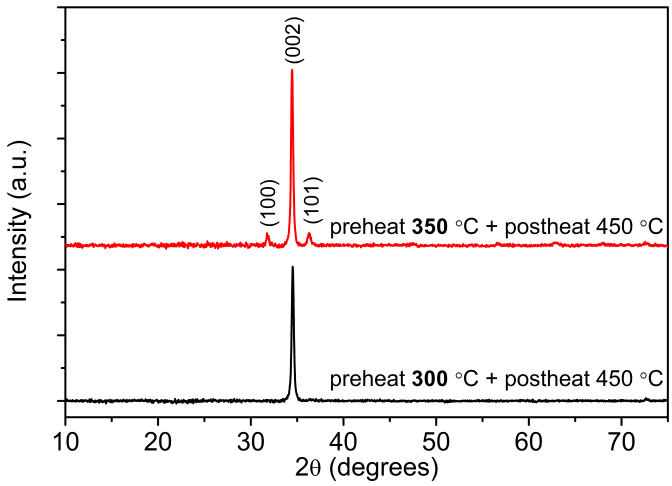


Figure 3.3 XRD patterns for glass/ZnO stacks with different preheating temperatures.

To further detect the nanoscale crystallinity, the ZnO films at 110 °C were measured by transmission electron microscopy (TEM). Structural characterisation of macroscopic view was carried out by XRD as shown above which indicated ZnO at 110 – 300 °C are amorphous and ZnO at 450 °C is crystalline. However, the TEM result here indicates that from microscopic view films processed at 110 °C are comprised of ZnO nanocrystals embedded in an amorphous matrix. Figure 3.4 shows a 110 °C annealed ZnO layer

between the ITO and PTB7:$PC_{71}BM$ layers within the device. The presence of nanocrystalline areas can be clearly seen within the 110 °C ZnO layer. A selection of lattice fringes has been labeled with the measureable lattice spacings, annotated corresponding to wurtzite ZnO. The Fast Fourier Transform (FFT) inset further demonstrates the presence of multiple crystals within this layer.

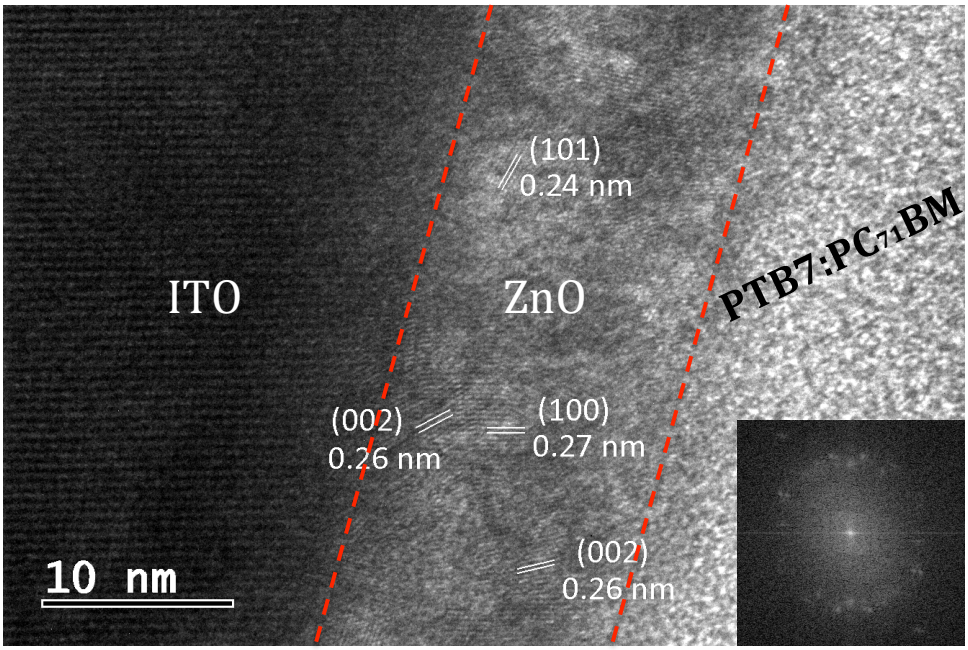


Figure 3.4 TEM image showing the 110 °C annealed ZnO layer between the ITO (left) and PTB7:PC71BM (right) layers within the device.

From Figure 3.4, an amorphous area is also observed where the fringes disappear and between discrete crystalline regions. Thus, the ZnO 110 °C film is assumed to be a mixture of nanocrystalline ZnO and amorphous material. This is further supported by the scanning transmission electron microscopy (STEM) dark field image, as shown in Figure 3.5, from the varying brightness within the ZnO 110 °C films. In addition, Figure 3.4 and Figure 3.5 indicate the pinhole-free and compact coverage of ZnO layer and the subsequent PTB7:$PC_{71}BM$. No disorder is detected on both ITO/ZnO and ZnO/PTB7:$PC_{71}BM$ interfaces. These result in the excellent organic solar cell performance that is discussed in the next chapter. To investigate what exactly the amorphous substance is, chemical analysis was conducted.

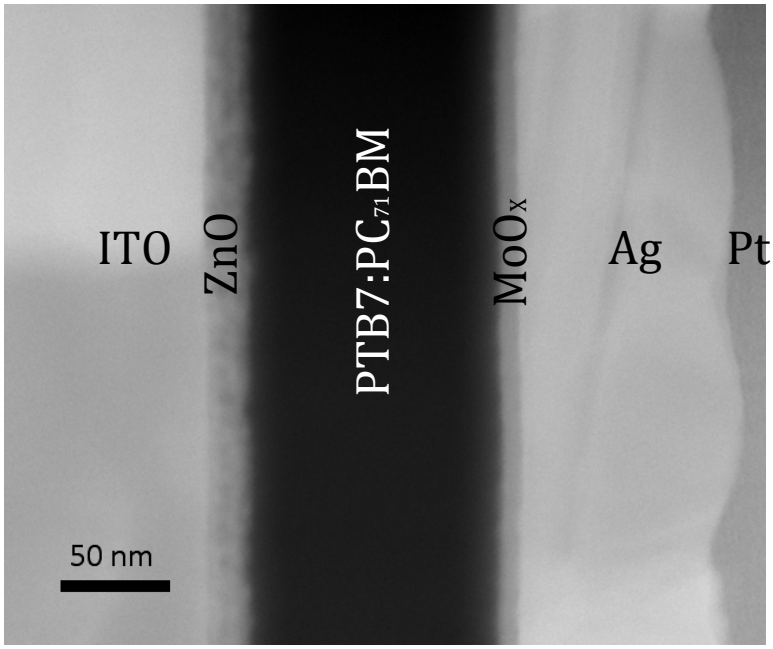


Figure 3.5 STEM dark field image of full device showing, from left to right, the ITO, ZnO (110 °C), PTB7:$PC_{71}BM$, MoO_3 and Ag layers.

3.3.2 Chemical analysis

To understand how the composition of the films changes with processing temperature we performed X-Ray photoelectron spectroscopy (XPS) analysis of the different samples. XPS spectra of C 1*s* and O 1*s* core levels are shown in Figure 3.6 and Figure 3.7, respectively. Both the carbon and the oxygen signals are dramatically affected by the processing temperature. For the C 1*s* spectra, films treated at 110 °C, there are two distinct peaks; the peak at higher binding energy 288 eV is characteristic of the C=O in the carbonyl group and is therefore ascribed to acetate precursor still present in the film. The lower energy signal (285 eV) originates from C-C bonds (including any surface carbon contamination). Both signals diminish as the temperature is increased. Albeit showing lower intensity, C=O signal is also present the films treated at 200 and 300 °C. Although the decomposition temperature of zinc acetate is 240 °C[1], the C=O signal still exists for films at 300 °C. This is probably because more energy is needed to break the bonds in zinc complexes containing acetate[2,3]. The sample annealed at 450 °C show an almost absent signal for the C=O component, suggesting that the precursor is practically all removed between 300 - 450 °C.

The O 1*s* spectra follow similar behaviour; the sample treated at 110 °C shows a number of overlapping peaks, one at lower binding energy assigned to the Zn-O (oxide) peak and one at higher binding energy assigned to the carbonyl group. There is also likely to be small contributions from –OH, trace precursor and sub-stoichiometry of the oxide,[5] but a detailed peak-fitting analysis of the O 1*s* core level is beyond the scope of this work.

What can clearly be seen though is a systematic decrease in the intensity of the carbonyl peak as the temperature increases relative to the Zn-O (oxide) peak, in agreement with the signal from the C 1*s* peaks.

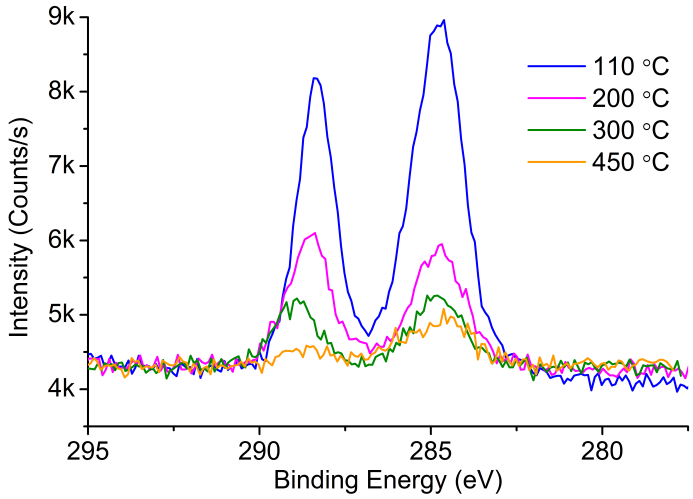


Figure 3.6 ZnO XPS spectra of C 1*s*, with different processing temperatures.

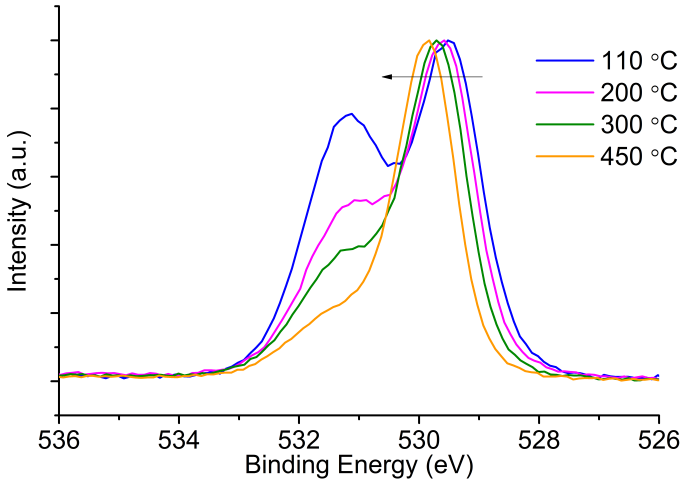


Figure 3.7 ZnO XPS spectra of O 1*s*, with different processing temperatures.

It is also observed that the binding energy (B.E.) position of the Zn-O (oxide) peak shifts from lower to higher binding energy upon annealing from 110 °C to 450 °C. This is indicative of a shift in the Fermi level position, which we would expect to manifest itself as a rigid shift of the core levels, and is indeed what we see in the Zn-O (oxide) environment of the O 1*s*. The same trend of peak shift is also observed in Zn 2*p* signals, Figure 3.8. The $2p_{1/2}$ and $2p_{3/2}$ peaks both show a 0.3 eV shift towards higher binding energy with the increase of ZnO processing temperature, *i.e.* from 1020.8 to 1021.1 eV

for $2p_{1/2}$ and from 1043.9 to 1044.2 eV for $2p_{3/2}$ peaks. Therefore as a function of annealing we observe an increase in the work function of the material.

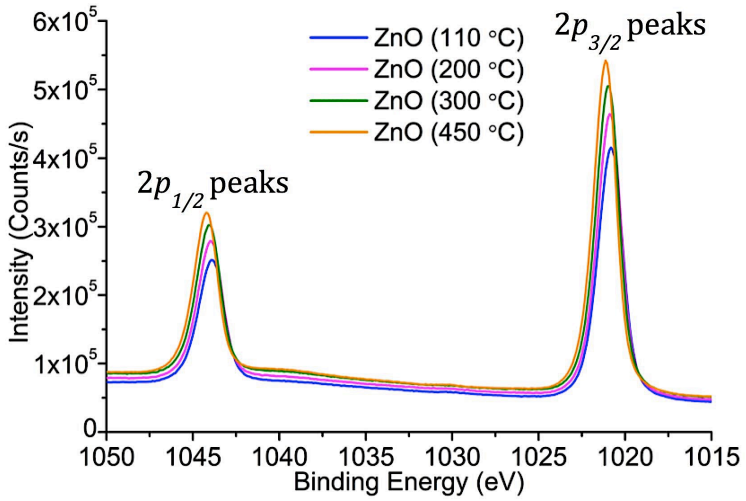


Figure 3.8 ZnO XPS spectra of Zn 2*p*, with different processing temperatures.

N 1*s* signals are shown in Figure 3.9, to probe the existence of MEA. An obvious N 1*s* signal is seen for ZnO (110 °C), which is diminished for ZnO (200 °C) and is negligible for ZnO at 300 °C. The weak signal at ZnO (450 °C) may come from the background environment. The results indicate ZnO at 110 and 200 °C have MEA residues but removed for processing temperature above 300 °C.

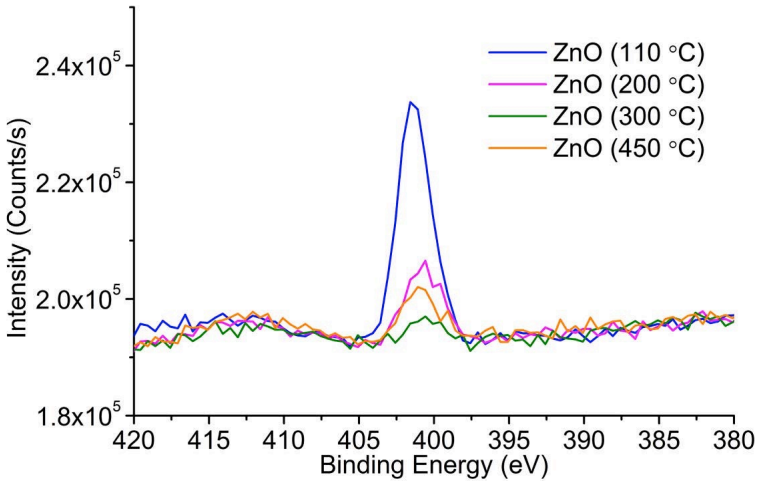


Figure 3.9 ZnO XPS spectra of N 1*s*, with different processing temperatures.

FTIR spectroscopy was also performed, attempting to further confirm the presence of unreacted precursor/solvent with the processing temperature changing, as shown in Figure 3.10. The as-deposited film and those < 300 °C show strong –OH and C=O stretching features, both diminishing with processing temperature increase and

eventually disappearing at 450 °C due to the formation of crystalline ZnO. The C=O stretching result is in agreement with the C 1*s* analysis by XPS. Therefore, the amorphous substance in low temperature processed ZnO contains organic residues.

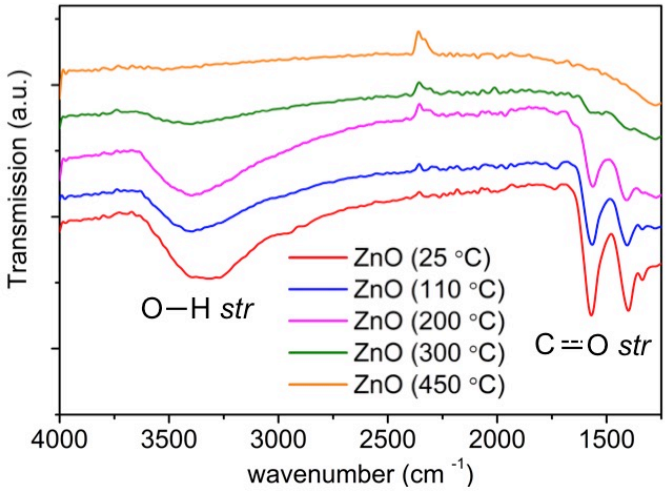


Figure 3.10 FTIR spectra of ZnO with different processing temperatures.

To be specific, due to the boiling point of solvent 2-methoxyethanol is 125 °C and that of stabiliser MEA is 171 °C, the ZnO 110 °C films should be nanocrystalline ZnO with amorphous substance containing 2-methoxyethanol, MEA and acetate ligand. For ZnO 200 °C, 2-methoxyethanol should be removed after sufficient evaporation, while MEA and acetate residue still exist due to the complexation of zinc cation with MEA and acetate, respectively[2,3]. This is also in agreement with the TGA results of zinc acetate dihydrate, as shown in Appendix A, which indicates that the decomposition of zinc acetate starts at around 200 °C and the full transfer to ZnO finishes at around 370 °C. ZnO 300 °C may be a nanocrystalline film which still has a little acetate residue. For the ZnO 450 °C, the thermal energy is sufficient for the formation of polycrystalline ZnO film at macroscopic view.

Hence, from the combined TEM, XPS and FTIR analysis we conclude that the film processed at low temperature is a mixture of nanocrystalline ZnO and amorphous organic substance. With the temperature increase, the organic residues gradually diminish and the ZnO nanoparticles get together until a sufficient energy to form the highly (002) oriented polycrystalline ZnO film.

3.3.3 Optical properties

For the typical solar cell architecture, the incident light needs to transmit through the transparent conducting electrode and electron transport layer before reaching the photoactive layers. Thus, the high optical transparency of the oxide layer is required in

the wavelength range of the photoactive material absorption. First, the transmission of ZnO films under different heat treatment conditions was investigated, against an air reference, shown in Figure 3.11. To accurately consider the situation in solar cells, films were deposited on ITO substrates. At all deposition temperatures from 110 ˚C to 450 ˚C high transmission is obtained in the visible region. Highly uniform, planar films are deposited which is confirmed from the Fabry Perot oscillations observed.

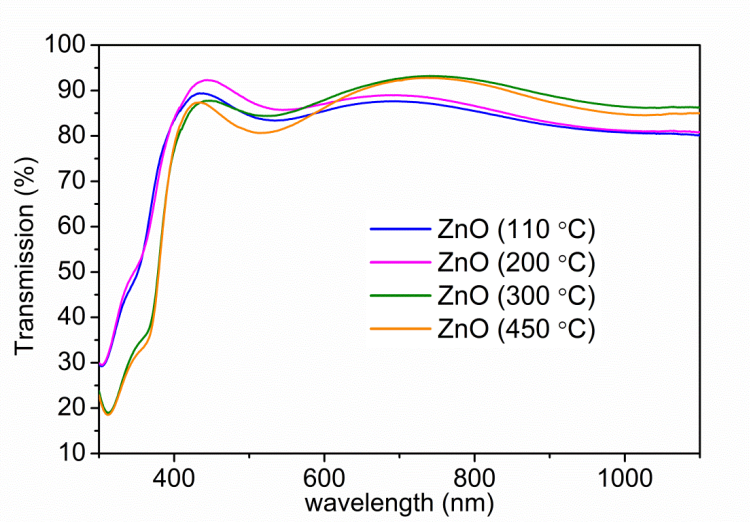


Figure 3.11 UV-vis spectra for Glass/ITO/ZnO stacks with different processing temperatures.

For the Tauc plot analysis, films were deposited on quartz substrates. The Tauc plots $((\alpha(h\nu))^2 \sim h\nu)$ and the estimated E_g of different films are shown in Figure 3.12, against a quartz reference. The measured absorption edge of ZnO (200 – 450 °C) is around 380 nm, which is close to the intrinsic bandgap of ZnO. The calculated optical bandgaps, based on Eqn 2.3 and 2.4, are largely consistent at approximately 3.25 eV. But E_g of the ZnO processed at 110 °C is somewhat higher at 3.38 eV. This is in agreement with our TEM image that the crystal size is only several nanometers in 110 °C ZnO layers, derived from the quantum confinement of ZnO nanoparticles[6][7]. Also, the difference of bandgap between 110 °C and higher temperature may originate from that the nanoparticles are surrounded by the amorphous organic substance in the 110 °C film. However, for higher temperature the nanoparticles are connected more firmly as organic residues are decreased therefore confinement effect is diminished.

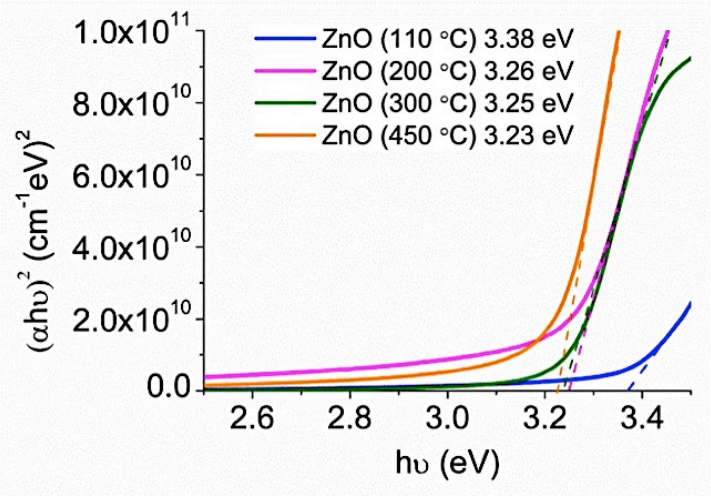


Figure 3.12 Tauc plots calculated from ZnO on quartz substrates.

The optical bandgap variation with ZnO processing temperature was further confirmed from the room temperature photoluminescence (PL) results. With 325 nm as excitation wavelength, the near-band-edge (NBE) emission of 110 °C ZnO shows blueshift compared to that of ZnO with higher temperatures, as shown in Figure 3.13. All spectra are normalised to the peaks in the NBE region.

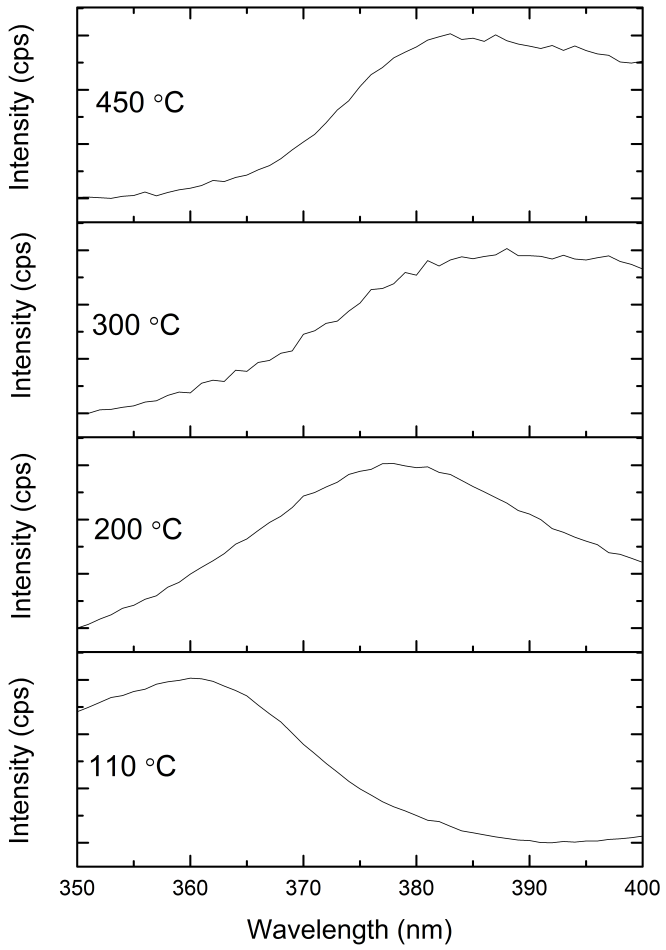


Figure 3.13 Room temperature PL spectra of ZnO films with different processing temperatures, all normalised to the peak intensity in the NBE region.

The transmission spectra of ZnO planar films with different thicknesses against an air reference were also investigated, as shown in Figure 3.14. All the films were processed at 450 ˚C. An ITO substrate with same 450 ˚C annealing was set as a control sample. The transmission exceeds 80% in the visible region for all the samples. The interference between the top and the bottom surfaces of the film could be speculated due to the observed fringes in the curves. The fringes vary with the film thickness, which can modulate higher transmission in the wavelength range where the active materials absorb light in solar cells.

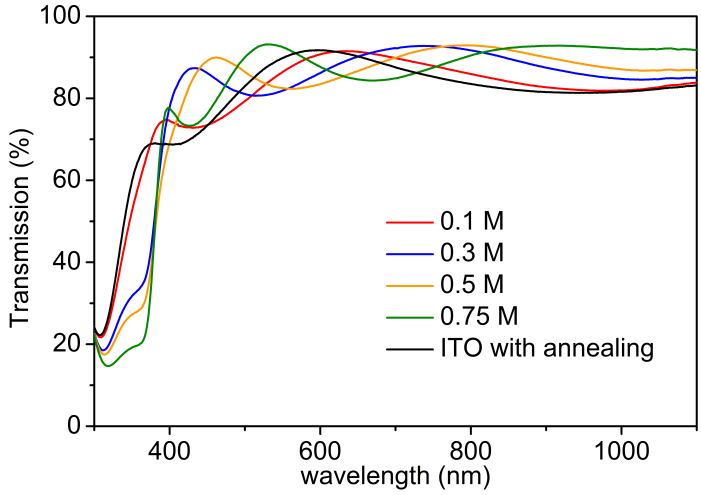


Figure 3.14 UV-vis spectra for Glass/ITO/ZnO stacks with different thicknesses.

3.3.4 Surface morphology

The morphology of ZnO layers on ITO substrates was characterised by scanning electron microscopy (SEM). The morphology of ZnO films with different heat treatment conditions is shown in Figure 3.15. The films become denser with the increase of processing temperature, companying with the decomposition of organic residues[3]. At the temperature of 110 ˚C, a large amount of organic residue still remains which results in smooth films. As the temperature is elevated to 200 ˚C, obvious feature appears with the decomposition of precursors and the vaporisation of solvents that will result in a densification in the film. For the film at 300 ˚C, clear grains can be observed. A significant increase of grain size occurs with the films at 450˚C. This results from the completed crystallisation of ZnO under enough annealing temperature and time.

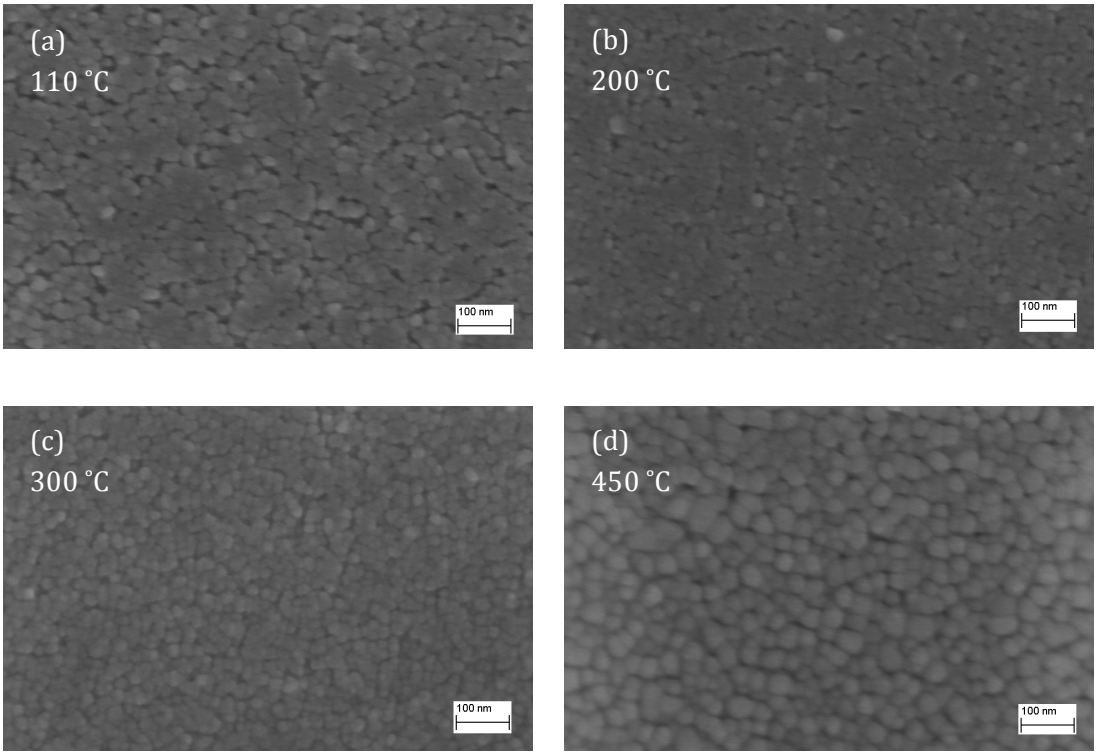


Figure 3.15 SEM images of ZnO layers with different processing temperatures.

The surface morphology was also investigated by atomic force microscope (AFM). The AFM images of ZnO films (around 60 nm) with processing temperatures are shown in Figure 3.16. The as-deposited film reveals a large surface roughness. For the films processed between 110 and 450 ˚C, the typical rms roughness values are similar, in the region of 2 nm under 2×2 μm^2 area. Surface roughness of ZnO layers by sol-gel has been proved to have influence on the device performance of inverted organic solar cells[8]. So our films exclude the influence of surface roughness on device performance.

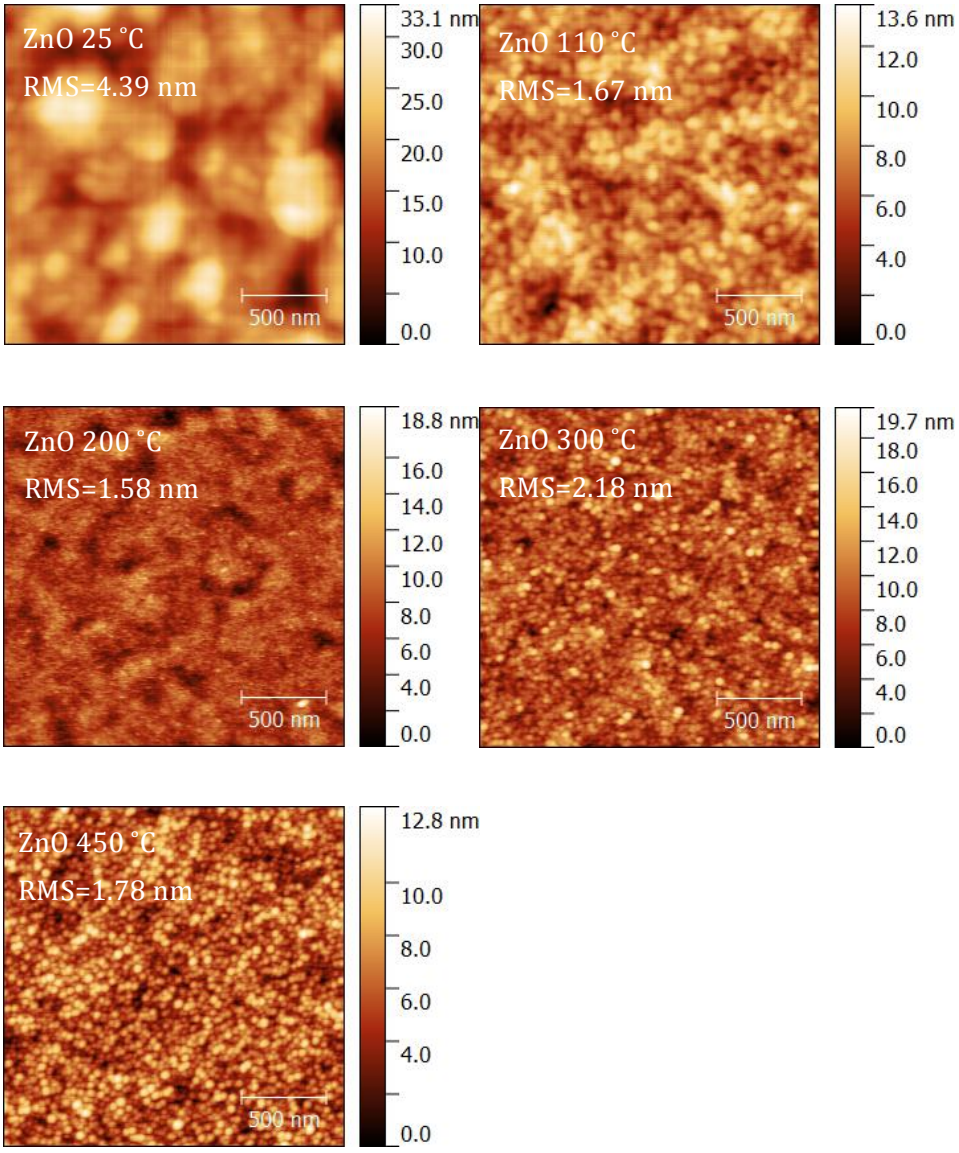


Figure 3.16 AFM image of ZnO films on ITO substrates, inset is the RMS of the films.

The surface morphology of layers with different thicknesses was also investigated by SEM. Dense and uniform films are obtained in large area, as shown in Figure 3.17. The grain size determined from the SEM images is shown in Table 3.2. The grain size increases with the increase in film thickness, which is consistent with the trend obtained from XRD. Although the trend of the results by XRD and SEM is the same, the values estimated from XRD are higher than that from SEM. This may come from that the grain size evaluated by XRD is in the z-axis direction while the grain size evaluated by SEM is in the x-y plane. And XRD results show highly (002) oriented films thus the grain size values from XRD is higher.

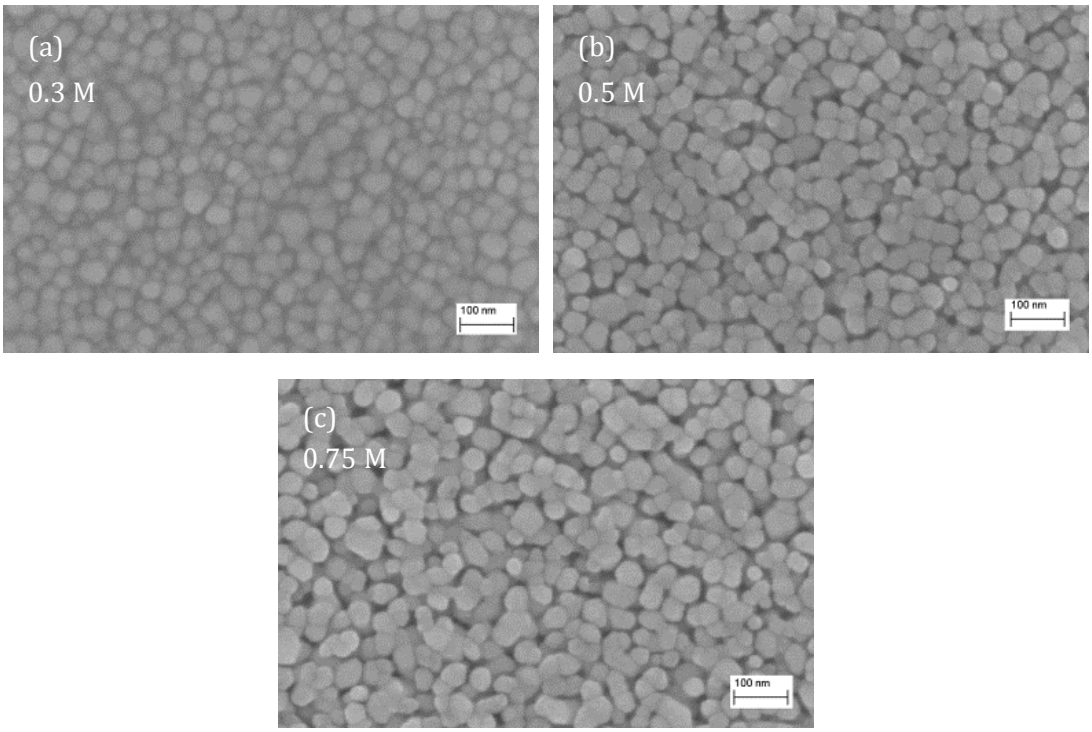


Figure 3.17 SEM images of ZnO layers prepared from concentrations indicated, measured thicknesses (a) 58 nm; (b) 90 nm; (c) 158 nm.

Table 3.2 The grain size calculated by SEM images for films at 450 °C

Concentration of sol solution	0.1 M	0.3 M	0.5 M	0.75 M
Thickness of seed layers (nm)	33.0	61.0	88.2	158.7
Average grain size (nm)	---	34.2	38.3	40.1
Standard deviation (nm)	---	7.3	7.4	7.1

3.3.5 Electrical properties

All tests of electrical properties here were conducted at room temperature, in which temperature the ZnO electron conduction mechanism is the transport in the conduction band (above 250 K)[9].

Bottom gate, bottom contact thin film transistors (TFTs) of ZnO films with different processing temperatures were prepared to investigate the electron transport properties of these materials, as shown in Figure 3.18. The transfer curves for the TFT with ZnO at 110 °C showed no field effect and the measured channel current was at the detection limit of the measurement apparatus. This originates from that the electrons need to pass through a long channel (20 μm) that is a mixture of nanocrystalline ZnO and amorphous organic substances. Between 200 and 450 °C there is a steady current increase as temperature is increased with field modulation observed at 200 and 300 °C while not at

450 °C. At 450 °C the films exhibit a very small channel current dependence on the applied gate field, however over the large gate voltage range applied these TFTs were always on – indicative of a large free carrier concentration. A change in film composition with increasing temperature will be occurring and the enhanced current observed in high temperature devices is a combined effect of improved crystallinity and intrinsic defect concentration as well as the removal of unreacted precursor residue and solvent. Enhanced electron transport as the annealing temperature increases from 110 °C to 300 °C is also demonstrated from the field effect mobility calculated from saturation region based on Eqn 2.6, Figure 3.19. While further annealing at 450 °C results in a decreased mobility compared with 300 °C processed films.

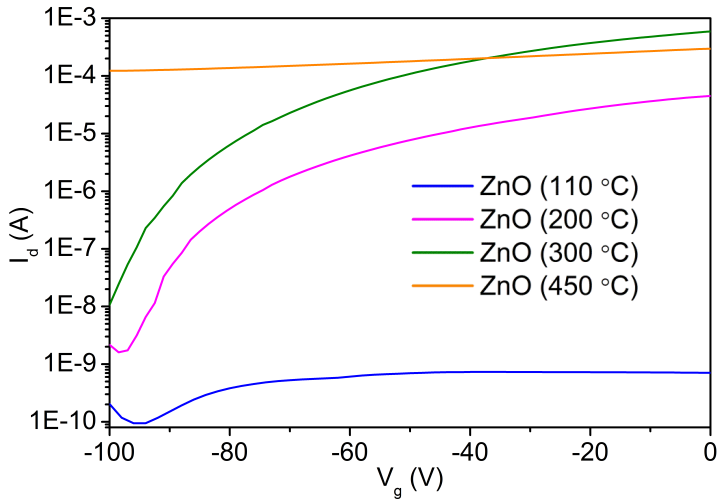


Figure 3.18 Transfer curves of TFT with ZnO films in saturation region, V_d = 45 V.

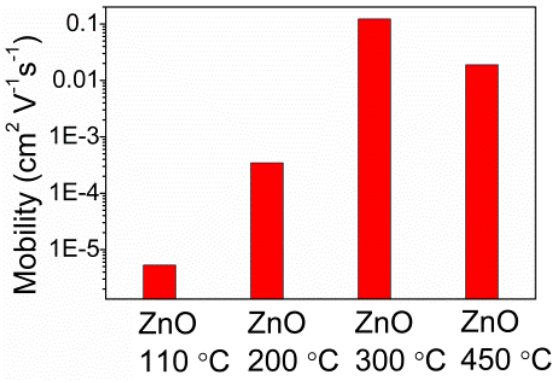


Figure 3.19 The field effect mobility of ZnO films calculated from the transfer curves of TFTs.

In parallel addition to TFT measurements we used AC Hall to measure resistivity, Hall mobility and carrier concentration of our ZnO. Here measurements could only be obtained on the 300 and 450 °C heated ZnO owing to the high resistivity of the other films. The high resistivity of low temperature processed films may come from the

solvent and unreacted precursor residues. The results are shown in Table 3.3. The carrier concentration of ZnO (300 °C) is lower than that of ZnO (450 °C), which is in agreement with the TFT transfer curves. This may derive from the change of intrinsic defects or trap states under higher temperature annealing in air[10][11]. The Hall mobility also shows the same trend with the field effect mobility that the mobility of ZnO (300 °C) is higher than that of ZnO (450 °C). Although the ZnO at 450 °C has improved crystallinity, the ZnO at 300 °C still has a higher mobility that may benefit from the ZnO intrinsic nature that the conduction band minimum state is dominated by Zn s orbital so that the disorder of ZnO crystalline structure has rather weak influence on electron transport[12][13]. Another possible reason is that the electron transport in measurements of TFT and Hall effect are both in lateral direction that is perpendicular to the film orientation of highly oriented (002) ZnO (450 °C), *i.e.* grain boundary effects.

Table 3.3 Resistivity, mobility and carrier concentration of ZnO films by Hall measurement

	ZnO (300 °C)	ZnO (450 °C)
Resistivity (Ω cm)	1.65×10^{4}	2.29×10^{3}
Hall Mobility (cm^2 / V s)	1.17×10^{-1}	2.61×10^{-2}
Carrier Concentration (cm^{-3})	3.23×10^{15}	1.04×10^{17}

The Fermi levels (E_F) of the ITO substrates and ZnO films on ITO were calculated from the contact potential difference measured by Kelvin Probe in air. The reference used was freshly cleaved highly oriented pyrolitic graphite (work function = 4.47 eV). The data reveal interesting shift in E_F as the ZnO processing temperature is changed, Figure 3.20. Heating from 25 to 110 °C results in a slight E_F reduction, from −4.23 to −4.13 eV, however continued heating induces a monotonical shift of E_F, to −4.6 eV for the ZnO at 450 °C, which is in excellent agreement with the XPS results. We attribute the E_F changes to the compositional and structural modifications occurring during the heat treatment which can be separated into three parts;

(1) ZnO 110 - 200 °C: The work function difference between 110-200 °C may be attributed to the presence of residual unreacted precursor. The MEA boiling point is 170 °C[1]. The low work function of ZnO at 110 °C may come from MEA, which has been demonstrated previously as a work function modifier and a dispersal solvent for ZnO nanoparticles[14]. Interfacial dipoles may form between electron accepting ZnO (oxygen parts) and the electron donating amine group (nitrogen parts)[15]. This may be because the electronegativity of O element is stronger than N. DEA (diethanolamine) has also

been proven to reduce the cathode work function when doped into ZnO films[16]. In addition, the surface modifiers based on polymers containing simple aliphatic amine group could substantially reduce the work function of metals and oxides[15].

(2) ZnO 200 - 300 °C: The WF difference between ZnO (200 °C) and ZnO (300 °C) may be partially attributed to the residual hydroxyl species acting as shallow surface donors[17-19]. This is ascribed to the partial decomposition of the acetate species which starts to decompose at 190 °C and finishes at 310 °C[20]. In addition, MEA is completely removed in the range of 200 – 300 °C, according to the aforementioned chemical analysis, which also contributes to the WF shift.

(3) ZnO 300 °C – ZnO 450 °C: The ZnO at 300 °C is more heavily n-doped by native defects, including Zn interstitials and oxygen vacancies, which are partially recovered in ZnO at 450 °C by the enhanced thin film crystallinity[9,11,21].

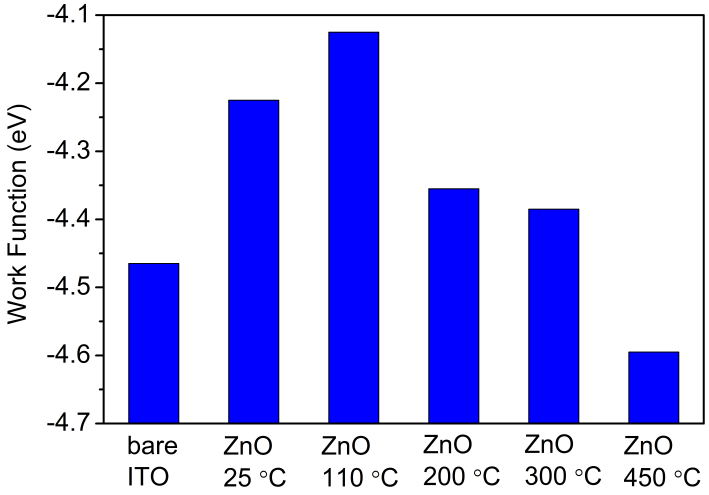


Figure 3.20 Work functions of the ITO and ITO/ZnO films by Kelvin probe.

3.4 Conclusions

ZnO, electron transport material in organic and perovskite solar cells, has been fabricated using a sol-gel method. The thin film properties were investigated as a function of processing temperature. For low temperature processed ZnO film derived from sol-gel method, although it macroscopically shows amorphous by X-ray diffraction, the microscopic view from transmission electron microscopy confirms it actually is nanocrystalline ZnO embedded in an organic amorphous matrix. The chemical analysis by X-ray photoelectron spectroscopy and Fourier transform infrared spectroscopy reveals that the amorphous organic substances gradually diminish with processing temperature increase. The enlarged optical band gap at low temperature processing is observed by both UV-vis spectroscopy and room temperature photoluminescence,

confirming the existence of nanoparticles with several nanometers crystal size due to quantum confinement.

With increasing processing temperature, the organic substance is gradually removed and the nanocrystalline domains are interconnected to form larger grain size. Thus, the composition of the film is changing from a mixture of organic amorphous/nanoparticle at 110 °C to a polycrystalline and highly (002) oriented ZnO layer without organic residues at 450 °C. Specifically, ZnO (110 °C) contains ZnO nanoparticles with 2-methoxyethanol, MEA and acetate ligand. ZnO (200 °C) contains ZnO particles with reduced MEA and acetate. ZnO (300 °C) contains ZnO particles with a trace of acetate residues. ZnO (450 °C) is pure polycrystalline ZnO.

While within the whole processing temperature region we focus on, the films all show excellent optical transparency, higher than 80% in the visible region. In addition, their surface morphology all presents compact and smooth coverage with similar surface roughness.

The film electrical properties, however, vary significantly with processing temperature, which is driven by changes in the film composition. The resistivity decreases as the processing temperature increases. For thin film transistors made with ZnO films, the devices with ZnO at 200 and 300 °C show good field modulation while ZnO at 110 °C and 450 °C do not work, the former because of high resistivity, the latter because of high free carrier concentration. Also, the work function of ZnO films, measured by Kelvin probe, is greatly influenced by the heat treatment, increasing with processing temperature in the region of 110 to 450 °C.

In this chapter we reveal the close relationship between the ZnO film properties and the film composition. In the next chapter, the relationship between these two factors and the organic solar cell device performance is investigated.

In addition, ZnO nanostructures by hydrothermal growth based on sol-gel derived ZnO planar films as seed layers are shown in Appendix A, indicating the formation of all low temperature (< 110 °C) processed ZnO nanorods, nanowalls and thick planar layers.

References

[1] T. Y. Masashi Ohyama, Hiromitsu Kozuka, *Thin Solid Films* **1997**, *306*, 78.

[2] L. Znaidi, *Mater. Sci. Eng. B* **2010**, *174*, 18.

[3] S. Fujihara, C. Sasaki, T. Kimura, *Appl. Surf. Sci.* **2001**, *180*, 341.

[4] J. H. Lee, K. H. Ko, B. O. Park, *J. Cryst. Growth* **2003**, *247*, 119.

[5] B. A. MacLeod, B. J. Tremolet de Villers, P. Schulz, P. F. Ndione, H. Kim, A. J. Giordano, K. Zhu, S. R. Marder, S. Graham, J. J. Berry, A. Kahn, D. C. Olson, *Energy Environ. Sci.* **2015**, *8*, 592.

[6] J. G. Lu, Z. Z. Ye, Y. Z. Zhang, Q. L. Liang, S. Fujita, Z. L. Wang, *Appl. Phys. Lett.* **2006**, *89*, 4.

[7] H. M. Cheng, K. F. Lin, H. C. Hsu, W. F. Hsieh, *Appl. Phys. Lett.* **2006**, *88*, 261909.

[8] Z. Ma, Z. Tang, E. Wang, M. R. Andersson, O. Ingana, F. Zhang, *J. Phys. Chem. C* **2012**, *116*, 24462.

[9] Y. Natsume, H. Sakata, *Thin Solid Films* **2000**, *372*, 30.

[10] K. Vanheusden, C. H. Seager, W. L. Warren, D. R. Tallant, J. A. Voigt, *Appl. Phys. Lett.* **1995**, *403*, 403.

[11] P. Nunes, E. Fortunato, R. Martins, *Thin Solid Films* **2001**, *383*, 277.

[12] D. S. Ginley, J. D. Perkins, *Handbook of Transparent Conductors*, **2011**.

[13] J. S. Discrete, K. Nomura, H. Ohta, A. Takagi, T. Kamiya, *Nature* **2004**, *432*, 488.

[14] I. Jeon, J. W. Ryan, T. Nakazaki, K. S. Yeo, Y. Negishi, Y. Matsuo, *J. Mater. Chem. A* **2014**, *2*, 18754.

[15] Y. Zhou, C. Fuentes-hernandez, J. Shim, J. Meyer, A. J. Giordano, H. Li, P. Winget, T. Papadopoulos, H. Cheun, J. Kim, M. Fenoll, A. Dindar, W. Haske, E. Najafabadi, T. M. Khan, H. Sojoudi, S. Barlow, S. Graham, J. Brédas, S. R. Marder, A. Kahn, B. Kippelen, *Science* **2012**, *873*, 327.

[16] Y. J. Lee, J. Wang, S. R. Cheng, J. W. P. Hsu, *ACS Appl. Mater. Interfaces* **2013**, *5*, 9128.

[17] L. Krishnan Jagadamma, M. Abdelsamie, A. El Labban, E. Aresu, G. O. Ngongang Ndjawa, D. H. Anjum, D. Cha, P. Beaujuge, A. Amassian, *J. Mater. Chem. A* **2014**, *2*, 13321.

[18] Y. Sun, J. H. Seo, C. J. Takacs, J. Seifter, A. J. Heeger, *Adv. Mater.* **2011**, *23*, 1679.

[19] M. C. Gwinner, Y. Vaynzof, K. K. Banger, P. K. H. Ho, R. H. Friend, H. Sirringhaus, *Adv. Funct. Mater.* **2010**, *20*, 3457.

[20] B. S. Ong, C. Li, Y. Li, Y. Wu, R. Loutfy, *J. Am. Chem. Soc.* **2007**, *129*, 2750.

[21] C. Jiang, R. R. Lunt, P. M. Duxbury, P. P. Zhang, *RSC Adv.* **2014**, *4*, 3604.

Chapter 4 - Sol-gel derived ZnO as Electron Transport Layers for Organic Solar cells

4.1 Introduction

In this chapter, sol-gel derived ZnO planar films are employed as electron transport layers (ETLs) in organic solar cells. The ZnO processing temperature dependence on device performance is investigated, based on the film properties evaluated in the previous chapter.

Organic solar cells are first fabricated with a prototype active layer mixture, consisting of P3HT as donor and ICBA as acceptor, configured in the inverted device architecture. Initially, the contact angle of P3HT:ICBA solution droplets on top of the ZnO films is investigated, to study the wetting properties. Then the device performance as a function of ZnO processing temperature is presented. The influence of ZnO temperatures on device parameters: open circuit voltage (V_{OC}), short circuit current density (J_{SC}), series resistance (R_s) and shunt resistance (R_{sh}) are discussed separately.

High performance active layer combination – PTB7 as e^- donor and $PC_{71}BM$ as e^- acceptor – is also employed. The difference in sensitivity of device performance on ZnO processing temperature in the two systems is investigated due to the difference of LUMO levels of ICBA and $PC_{71}BM$. The origin of V_{OC} loss in solar cells with high temperature processed ZnO is further studied using transient photovoltage and transient photocurrent techniques.

4.2 Experimental methods

4.2.1 Solar cells fabrication

Patterned indium tin oxide (ITO: PsiOteC UK Ltd; 12-16 Ω/sq) glass substrates were used for material characterisation and photovoltaic device fabrication. Substrates were cleaned by sonicating in acetone, isopropanol and distilled water for 10 minutes, respectively. Then, they were dried with compressed N_2 followed by UV-ozone treatment (UVOCS) for 10 minutes.

Inverted planar organic solar cells were made with the architecture: glass/ITO/ZnO (30-50 nm)/active layer/MoO_X (10 nm)/Ag (100 nm). ITO was the light incident electrode with the ZnO layer (precursor concentration: 0.3 M) used as the ETL; MoO_3 played the role of the HTL and silver as the back electrode.

For P3HT:ICBA as active layer, P3HT and ICBA blends were mixed in chlorobenzene solvent, at concentrations of 40 mg/ml (1:1 w/w). The solutions were subsequently heated at 70 ˚C in a glovebox (dry nitrogen atmosphere) and stirred for 16 hours. The spin coating process was done in the same glovebox with the parameters set at 500 rpm loading for 2 s and a 2000 rpm spinning for 60 s. The active layer coated substrates subsequently were annealed at 150 ˚C for 10 min in the glove box.

For PTB7:$PC_{71}BM$ active layers, PTB7 and $PC_{71}BM$ (1:1.5 w/w) were dissolved in a mixed solvent of chlorobenzene and 1,8-diiodooctane (97:3 v/v) at a concentration of 25 mg/ml. Then the solutions were subsequently heated at 60 ˚C in the glovebox (dry nitrogen atmosphere) and stirred for 16 hours. The spin coating process was done in a N_2 filled glove box with the parameters set at 1000 rpm spinning for 120 s. All the PTB7:$PC_{71}BM$ blend films were non-annealed but left in vacuum for 20 min to remove the solvent residues. All devices were completed by evaporation of 10 nm MoO_3 followed by 100 nm Ag. The device pixel area was 4.5 mm^2 as defined by the spatial overlap of the ITO and Ag electrodes.

4.3 Results and discussion

4.3.1 Wetting

The deposition method used for the active layers was spin coating. In spin coating, the wetting of the active layer solution droplet on the layer beneath is extremely important to the surface morphology of the active layer. To check the wetting properties, the contact angle of a P3HT:ICBA solution droplet with chlorobenzene as sovent was measured on the ZnO films prepared at different processing temperatures. The results, shown in Table 4.1, indicate that all samples have good wetting. Thus, the wetting will show minor influence on the device performance with ZnO processing temperature changing.

Table 4.1 Contact angles of P3HT:ICBA blend solution droplet (solvent: chlorobenzene) on top of the surface of ZnO layers.

	ZnO (as cast)	ZnO (110 °C)	ZnO (200 °C)	ZnO (300 °C)	ZnO (450 °C)
Contact angle (°)	16.3 ± 2.3	13.4 ± 2.2	13.3 ± 1.3	13.7 ± 1.5	17.3 ± 3.2

4.3.2 Device performance

The ZnO layers prepared at the temperatures shown in Table 4.1 were investigated as ETLs for organic solar cells. The device structure of the organic solar cells is shown in the inset of Figure 4.1, which is glass/ITO/ZnO (30-50 nm)/P3HT:ICBA (170 nm)/MoO_X (10 nm) /Ag (100 nm). The light was illuminated from the ITO side, and ZnO as electron

transport layer, P3HT:ICBA blend as active layer, MoO_X as hole transport layer and silver as the top electrode. The typical current density (J) - voltage (V) curves of devices with ZnO under different heat treatment conditions are shown in Figure 4.1. The open circuit voltage V_{OC}, short circuit current density J_{SC}, fill factor FF, power conversion efficiency PCE, series resistance R_s and shunt resistance R_{sh} are shown in Figure 4.2. It is clear that the processing temperature of ZnO plays a great role in device performance. From the J-V curves it can be seen that devices without ZnO or with ZnO at room temperature (25 °C) have very low V_{OC}, J_{SC}, FF and PCE. Working devices are obtained with ZnO prepared at 110 – 450 °C. For the devices with ZnO (110 – 450 °C), the V_{OC} decreases monotonously with the temperature increase. The J_{SC} increases with the ZnO temperature until a plateau in the region of 300 – 450 °C. The FF decreases monotonously as temperature increases. The PCE remains similar for ZnO (110 – 300 °C) and shows a large decrease for ZnO at 450 °C. The R_s increases as temperature increases while the R_{sh} decreases as temperature increases.

From the results we see that ZnO at 110 °C works well as an electron transport layer in organic solar cells, even with the existence of solvent and precursor residues as shown in the previous chapter. The bad result of devices without ZnO shows the necessity of electron transport layer in organic solar cells. For the devices with ZnO at 25 °C, the poor device behavior may partially come from the poor electron transport due to too much solvent and precursor residues. In addition, the surface roughness of ZnO at 25 °C is much higher than that of ZnO at 110 – 450 °C as shown in the AFM results in the previous chapter, which means ZnO (25 °C) may have worse interfacial contact with the active layer. Hence, we focus on the influence of ZnO at 110 – 450 °C on device performance.

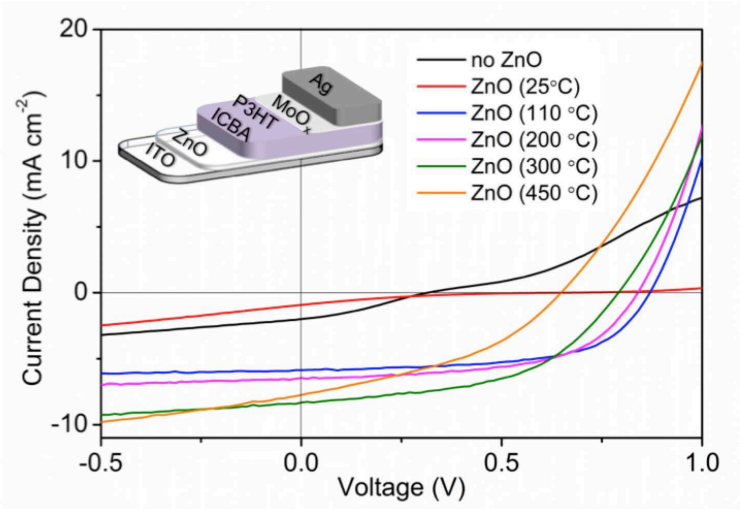


Figure 4.1 Representative J-V curves for devices prepared using ZnO electron transport layers (ETLs) deposited at the temperatures indicated. Inset shows a schematic illustration of the devices.

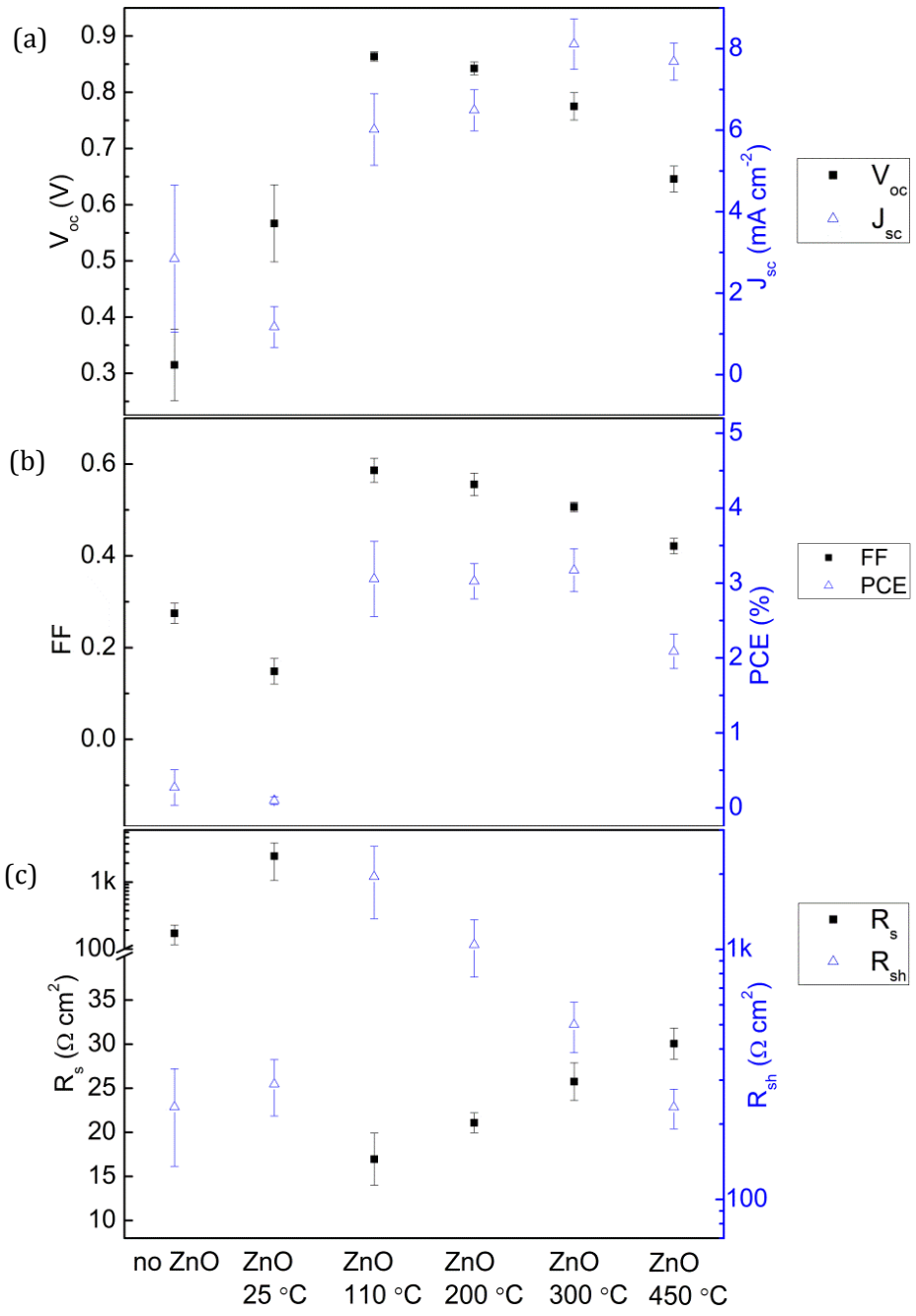


Figure 4.2 Measured device performance characteristics for P3HT:ICBA based photovoltaic devices fabricated with ZnO ETLs processed at the temperatures indicated. a) Open circuit voltage (V_{OC}) and short circuit current density (J_{SC}). b) Fill factor (FF) and power conversion efficiency (PCE). c) Series resistance (R_S) and shunt resistance (R_{Sh}).

Apart from the processing temperature, we also investigated the influence of ZnO thickness on device performance in the whole range of 110 – 450 °C, as shown in Appendix B.

4.3.3 Operating principles

To better understand the influence by ZnO processing temperature on devices, the device parameters will be discussed separately. Figure 4.3 shows the flat band energy diagram of the P3HT:ICBA devices, in which the shift of Fermi level of ZnO measured by Kelvin probe is highlighted. Comparing the ZnO (450 °C) with the ETLs prepared at 110 °C, there is a shift in the measured E_F of almost 0.5 eV away from the vacuum level. This enhances the built-in electric field across the device and improves movement of photogenerated electrons toward ZnO[1], which consequently increases the V_{OC} from 0.65 V (450 °C) to 0.86 V (110 °C).

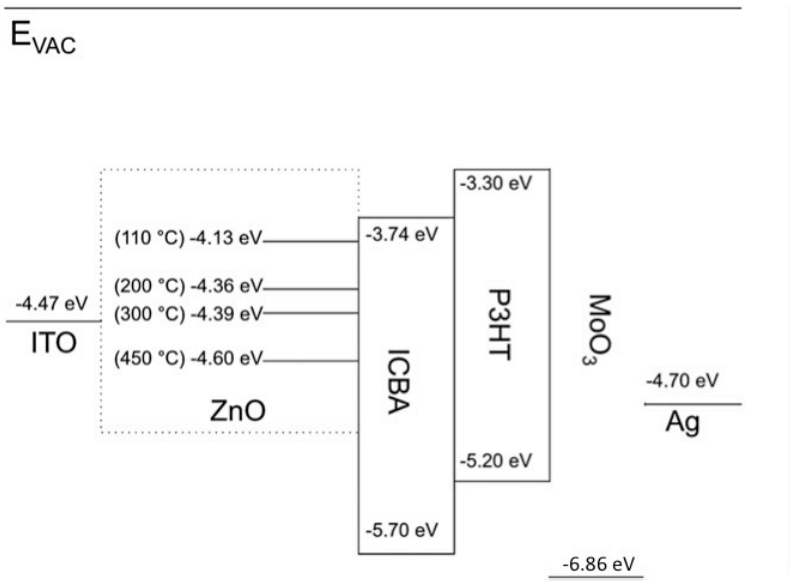


Figure 4.3 Flat band energy diagram showing the energy levels of the various materials contained in our device stacks[2–4]. The measured change in work function of the ETLs is highlighted which falls below the work function of the ITO cathode when processed at 450 °C.

For J_{SC}, it increases with the ZnO temperature from 110 to 300 °C and then slightly decreases at 450 °C. This trend corresponds to that of ZnO mobility, as shown in the previous chapter when discussing the ZnO mobility by TFT measurement. Higher mobility of electron transport layer can enhance the extraction of photogenerated electrons.

FF is influenced by both series and shunt resistances so we do not describe the FF here. Instead, we will discuss the series resistance and shunt resistance separately.

From the J–V characteristics we see that the device R_s values increase when the ZnO processing temperature is increased in the range of 110 – 450 °C. Generally, the series resistance in solar cells is caused by the bulk resistance of the active layer, functional layers and electrodes, in addition to the contact resistance of every interface and the probe resistance[5]. We exclude variation in anode and probe resistance, which remains

constant and consider rather the cathode and the contact resistance at the ITO/ZnO and ZnO/active layer interfaces. For the cathode, we consider the change in the ITO film under different heat treatment. The sheet resistance changes from 11.3 Ω/sq at room temperature to 51.7 Ω/sq at 450 °C, demonstrating cathode resistance partially contributes to the series resistance changing, as shown in Figure 4.4.

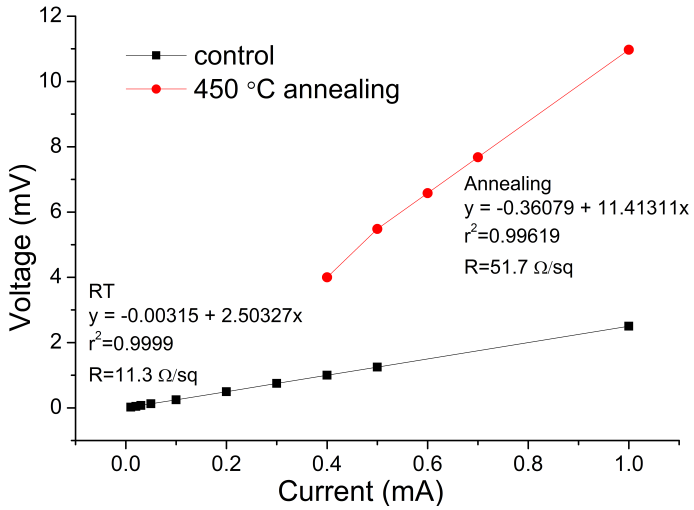


Figure 4.4 Sheet resistances of ITO substrates with and without 450°C annealing.

For the ITO/ZnO interface, Ohmic contact was confirmed by constructing metal-ZnO-metal structures (ITO/ZnO/Ca (20 nm)/Ag (85 nm)), for ZnO films processed from 25 to 450 °C, as shown in Figure 4.5. In terms of the ZnO/active layer interface, the reduced work function of low temperature ZnO causes an enhanced built-in electric field. Under the short circuit conditions, the enhanced built-in electric field contributes to the larger energy band bending of the active layer, which results in the faster movement of photogenerated electrons towards the ZnO direction[1]. This may also reduce the contact resistance.

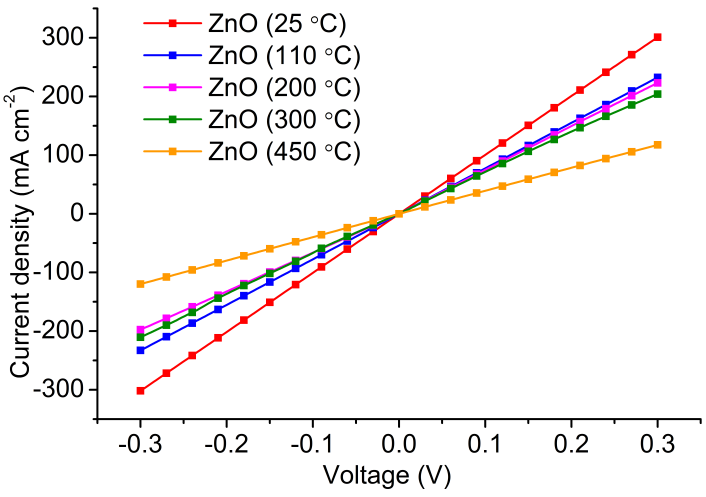


Figure 4.5 Representative current density - voltage plots of ITO/ZnO/Ca/Ag stacks.

As for the shunt resistance R_{sh}, it decreases as the ZnO processing temperature is increased in the range of 110 – 450 °C. Generally, the shunt resistance in solar cells comes from the leakage current induced by the pinhole, the edge and the traps in the device[5]. To detect the leakage current, we measured the J-V curves under dark condition, as shown in Figure 4.6. There is a systematic increase in the leakage current when processing temperature is increased and it is noteworthy that the 25 °C ETL based device shows a nonzero bias at short-circuit due to carrier accumulation at the interface associated with the high resistivity of the film. The leakage in the high temperature ZnO may also account for the reduction in V_{OC}. While active layer thickness, illumination intensity, and interfacial effects have been shown to influence R_{sh} in OPVs[6] here only the interface is varied thus we conclude that the observed differences in R_{sh} are driven by modulation at this interface.

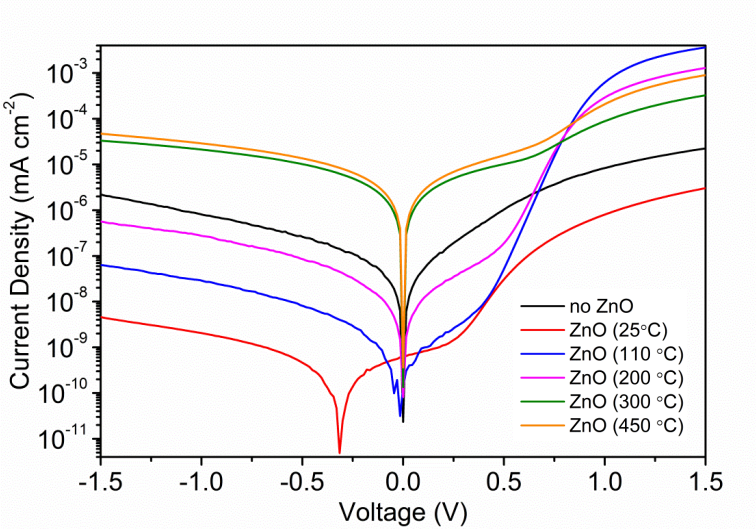


Figure 4.6 Dark J–V characteristics shown for all devices, a clear increase in leakage current is observed as the ETL processing temperature is increased (semi-log scale).

It is desirable to know what influences the leakage current at this interface. The impact of the ZnO surface morphology was investigated. For the cracks in ZnO layer, from the SEM images in the previous chapter, we find that the low temperature ZnO has more cracks, which should result in higher leakage current. However, the R_{sh} results show an opposite trend, which means the cracks have small effect. This may attribute to the relatively large difference in surface energy between ZnO and active layer, which makes it difficult for the active layer solution to completely penetrate the voids in the ZnO buffer layer[7]. For the influence of roughness of ZnO layer, Liang et al[8] showed that a rough surface could trap some voids resulting in inferior contact. While from the AFM results in the previous chapter, the surface roughness does not change too much with the temperature under a certain thickness. Thus, the ZnO surface morphology does not

play a dominant role in the R_{sh}. Thus, the R_{sh} may also contribute to the contact resistance [9] as discussed in the section discussing R_s.

4.3.4 OPV with other active layer materials

We also utilised the sol-gel derived ZnO electron transport layer for OPVs with other active layer materials, namely PTB7:$PC_{71}BM$. Representative J-V characteristics are included in Figure 4.7 for ZnO processing temperatures of 25 – 450 °C and without ZnO. Similar to the P3HT:ICBA system, at 25 °C or when ZnO is not present poor quality devices are prepared. Devices with reasonable performance characteristics are prepared over the ZnO processing temperatures 110 – 450 °C. The champion device is with 110 °C ZnO, showing 8% PCE with V_{OC} 0.74 V, J_{SC} 16.3 mA/cm^2 and FF 65%.

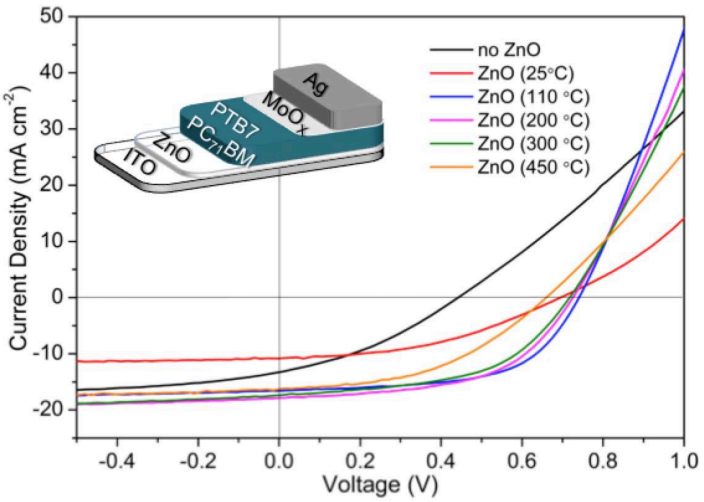


Figure 4.7 Representative J-V curves for devices prepared using ZnO electron transport layers (ETLs) deposited at the temperatures indicated. Inset shows a schematic illustration of the devices.

Statistical data for the devices are also shown in Figure 4.8. The device performances with ZnO 110 – 300 °C are similar, however an obvious drop occurs with ZnO 450 °C. About 34% PCE reduction with 450 °C ZnO compared with the other temperatures is mainly attributed to the V_{OC} loss from 0.73 V to 0.62 V and the FF loss from 57% to 42%. The dark J-V curves also illustrate ZnO at lower processing temperature has better blocking behavior at reverse bias, as shown in Figure 4.9. For P3HT:ICBA based OPVs the sensitivity to processing temperature over the 110 – 300 °C range was more profound than observed here with PTB7:$PC_{71}BM$, with significant V_{OC} and FF loses observed as temperature increases above 110 °C - attributed to pinning effects at the organic/ETL interface[10][11]. Specifically, if the work function of ZnO is smaller than the electron affinity of fullerenes, the Fermi level (E_F) of ZnO becomes pinned to the LUMO level of fullerenes. As the LUMO of $PC_{71}BM$ is lower than that of ICBA (-3.91 eV *vs.* -3.74 eV)[12], the E_F of the ETL is more likely to be pinned in the PTB7:$PC_{71}BM$ devices

compared with the P3HT:ICBA devices. This finding further supports our viewpoint that the work function shift of ZnO tuned by ZnO processing temperature is important on OPV performance.

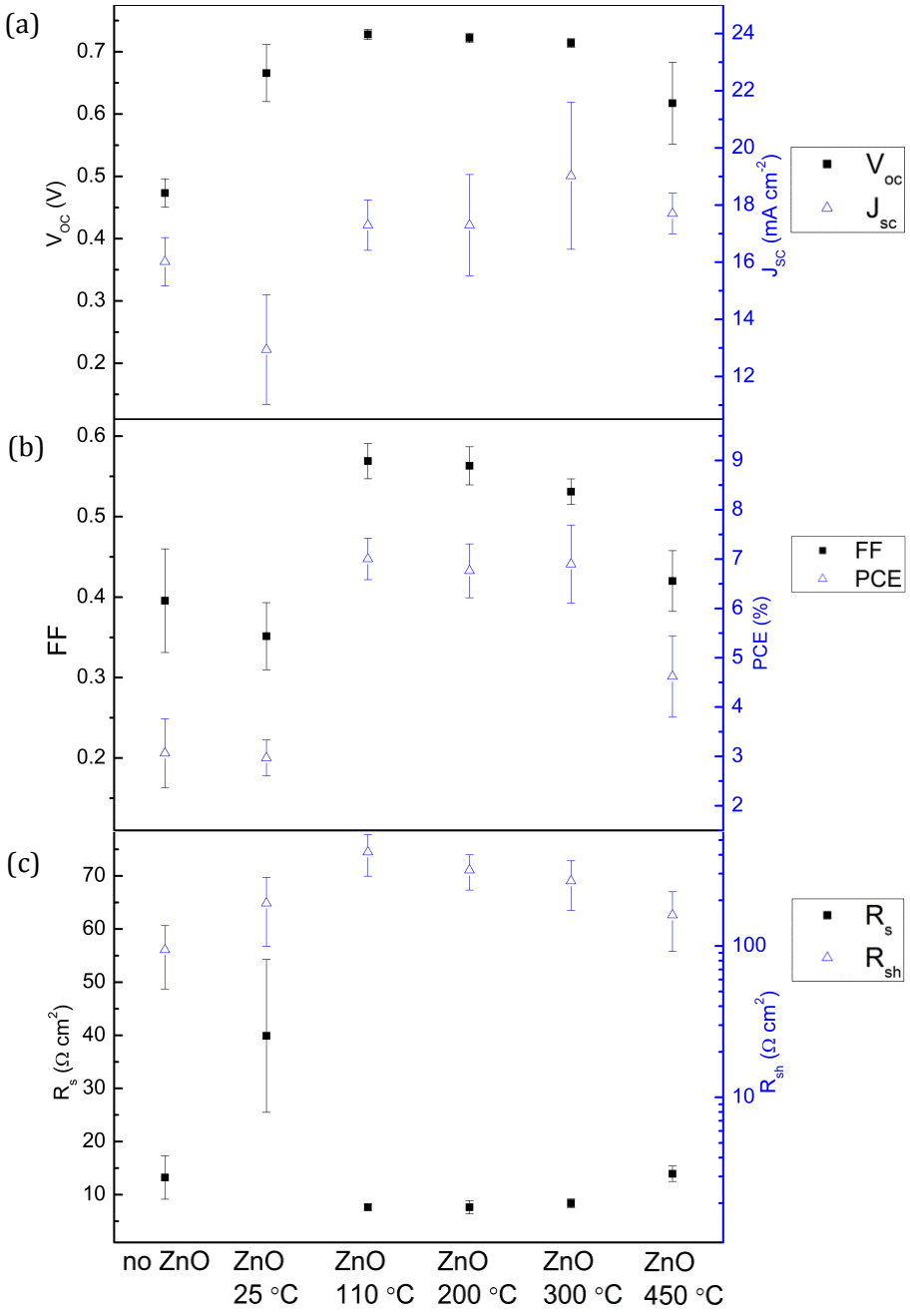


Figure 4.8 Measured device performance characteristics for PTB7:$PC_{71}BM$ based photovoltaic devices fabricated with ZnO ETLs processed at the temperatures indicated. a) Open circuit voltage (V_{OC}) and short circuit current density (J_{SC}). b) Fill factor (FF) and power conversion efficiency (PCE). c) Series resistance (R_s) and shunt resistance (R_{sh}).

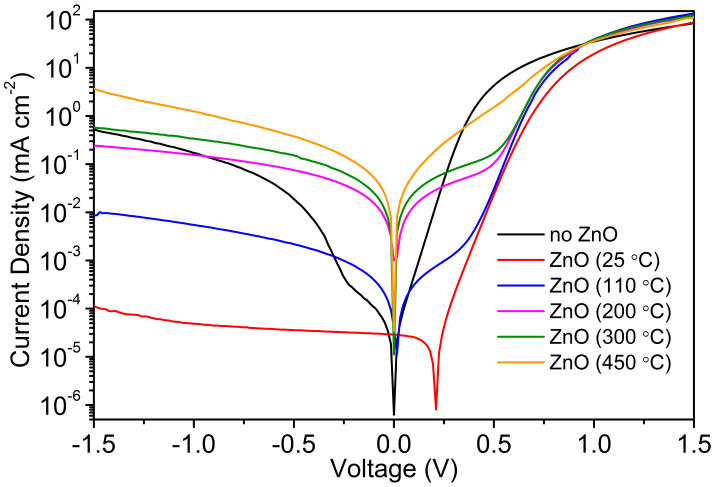


Figure 4.9 Representative dark J-V curves for devices prepared using ZnO ETLs deposited at the temperatures indicated.

In order to probe further the effect of ETL processing temperature on device performance, and particularly the V_{OC} loss at high processing temperatures, charge carrier densities and lifetime were measured using transient photocurrent (TPC) and transient photovoltage (TPV) measurements for devices employing the 110 and 450 °C processed ETL layers. The detailed description of this method refers to Ref[13].

The V_{OC} of OPV could be expressed as the sum of an energetic part and a kinetic part[13]:

$$V_{oc} = \frac{1}{e}(IP_D - EA_A) - \frac{n_{id}kT}{e}\ln\left(\frac{J_{rec}}{J_{SC}}\right) \qquad \textbf{Eqn 4.1}$$

where IP_D is the ionisation potential of the donor and EA_A is the electron affinity of the acceptor if the energetics of cathode and anode are ideal (in this case, the energetics of the contacts). The right side term is the kinetic component, where n_{id} is the ideality factor, J_{rec} is the recombination current related to carrier density and lifetime, and J_{SC} is short circuit current.

The charge carrier density (n) at V_{OC} measured through differential charging is plotted in Figure 4.10a, whilst Figure 4.10b shows the charge carrier lifetimes (τ) measured as a function of n. These data give a good reconstruction of V_{OC} dependence with light intensity for both devices using predictions based on experimental measurements of the density dependence of charge-carrier lifetime[13], confirming the validity of these data, as shown in Figure 4.11b.

The major difference between 110 and 450 °C is the large shift in V_{OC} at a given n, corresponding to 160 mV at $n = 5\times10^{16}$ cm^{-3}, Figure 4.10a. While at the same carrier density the average lifetimes of charge carriers which are able to contribute to device

voltage are very similar for both temperatures, Figure 4.10b, which indicates that the kinetic component in aforementioned V_{OC} equation shows little influence on V_{OC}[13]. These data are analogous to those we observed previously for PCDTBT:PCBM devices as a function of NiO hole collection layer work function, and assigned by correlation with numerical device modeling to the effect of surface recombination losses[13].

Our results confirm that the lower V_{OC} of device with ZnO 450 °C mainly comes from an enlarged ZnO work function. We assume this originates from the enhanced surface recombination loss. In TPV and TPC analysis, if the shunt current is not obvious, the value of ideality factor can be used to indicate the dominant recombination mechanism[13]. While we note that the shunt dark current in the 450 °C device is high (Figure 4.11a), it is not possible to analyse the dominant recombination mechanism by ideality factors. However, the significant difference of leakage currents under reverse bias of devices with 110 and 450 °C supports our assumption because the bulk active layer should be the same for two devices. The enhanced surface recombination in 450 °C devices may be associated with the hole collection by ZnO side due to the high ZnO work function.

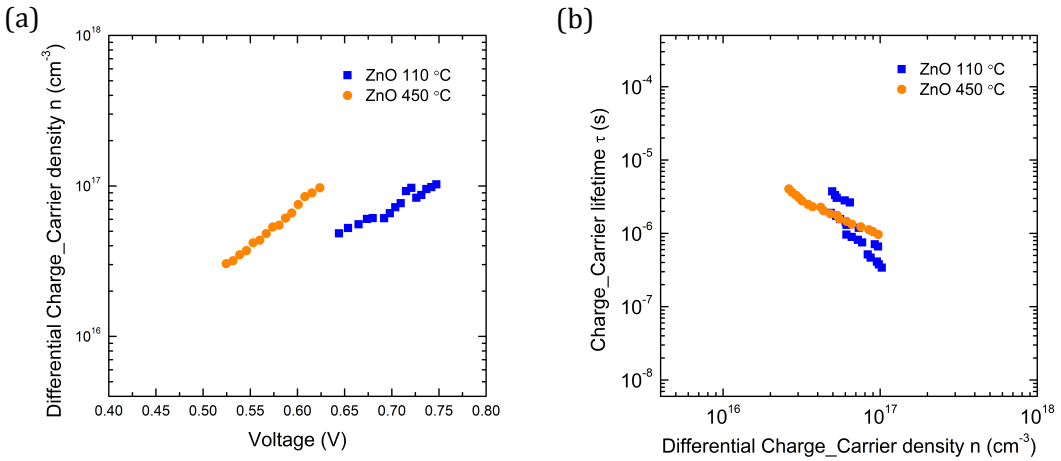


Figure 4.10 The device charge carrier density and lifetime were measured by (a) transient photocurrent (TPC) and (b) transient photovoltage (TPV) of PTB7:$PC_{71}BM$ solar cells with ZnO at 110 and 450 °C.

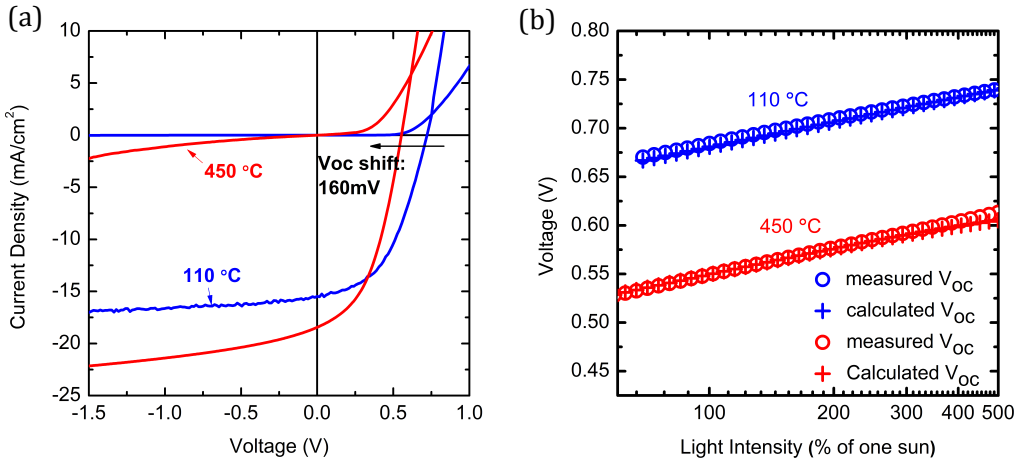


Figure 4.11 (a) Representative J-V curves of PTB7:$PC_{71}BM$ solar cells with 110 and 450 °C ZnO ETLs under dark and illumination; (b) open circuit voltage V_{OC} measured value and reconstruction from charge density *n* and charge carrier lifetime τ for 110 and 450 °C processed devices as a function of light intensities, the description of the method of V_{OC} reconstruction refers to Ref[13].

Ultimately, we wish to further explore ZnO films at 110 °C as the ETL for OPV. The previous chapter has shown that the films processed at 110 °C are nanocrystalline/amorphous mixtures. This explains why the device with ZnO (110 °C) still works well, regardless of the low electron field effect mobility of ZnO (110 °C) which is about 10^{-5} times lower than that of ZnO (300 °C)[14]. In solar cells the free electrons only pass through several tens nm of ZnO layer, rather than pass the long channel (several μm) in a TFT. In OPVs the photogenerated electron transport inside ZnO 110 °C may be hopping in crystalline domains and tunneling in the organic matrix under the applied electric field. This charge transport process may be assisted by the conduction band minimum in ZnO which is dominated by Zn 2*s* orbitals, thus the disorder of the ZnO crystalline structure has a rather weak influence on electron transport[15].

Compared with a ZnO nanocrystalline domain which likely facilitates electron transport, the organic amorphous domain is also not 'redundant'. The MEA, which is the stabiliser in sol-gel solution, remains in ZnO 110 °C and 200 °C films due to its high boiling point and the complexation with zinc cation[16]. It is considered to act as a work function modifier[14][17][18]. There may also be an advantage to preserving the organic matrix in that the densification observed in crystalline films, which may create cracks, does not occur thus explaining the low leakage currents observed. The feasibility of ZnO nanoparticle/MEA mixture has been proved as a working ETL by mixing ZnO nanoparticles with MEA as solvent[19]. In comparison to complex nanoparticle synthesis our current work illustrates a rather simple means of fabricating ZnO

nanoparticle/amorphous organic matrices and opens the possibility of controlled mixing and doping for compositional variation and further control of the electro optical properties.

4.4 Conclusions

Organic solar cells are characterised in terms of ZnO processing temperature. In both P3HT:ICBA and PTB7:$PC_{71}BM$ systems, devices without ZnO and with ZnO (25 °C) show poor performance. The ZnO processed at 110 – 450 °C provides working devices, in which lower ZnO temperature performs better.

The ZnO processing temperature exhibits significant influence on device parameters, including V_{OC}, J_{SC}, R_s and R_{sh}. In the two systems, J_{SC} shifts with ZnO temperature are similar, influenced by ZnO electron mobility. Modulations in R_s and R_{sh}, induced by changes in the ETL transport properties, are observed in parallel to significant changes in V_{OC} attributed to changes on the E_F of the ETLs. While the V_{OC}, R_s and R_{sh} shifts in the region of ZnO 110 - 300 °C is more apparent in P3HT:ICBA system than in PTB7:$PC_{71}BM$ system, which is attributed to pinning effects at the organic/ETL interface. The relationship between V_{OC} and ZnO work function is further confirmed from the TPV and TPC results. The V_{OC} loss of device with high temperature processed ZnO mainly comes from a nonideal high ZnO work function enhancing surface recombination losses.

Combined with the results shown in the previous chapter, the relationship between OPV performance and ZnO film composition is clear now. The low temperature processed film is nanocrystalline ZnO embedded in an organic amorphous matrix. As electron transport layer for OPV, ZnO nanoparticles are responsible for the carrier transport while MEA in amorphous matrix contributes to the work function modulation. With the processing temperature increasing, the organic substance is gradually removed and the nanocrystalline domains are interconnected to form larger grain size. The MEA removal and ZnO crystallisation process cause the work function shift, which has been proven to greatly influence the device open circuit voltage, series and shunt resistances. And the increased ZnO grain size results in enhanced short circuit current density.

References

[1] S. Woo, W. Hyun Kim, H. Kim, Y. Yi, H. K. Lyu, Y. Kim, *Adv. Energy Mater.* **2014**, *4*, 1.

[2] S. H. Park, A. Roy, S. Beaupré, S. Cho, N. Coates, J. S. Moon, D. Moses, M. Leclerc, K. Lee, A. J. Heeger, *Nat. Photonics* **2009**, *3*, 297.

[3] S. H. Liao, H. J. Jhuo, Y. S. Cheng, S. A. Chen, *Adv. Mater.* **2013**, *25*, 4766.

[4] M. Kröger, S. Hamwi, J. Meyer, T. Riedl, W. Kowalsky, A. Kahn, *Org. Electron.* **2009**, *10*, 932.

[5] D. Gupta, S. Mukhopadhyay, K. S. Narayan, *Sol. Energy Mater. Sol. Cells* **2010**, *94*, 1309.

[6] M. S. Kim, B. G. Kim, J. Kim, *ACS Appl. Mater. Interfaces* **2009**, *1*, 1264.

[7] X. Bulliard, S. G. Ihn, S. Yun, Y. Kim, D. Choi, J. Y. Choi, M. Kim, M. Sim, J. H. Park, W. Choi, K. Cho, *Adv. Funct. Mater.* **2010**, *20*, 4381.

[8] Z. Liang, Q. Zhang, O. Wiranwetchayan, J. Xi, Z. Yang, K. Park, C. Li, G. Cao, *Adv. Funct. Mater.* **2012**, *22*, 2194.

[9] A. Moliton, J. M. Nunzi, *Polym. Int.* **2006**, *55*, 583.

[10] M. T. Greiner, M. G. Helander, W. M. Tang, Z. Bin Wang, J. Qiu, Z. H. Lu, *Nat. Mater.* **2012**, *11*, 76.

[11] M. T. Greiner, Z. H. Lu, *NPG Asia Mater.* **2013**, *5*, e55.

[12] P. Cheng, Y. Li, X. Zhan, *Energy Environ. Sci.* **2014**, *7*, 2005.

[13] S. Wheeler, F. Deledalle, N. Tokmoldin, T. Kirchartz, J. Nelson, J. R. Durrant, *Phys. Rev. Appl.* **2015**, *4*, 29.

[14] J. Zhang, J. C. D. Faria, M. Morbidoni, Y. Porte, C. H. Burgess, K. Harrabi, M. A. McLachlan, *Adv. Electron. Mater.* **2016**, *2*, 1600008.

[15] D. S. Ginley, J. D. Perkins, *Handbook of Transparent Conductors*, **2011**.

[16] T. Y. Masashi Ohyama, Hiromitsu Kozuka, *Thin Solid Films* **1997**, *306*, 78.

[17] Y. Zhou, C. Fuentes-hernandez, J. Shim, J. Meyer, A. J. Giordano, H. Li, P. Winget, T. Papadopoulos, H. Cheun, J. Kim, M. Fenoll, A. Dindar, W. Haske, E. Najafabadi, T. M. Khan, H. Sojoudi, S. Barlow, S. Graham, J. Brédas, S. R. Marder, A. Kahn, B. Kippelen, *Science* **2012**, *873*, 327.

[18] Y. J. Lee, J. Wang, S. R. Cheng, J. W. P. Hsu, *ACS Appl. Mater. Interfaces* **2013**, *5*, 9128.

[19] I. Jeon, J. W. Ryan, T. Nakazaki, K. S. Yeo, Y. Negishi, Y. Matsuo, *J. Mater. Chem. A* **2014**, *2*, 18754.

Chapter 5 - Sol-gel derived ZnO as Electron Transport Layers for Perovskite Solar Cells

5.1 Introduction

In this chapter, sol-gel derived ZnO films are employed as electron transport layers (ETLs) in perovskite solar cells. First, the influence of ZnO layers on perovskite films are investigated by directly depositing perovskite on ZnO films. The wetting properties are studied by measuring the contact angle of perovskite solution droplets on ZnO films. Then the perovskite thermal stability on ZnO films is investigated by XRD. Both ZnO processing temperature and perovskite annealing time, and their impact on perovskite stability and decomposition are studied. The surface morphology of perovskite films on ZnO films is also assessed using SEM.

Interfacial modification is then conducted by inserting a PCBM interlayer between ZnO and perovskite layers, with the aim to improve the perovskite thermal stability. Perovskite solar cells are then fabricated with ZnO layers, PCBM layers and ZnO/PCBM bilayers as ETLs.

Subsequently, the influences of ETL film properties on device performance, including optical transmittance, surface morphology and surface potentials, are discussed. Finally, the carrier transfer on the interface between perovskite and ETLs is evaluated using transient absorption techniques.

5.2 Experimental methods

5.2.1 Perovskite films

The precursor of $CH_3NH_3PbI_3$ was prepared by dissolving 1.25 M lead iodide and methylammonium iodide (MAI) together in mixed solvent of gamma-butyrolactone (GBL) and dimethyl sulfoxide (DMSO) (7:3 by volume). The solutions were stirred at 60 °C for 2 hours and were filtered through a 0.45 μm PTFE filter before use. The perovskite photoactive layers were formed *via* a "toluene-dripping" method reported by Jeon et al[1] and described in subsection 1.3.1. The precursor solution was first spun at 500 rpm for 5 s and then 2000 rpm for 20 s. 50 ml of toluene was instantly dripped onto the film right at the end of second stage of spinning, and followed by spinning at 4000 rpm for 20 s. After spin coating, the films were heated on a 100 °C hotplate to

crystallise the perovskite. Both the spin coating and annealing process were carried out in a N_2 filled glovebox.

5.2.2 Perovskite solar cells

ITO substrates and the zinc precursor solutions were prepared using the processes outlined in Chapter 4. Each ZnO film was spin casted for one time with a 0.45 M solution. The spin coating parameters included a 500 rpm loading for 12 s and a 3000 rpm spinning for 30 s with an acceleration rate of 500 rpm/s.

PCBM layers were deposited as interfacial modifiers. PCBM was dissolved in chlorobenzene and heated at 60 ˚C with stirring overnight in a N_2 filled glovebox. Spin coating was carried out in a glovebox at 1000 rpm for 30 s and then annealed at 70 °C for 3 min.

The solution of hole transport layers (HTLs) was prepared by dissolving 82 mg 2,2',7,7'-tetrakis[*N,N*-di(4-methoxyphenyl)amino]-9,9'-spirobifluorene (spiro-OMeTAD) in 1 ml chlorobenzene. 15.6 µl of bis(trifluoromethane)sulfonimide lithium salt (Li-TFSI) solution (450 mg in 1 ml of acetonitrile) and 24.4 µl of 4-tert-butylpyridine were added to the pristine solution as additives. The solution was stirred for 30 min and was filtered through a 0.45 µm PTFE filter before use. HTLs were formed by spinning the solution onto perovskite films at 3500 rpm for 45 s. The substrates were kept at dry ambient conditions for 24 h to allow the oxidation of Spiro-OMeTAD.

MoO_X and Ag evaporations are identical to those in Chapter 4.

5.3 Results and discussion

5.3.1 ZnO/perovskite interface

5.3.1.1 Wetting

To assess the wetting properties, the contact angles of $CH_3NH_3PbI_3$ solution droplets with GBL and DMSO as co-solvent (7:3 by volume) were measured on the ZnO films prepared at different processing temperatures. The results indicate that the wetting becomes better with the increase of ZnO processing temperature, as shown in Table 5.1.

The contact angle can be tuned by the surface roughness and the chemical properties of the underlying solid films. Our ZnO films processed by different temperatures have similar surface roughness as shown in Chapter 3. So the contact angle difference may be attributed to the surface hydroxyl groups and residual acetate ligands on the ZnO surface.

Table 5.1 Contact angles of $CH_3NH_3PbI_3$ precursor droplet (solvents: GBL:DMSO) on top of ZnO films.

	ZnO (as cast)	ZnO (110 °C)	ZnO (200 °C)	ZnO (300 °C)	ZnO (450 °C)
Contact angle (°)	41.5 ± 1.9	43.0 ± 1.9	33.2 ± 2.9	19.0 ± 2.8	11.6 ± 4.3

5.3.1.2 Structural characterisation

To investigate the influence of underlying ZnO substrates on the $CH_3NH_3PbI_3$ thermal stability, we annealed glass/ITO/ZnO/$CH_3NH_3PbI_3$ stacks at 100 °C for 60 s in a N_2 filled glovebox and subsequently measured them using XRD, Figure 5.1a. The (001) peak of PbI_2 is at 12.8 °2θ and the (110) peak of $CH_3NH_3PbI_3$ is at 14.2 °2θ[2][3]. From the normalised XRD results, the portion of PbI_2:$CH_3NH_3PbI_3$ relative peak intensity increases when the ZnO processing temperature decreases from 450 °C to 110 °C, showing higher thermal instability of the perovskite film. To further confirm this, the $CH_3NH_3PbI_3$ annealing time was extended to 10 min, Figure 5.1b. The results show that the perovskite films with ZnO processed at 110 °C and 200 °C have totally decomposed while the films with ZnO (300 °C) partially decomposed and the films with ZnO (450 °C) hardly decomposed. Thus, the thermal stability of $CH_3NH_3PbI_3$ films deposited on sol-gel derived ZnO films increases as the ZnO processing temperature increases.

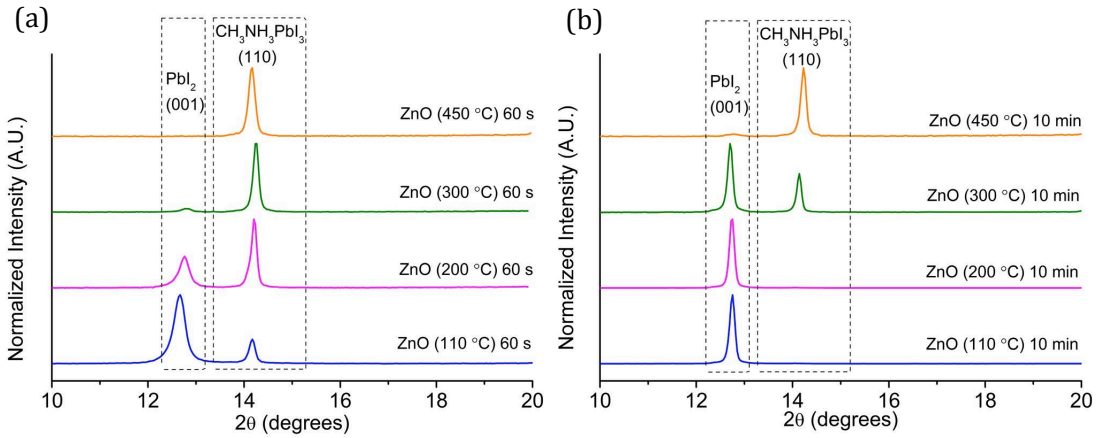


Figure 5.1 XRD patterns of glass/ITO/ZnO/$CH_3NH_3PbI_3$ stacks annealed at 100 °C in a N_2 filled glovebox for (a) 60 s; (b) 10 min.

We also investigated the influence of $CH_3NH_3PbI_3$ annealing time on the $CH_3NH_3PbI_3$ thermal stability. For the glass/ITO/ZnO/$CH_3NH_3PbI_3$ stacks with ZnO (200 °C), from the normalised XRD results, Figure 5.2a, the $CH_3NH_3PbI_3$ starts to decompose and eventually is completely decomposed as the annealing time increases. From the original XRD data, Figure 5.2b, it is found that the (110) peak intensity of $CH_3NH_3PbI_3$ increases as the annealing time increases from 5 s to 60 s, which may indicate the further crystallisation process and the decomposition process occur simultaneously. For the stacks with ZnO (450 °C), Figure 5.2c, it is also found that the $CH_3NH_3PbI_3$ (110) peak

intensity increases as the annealing time increases from 5 s to 60 s, but without perovskite degradation identified from the PbI_2 (001) diffraction peak.

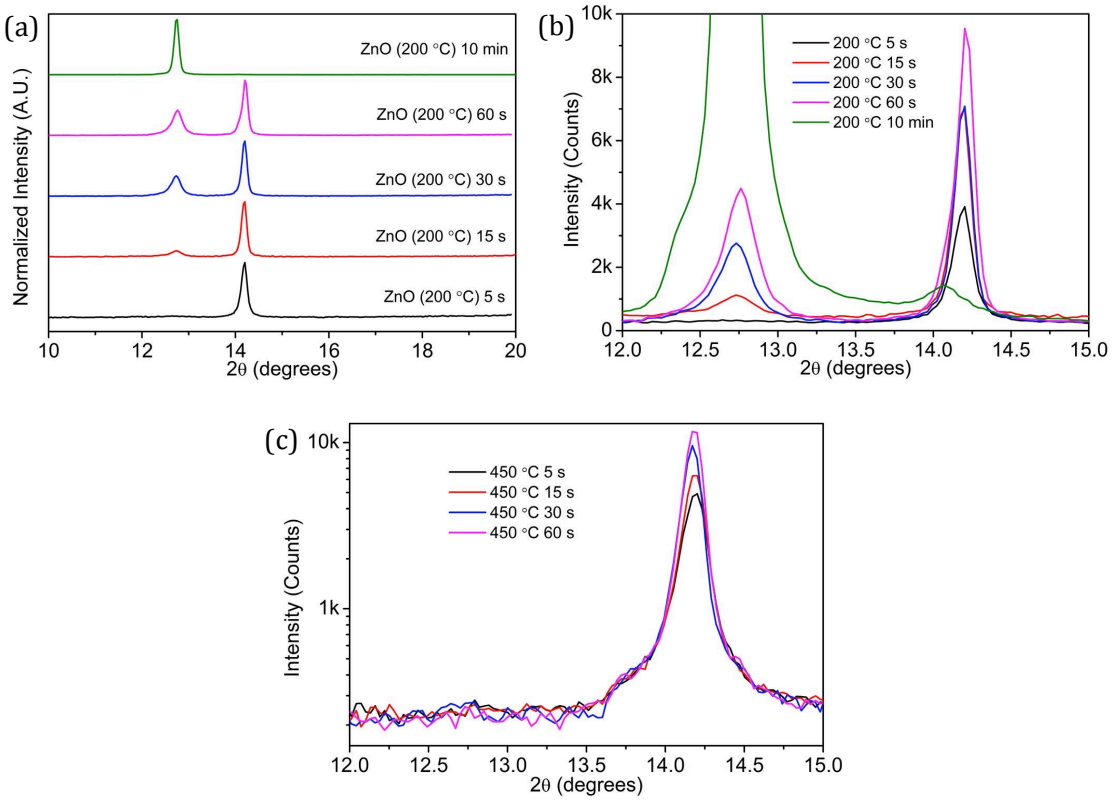


Figure 5.2 (a) Normalised and (b) original XRD patterns of glass/ITO/ZnO (200 °C)/$CH_3NH_3PbI_3$ stacks annealed at 100 °C; (c) original XRD patterns of glass/ITO/ZnO (450 °C)/ $CH_3NH_3PbI_3$ stacks annealed at 100 °C.

When decreasing the annealing time, the XRD pattern of $CH_3NH_3PbI_3$ on ZnO (110 °C) confirms that the degradation of the material begins even before the complete transformation of MAI-PbI_2-DMSO[1][4], as shown in Figure 5.3.

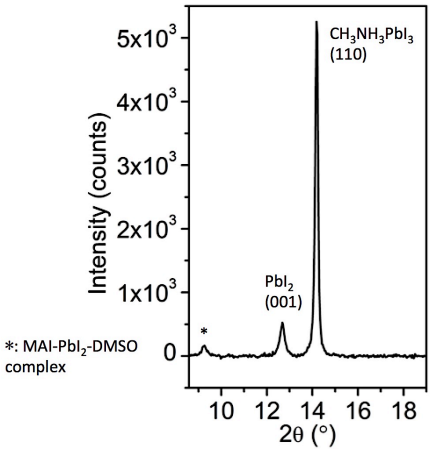


Figure 5.3 XRD pattern of $CH_3NH_3PbI_3$ on ZnO (110 °C), by controlling the perovskite annealing time we confirm the co-existence of diffraction peaks of MAI-PbI_2-DMSO and PbI_2 (001), indicating that the perovskite degradation has begun before the complete transformation of MAI-PbI_2-DMSO.

5.3.1.3 Surface morphology

The surface morphology of $CH_3NH_3PbI_3$ films on top of ZnO films was investigated using SEM, as shown in Figure 5.4. Although the contact angle data show a large difference between different ZnO films which may influence the surface coverage of $CH_3NH_3PbI_3$ films, it can be seen that the perovskite films annealed for 60 s with different ZnO films are all compact with very few voids.

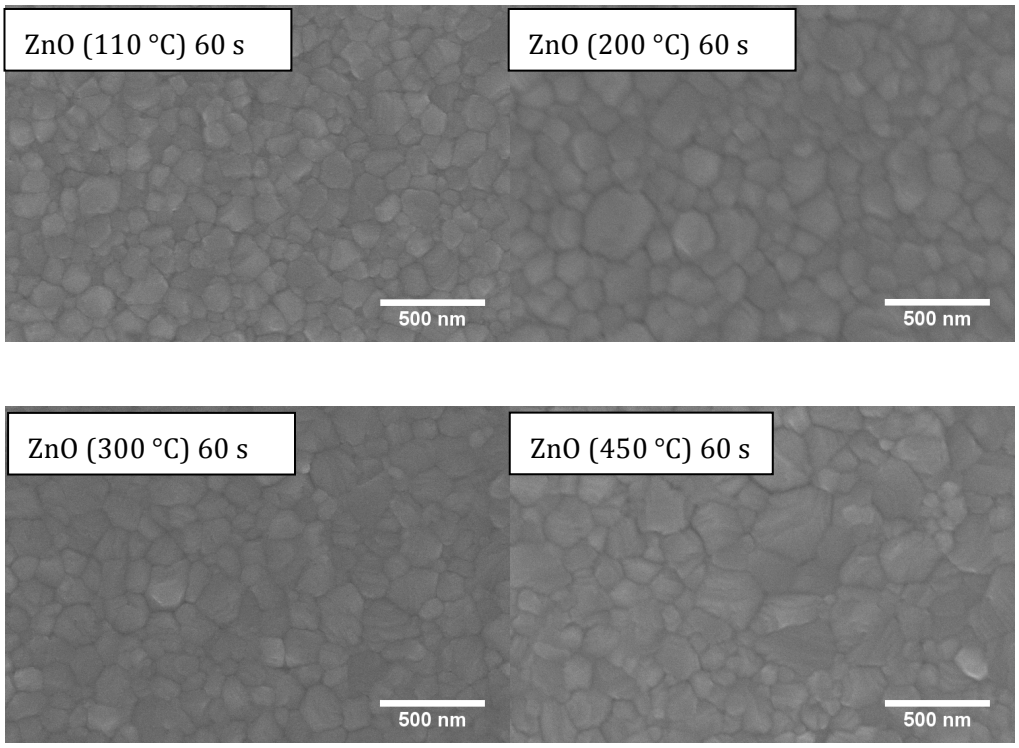


Figure 5.4 SEM images of $CH_3NH_3PbI_3$ on top of ZnO films, annealed at 100 °C for 60 s.

We also investigated the influence of $CH_3NH_3PbI_3$ annealing time on the $CH_3NH_3PbI_3$ surface morphology on top of low temperature processed ZnO substrates, Figure 5.5. As the annealing time increases, the grain size becomes larger. The films annealed for 5 – 60 s all present compact surfaces. However, the film annealed for 10 min shows many voids, which is ascribed to the presence of PbI_2 due to the decomposition process.

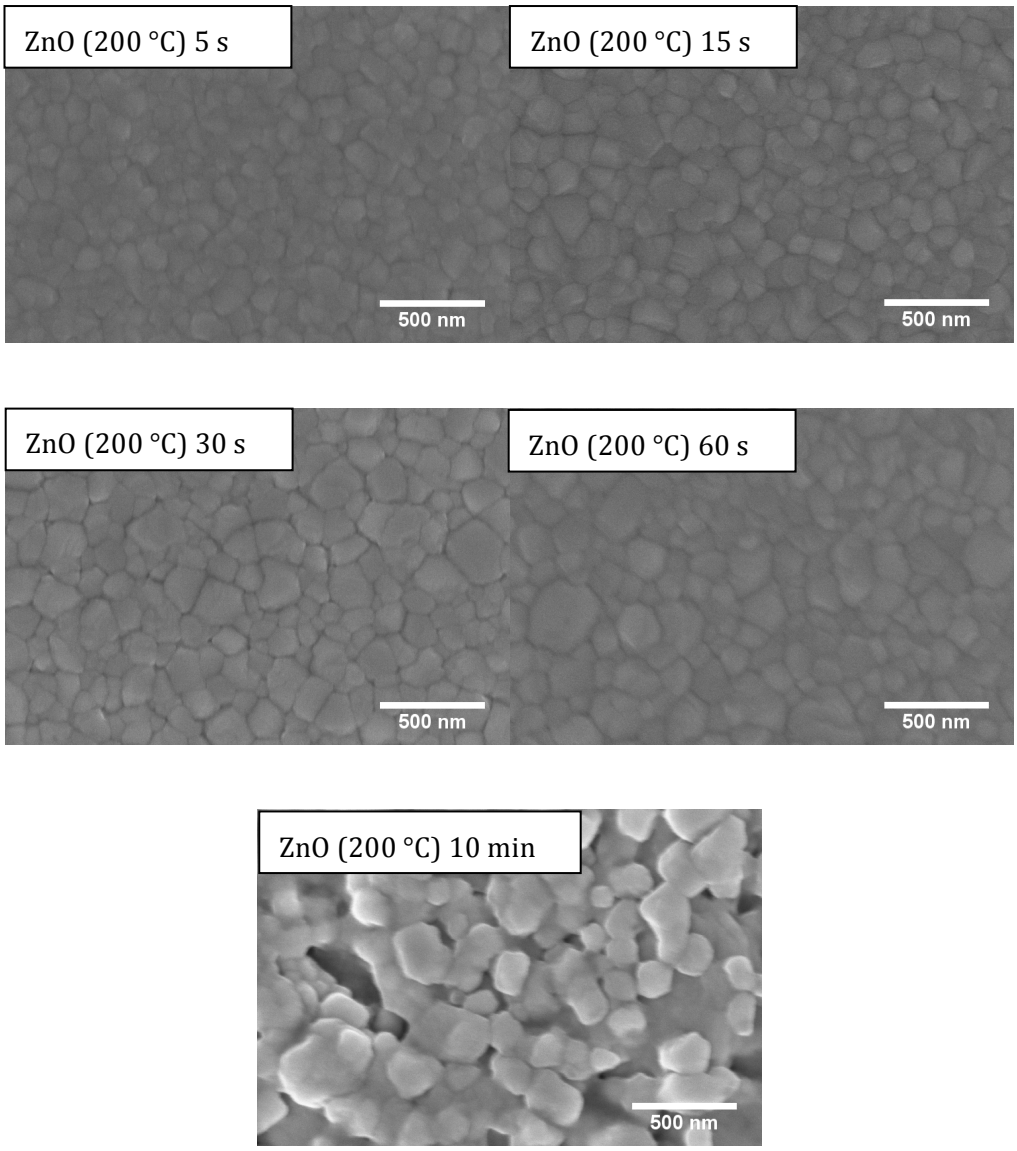


Figure 5.5 SEM images of $CH_3NH_3PbI_3$ on top of ZnO (200 °C) films, annealed at 100 °C.

5.3.2 Interfacial modification

Due to the poor thermal stability of $CH_3NH_3PbI_3$ films when directly deposited on low temperature processed ZnO, interfacial modification was attempted for the purpose of low temperature processed cathode for perovskite solar cells. The modification material we chose is PCBM that has been proved as a good passivation layer in perovskite solar cells[5][6–9].

5.3.2.1 Enhanced perovskite thermal stability

After annealing at 100 °C in a N_2 filled glovebox for 20 min, a small peak of PbI_2 appears for the $CH_3NH_3PbI_3$ on ZnO (450 °C) but does not appear for the $CH_3NH_3PbI_3$ on ZnO (110 °C)/PCBM, Figure 5.6. This indicates that even high temperature processed ZnO[10]

does not result in highly stable perovskite films. It may come from the proton-transfer reaction at the ZnO/$CH_3NH_3PbI_3$ interface due to the basic nature of the ZnO surface[11]. However, the insertion of PCBM dramatically increases the thermal stability of perovskite, which uncovers the possibility of low temperature processed sol-gel ZnO in perovskite solar cells.

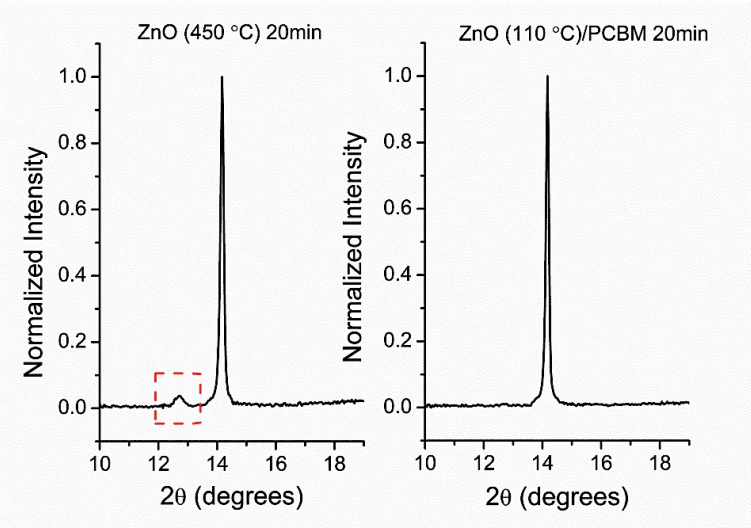


Figure 5.6 XRD patterns of glass/ITO/ZnO (450 °C)/$CH_3NH_3PbI_3$ (left) and glass/ITO/ZnO (110 °C)/ PCBM/ $CH_3NH_3PbI_3$ (right) stacks annealed at 100 °C in a N_2 filled glovebox for 20 min.

5.3.2.2 Perovskite solar cell performance

We prepared perovskite solar cells with ZnO (110 °C) and ZnO (110 °C)/PCBM as ETLs, with the purpose of obtaining a low temperature processed ETL. The conventional device architecture had a typical structure (layer thicknesses in parenthesis) of glass / ITO (140 nm) / ETL / $CH_3NH_3PbI_3$ (300 nm) / spiro-OMeTAD (100 nm) / MoO_X (10 nm) / Ag (100 nm), a schematic illustration of which is shown in Figure 5.7b. The ETL, perovskite and spiro-OMeTAD layers were deposited using solution processing and the MoO_X/Ag thermally evaporated. Representative J-V characteristics are included in Figure 5.7. It can be seen that device performance with ZnO (110 °C)/PCBM is much better than that with ZnO (110 °C). Poor device performance with ZnO (110 °C) comes from the perovskite degradation due to its thermal instability on ZnO (110 °C). In addition, device with ZnO (110 °C)/PCBM showed negligible J-V hysteresis, as shown in Figure 5.7b. The champion device with negligible J-V hysteresis is with ZnO (110 °C) (30 nm)/PCBM (30 nm) bilayer as ETL, showing 12.3% PCE with V_{OC} 1.1 V, J_{SC} 19.1 mA/cm^2 and FF 58.8 %. This proves that PCBM can eliminate J-V hysteresis in conventional perovskite device structure without the need for PCBM to infiltrate into perovskite grain boundary, a process commonly seen in inverted device structure[12].

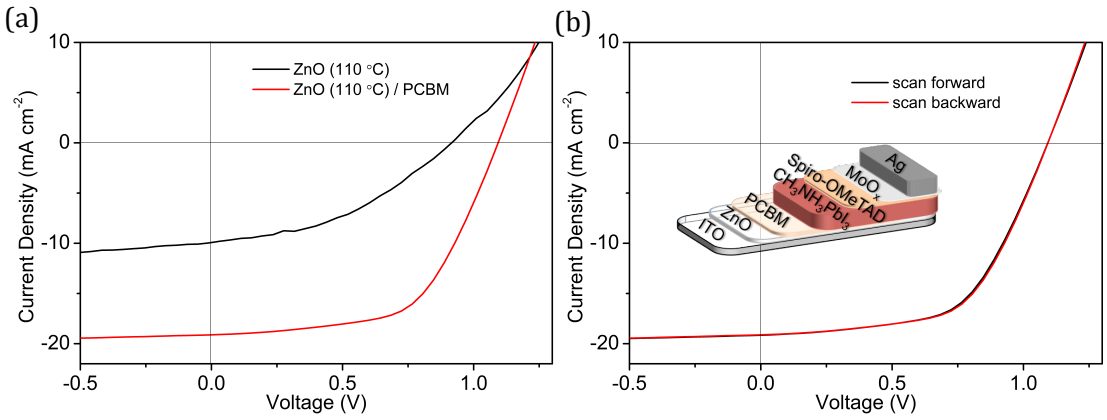


Figure 5.7 (a) Representative J-V curves for perovskite devices prepared using ZnO (110 °C) and ZnO (110 °C)/PCBM as ETLs; (b) J-V curves for perovskite devices using ZnO (110 °C)/PCBM bilayer as ETLs measured by forward and reverse scans, with 0.2 V/s scan rate.

As ZnO (110 °C)/PCBM works well as ETL, unlike ZnO (110 °C) alone, we investigated whether PCBM on its own can work as ETL in conventional device structure. Representative J-V curves are shown for both scan directions, with different PCBM thicknesses, as shown in Figure 5.8. It is apparent that when PCBM is not present a large J-V hysteresis appears. With 30 nm PCBM, the hysteresis is reduced compared to that without PCBM. With 35 nm PCBM, the hysteresis is further reduces but an s-shaped curve emerges, due to increased series resistance that can be seen at J=0. With 50 and 100 nm PCBM, the hysteresis gradually disappears but s-shaped curve becomes more obvious. The high sensitivity of device series resistance to the PCBM film thickness may partially come from the bulk resistance of PCBM films, caused by low electron mobility[13]. Thus, the co-existence of J-V hysteresis and s-shaped curve for device with 35 nm PCBM indicates that PCBM on its own is not suitable as ETL in perovskite cells with conventional device structure.

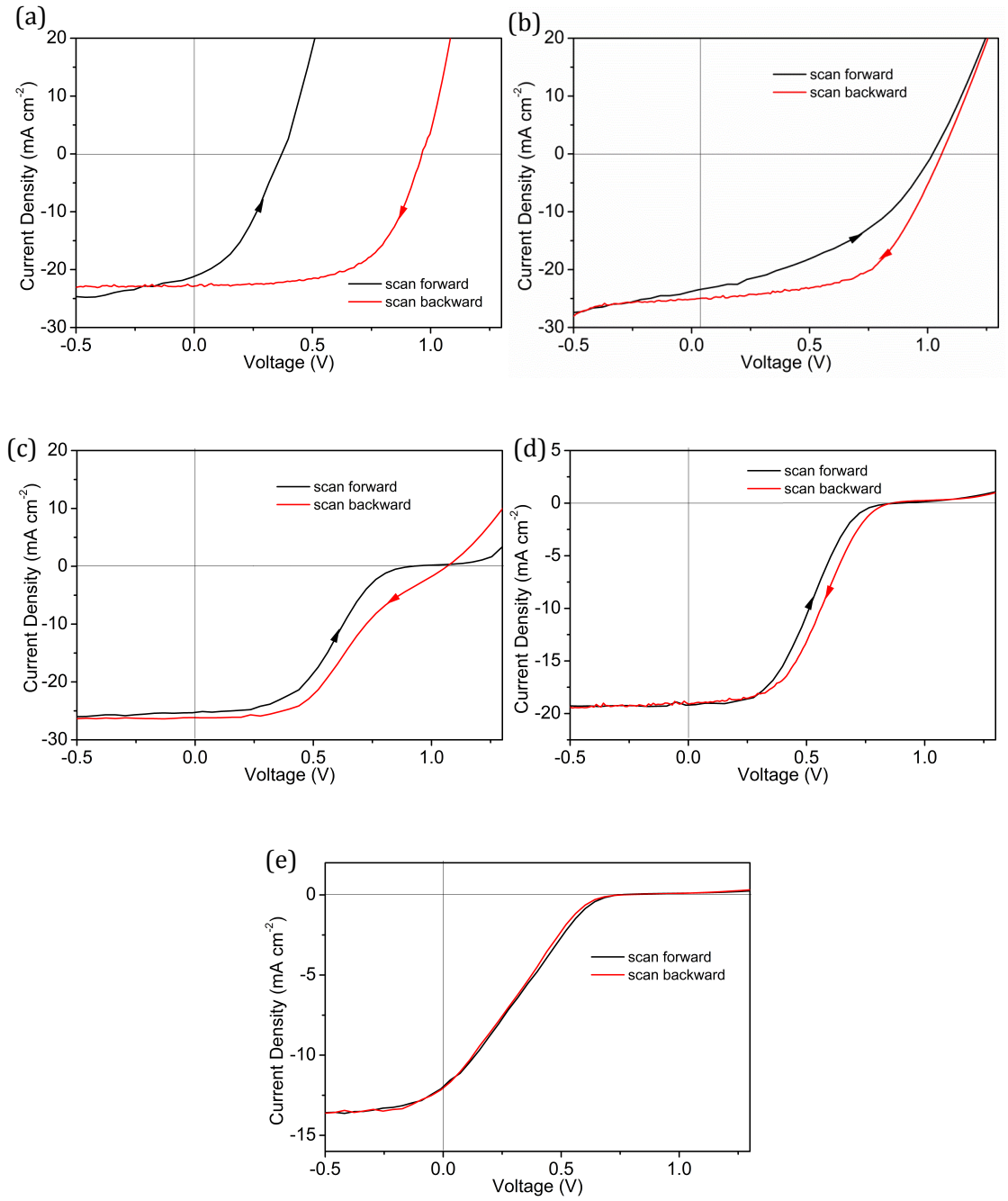


Figure 5.8 Representative J-V curves of illuminated devices with PCBM-only as ETLs, the thickness of PCBM: (a) 0 nm; (b) 30 nm; (c) 35 nm; (d) 50 nm; (e) 100 nm.

5.3.2.3 ETL characterisation

To understand why the use of PCBM yield working devices only when combined with ZnO, we carried out a range of complementary measurements. Good optical transmission (70-85%) of ZnO (110 °C)/PCBM bilayer and PCBM layer is both observed in the visible region, although for the former is slightly lower, as shown in Figure 5.9.

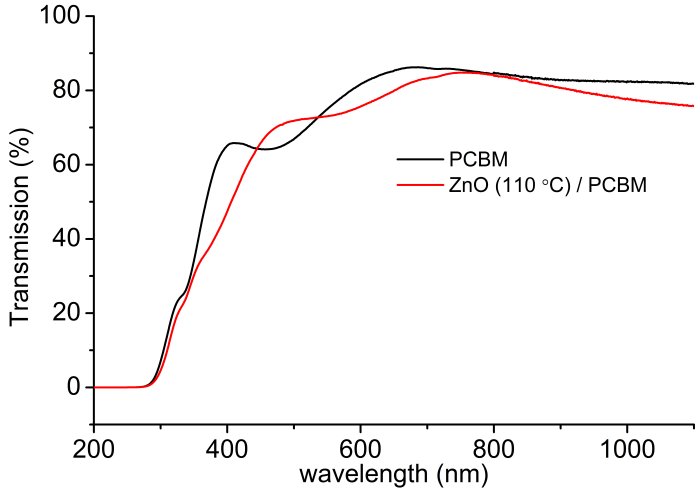


Figure 5.9 UV-visible transmission spectra of glass/ITO/PCBM and glass/ITO/ZnO (110 °C)/PCBM stacks.

The crystallinity of $CH_3NH_3PbI_3$ on top of PCBM-only and ZnO (110 °C)/PCBM is similar from the XRD results and no PbI_2 or precursor peak is observed for either of them, suggesting that pure $CH_3NH_3PbI_3$ films are formed on both ETLs, as shown in Figure 5.10.

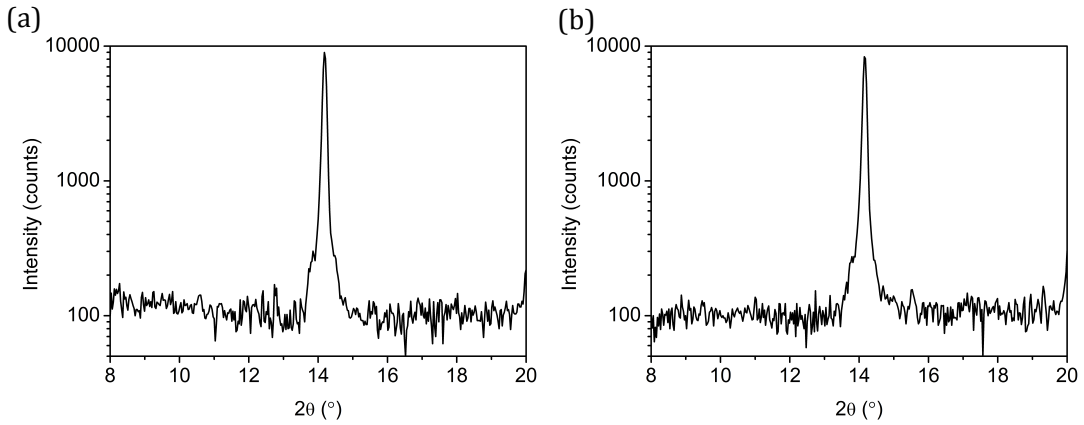


Figure 5.10 XRD patterns of (a) ITO/PCBM/$CH_3NH_3PbI_3$ and (b) ITO/ZnO(110 °C)/PCBM/ $CH_3NH_3PbI_3$, both showing pure $CH_3NH_3PbI_3$ phases without precursor or PbI_2 peaks.

AFM imaging of PCBM and ZnO (110 °C)/PCBM on ITO substrates are shown in Figure 5.11, indicating both smooth and compact surface morphologies, with RMS roughness of 0.24 nm and 0.19 nm, respectively.

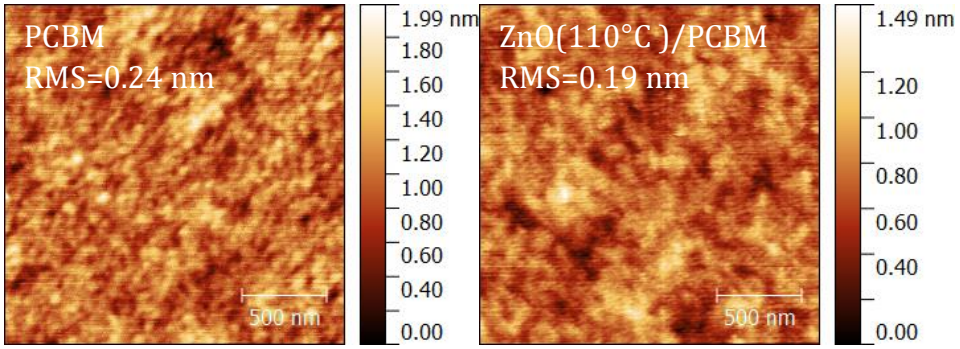


Figure 5.11 Representative AFM images of PCBM-only and ZnO (110 °C)/PCBM films on ITO substrates.

This is further confirmed from the SEM results, as shown in Figure 5.12. The smooth surface of ZnO (110 °C)/PCBM bilayer hints at the fact that layer by layer contact between PCBM and perovskite layers is sufficient for PCBM to passivate the perovskite and to eliminate the J-V hysteresis therefore there is no need for PCBM infiltration into perovskite grain boundary. The SEM images of $CH_3NH_3PbI_3$ films on top of PCBM and ZnO (110 °C)/ PCBM are also shown in Figure 5.12. We can observe a dense-grained uniform surface morphology with grain sizes in the range 100-400 nm.

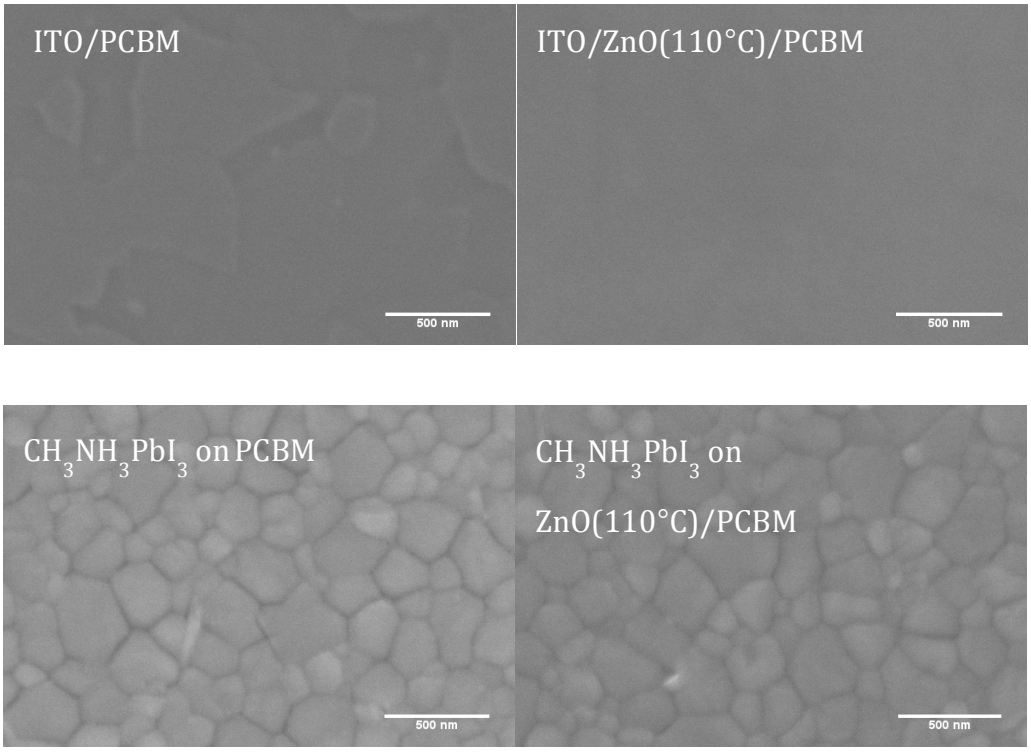


Figure 5.12 SEM images of (a) PCBM, (b) ZnO (110 °C)/PCBM, (c) $CH_3NH_3PbI_3$ on PCBM and (d) $CH_3NH_3PbI_3$ on ZnO (110 °C)/PCBM films.

The XRD patterns confirm that the perovskite films on both PCBM-only and ZnO (110 °C)/PCBM are pure phase, without a detectable PbI_2 signal. The perovskite films on both ETLs show similar grain size, Table 5.2. Grain boundaries have been shown to dominate ion migration in polycrystalline perovskite films and the perovskite single-crystal devices display negligible J-V hysteresis[14]. In our cells, where similar grain size, i.e. grain boundary concentrations are observed, this is not the origin of difference in J-V hysteresis with PCBM-only and ZnO (110 °C)/PCBM ETLs.

Table 5.2 The grain size measured by SEM images for $CH_3NH_3PbI_3$ films on top of PCBM layer and ZnO (110 °C)/PCBM bilayers.

	$CH_3NH_3PbI_3$ on PCBM	$CH_3NH_3PbI_3$ on ZnO (100 ˚C)/PCBM
Average grain size (nm)	194.2	225.5
Standard deviation (nm)	58.8	75.7

The Fermi levels (E_F) of our ETLs and ITO substrate were calculated from the contact potential difference measured by Kelvin probe in ambient air, Table 5.3. The reference used was freshly cleaved highly oriented pyrolitic graphite (HOPG, work function = 4.47 eV). The E_F of PCBM (-4.81 eV) is deeper than that of ITO substrates (-4.47 eV), which may cause a charge extraction barrier towards the ITO cathode. One origin of the J-V hysteresis in perovskite solar cells is the charge accumulation at the interfacial contact due to the inefficient charge transfer[15]. Hence, the hysteresis in the working device with PCBM as its own may come from the electron extraction barrier between ITO and PCBM layers. However, the work function is significantly reduced by inserting a ZnO (110 °C) layer between ITO and PCBM, from -4.81 to -4.44 eV. The low work function of the sol-gel derived ZnO (110 °C) films (-4.34 eV) is ascribed to the interfacial dipole formed between the electron accepting ZnO and the electron donating amine group due to the MEA residues[10]. The schematic energy level of each layer in devices is shown in Figure 5.13[16][17], with measured ITO and ETL work functions. Lowered work function by the insertion of ZnO (110 °C) enhances the energy level alignment, which increases the electron extraction speed and subsequently reduce the J-V hysteresis[16].

Table 5.3 Work functions of ETLs on ITO substrates, measured by Kelvin Probe

	ITO	PCBM	ZnO (110 °C)	ZnO (110 °C)/PCBM
Work Function (eV)	4.47 ± 0.01	4.81 ± 0.01	4.34 ± 0.01	4.44 ± 0.01

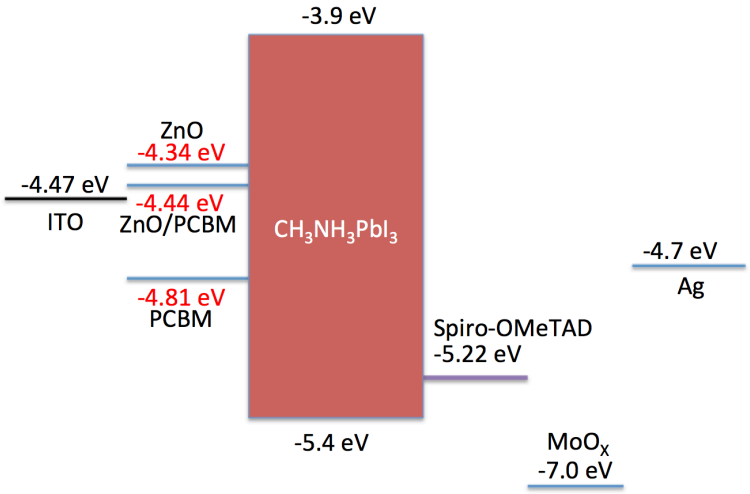


Figure 5.13 Flat band energy diagram showing the energy levels of the various materials contained in our device stacks. The measured change in work function of the ETLs is highlighted.

Figure 5.14a shows µs-transient absorption (TA) kinetics of PCBM/$CH_3NH_3PbI_3$ with and without ZnO excited selectively at $CH_3NH_3PbI_3$ region (500 nm) and probed at the bleaching region of $CH_3NH_3PbI_3$ (750 nm) (Figure 5.14b)[18]. This bleaching signal which has a power law decay is assigned to the carrier transfer from $CH_3NH_3PbI_3$ to PCBM layer[18]. When a layer of ZnO is added next to the PCBM layer, the signal of the carrier diminishes within our instrument respond time (faster than 1 µs) suggesting the carriers are more efficiently extracted with the combination of ZnO/PCBM bilayer than that PCBM-only layer.

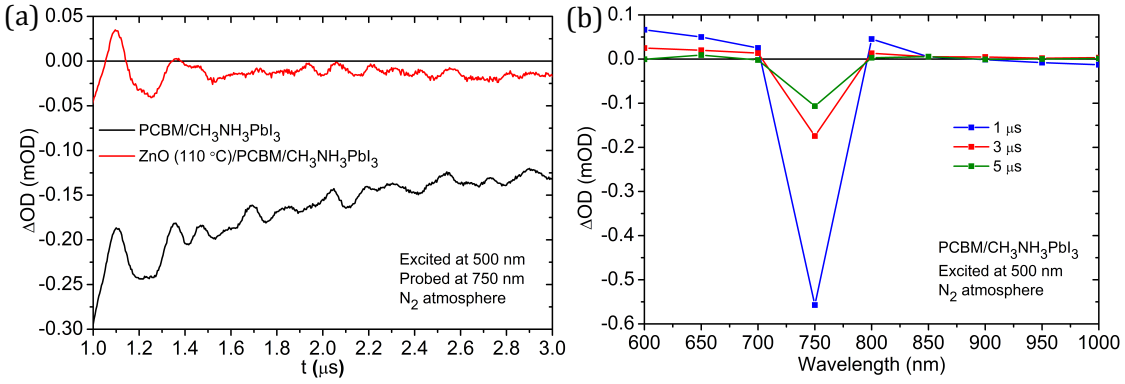


Figure 5.14 (a) Transient absorption kinetics of glass/PCBM/$CH_3NH_3PbI_3$ and glass/PCBM/ZnO (110 °C)/$CH_3NH_3PbI_3$ excited at 500 nm (7 uJ/cm²) and probed at 750 nm in N_2 atmosphere; (b) Transient absorption spectra of PCBM/$CH_3NH_3PbI_3$ excited at 500 nm (15 uJ/cm²) in N_2 atmosphere.

5.4 Conclusions

We have investigated an electron transport bilayer fabricated <110 °C to form a low temperature processed, thermally stable, low hysteresis and efficient perovskite solar cell with conventional structure. The bilayer contains a sol-gel derived ZnO layer to facilitate better energy level alignment and enhanced carrier extraction rate and a PCBM layer to eliminate the hysteresis and to enhance perovskite thermal stability.

Neither ZnO nor PCBM alone are proven to be a good ETL. ZnO on its own shows low perovskite thermal stability. The perovskite thermal stability increases as the ZnO processing temperature increases. However, even high temperature processed highly (002) oriented crystalline ZnO films did not result in highly stable perovskite films, which may come from the proton-transfer reaction at the ZnO/$CH_3NH_3PbI_3$ interface due to the basic nature of the ZnO surface.

PCBM on its own shows poor energy level alignment in conventional perovskite device structure, which results in decreased carrier extraction rate. The increased series resistance with the increase of PCBM film thickness may partially originate from its low carrier mobility nature.

The ZnO/PCBM bilayer ETL suggests that some materials that are not suitable when directly contacted with perovskite can be combined with fullerene to form efficient ETLs in perovskite solar cells.

References

[1] N. J. Jeon, J. H. Noh, Y. C. Kim, W. S. Yang, S. Ryu, S. Il Seok, *Nat. Mater.* **2014**, *13*, 1.

[2] T. Oku, *Crystal Structures and Related Perovskite Compounds Used for Solar Cells*, **2015**.

[3] N. Onoda-Yamamuro, O. Yamamuro, T. Matsuo, H. Suga, *J. Phys. Chem. Solids* **1992**, *53*, 277.

[4] T. Zhang, M. Yang, Y. Zhao, K. Zhu, *Nano Lett.* **2015**, *15*, 3959.

[5] J. Kim, G. Kim, T. K. Kim, S. Kwon, H. Back, J. Lee, S. H. Lee, H. Kang, K. Lee, *J. Mater. Chem. A* **2014**, *2*, 17291.

[6] Y. Hou, C. O. R. Quiroz, S. Scheiner, W. Chen, T. Stubhan, A. Hirsch, M. Halik, C. J. Brabec, *Adv. Energy Mater.* **2015**, *5*, 1501056.

[7] A. H. Ip, L. N. Quan, M. M. Adachi, J. J. McDowell, J. Xu, D. H. Kim, E. H. Sargent, *Appl. Phys. Lett.* **2015**, *106*, 143902.

[8] C. Tao, S. Neutzner, L. Colella, S. Marras, A. Ram, S. Kandada, M. Gandini, M. De Bastiani, G. Pace, L. Manna, M. Caironi, C. Bertarelli, A. Petrozza, *Energy Environ. Sci.* **2015**, *8*, 2365.

[9] S. Ryu, J. Seo, S. S. Shin, Y. C. Kim, N. J. Jeon, J. H. Noh, S. Il Seok, *J. Mater. Chem. A* **2015**, *3*, 3271.

[10] J. Zhang, J. C. D. Faria, M. Morbidoni, Y. Porte, C. H. Burgess, K. Harrabi, M. A. McLachlan, *Adv. Electron. Mater.* **2016**, *2*, 1600008.

[11] J. Yang, B. D. Siempelkamp, E. Mosconi, F. De Angelis, T. L. Kelly, *Chem. Mater.* **2015**, 4229.

[12] Y. Shao, Z. Xiao, C. Bi, Y. Yuan, J. Huang, *Nat. Commun.* **2014**, *5*, 1.

[13] E. Von Hauff, V. Dyakonov, J. Parisi, *Sol. Energy Mater. Sol. Cells* **2005**, *87*, 149.

[14] Y. Shao, Y. Fang, T. Li, Q. Wang, Q. Dong, Y. Deng, Y. Yuan, H. Wei, M. Wang, A. Gruverman, J. Shield, J. Huang, *Energy Environ. Sci.* **2016**, *501*, 395.

[15] B. Wu, K. Fu, N. Yantara, G. Xing, S. Sun, T. C. Sum, N. Mathews, *Adv. Energy Mater.* **2015**, *5*, 1500829.

[16] L. Zuo, Z. Gu, T. Ye, W. Fu, G. Wu, H. Li, H. Chen, *J. Am. Chem. Soc.* **2015**, 2674.

[17] H. Zhou, Q. Chen, G. Li, S. Luo, T. B. Song, H. S. Duan, Z. Hong, J. You, Y. Liu, Y. Yang, *Science* **2014**, *345*, 542.

[18] T. Leijtens, G. E. Eperon, A. J. Barker, G. Grancini, W. Zhang, J. M. Ball, A. R. S. Kandada, H. J. Snaith, A. Petrozza, *Energy Environ. Sci.* **2016**, *9*, 3472.

Chapter 6 - Aqueous processed ZnO as Electron Transport Layers for Organic and Perovskite Solar Cells

6.1 Introduction

In this chapter, another ZnO thin film fabrication method based on an aqueous, carbon-free metal-oxide precursor route is investigated. First, the ZnO thin films have been characterised in a range of complimentary experiments. The processing temperature dependence of ZnO properties is studied. XRD and TEM are carried out to assess the film crystallinity. The chemical composition analysis is conducted by XPS and FTIR. The optical properties are characterised by UV-vis spectroscopy. SEM and AFM are carried out to present the surface morphology. The electrical properties are studied, TFT reflecting the ZnO electron transport behaviour and Kelvin probe showing the work function of ZnO films.

Then, the suitability of aqueous based ZnO as ETLs in OPVs are investigated with PCDTBT:$PC_{71}BM$ active layer mixture, configured in the inverted device architecture. The ZnO processing temperature dependence of device performance is presented.

Next, aqueous based ZnO thin films are employed as ETL in perovskite solar cells. In addition to the device performance, we study the influence of the processing temperature of ZnO films on overlying perovskite thermal stability by XRD. The influence of ZnO films on overlying perovskite grain size is also investigated by SEM. We also employed the same PCBM interfacial modification as that in the previous chapter.

In this chapter not only the aqueous ZnO work itself is presented, but also the comparison between sol-gel derived and aqueous based ZnO is given.

6.2 Experimental methods

6.2.1 Zinc precursor solution

Ammine-hydroxo zinc solutions were prepared by mixing ZnO powders in ammonium hydroxide solution (5.0 M) to molar concentration of 0.1 M. Ammonium hydroxide solution (5.0 M) was stored in the fridge (5 ˚C) before use. The solutions were then stirred overnight in dark, in air, at room temperature. Before spin coating, the solutions were filtered through a 0.45 μm PTFE filter.

6.2.2 ZnO film formation

ZnO films were formed by spin coating using a static loading method. The spin coating was a 2000 rpm spin for 30 s with an acceleration rate of 1000 rpm/s. Four coatings were applied to achieve a dense layer. The back of the substrate was cleaned using isopropanol after every deposition to ensure optical properties were not compromised. The films were also preheated at a given temperature for 10 min on a hotplate (VWR) after each coating. Some samples were also treated with postannealing (Carbolite 5L RWF) at 450 ˚C for 1 hour in air with a cooling gradient of 5 ˚C/min to 300 ˚C, then left to cool to room temperature.

6.2.3 OPV fabrication

For OPV fabrication, PCDTBT:$PC_{71}BM$ (1:2 w/w), 18 mg/ml blend solution in chlorobenzene was spin coated on the top of ZnO at 2500 rpm in order to achieve an active layer thickness around 80-90 nm.

All other organic and perovskite solar cell fabrication procedures are identical to those in Chapter 4 and 5.

6.3 Results and discussion

6.3.1 ZnO films

6.3.1.1 Crystallinity

A range of complementary measurements were carried out on the ZnO layers beginning with an assessment of the crystallinity by XRD. The influence of processing temperature on the crystallinity of ZnO films was investigated, as shown in Figure 6.1. To get clear XRD signal, we increased the spin coating to 12 cycles, instead of 4 cycles used in solar cell fabrication. No peaks corresponding to crystalline ZnO are seen in the XRD patterns of the films deposited at 100 ˚C. Films deposited at 200 ˚C and those with extra postannealing at 450 ˚C show similar behavior, strong (100), (101) peaks and weak (002) peaks of ZnO, consistent with the reference pattern (ICSD 01-076-0704). The intensities of (100) and (101) peaks of ZnO (450 ˚C) are greater than those of ZnO (200 ˚C). The grain size of ZnO layers was calculated by the Scherrer method, Eqn 2.1, shown in Chapter 2. An increase in the $d_{(101)}$ crystallite size from 31.0 nm (200 ˚C) to 52.3 nm (450 ˚C) can be observed in Table 6.1. Also a slight increase in the $d_{(100)}$ crystallite size from 51.6 nm (200 ˚C) to 59.0 nm (450 ˚C) is confirmed. Calculations from both peaks illustrate that ZnO (450 ˚C) has larger grain than ZnO (200 ˚C). Thus, from the XRD results the ZnO films processed at 100 ˚C appear to be macroscopically amorphous, while ZnO (200 ˚C) and (450 ˚C) show polycrystalline behaviour.

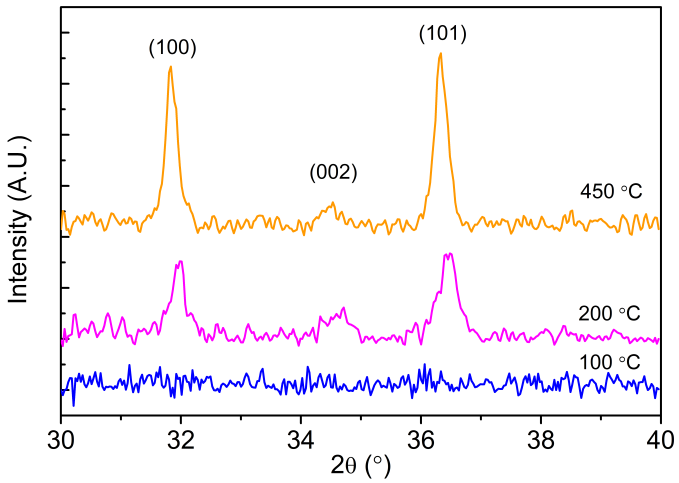


Figure 6.1 XRD patterns of ZnO films processed by the aqueous method on glass, with different processing temperatures.

Table 6.1 The grain sizes calculated from XRD patterns for ZnO layers with different temperatures

	100 ˚C	200 ˚C	450 ˚C
FWHM (°) of (101) peak	---	0.36	0.25
Grain size (estimated from (101) peak)	---	31.0 nm	52.3 nm
FWHM (°) of (100) peak	---	0.25	0.23
Grain size (estimated from (100) peak)	---	51.6 nm	59.0 nm

It should be noted that when annealed at 450 ˚C, both the ZnO films by ammonia method and those by sol-gel method have different crystalline orientation. This difference may come from the different rates of the evaporation of the solvents and the thermal decomposition of the precursors in the two systems. For the solvents, the boiling point of ammonium hydroxide (25 % w/w) is 27 ˚C and that of 2-methoxyethanol is 125 ˚C. The rapid kinetics of dehydration, condensation, and ammine decomposition reactions of carbon-free ZnO preparation[1] hinder the growth towards (002) preferential orientation. While for the sol-gel method, the low rate of evaporation of the solvents and the thermal decomposition of the precursors enables enough time during crystallisation to get minimum surface energy so that highly (002) oriented films are synthesised.

Further investigation on the nanoscale crystallinity of ZnO (100 ˚C) was conducted by high resolution transmission electron microscopy (HRTEM), Figure 6.2. Here the TEM result clearly shows that the 100 °C processed film comprises of nanocrystalline ZnO. Figure 6.2 shows ZnO (100 ˚C) deposited on ITO substrate (lower dark regions) and a number of lattice fringes have been annotated with their spacing and the corresponding wurtzite ZnO plane. The inset shows a fast Fourier transform (FFT) further

demonstrating the presence of multiple crystalline domains within the film. Peak broadening caused by the small grain size combined with the low film thickness could explain the absence of diffraction peaks for ZnO (100 ˚C) in XRD.

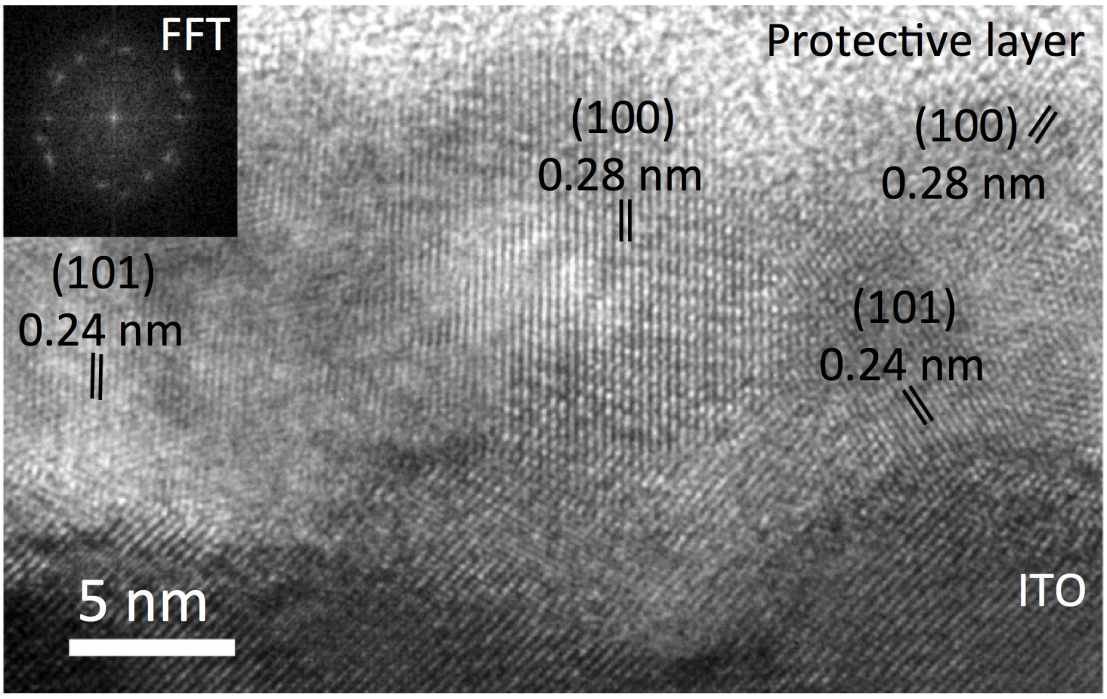


Figure 6.2 HRTEM image showing the 100 °C annealed ZnO layer deposited on ITO substrate (lower dark area), indicating the nanocrystalline nature of ZnO (100 °C) films. A selection of fringe spacings and corresponding wurtzite ZnO planes are annotated and the inset shows a fast Fourier transform (FFT).

6.3.1.2 Chemical analysis

To understand the composition evolution with processing temperature, we first performed FTIR analysis, as shown in Figure 6.3. The as cast film shows strong O-H stretching and N-H deformation features, indicating the presence of $Zn(OH)_x(NH_3)_y^{(2-x)+}$ precursor. While for the films annealed at 100 and 200 ˚C, the signal is almost the same, no obvious O-H stretching and N-H deformation features detected. This illustrates that the precursor has been fully decomposed into ZnO after annealing at 100 ˚C, and that the H_2O solvent has evaporated.

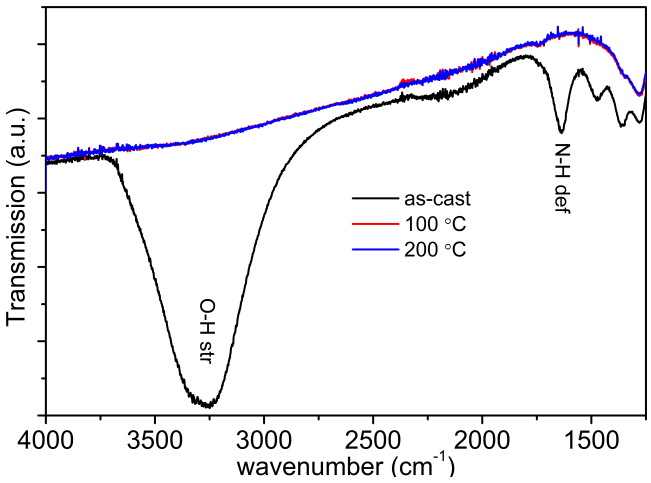


Figure 6.3 FTIR spectra of ZnO with different processing temperatures.

The chemical composition was further investigated by XPS. Spectra of the O 1*s* core levels are shown in Figure 6.4, with data for the C 1*s*, N 1*s*, Zn 2*p* in Figure 6.5. To ensure a fair comparison among peak positions, all spectra with different ZnO temperatures are corrected to the adventitious C 1*s* signal at 284.8 eV. The O 1*s* spectra display two overlapping peaks, the lower binding energy peak assigned to Zn-O (oxide) peak and the higher binding energy assigned to the O-H[2]. The O-H (oxide) signal may come from adsorbed water from the atmosphere, -OH dangling bond at the surface and/or zinc hydroxide impurities. A systematic decrease in the intensity of the O-H, relative to the Zn-O (oxide) peak, can be observed as the temperature increases.

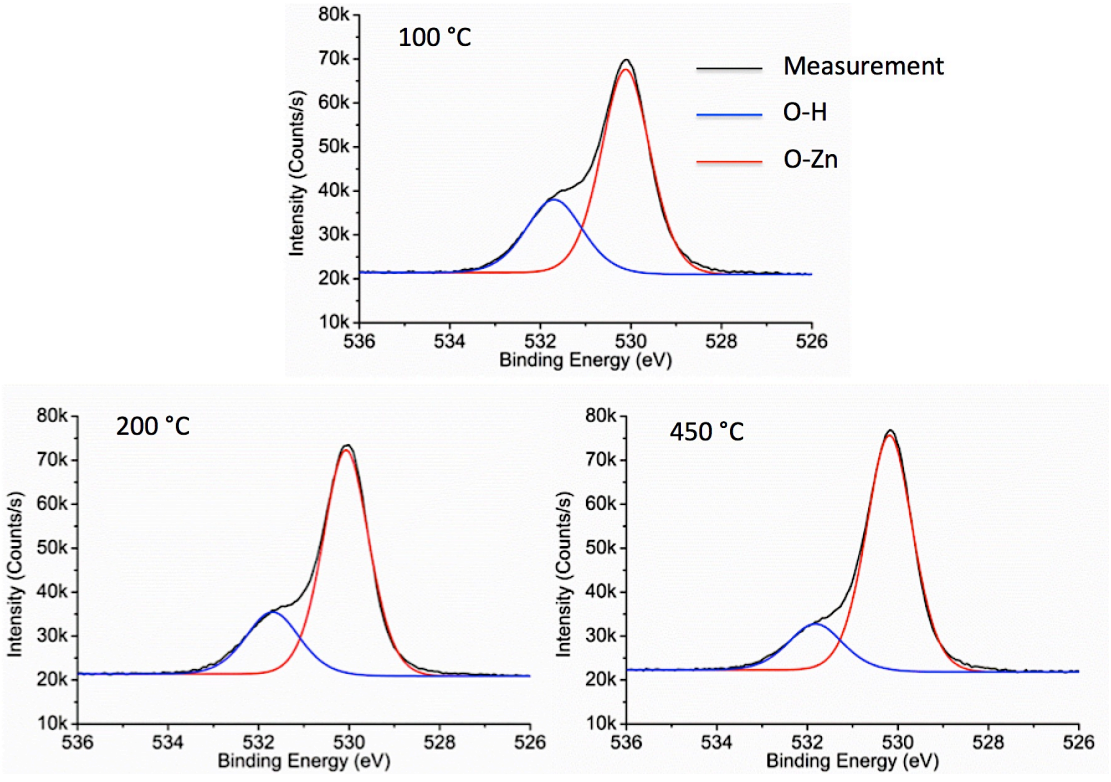


Figure 6.4 ZnO XPS spectra of O 1*s*, with different processing temperatures.

The N 1*s* spectra does not show any observable peaks for ZnO processed between 100 °C and 450 °C; this is in excellent agreement with the FTIR results, indicating that no zinc precursor residue remains. Combined with the aforementioned results, assuming that the amount of adsorbed water is similar for ZnO films processed between 100 and 450 °C, it was concluded that the 100 °C annealed film is mainly composed of ZnO nanoparticles but with a small amount of –OH dangling bond and/or zinc hydroxide impurities.

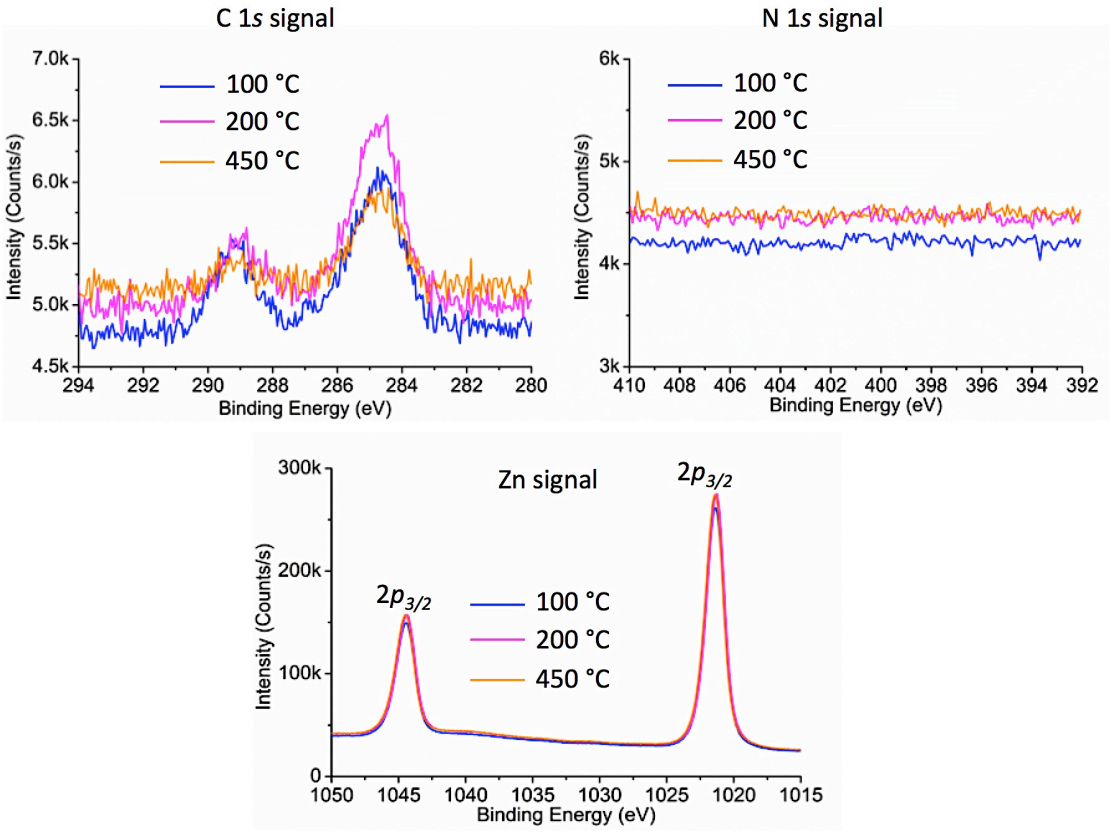


Figure 6.5 ZnO XPS spectra of C 1*s*, N 1*s* and Zn 2*p*, with different processing temperatures.

The FTIR and XPS results reveal that when fabricating low temperature processed ZnO layers, the precursor can be removed in ammonia-based carbon-free chemistry, while still remains in sol-gel method presented in Chapter 3.

6.3.1.3 Optical properties

For the use of the ETL attached to transparent electrode, the transmission of ZnO films by carbon-free method under different processing temperatures was investigated, against an air reference, shown in Figure 6.6. To accurately consider the situation in solar cells, films were deposited on ITO substrates. High transmission (75-95%) was obtained in the visible region at all ZnO deposition temperatures. Highly uniform, planar films were deposited which is confirmed from the Fabry Perot oscillations observed.

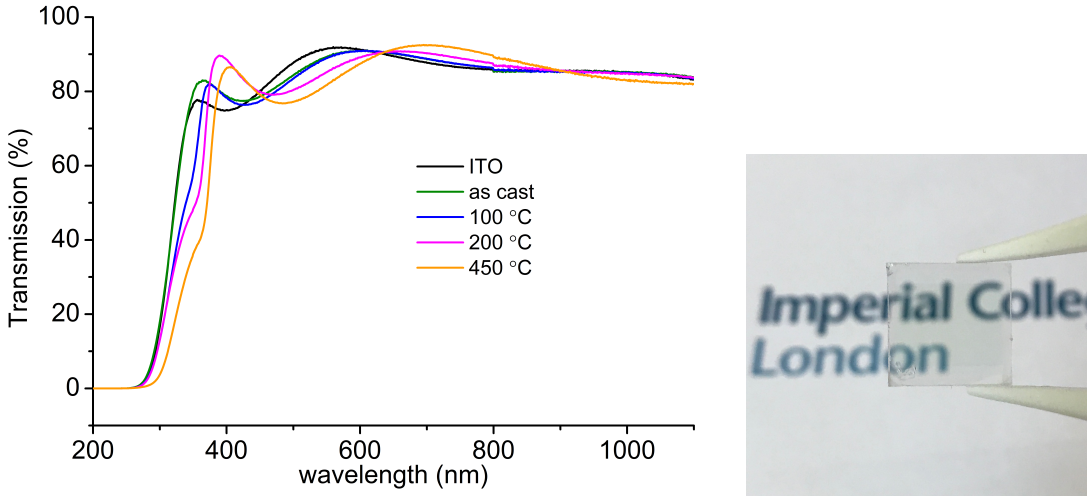


Figure 6.6 Left: UV-vis spectra for glass/ITO/ZnO stacks with different processing temperatures; Right: An optical photo of a glass/ITO/ZnO (100 °C) substrate.

We also calculated the optical bandgap based on the method described in Chapter 3. The Tauc plot ($[\alpha(h\nu)]^2 \sim h\nu$) and the estimated E_g of different films are shown in Figure 6.7, against a quartz reference. The E_g of the as cast film is 5.54 eV based on the direct bandgap model. Because quartz is used as a reference, the signal is considered only from the deposited film, *i.e.* the $Zn(OH)_x(NH_3)_y^{(2-x)+}$ precursor. For films processed from 100 to 450 °C, the measured absorption edge is red shifted as the temperature increases from 367 nm (100 °C) to 382 nm (450 °C). The corresponding optical bandgaps are from 3.38 eV (100 °C) to 3.24 eV (450 °C). The E_g of ZnO (450 °C) is similar to that of high temperature processed ZnO by sol-gel method in Chapter 3, which is close to the intrinsic bandgap of ZnO. The E_g value of the ZnO processed at 100 °C by ammonia method is identical to that of ZnO processed at 110 °C by sol-gel methods. This suggests that 100 °C annealed film by ammonia method may also have nanoscale ZnO components, derived from the quantum confinement of ZnO nanoparticles[3][4], which corroborates our TEM results. With the temperature increase, the crystalline size increases, which is commensurate with the XRD results.

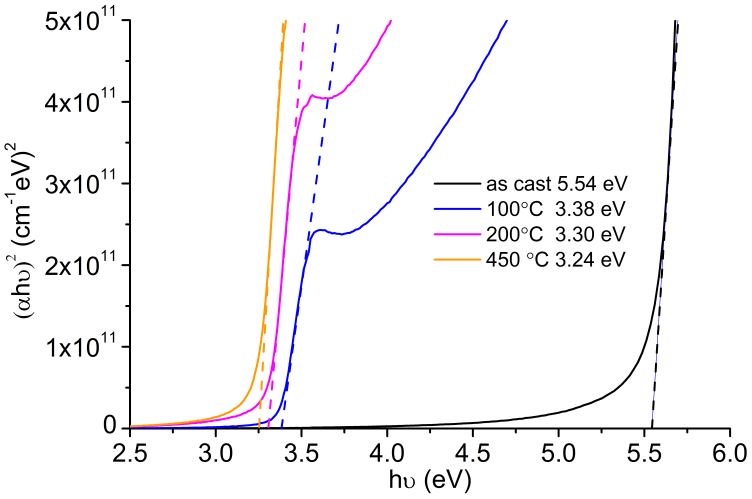


Figure 6.7 Tauc plots calculated from ZnO films on quartz substrates.

Although both are nanoparticles, the low temperature processed ZnO films by ammonia and sol-gel methods are different. Unlike sol-gel derived films, ZnO (100 °C) by ammonia is pure nanoparticles without solvent and precursor residues, as confirmed by XPS and FT-IR results.

6.3.1.4 Surface morphology

The morphology of ZnO layers on ITO substrates was characterised by AFM and SEM. The AFM results are shown in Figure 6.8. Film surface (thickness: 30 nm) at all processing temperatures are smooth. And a well-defined granular structure is observed on ZnO (100 – 450 ˚C) surfaces. The smooth surface of as-cast films (rms roughness: 0.56 nm) may come from residue of solvent and precursor complex. When processed at 100 ˚C, the rms roughness increases to 3.22 nm. This may be because the energy from heating is just enough to remove the solvent and to break the bond of precursor complexes, as confirmed from the XPS and FT-IR results. When the temperature increased to 200 ˚C, rms roughness drops to 1.90 nm. The extra energy may allow the particles to move towards the film surface, resulting in a smoother film. When the temperature reaches 450 ˚C, larger grains are formed as confirmed from the XRD results, and the surface has a higher roughness of 2.73 nm.

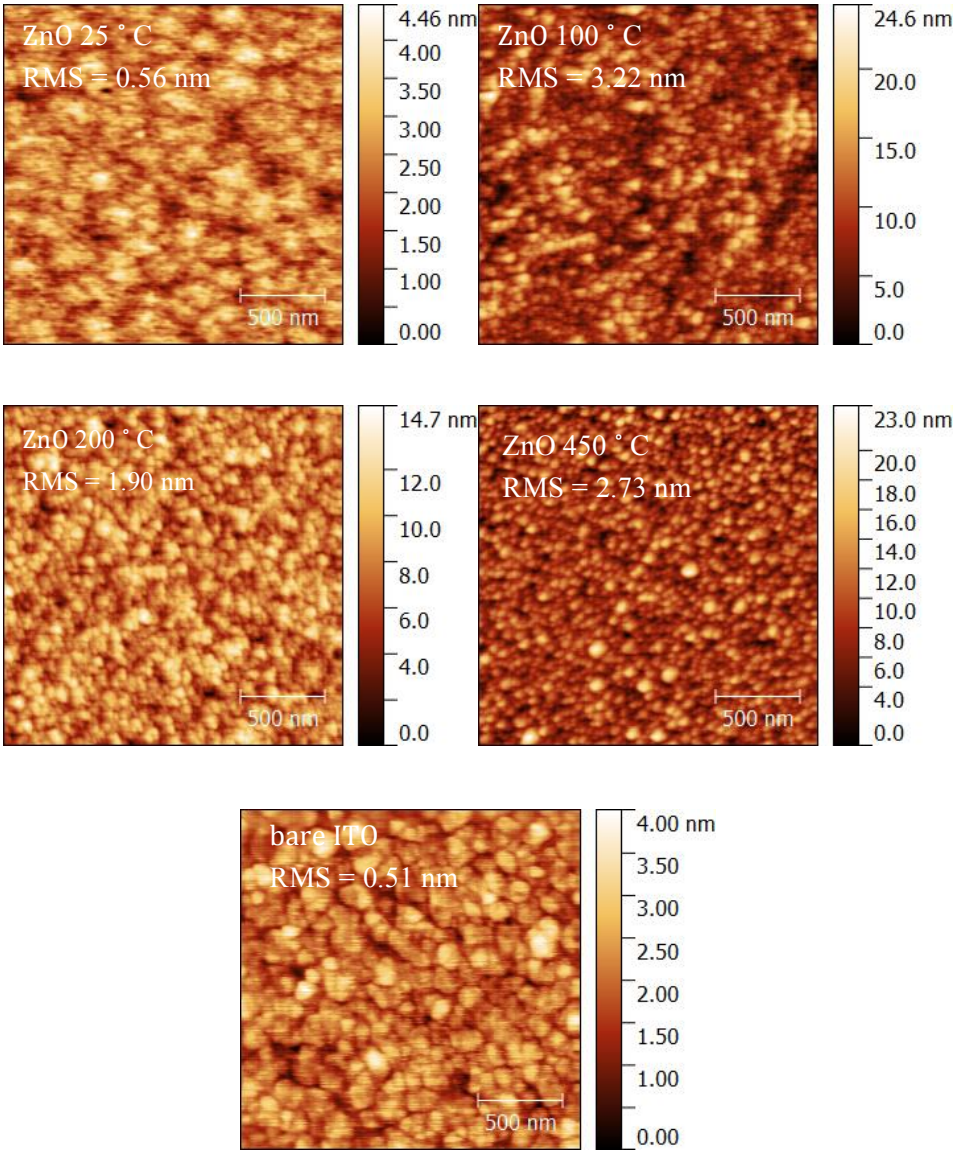


Figure 6.8 AFM image of ZnO films on ITO substrates, inset is the rms roughness of the films.

The SEM images indicate excellent spatial uniformity for all ZnO films, as shown in Figure 6.9. Large area images show full coverage for all films, as shown in Appendix D. The as cast film displays 'cloud-like' morphology due to the unreacted precursor and solvent residue. After annealing, a granular morphology is shown for all films prepared >100 °C. The surface roughness in SEM images is in agreement with the AFM results, especially clear with large area images in Appendix D. In addition, no detectable cracks are observed in all ZnO films processed at 100 to 450 °C.

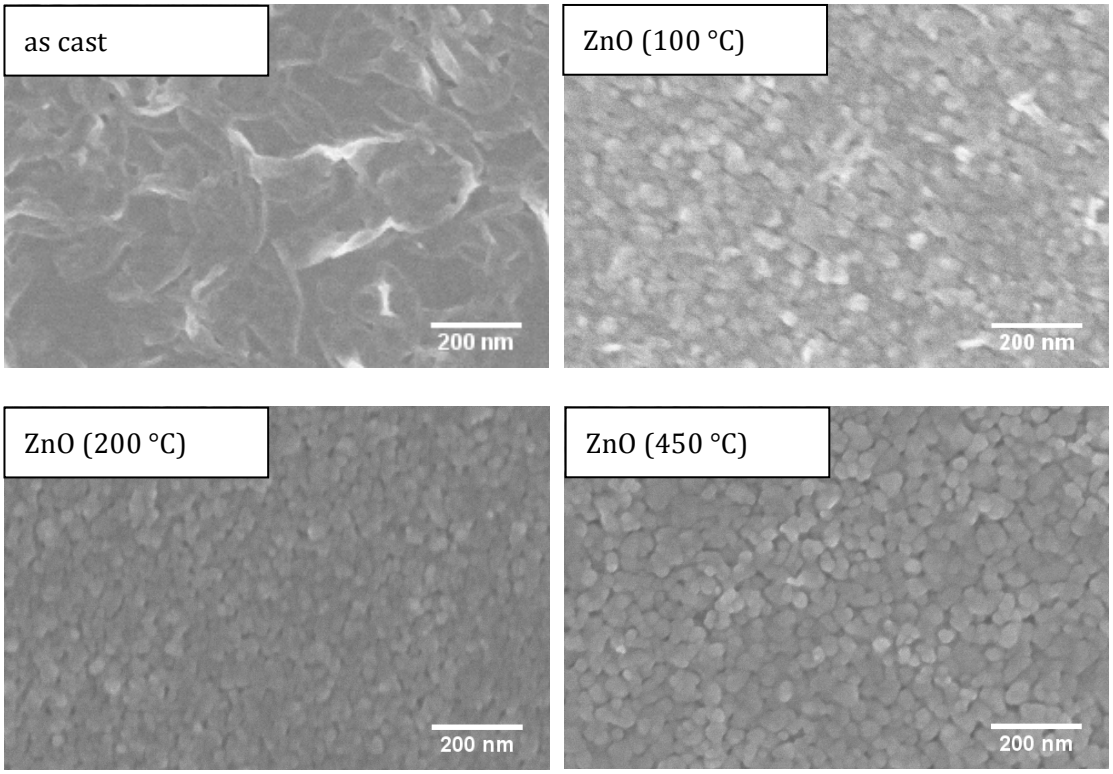


Figure 6.9 SEM images of ZnO layers with different processing temperatures.

The granular size measured from SEM images is shown in Table 6.2, indicating larger granular size with increasing annealing temperature. It should be noticed that the granular size of ZnO (100 °C) is around 20 nm, which should not be the grain size according to the aforementioned discussion of structural and optical results. We suppose the granular morphology in ZnO (100 °C) is clusters of congregated nanoparticles after 100 °C moderate heating. As for ZnO 200 and 450 °C, the average size measured by SEM images is lower than the grain size calculated from XRD. But the trend is the same. The difference of grain size measured by SEM and XRD is because that the value by XRD is measured in the vertical direction while the value by SEM is evaluated along a horizontal axis.

Table 6.2 The granular size calculated by SEM images for ZnO films with annealing temperatures

	as cast	100 ˚C	200 ˚C	450 ˚C
Average grain size (nm)	---	20.4	29.1	38.2
Standard deviation (nm)	---	5.8	6.8	8.6

6.3.1.5 Electrical properties

Bottom gate, bottom contact thin film transistors (TFTs) of ZnO films were prepared to investigate the electron transport properties of these materials. Transfer curves

measured under ambient conditions for several unencapsulated transistors annealed between 100 ˚C and 450 ˚C are shown in Figure 6.10. The curve for as cast film is too resistive and showing no on/off effect, so it was not displayed here. Between 100 ˚C and 450 ˚C, lower threshold voltages and higher channel current on/off ratios were observed with increasing temperatures, indicating improved electron transport. The turn-on voltage shifts towards more negative V_G with the increase in processing temperature. This shift suggests that higher annealing temperature leads to higher concentration of free carriers within the channel. Enhanced electron transport with higher annealing temperature is also demonstrated from the field effect mobility calculated from saturation region based on Eqn 2.6, shown in Figure 6.11. The as cast film has very low mobility, 3.4×10^{-6} cm^2 $V^{-1}s^{-1}$, which may be due to the unreacted precursor and solvent. For films at 100 – 450 ˚C, the mobility increases monotonically with the processing temperature, from 0.05 to 0.39 cm^2 $V^{-1}s^{-1}$.

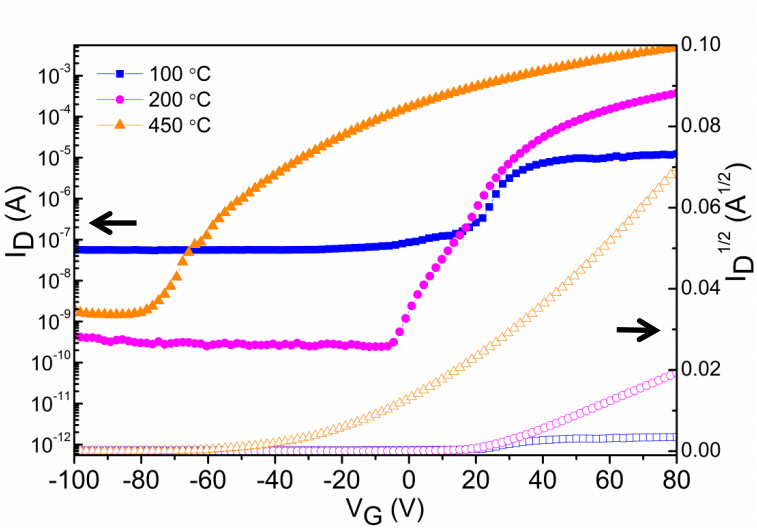


Figure 6.10 Transfer curves of TFT with ZnO films in saturation region, V_D = 35 V.

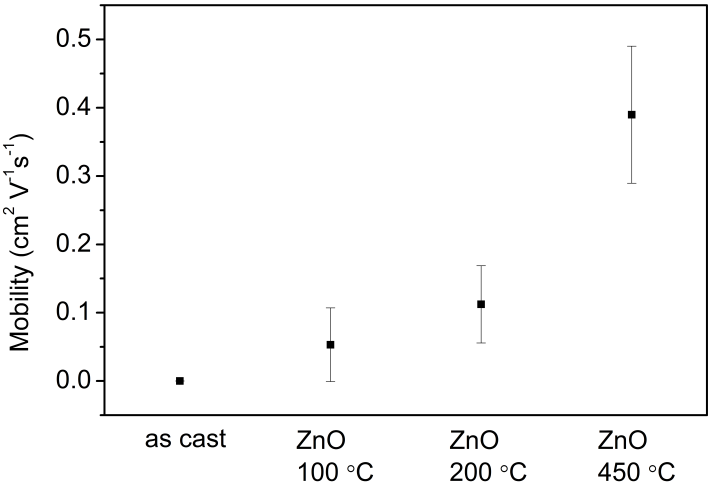


Figure 6.11 Field effect mobilities of ZnO films calculated from transfer curves in saturation region.

We compare the processing temperature dependence of mobility in two systems: ammonia *vs.* sol-gel. Higher temperature brings higher mobility in the ammonia system; while in the sol-gel system, high temperature annealed films have decreased mobility. This may come from different film orientation in two systems. High temperature films by sol-gel method are highly (002) oriented, while those by the ammonia method have (100) and (101) orientations. The mobility measured by TFT is related to the electron transport in the lateral direction *i.e.* parallel to the substrate. So higher (002) orientation may not increase the grain size in the lateral direction. But in the ammomia system, the (002) growth in lateral direction may increase with improved (100) and (101) orientation, accompanying with larger particle size. So the measured TFT mobility is increased with annealing temperature in the ammonia system. For low temperature processed ZnO, although both are ZnO nanoparticles, the mobility of ZnO by ammonia (0.05 $cm^2V^{-1}s^{-1}$) is nearly 10^4 higher than that by sol gel (5.3×10^{-6} $cm^2V^{-1}s^{-1}$). This is because the sol-gel derived one has organic residue left, which significantly hinders the lateral electron transport. However, when ZnO acts as an ETL in solar cells, the electron transport is in the vertical direction, typically only 10's nm path, which reduces the impact by electron field effect mobility.

The Fermi levels (E_F) of ZnO films on ITO substrates were calculated from the contact potential difference measured by Kelvin Probe in air, Table 6.3. Heating from the as-cast film to 100 ˚C does not shift the E_F, which remained stable at -4.46 eV. Continued heating to 200 ˚C leads to a slight reduction in E_F (-4.40 eV). On the contrary, the E_F was significantly shifted downward to -4.63 eV with further annealing at 450 ˚C. Native defects in ZnO (200 °C), including Zn interstitials and oxygen vacancies, may be partially recovered in ZnO at 450 °C by the enhanced thin film crystallinity[5–7](confirmed by the XRD results); this may be the cause of the deeper E_F shown by the latter. In addition, the work function shift measured by Kelvin probe is in excellent agreement with our XPS results: the B.E. position of the Zn-O (oxide) peak shifts towards higher binding energy upon annealing at 450 °C, Appendix D. This is indicative of a shift in the Fermi level position, which we would expect to manifest itself as a rigid shift of the core levels, and is indeed what we see in the Zn-O (oxide) environment of the O 1*s*. The same trend is also observed from the Zn 2*p* spectra, Appendix D.

Table 6.3 Work functions of ZnO prepared on ITO substrates, measured by Kelvin probe

	ITO	as cast	ZnO (100 °C)	ZnO (200 °C)	ZnO (450 °C)
Work Function (eV)	4.47	4.46	4.46	4.40	4.63

The work functions in two systems, sol-gel *vs.* ammonia, are compared. For low temperature processed films, sol-gel derived ZnO (110 °C) exhibits lower work function, 4.13 eV in Chapter 3 and 4.34 eV in Chapter 5, than aqueous processed ZnO (100 °C) 4.46 eV. MEA residues contribute to the lower work function in sol-gel derived films. With the processing temperature increasing, work functions both become larger in higher temperature processed ZnO during the enhanced crystallisation process, 4.60 eV (sol-gel) *vs*. 4.63 eV (ammonia).

6.3.2 ZnO films for organic solar cells

We also proved the suitability of ZnO as ETL in OPVs. OPVs were fabricated in the inverted architecture, with a typical structure (layer thicknesses in parenthesis) of glass / ITO (140 nm) / ZnO (20 nm) / PCDTBT:$PC_{71}BM$ (100 nm) / MoO_x (10 nm) / Ag (100 nm), shown schematically in Figure 6.12a, alongside the relevant energy levels of the materials[8–11] in Figure 6.12b and molecular structure of the active layer materials in Figure 6.12c. Both ZnO and the active layer were deposited from solution and the MoO_x/Ag thermally evaporated. Representative current-voltage (J-V) characteristics are shown in Figure 6.12d where the ZnO processing temperature is varied over the range 100 - 450 °C, also included is data for a control device prepared without ZnO. Statistical data for all devices prepared are summarized in Table 6.4. From these data it is clear that the ETL processing temperature is having a significant impact on device performance. Overall the best performing devices are observed at processing temperatures of 100 °C, where the champion device shows > 4.3% PCE and average V_{OC}, J_{SC} and FF of 0.89 V, 8.5 mA/cm^2 and 52% respectively. The device characteristics over the temperature range 100 – 200 °C are comparable, and drop at 450 °C, consistent with our previous report[12] where the onset of crystallisation in the ETL and a change in work function result in V_{OC} and FF losses. The dark J-V scans show improved blocking behavior at the lower processing temperatures, Figure 6.13, thus our ETL fulfills the low temperature and charge selective transport criteria of such an interlayer. Unsurprisingly poor performing devices are measured when no ETL is included in the device stack, suggesting that the necessity of ZnO ETL that enables device operation.

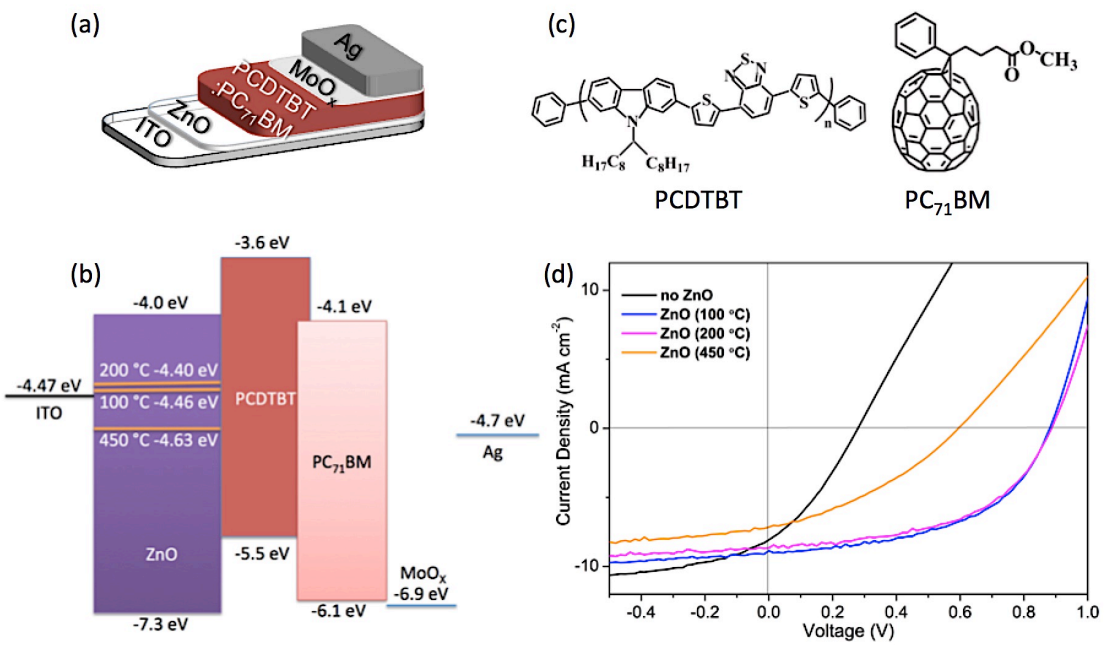


Figure 6.12 (a) Schematic illustration of OPVs with inverted device architecture; (b) Energy level diagram of devices; (c) Molecular structure of electron donor (PCDTBT) and acceptor ($PC_{71}BM$) active layer materials and (d) representative J-V curves for devices prepared using ZnO ETLs deposited at the temperatures indicated.

Table 6.4 Statistical data of PCDTBT:$PC_{71}BM$ based OPV devices

	V_{oc} (V)	J_{sc} (mA/cm²)	FF (%)	PCE (%)	R_s (Ω cm²)	R_{sh} (Ω cm²)
no ZnO	0.242 ± 0.049	6.61 ± 1.00	31.6 ± 2.7	0.52 ± 0.16	26.2 ± 3.2	67.7 ± 27.7
ZnO (100 °C)	0.886 ± 0.003	8.47 ± 0.72	52.1 ± 1.3	3.97 ± 0.28	18.5 ± 2.4	569.9 ± 39.0
ZnO (200 °C)	0.883 ± 0.004	8.41 ± 0.37	51.1 ± 0.6	3.86 ± 0.22	20.3 ± 0.8	607.3 ± 163.6
ZnO (450 °C)	0.591 ± 0.011	6.65 ± 0.61	36.1 ± 1.4	1.43 ± 0.08	43.1 ± 2.4	255.5 ± 51.1

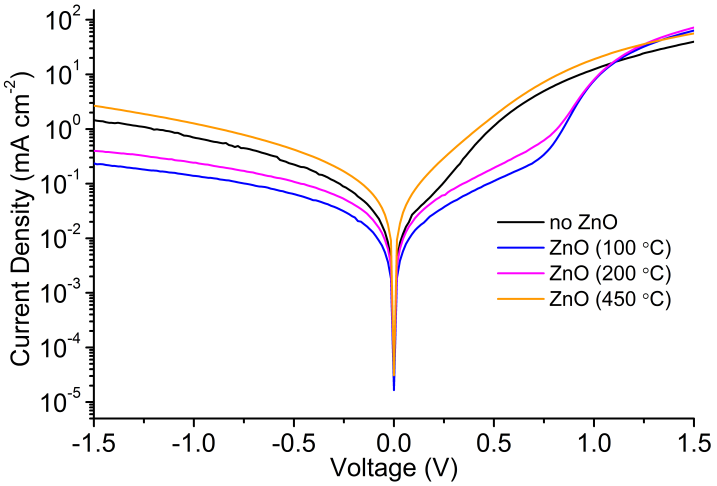


Figure 6.13 Representative dark J-V curves for PCDTBT:$PC_{71}BM$ solar cells prepared using ZnO ETLs deposited at the temperatures indicated.

6.3.3 ZnO films for perovskite solar cells

6.3.3.1 Wetting

To check the wetting properties, the contact angle of a $CH_3NH_3PbI_3$ precursor droplet with GBL and DMSO as co-solvent (7:3 by volume) was measured on the ZnO layers and ZnO/PCBM bilayer. The solvent is the same as the one in the previous chapter, the mixture of GBL and DMSO (7:3 by volume). The results show that the wetting is good on all ZnO films and it becomes better with the increase of ZnO processing temperature, Table 6.5. A dramatically improved wetting is shown on ZnO (450 °C). Although here the wetting is worse when dropped on PCBM surface, we still can get fully covered perovskite films on top of PCBM by ameliorating the wetting via preheating the PCBM substrates at around 80 °C before spin coating.

Table 6.5 Contact angles of $CH_3NH_3PbI_3$ precursor droplet (solvents: GBL:DMSO) on ZnO and ZnO/PCBM surfaces

	as cast	ZnO (100 °C)	ZnO (200 °C)	ZnO (450 °C)	ZnO (100 °C) /PCBM
Contact angle (°)	34.5 ± 6.1	28.4 ± 1.77	27.1 ± 2.8	7.5 ± 0.1	59.4 ± 8.3

6.3.3.2 Thermal stability

To investigate the influence of underlying aqueous processed ZnO layers on the $CH_3NH_3PbI_3$ thermal stability, we annealed glass/ITO/ZnO/$CH_3NH_3PbI_3$ stacks at 100 °C in a N_2 filled glovebox for 60 s, as discussed in Chapter 5. The normalised XRD patterns are shown in Figure 6.14. The (001) peak of PbI_2 is at 12.8 °2θ and the (110) peak of

$CH_3NH_3PbI_3$ is at 14.2 °2θ[13][14]. We can see that as-cast film induces high thermal instability in perovskite films. These have been almost totally decomposed into PbI_2, with only a small $CH_3NH_3PbI_3$ (110) peak left. This result may originate from the residue of unreacted precursor and H_2O. When ZnO films were annealed at temperatures ranging from 100 to 450 °C, the overlying perovskite film displayed similar thermal stability: only weak PbI_2 peaks were formed indicating the presence of traces of PbI_2, with similar PbI_2:$CH_3NH_3PbI_3$ peak intensity ratios on all three films. As aforementioned, aqueous processed ZnO films (100 – 450 °C) are polycrystalline films, with the crystallite size increases with the processing temperatures. Thus, the XRD data shown here proves that ZnO crystalline size has little influence on the perovskite thermal stability.

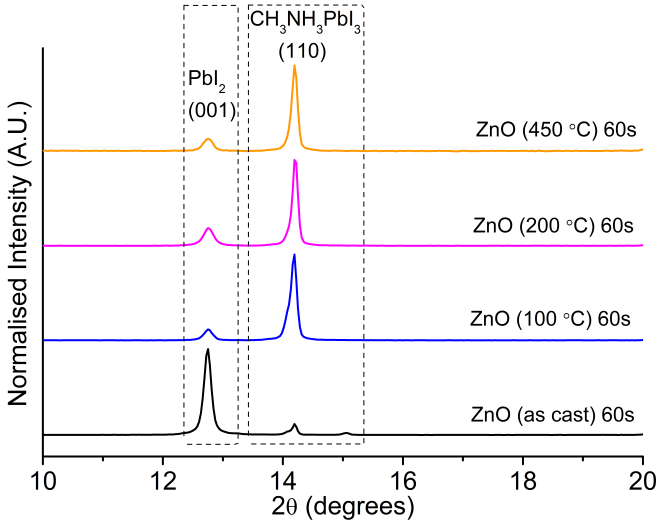


Figure 6.14 XRD patterns of glass/ITO/ZnO/$CH_3NH_3PbI_3$ stacks annealed at 100 °C in a N_2 filled glovebox, normalised data with different ZnO films under 1 min thermal stability test.

We also compared the perovskite thermal stability with low temperature processed ZnO by two methods. From the XRD results in Figure 6.14 and in Chapter 5, the low temperature aqueous processed ZnO has better perovskite thermal stability than the sol-gel derived counterpart. This originates from the difference of their chemical composition. Aqueous processed ZnO at 100 °C is pure ZnO nanoparticles without unreacted residues, which is confirmed by FT-IR, XPS and TEM. But sol-gel derived ZnO at 110 °C has lots of organic residues left, which may accelerate the perovskite decomposition while heating.

Here we did not calculate the grain size of perovskite using the Scherrer method. This is because the instrumental broadening is confirmed as 0.09° by a single silicon substrate while the FHWM of $CH_3NH_3PbI_3$ is only 0.11° that is too small to estimate the exact grain

size. So SEM measurement was conducted to investigate the processing temperatures of aqueous processed ZnO dependence of perovskite grain size and surface morphology.

6.3.3.3 Surface morphology

The morphology study of perovskite films was conducted by SEM, Figure 6.15. The thermal stability test condition was the same as that for XRD. Compact surface were formed for all the films. Statistic data of grain size is shown in Table 6.6. The average grain size of iodide compound films on top of as cast zinc precursor film is large, around 335 nm and together with the XRD results, suggested that PbI_2 was the main component of this film. This large grain size may originate from the crystallisation process of PbI_2. As for perovskite films on top of ZnO 100-450 °C, although the XRD figure shows similar ratios for PbI_2:$CH_3NH_3PbI_3$ peak intensity, the perovskite average grain size increases from 182 nm on ZnO (100 °C) to 351 nm on ZnO (450 °C). We suppose the ZnO particle size may be a cause for this trend. It may influence the surface density of initial nucleation sites for perovskite. More nucleation sites may form in cavities of ZnO films processed at low temperatures, which have smaller particle size with respect to films treated at higher temperatures. Thus, smaller grains will form due to the competition of more nucleation sites during crystalline growth[15]. Wetting may be another reason. The aforementioned results show that the wetting is good on all ZnO films and it becomes better with the increase of ZnO processing temperature.

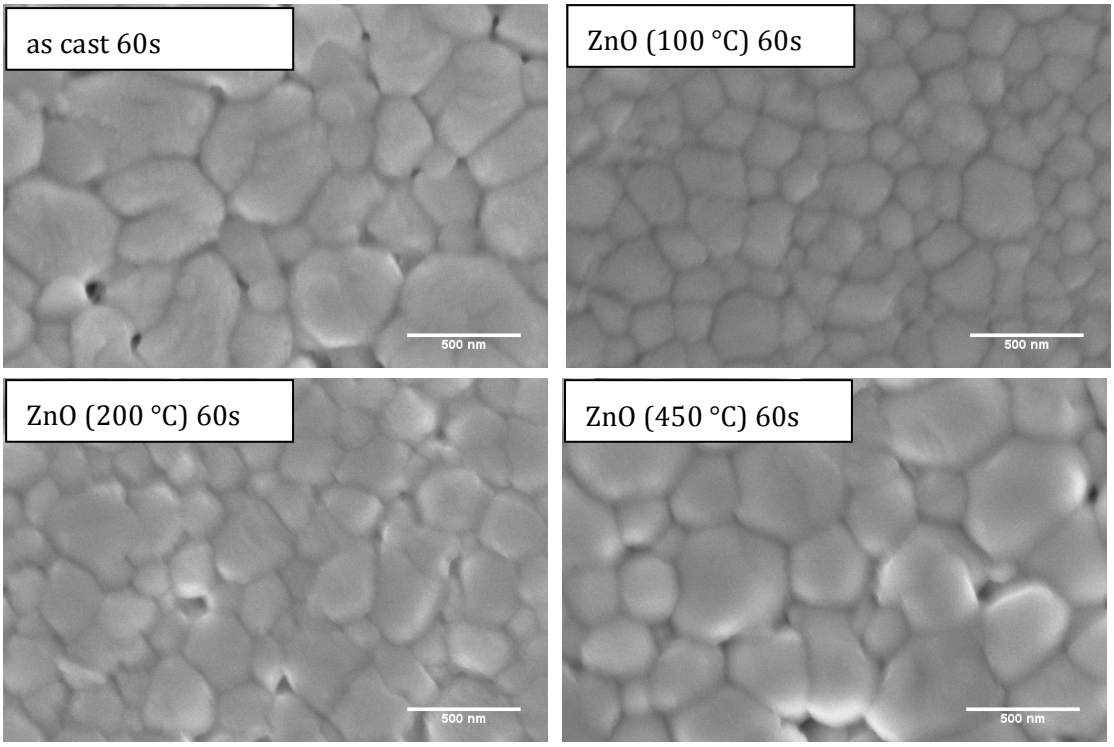


Figure 6.15 SEM images of $CH_3NH_3PbI_3$ on top of ZnO films, annealed at 100 °C in a N_2 filled glovebox for 60 s.

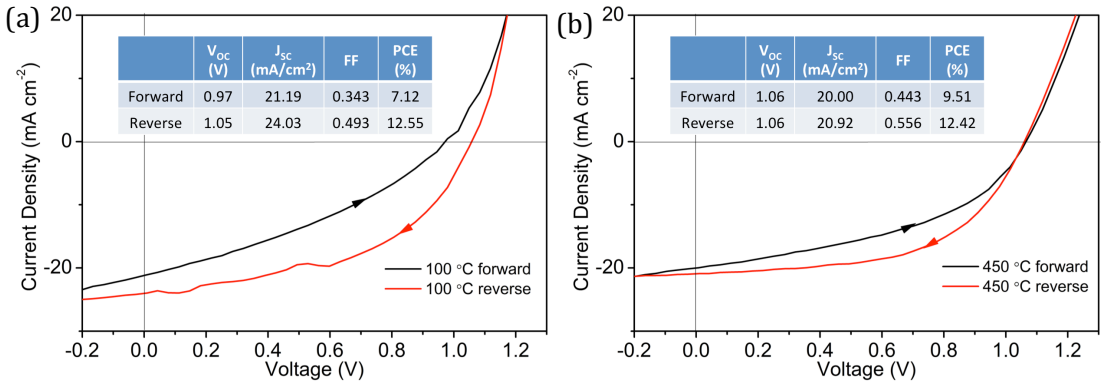
Table 6.6 The grain size measured by SEM images for perovskite films on ZnO films, annealed at 100 °C in a N_2 filled glovebox for 60 s.

	as cast	ZnO (100 °C)	ZnO (200 °C)	ZnO (450 °C)
Average grain size (nm)	334.6	182.0	234.6	350.9
Standard deviation (nm)	115.1	48.5	62.4	113.6

6.3.3.4 Device performance

We subsequently prepared perovskite solar cells with ZnO (100 °C) and ZnO (450 °C) to check the suitability of aqueous processed ZnO films as ETLs. The conventional device architecture is the same as that in the previous chapter, a typical structure of glass / ITO (140 nm) / ZnO (20 nm) / $CH_3NH_3PbI_3$ (300 nm) / spiro-OMeTAD (100 nm) / MoO_X (10 nm) / Ag (100 nm). Representative J-V characteristics are included in Figure 6.16. It can be seen that devices with ZnO (100 °C) and ZnO (450 °C) both work reasonably well, resulting in PCE values greater than 12% with a 0.2 V/s rate reverse scan. However, a J-V hysteresis is present in both of them; this is a common problem in bilayer oxide ETL in conventional perovskite device structures[16–18]. The hysteresis issue is less pronounced in devices with ZnO (450 °C), which also showed higher FF than those with ZnO (100 °C). This may originate from two factors. One is the perovskite grain size with two ZnO films. Grain boundary is proved to dominate ion migration in polycrystalline perovskite films and single-crystal perovskite devices display negligible J-V hysteresis[19]. In our cells, larger perovskite grain size with ZnO (450 °C) reduced the number of grain boundaries, which may reduce the J-V hysteresis. The other factor is the electron mobility of the different ZnO films. Higher mobility in ZnO (450 °C) may reduce the charge accumulation at the perovskite interface, which also decreases the J-V hysteresis[18].

Compared to the low temperature processed ZnO by sol-gel, aqueous processed ZnO (100 °C) brings better device performance. This is because the latter displays better perovskite thermal stability, which results in less perovskite decomposition during the crystallisation process by annealing. The corresponding less defects may be responsible for the better cell performance.



	V_{OC} (V)	J_{SC} (mA/cm^2)	FF	PCE (%)
Forward	0.97	21.19	0.343	7.12
Reverse	1.05	24.03	0.493	12.55

	V_{OC} (V)	J_{SC} (mA/cm^2)	FF	PCE (%)
Forward	1.06	20.00	0.443	9.51
Reverse	1.06	20.92	0.556	12.42

Figure 6.16 Representative J-V curves for perovskite devices prepared using (a) ZnO (100 °C) and (b) ZnO (450 °C) as ETLs, measured by forward and reverse scans with a 0.2 V/s scan rate.

6.3.3.5 Interfacial modification

We also carried out interfacial modification between ZnO and perovskite by PCBM, the same as that in the Chapter 5. To be consistent with our aim to make low temperature processed ETL, the modification was conducted on ZnO treated at 100 °C. We compared the XRD patterns of perovskite on ZnO (450 °C) and ZnO (100 °C)/PCBM, Figure 6.17. After annealing at 100 °C in N_2 for 20 min, a strong peak of PbI_2 appears for the $CH_3NH_3PbI_3$ on ZnO (450 °C), while it is negligible for the $CH_3NH_3PbI_3$ on ZnO(100 °C)/PCBM. This result proves that the insertion of PCBM significantly improves perovskite thermal stability.

Here we notice that after 20 min thermal stability test, the film on aqueous processed ZnO (450 °C) has larger PbI_2:$CH_3NH_3PbI_3$ peak intensity ratio than that with sol-gel derived ZnO (450 °C), which means sol-gel derived ZnO (450 °C) has better perovskite thermal stability than that by aqueous processing. High temperature processed ZnO films by two methods show similar average particle size: 34.2 nm (sol-gel) and 38.2 nm (aqueous) by SEM. There are two possible factors which influence their difference on perovskite thermal stability. One factor is the surface roughness, RMS 1.78 nm (sol-gel) *vs.* 2.73 nm (aqueous). Larger roughness brings more exposed dangling bond, which may enhance the perovskite decomposition during annealing. The other factor is the ZnO film orientation, (002) by sol-gel vs. (100) and (101) by aqueous method. The surface atomic densities of (110), (100) and (002) are 0.22×10^{16}, 0.12×10^{16} and 0.11×10^{16}, respectively[20]. Because the atomic ratio of Zn/O is 1, higher surface atomic density in aqueous processed ZnO films may lead to enhanced perovskite decomposition via deprotonation. Specifically, the methylammonium cations produce methylamine, with the released protons adsorbed on vicinal ZnO surface oxygen atoms[21].

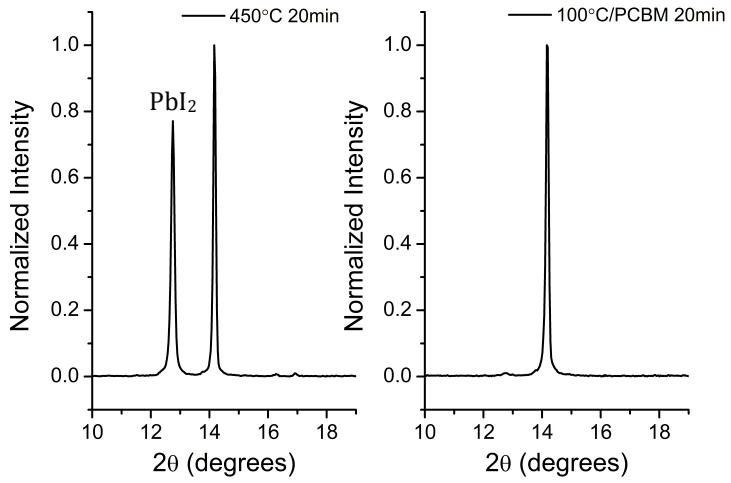


Figure 6.17 XRD patterns of glass/ITO/ZnO (450 °C)/$CH_3NH_3PbI_3$ (left) and glass/ITO/ZnO (100 °C)/ PCBM/$CH_3NH_3PbI_3$ (right) stacks annealed at 100 °C in a N_2 filled glovebox for 20 min.

The PCBM modification was also shown to reduce the photocurrent hysteresis of perovskite solar cells, Figure 6.18. Excellent performances were achieved with ZnO/PCBM bilayer as ETLs, with negligible J-V hysteresis under 0.2 V/s scan rate. The device gave a PCE of 15.1%, a V_{OC} of 1.0 V, a J_{SC} of 20.5 mA/cm^2 and a FF of 0.737 under standard AM1.5 solar illumination. Thus, a low-temperature processed (< 100 °C), thermally stable, and efficient perovskite solar cells with conventional structure, showing negligible hysteresis, are obtained with solution processed ZnO (100 °C) / PCBM stack as ETLs. The incorporation of PCBM was found to shift the V_{OC}, J_{SC} and FF compared to the device with bare ZnO as ETL. To understand the influence of PCBM on the device performance change, we carried out a range of experiments.

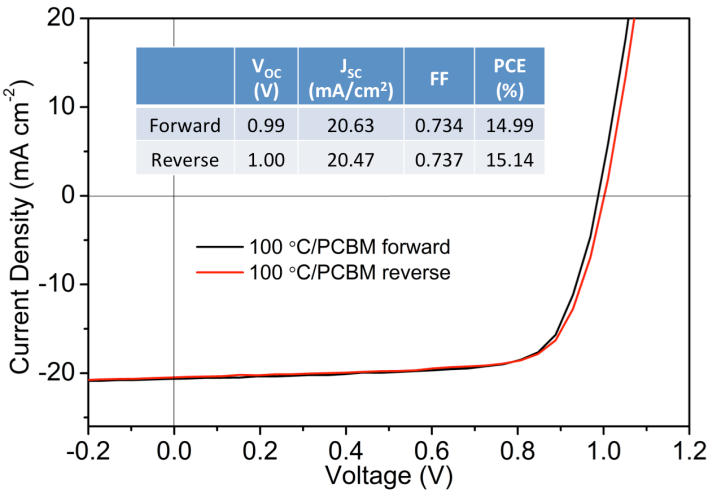


Figure 6.18 Representative J-V curves for perovskite devices prepared using ZnO (100 °C)/PCBM as ETLs, measured by forward and reverse scans with 0.2 V/s scan rate.

The addition of PCBM led to a small loss of J_{SC}, 20.5 mA/cm² (ZnO/PCBM) compared to 24.0 mA/cm² (ZnO as its own). This may be caused by increased light absorption from PCBM, confirmed from UV-visible transmission spectra of ZnO (100 °C) and ZnO (100 °C)/PCBM on ITO substrates, Figure 6.19. The insertion of PCBM decreased the transmission in visible region. Thus, the adjacent perovskite absorbed less light, which results in J_{SC} loss.

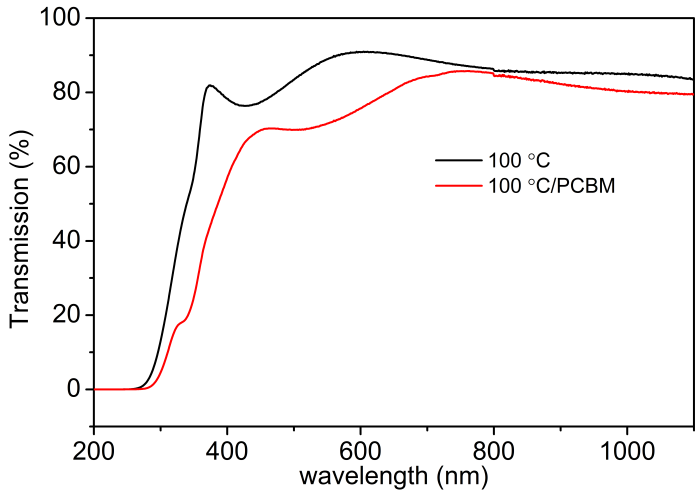


Figure 6.19 UV-visible transmission of glass/ITO/ZnO (100 °C) and glass/ITO/ZnO (100 °C)/PCBM stacks.

As for V_{OC}, ZnO as its own as ETL shows higher value (1.05 V), compared to 1.00 V with ZnO/PCBM bilayer as ETL. From the aforementioned XRD results, direct contact between perovskite and ZnO caused a trace of PbI_2. PbI_2, originated from thermal decomposition, was reported at the perovskite grain boundaries and was shown to effectively passivate the perovskite films[22]. This passivation may reduce recombination in the grain boundaries and therefore increase the V_{OC}.

However, the most significant influence of PCBM is the FF enhancement, from about 50% (ZnO) to above 73% (ZnO/PCBM). This may originate from several factors. First, the surface morphology of ZnO and ZnO/PCBM films was investigated by AFM, Figure 6.20. The insertion of PCBM reduced the surface roughness, changing from 3.22 nm to 0.34 nm. This may improve the interfacial contact between the ETLs and perovskites, which increases the FF.

Second, the presence of PCBM beneath the perovskite film could passivate the perovskite trap states at the surface, which has been proved on both inverted[23] and conventional[24–26] perovskite device structures, enhancing the FF as well as eliminating the J-V hysteresis.

Third, PCBM modified the work function of ETLs. The Fermi levels (E_F) of ZnO (100 °C) and ZnO (100 °C)/PCBM on ITO substrates were calculated from the contact potential difference measured by Kelvin probe in air, Table 6.7. With the addition of PCBM layer, the work function decreases from 4.46 eV at ZnO (100 °C) to 4.35 eV. This shift may facilitate the electron collection in perovskite solar cells, which contributes to the increased FF and reduced J-V hysteresis[27]. Schematic energy level of each layer in devices is shown in Figure 6.21[27][28].

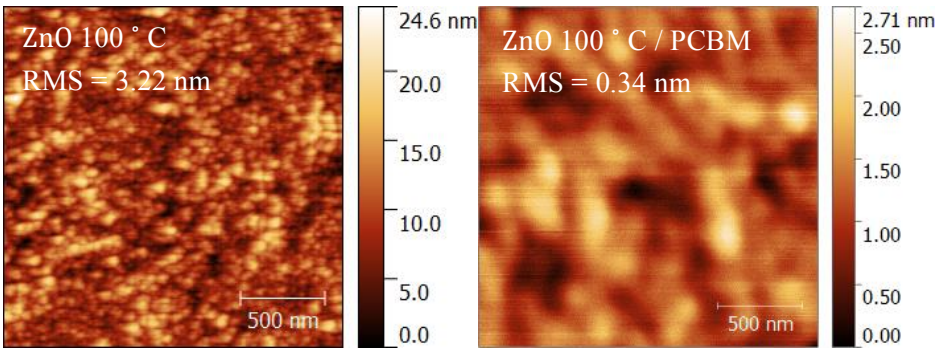


Figure 6.20 AFM images of ZnO (100 °C) and ZnO (100 °C)/PCBM on ITO substrates.

Table 6.7 Work functions of ZnO (100 °C) and ZnO (100 °C)/PCBM on ITO substrates, measured by Kelvin Probe.

	ZnO (100 °C)	ZnO (100 °C)/PCBM
Work Function (eV)	4.46	4.35

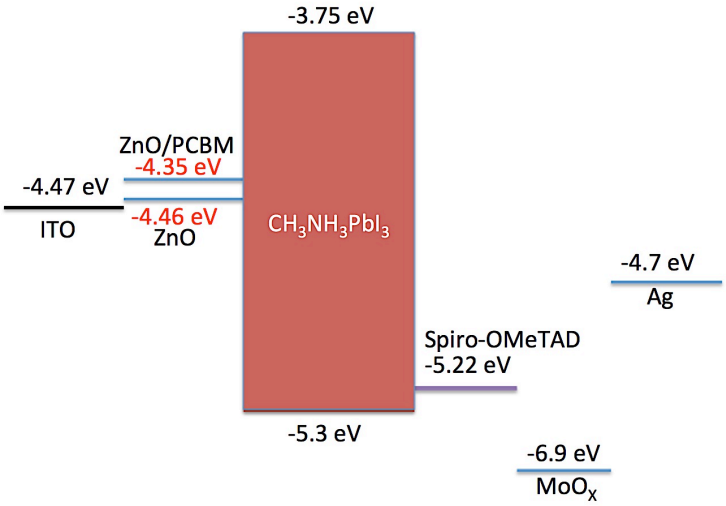


Figure 6.21 Flat band energy diagram showing the energy levels of the various materials contained in our device stacks. The measured change in work function of the aqueous processed ZnO (100 °C) and ZnO (100 °C)/PCBM is highlighted.

Here we notice that the introduction of PCBM on aqueous processed ZnO (100 °C) gives an opposite work function shift when compared to that by sol-gel method, as shown in the Chapter 5. This can be explained by the difference of the chemical component in two ZnO films. In sol-gel method, the low work function of sol-gel derived ZnO (110 °C) films is ascribed to the interfacial dipole formation between electron accepting ZnO and the electron donating amine group due to the MEA residues[12]. The influence of the interfacial dipole on film work function is alleviated by the PCBM coating. While in aqueous method, ZnO processed at 100 °C is already pure ZnO nanoparticles, thus the PCBM coating shows its ability to decrease the work function. To further confirm this, we measured the work function shift of sol-gel derived ZnO (450 °C) with PCBM layers, as shown in Table 6.8. In Chapter 3, sol-gel derived ZnO (450 °C) has been confirmed to be pure ZnO without organic residues. With the insertion of PCBM, the work function is shifted from 4.61 to 4.57 eV, which is the same trend with aqueous processed ZnO (100 °C).

Table 6.8 Work functions of sol-gel derived ZnO (450 °C) and ZnO (450 °C)/PCBM on ITO substrates, measured by Kelvin Probe.

	ZnO (450 °C)	ZnO (450 °C)/PCBM
Work Function (eV)	4.61	4.57

6.4 Conclusions

Here we successfully fabricate ZnO thin films processed using a remarkably simple solution processing and environmental friendly route. By carrying out a range of complementary measurements, we demonstrate the importance of the processing temperature on tuning structural, optical, compositional, surface morphological and electrical properties of the ZnO films. Using a combination of TEM and XPS, 100 ˚C processed films are confirmed as ZnO nanoparticles, without precursor and water left. The ZnO particle size increases with annealing temperature, which is supported by the XRD, SEM and UV-Vis results. Significant changes on electron mobility and work function with ZnO processing temperature are shown by thin film transistor and Kelvin probe, respectively.

We prove the 100 - 200 ˚C processed ZnO films as excellent ETLs in PCDTBT:$PC_{71}BM$ organic solar cells. Our objective was to develop a low temperature, environmental friendly, easy solution processable charge selective interlayer for organic photovoltaic devices that had high optical transparency, good charge transport and smooth compact surface morphology. The ZnO films we have developed fulfills the criteria for OPV interlayers.

Aqueous based ZnO films are also used as ETLs for methylammonium lead iodide perovskite solar cells. The processing temperature of ZnO influenced the surface morphology of perovskite films and, to a lesser degree, affected their thermal stability. ZnO films as ETLs resulted in efficient solar cells but did not overcome the issue of J-V hysteresis. By introducing PCBM as an interfacial modifier, the perovskite thermal stability was enhanced and the photocurrent hysteresis significantly reduced. The ZnO/PCBM bilayer ETLs fabricated at temperatures lower than 100 °C enable low-temperature processed, thermally stable, and efficient perovskite solar cells with conventional structure which showed negligible hysteresis.

References

[1] S. Meyers, J. Anderson, *J. Am. Chem. Soc.* **2008**, 17603.

[2] B. A. MacLeod, B. J. Tremolet de Villers, P. Schulz, P. F. Ndione, H. Kim, A. J. Giordano, K. Zhu, S. R. Marder, S. Graham, J. J. Berry, A. Kahn, D. C. Olson, *Energy Environ. Sci.* **2015**, *8*, 592.

[3] J. G. Lu, Z. Z. Ye, Y. Z. Zhang, Q. L. Liang, S. Fujita, Z. L. Wang, *Appl. Phys. Lett.* **2006**, *89*, 4.

[4] H. M. Cheng, K. F. Lin, H. C. Hsu, W. F. Hsieh, *Appl. Phys. Lett.* **2006**, *88*, 261909.

[5] C. Jiang, R. R. Lunt, P. M. Duxbury, P. P. Zhang, *RSC Adv.* **2014**, *4*, 3604.

[6] P. Nunes, E. Fortunato, R. Martins, *Thin Solid Films* **2001**, *383*, 277.

[7] Y. Natsume, H. Sakata, *Thin Solid Films* **2000**, *372*, 30.

[8] J. Liu, S. Shao, G. Fang, B. Meng, Z. Xie, L. Wang, *Adv. Mater.* **2012**, *24*, 2774.

[9] S. H. Park, A. Roy, S. Beaupré, S. Cho, N. Coates, J. S. Moon, D. Moses, M. Leclerc, K. Lee, A. J. Heeger, *Nat. Photonics* **2009**, *3*, 297.

[10] X. Ouyang, R. Peng, L. Ai, X. Zhang, Z. Ge, *Nat. Photonics* **2015**, *9*, 520.

[11] M. Kröger, S. Hamwi, J. Meyer, T. Riedl, W. Kowalsky, A. Kahn, *Org. Electron.* **2009**, *10*, 932.

[12] J. Zhang, J. C. D. Faria, M. Morbidoni, Y. Porte, C. H. Burgess, K. Harrabi, M. A. McLachlan, *Adv. Electron. Mater.* **2016**, *2*, 1600008.

[13] T. Oku, *Crystal Structures and Related Perovskite Compounds Used for Solar Cells*, **2015**.

[14] N. Onoda-Yamamuro, O. Yamamuro, T. Matsuo, H. Suga, *J. Phys. Chem. Solids* **1992**, *53*, 277.

[15] C. Bi, Q. Wang, Y. Shao, Y. Yuan, Z. Xiao, J. Huang, *Nat. Commun.* **2015**, *6*, 7747.

[16] N. J. Jeon, J. H. Noh, Y. C. Kim, W. S. Yang, S. Ryu, S. Il Seok, *Nat. Mater.* **2014**, *13*, 1.

[17] Y. Zhang, M. Liu, G. E. Eperon, T. C. Leijtens, D. McMeekin, M. Saliba, W. Zhang, M. de Bastiani, A. Petrozza, L. M. Herz, M. B. Johnston, H. Lin, H. J. Snaith, *Mater. Horiz.* **2015**, *2*, 315.

[18] B. Wu, K. Fu, N. Yantara, G. Xing, S. Sun, T. C. Sum, N. Mathews, *Adv. Energy Mater.* **2015**, *5*, 1500829.

[19] Y. Shao, Y. Fang, T. Li, Q. Wang, Q. Dong, Y. Deng, Y. Yuan, H. Wei, M. Wang, A. Gruverman, J. Shield, J. Huang, *Energy Environ. Sci.* **2016**, *501*, 395.

[20] L. G. Bach, N. G. Nguyen, V. T. T. Ho, *Int. J. Photoenergy* **2016**, *2016*, 1217576.

[21] J. Yang, B. D. Siempelkamp, E. Mosconi, F. De Angelis, T. L. Kelly, *Chem. Mater.* **2015**, 4229.

[22] Q. Chen, H. Zhou, T. Bin Song, S. Luo, Z. Hong, H. S. Duan, L. Dou, Y. Liu, Y. Yang, *Nano Lett.* **2014**, *14*, 4158.

[23] Y. Shao, Z. Xiao, C. Bi, Y. Yuan, J. Huang, *Nat. Commun.* **2014**, *5*, 1.

[24] Y. Hou, C. O. R. Quiroz, S. Scheiner, W. Chen, T. Stubhan, A. Hirsch, M. Halik, C. J. Brabec, *Adv. Energy Mater.* **2015**, *5*, 1501056.

[25] A. H. Ip, L. N. Quan, M. M. Adachi, J. J. McDowell, J. Xu, D. H. Kim, E. H. Sargent, *Appl. Phys. Lett.* **2015**, *106*, 143902.

[26] C. Tao, S. Neutzner, L. Colella, S. Marras, A. Ram, S. Kandada, M. Gandini, M. De Bastiani, G. Pace, L. Manna, M. Caironi, C. Bertarelli, A. Petrozza, *Energy Environ. Sci.* **2015**, *8*, 2365.

[27] L. Zuo, Z. Gu, T. Ye, W. Fu, G. Wu, H. Li, H. Chen, *J. Am. Chem. Soc.* **2015**, 2674.

[28] H. Zhou, Q. Chen, G. Li, S. Luo, T. B. Song, H. S. Duan, Z. Hong, J. You, Y. Liu, Y. Yang, *Science.* **2014**, *345*, 542.

Chapter 7 - Conclusions and Future Work

In this thesis, ZnO thin films have been investigated as electron transport layers (ETLs) for organic photovoltaic (OPV) and perovskite solar cells. With the aim of low temperature, simple and solution processing of ZnO films, two fabrication methods were employed: a sol-gel route and another utilizing aqueous ammonia as a solvent. Thin film properties of ZnO films deposited by both methods were studied using a range of complementary measurements and techniques. It has been shown that sol-gel and aqueous processed ZnO films both are effective ETLs in the application of OPVs. In the application of perovskite solar cells, the intrinsic thermal instability of the perovskite fabricated on ZnO has been overcome by incorporating a PCBM interlayer, resulting in all-low-temperature, thermally stable, low hysteresis and high performance devices. The detailed comparisons of ZnO by two methods are as follows:

	Sol-gel chemistry	**Aqueous processing**
Composition	*Low temperature (Low-T):* ZnO nanoparticles embedded in an extended amorphous organic matrix. *With T increasing:* Organic residues are gradually removed; ZnO particle size increases. *High temperature (High-T):* (002) orientation due to slow processes of solvent evaporation and decomposition or zinc precursor.	*Low-T:* ZnO nanoparticles only. *With T increasing:* ZnO particle size increases. *High-T:* (100) & (101) orientation due to fast processes of solvent evaporation and decomposition or zinc precursor.
Surface morphology	*Roughness*: small *Compactness*: T↑, better	*Roughness*: large *Compactness*: all good
Thickness control by spin coating	Thickness easy control in the range of 10 – 200 nm Due to the high solubility	Hard to be thicker > 50 nm Due to the low solubility
Optical transmission	Both highly transparent in the visible region. Direct bandgaps calculated from the Tauc plots both increase as the processing temperature decreases.	
Work function	*Low-T*: sol-gel derived film shows smaller work function than aqueous film, because the former have MEA residues. *With T increasing:* work functions both become larger in higher temperature processed ZnO during the crystallisation process.	

TFT mobility	Low-T: very low High-T: good	Low-T: good High-T: good
OPVs	Low-T processed films by two methods both show better performance than high temperature processed films, indicating that work function is more important than carrier mobility for thin film ETLs. The V_{OC} loss and enhanced leakage current with high temperature processed ZnO are both attribute to the overlarge work function.	
Thermal stability of perovskite on ZnO	Low-T ZnO: terrible ZnO T↑, perovskite stability↑	Low-T ZnO: moderate ZnO T↑, perovskite stability→
	High-T ZnO: both moderate, but the former is better than the latter due to ZnO orientation difference.	
Low-T ZnO /PCBM bilayer ETLs	*Advantage*: (1) PCBM improves perovskite thermal stability on Low-T based ETLs. (2) PCBM decreases the ETL surface roughness. (3) PCBM significantly reduces the J-V hysteresis. *Disadvantage*: (1) PCBM absorbs partial visible light.	
	Work function shifts to higher value when PCBM deposited on Low-T ZnO	Work function shifts to lower value when PCBM deposited on Low-T ZnO

Further study based on this work can be divided into four topics as follows:

Flexible and large area devices

Because the organic and perovskite solar cells have been successfully fabricated using all low temperature processes, the corresponding devices fabricated on flexible substrates, such as PET foils, are of interest. First, the fracture resistance of low temperature processed ZnO films by both sol-gel and aqueous processing should be investigated using standard bend tests[1]. Given that one system comprises of ZnO nanoparticles embedded in an organic matrix and the solely of ZnO nanoparticles, the influence of the organic amorphous matrix on the fracture resistance may be interesting. It is clear from the data presented that there are likely significantly fewer pinholes or macroscopic defects as the organic matrix does not undergo shrinkage or densification; as is the case in conventional high temperature processed ZnO sol-gel derived films. Then, the effect of the bending cycles on the solar cell device performance is of interest.

In terms of processing, spin coating used in this work actually is not an ideal method for large area devices due to; edge effects, inefficient materials use and the requirement for multiple coats to create dense films. Slot-die coating is a promising candidate for up-scaling, offering precise control of the film thickness, this method has been

effectively applied to the photoactive layer coating in OPV[2] and perovskite solar cells[3]. Sol-gel derived ZnO was reported using slot-die coating[2] but currently no aqueous processed ZnO films by slot-die coating are found. This is clearly an area that is worth exploring, particularly in the possibilities to compare the two ZnO processing routes.

Extrinsic Dopants

Incorporating extrinsic dopants to tune the optoelectronic properties is an interesting area to explore, to further enhance and tailor the properties of the materials developed in this work. Alternatively transparent conducting oxides (TCO) can be achieved by doping ZnO films with donor *i.e.* group III elements. For sol-gel chemistry, doping is typically applied on the high temperature processed polycrystalline ZnO films[4][5]. The doping dependence of optoelectronic properties of low temperature sol-gel processed films is still unclear. For aqueous processing, alkali metal[6] and Al[7] doping has been applied on the ZnO TFT. We also conducted a preliminary work of Ga doping, shown in Appendix D. Currently little work has been reported using aqueous processed doped ZnO as TCO, which is a topic worth studying.

Role of organic matrix in one-step processed nanoparticle/organic mixture

The sol-gel derived, low temperature processed ZnO, which was previously commonly considered as amorphous ZnO, has been confirmed a mixture of ZnO nanoparticles embedded in organic matrix in this study. The MEA in the organic matrix, which is the stabiliser used for preparation of the sol-gel precursor, acts as a work function modifier in solar cells. This simple one-step preparation of nanoparticle/organic mixture film could be applied to other sol-gel systems, in which oxides and functional organic substances can form stable complex.

This idea can also be applied to aqueous processing by adding functional organic material into aqueous zinc precursor solution. For example, films containing ZnO particles embedded in a cross-linking polymer matrix may achieve enhanced fracture resistance. Besides, organic light absorber mixed in ZnO films (e.g. perylene bisimide) can obtain photoconductive ETLs for the application of solar cells[8].

Nanostructured ZnO for organic and perovskite solar cells

We have fabricated ZnO nanorods and nanowalls by hydrothermal growth, as shown in Appendix A. Although some works were reported using ZnO nanostructures in organic[9] and perovskite solar cells[10][11], they typically used high temperature processed ZnO films as seed layers. In our study, the ZnO nanostructures were fabricated at all low temperature processes. Thus, flexible devices can be fabricated and the influence of piezoelectric effect of ZnO nanostructure on solar cell performance is of interest[12][13].

The work presented here relies on a well-studied material, ZnO, however it is clear that there is still lots to learn about this fascinating material and the impact of processing on the resultant optoelectronic properties. There is even more to explore when we consider the incorporation of ZnO into an organic matrix, the incorporation of extrinsic dopants, controlling intrinsic doping *etc.*

References

[1] H. R. Choi, S. K. Eswaran, S. M. Lee, Y. S. Cho, *ACS Appl. Mater. Interfaces* **2015**, *7*, 17569.

[2] H. C. Cha, Y. C. Huang, F. H. Hsu, C. M. Chuang, D. H. Lu, C. W. Chou, C. Y. Chen, C. S. Tsao, *Sol. Energy Mater. Sol. Cells* **2014**, *130*, 191.

[3] K. Hwang, Y. S. Jung, Y. J. Heo, F. H. Scholes, S. E. Watkins, J. Subbiah, D. J. Jones, D. Y. Kim, D. Vak, *Adv. Mater.* **2015**, *27*, 1241.

[4] J. H. Lee, B. O. Park, *Thin Solid Films* **2003**, *426*, 94.

[5] W. J. Park, H. S. Shin, B. Du Ahn, G. H. Kim, S. M. Lee, K. H. Kim, H. J. Kim, *Appl. Phys. Lett.* **2008**, *93*, 83508.

[6] S. Y. Park, B. J. Kim, K. Kim, M. S. Kang, K. H. Lim, T. Il Lee, J. M. Myoung, H. K. Baik, J. H. Cho, Y. S. Kim, *Adv. Mater.* **2012**, *24*, 834.

[7] Y. H. Lin, S. R. Thomas, H. Faber, R. Li, M. A. McLachlan, P. A. Patsalas, T. D. Anthopoulos, *Adv. Electron. Mater.* **2016**, *2*, 1.

[8] L. Nian, W. Zhang, N. Zhu, L. Liu, Z. Xie, H. Wu, F. Würthner, Y. Ma, *J. Am. Chem. Soc.* **2015**, *137*, 6995.

[9] L. Baeten, B. Conings, H.-G. Boyen, J. D'Haen, A. Hardy, M. D'Olieslaeger, J. V Manca, M. K. Van Bael, *Adv. Mater.* **2011**, *23*, 2802.

[10] D. Bi, G. Boschloo, S. Schwarzmüller, L. Yang, E. M. J. Johansson, A. Hagfeldt, *Nanoscale* **2013**, *5*, 11686.

[11] D. Son, J. Im, H. Kim, N. Park, *J. Phys. Chem. C* **2014**, *118*, 16567.

[12] Z. L. Wang, J. H. Song, *Science* **2006**, *312*, 242.

[13] S. Shoaee, J. Briscoe, J. R. Durrant, S. Dunn, *Adv. Mater.* **2014**, *26*, 263.

Appendix A - Sol-gel derived ZnO Films Properties

A.1 Starting materials

Table A.1 Starting materials

Materials	Formula	Parameters	Supplier
Zinc acetate dehydrate (ZAD)	$Zn(O_2CCH_3)_2{\cdot}2H2O$	≥ 99.0%	Sigma-Aldrich
2-amino ethanol (MEA)	$NH_2C_2H_4OH$	Not specified	Sigma-Aldrich
2-methoxyethanol	$HOCH_2CH_2OCH_3$	99.8%	Sigma-Aldrich
Zinc nitrate hexahydrate	$Zn(NO_3)_2{\cdot}6H_2O$	98%	Alfa Aesar
Hexamethylenetetramine (HMT)	$(CH_2)_6N_4$	≥99%	Alfa Aesar
Potassium chloride	KCl	≥ 99.0%	Sigma-Aldrich
Polyethylenimine (PEI)	$(C_2H_5N)_n$	Branched; M_w~25000 M_n~10000 PDI~2.5	Sigma-Aldrich
Potassium hydroxide	KOH	85%	VWR Chemicals
Indium tin oxide coated glass substrate (ITO substrate)	$In_2O_3 \cdot (SnO_2)_x$	12-16 Ω/sq 140 nm 12 × 12 mm^2	PsiOteC UK Ltd
Quartz substrate	SiO_2	10 × 10 mm^2	UQG Optics

A.2 Film thickness measurement

The thickness of ZnO layers was measured using a DekTak 150. The films were prepared by spin-coating the solution of concentrations of 0.11 M, 0.3 M, 0.5 M and 0.75 M respectively at a loading speed of 500 rpm and a coating speed of 3000 rpm. All the layers here were deposited at 300 ˚C and then postannealed at 450 ˚C. The solution concentration-dependent thickness is plotted in the Figure A.1. As can be seen, the thickness of ZnO seed layer increases with the increase of solution concentration. The average values and standard deviations in detail are shown in Table A.2. It is interesting that the film thicknesses obtained at a coating speed of 3000 rpm here are nearly equal to those at a coating speed of 2000 rpm as the thickness is normally considered to be proportional to ω^{-2}, where ω is the angular velocity[1]. The data of films with 2000 rpm speed is shown in Table A.3. The purpose of increasing the coating speed is to increase the large area uniformity which is required in the photovoltaic devices.

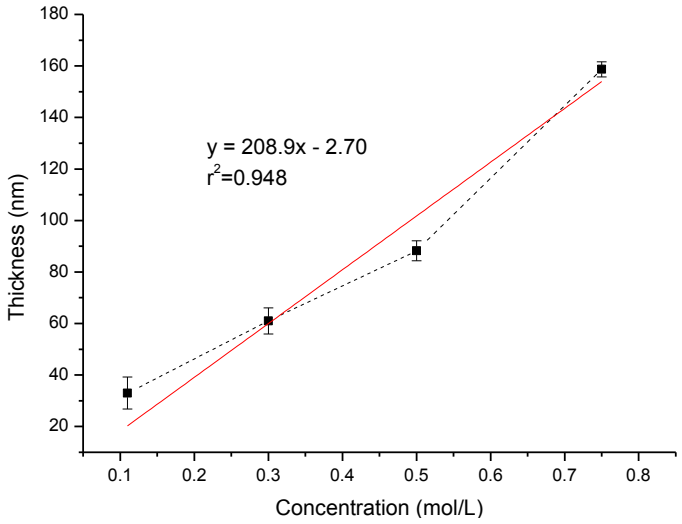


Figure A.1 The relationship between the thickness of ZnO planar films and the solution concentration. The average values are plotted and standard deviations are shown as error bars.

Table A.2 Thickness of ZnO planar films at 3000 rpm spinning speed

		Concentration			
		0.1 M	0.3 M	0.5 M	0.75 M
Measured thickness (nm)	1	34.6	65.3	95.2	154.1
	2	30.2	69.1	92.7	161.8
	3	28.4	62.5	90.2	162.3
	4	38.8	64.2	89.5	157.7
	5	41.0	58.7	91.4	161.9
	6	36.0	60.3	88.3	158.5
	7	30.3	57.8	84.6	154.8
	8	28.1	64.7	86.3	157.3
	9	24.7	54.4	90.0	160.9
	10	27.2	51.7	88.1	157.5
	11	43.9	62.0	83.8	
	12			81.2	
				85.8	
Average thickness (nm)		33.0	61.0	88.2	158.7
Standard deviation (nm)		6.3	5.1	3.9	3.0

Table A.3 Thickness of ZnO planar films at 2000 rpm spinning speed

		Concentration				
		0.1 M	0.3 M	0.5 M	0.75 M	0.95 M
Measured thickness (nm)	1	27.2	50.9	86.6	160.3	199.3
	2	24.8	49.8	85.1	163.1	193.7
	3	25.4	57.9	85.4	165.6	185.1
	4	14.8	65.8	74.9	154.0	183.2
	5	18.8	54.8	76.9	149.3	188.5
	6	19.1	65.1	92.5	158.6	198.2
	7	38.0	62.1	91.2	150.0	187.6
	8	37.5	67.1	90.1	151.6	185.1
	9	35.8	53.7	87.7	156.0	198.8
	10	39.2	63.1	81.5	143.3	194.0
Average thickness (nm)		28.1	59.0	85.2	155.2	191.3
Standard deviation (nm)		9.0	6.4	5.9	6.9	6.2

A.3 TGA results of zinc acetate dihydrate

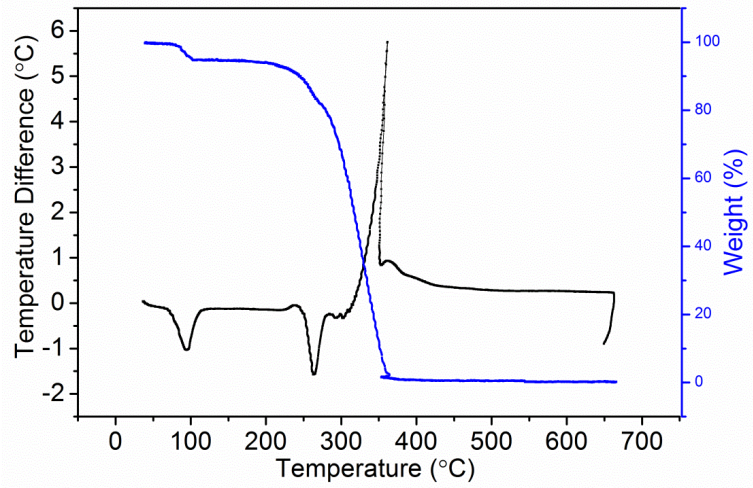


Figure A.2 TGA curve of ZnO formation from zinc acetate dihydrate.

A.4 ZnO nanostructures by hydrothermal growth

ZnO hydrothermal growth was studied with sol-gel derived ZnO thin film as seed layers. Different nanostructures, including dense thick planar layers, nanowalls and nanorods, were obtained by controlling the synthesis conditions.

Seeded substrates are suspended in a solution at a given temperature for the hydrothermal deposition. The formation of ZnO nanostructures is attributed to the different surface energies of the polar (002) and non-polar (100) surfaces[2]. The

nanorods obtained by this way has been proved to be single crystalline characterised using transmission electron microscopy (TEM)[3].

The recipe of ZnO nanorods growth in this project is mostly determined by the previous work in the research group[4]. The reaction of hydrothermal deposition is between $Zn(NO_3)_2$ and HMT of the same concentration – typically 25mM[2][5]. The concentration of reactants is proved to have an influence on the nanorod diameter[5]. To achieve a high aspect ratio nanorod array, the temperature of water bath is set to as high as 95°C because the growth rate along [001] direction is more sensitive to reaction temperature compared to those along [101] and [100] directions[6]. There are generally two kinds of additives - one is to influence the HMT degradation and the other is to affect adsorption of ions to ZnO crystalline surfaces. Ammonia is in the first kind as it slows down the HMT degradation resulting the enhancement of nanorod length[7]. As for the second kind, two nonreactive additives are available, which are surfactants and inorganic ionic additives. The addition of polyethylienamine (PEI) surfactant improves the aspect ratio of nanorods as PEI impedes the growth in the lateral direction via adsorption on the non-polar surfaces[8]. In terms of inorganic ionic additives, our research group developed a novel method using potassium chloride (KCl) to control the nanorod morphology[2]. The ability to stabilise the polar (002) surface enables KCl to tune the process of growth via changing the growth rates of different directions, which is shown in Figure A.3. By applying low concentration KCl, the length of nanorods is increased and the diameter is reduced. However, high concentration, which means the complete adsorption, will result in the near-coalesced formation with planar termination as the growth of <002> direction is hindered in comparison with that of non-polar <100> direction. In addition, the uniformity and vertical alignment of nanorod arrays are improved with the increasing KCl concentration. It is also found that the nucleation step is not influenced by KCl addition as the nucleation densities keep similar under different KCl concentrations. The nanorods prepared by this method are single crystals, confirmed by transition electron microscopy and selected area diffraction[4].

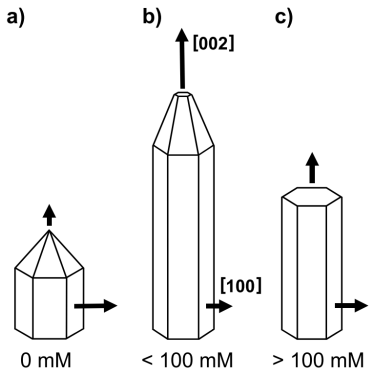


Figure A.3 Schematic diagram illustrating the variation of nanorod growth with KCl addition, a) 0 mM, b) <100 mM, c) >>100 mM. Adapted from Ref[2].

A.4.1 Experimental

Nanorod Synthesis: $Zn(NO_3)_26H_2O$ (25 mM) and KCl (0.1 M) were dissolved together with 980 ml deionized (DI) water in a 1 L glass reagent bottle, solution A. Branched low molecular weight polyethylene imine (PEI, 10 mM) and hexamethyltetra amine (HMT, 25 mM) were put in 20 ml deionized water and were sonicated for 2 hours for complete dissolution, solution B. The temperature of water bath was held at 95 ± 1˚C. Substrates were suspended at a fixed height in the bottle with seed layers facing down. The pictures of water bath settings are shown in Figure A.4.

Solution A ($Zn(NO_3)_26H_2O$ + KCl) was first mixed together with solution B (PEI + HMT) at room temperature. The substrates were subsequently put into the bottle filled with mixed solution. Then we put the bottle into the water bath already reaching 95 ± 1 ˚C to start the reaction. The growth time depends on the nanorod length needed provided the reactants were not completed consumed. Growth time of 85 minutes typically gains ~500 nm nanorods arrays. After deposition, the substrates are removed from the bottle immediately and are rinsed with DI water, then dried at 70 ˚C in air.

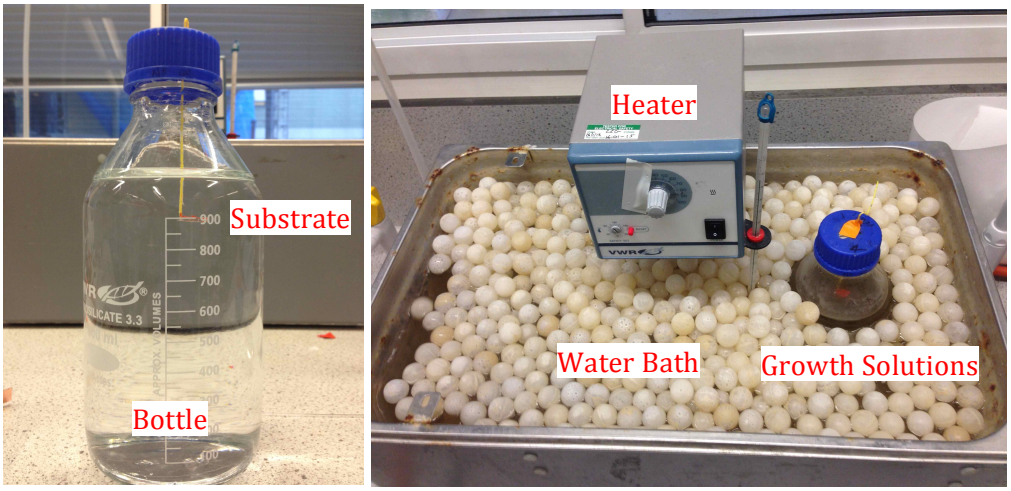


Figure A.4 Pictures of water bath apparatus.

Dense Bilayer: Solution A was changed to $Zn(NO_3)_26H_2O$ (0.1 M), without KCl. Solution B was changed to HMT (0.1 M), without PEI. The temperature of water bath was held at 75 ± 1 ˚C. Growth time was fixed at 3 hours. All other conditions were the same as nanorod synthesis.

Nanowalls: Nanowalls were obtained by selective-etching the dense bilayer with KOH. The etching was done by immersing the substrates with dense thick planar layer into 0.25 M KOH solution at 80 ˚C.

The diameter, length and areal density of the nanorods are quantified from SEM images utilizing ImageJ software.

A.4.2 Nanorods

First the necessary of seed layer on the nanorod growth was confirmed, Figure A.5. No nanorod was detected by SEM for hydrothermal growth on bare ITO substrate.

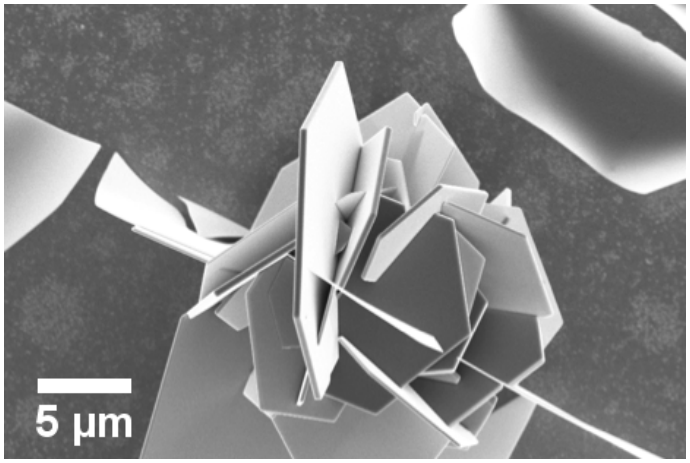


Figure A.5 Hydrothermal growth on bare ITO substrates, no nanorod arrays are found.

Then we investigated how seed layer influenced the nanorod growth. The transmission spectra of ZnO nanorods on seed layers with different heat treatment conditions against an air reference are shown in Figure A.6. The seed layers were deposited on ITO substrates with the solution concentration of 0.3 M. The transmission of nanorods all exceeds 70% in the visible region. An obvious fringe is observed in the nanorods on the seed layers with 450˚C postheating in comparison with the nanorods on the seed layers without postheating. A possible explanation could be that the seed layer with postheating is more uniform than that without postheating since rearrangement of ions and atoms occur and the defects are removed during the postheating process. Thus, the nucleation and growth of nanorods on a more uniform seed layer result in the uniform nanorods in thickness.

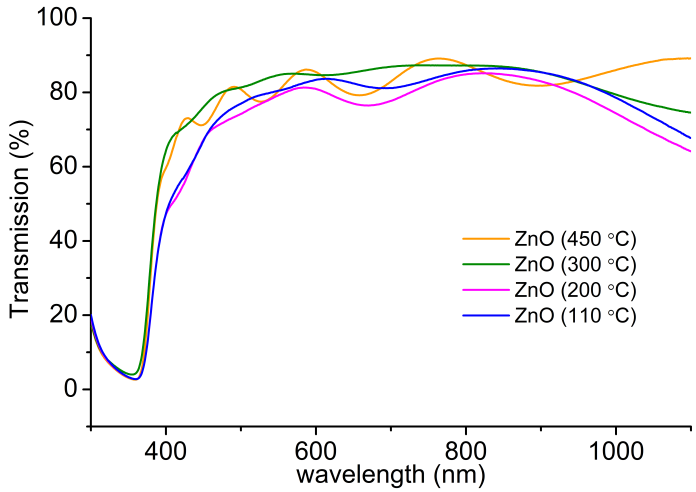


Figure A.6 UV-vis spectra for Glass/ITO/ZnO seed layers with different heat treatment conditions/ZnO nanorods in the range of 300-1100nm.

The influence of heat treatment conditions of seed layers on the nanorods has also been investigated by XRD, as shown in Figure A.7. The nanorods with postheated seed layers (450 ˚C) show much higher (002) peak intensity than the ones with non-postheated seed layers (110 – 300 ˚C). This may be attributed to that the ZnO (450 ˚C) already has (002) orientation, which will enhance the (002) peak intensity or a better alignment in the nanorods with postheated seed layers.

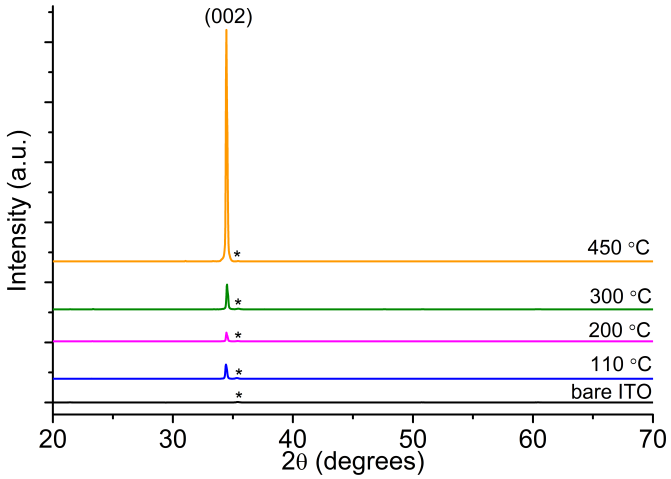


Figure A.7 XRD patterns of ITO/ZnO seed layers with varying processing temperatures/ZnO nanorod stacks. (* ITO diffraction Peaks)

Table A.4 The FWHM and (002) peak intensity obtained from XRD patterns of ZnO nanorods with seed layers of different heating conditions.

Heating conditions of seed layers	110 ˚C	200 ˚C	300 ˚C	450 ˚C
Thickness of seed layers (nm)	33.01	60.97	88.23	158.69
FWHM (º)	0.17	0.16	0.16	0.16
(002) Peak Intensity (Counts)	11669	6962	20067	184037

The morphology of ZnO nanorods was studied by SEM. The variation of nanorods with the thickness of seed layers is shown in Figure A.8 and the nanorod diameter, length and areal density are quantified in Table A.5. All the seed layers were deposited on ITO substrates, subsequently preheated at 350 ˚C and postheated at 450 ˚C. The diameters of nanorods on 0.1 M and 0.3 M seed layers are smaller than those on 0.5 M and 0.75 M seed layers. This observation may be related to the smaller grain size of first two seed layers[6]. Correspondingly, the areal density of nanorods grown on the seed layers with Zn concentrations of 0.1 M and 0.3 M are larger than that grown on the seed layers with concentrations of 0.5 M and 0.75 M as the density of nucleation sites where the initial nucleation occurs decreases with the increase of grain size. Also, a lower nucleation density allows the nanorods to have more free spaces to grow without interfering with each other, which results in the longer rods. In addition, according to the SEM images,

the degree of alignment of the nanorods on thinner seed layers (0.1 M and 0.3 M) shows a better alignment than that on thicker seed layers. This might also be ascribed to the lower density of nuclei formed in the thicker seed layers, leading to the inclination of the grown rods.

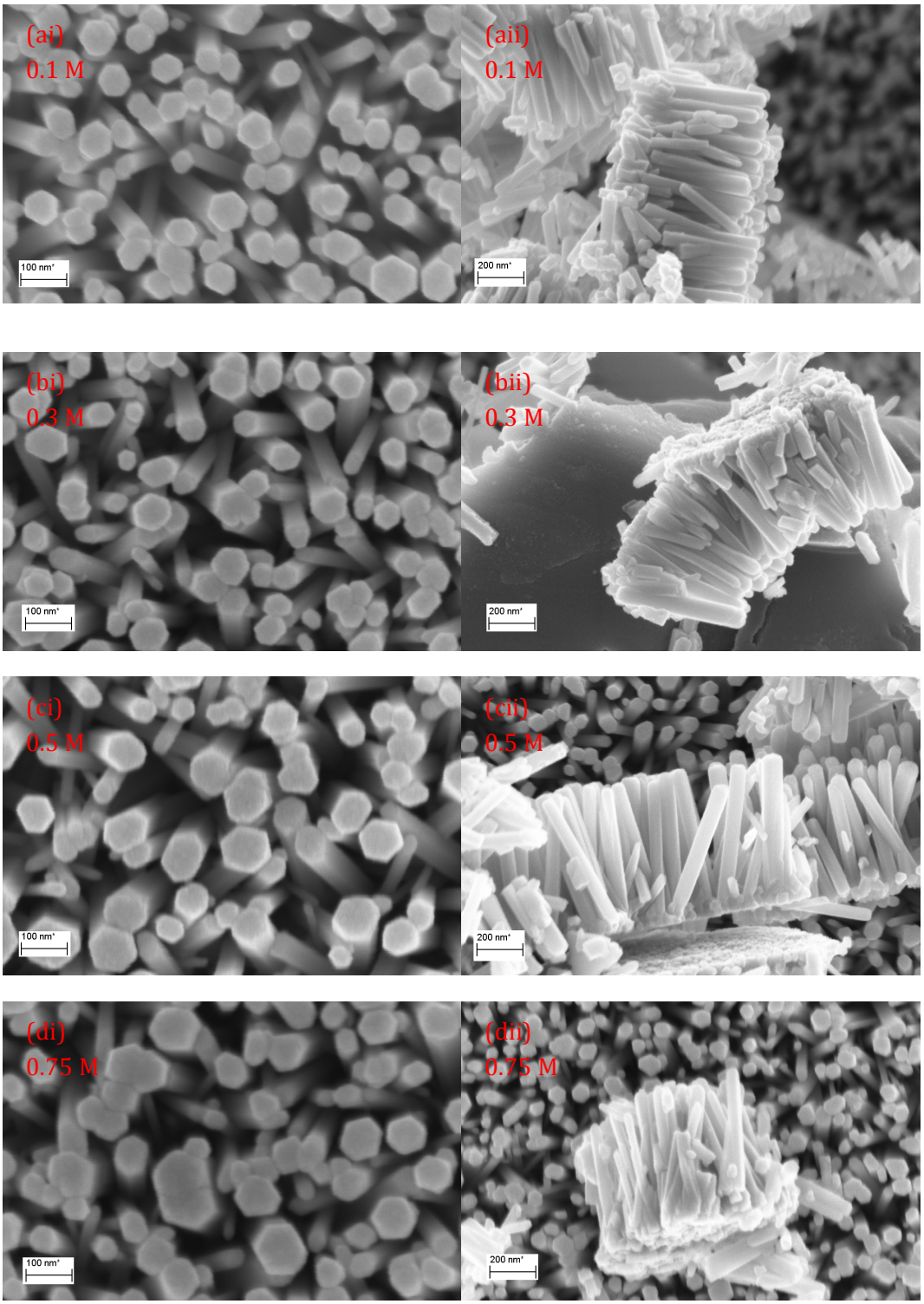


Figure A.8 SEM images of nanorods on the seed layers with different thicknesses, (a) 0.1 M, (b) 0.3 M, (c) 0.5 M, (d) 0.75 M.

Table A.5 The diameter, length and areal density of nanorods by variation of seed layer thickness

Concentration of sol solution	0.1 M	0.3 M	0.5 M	0.75 M
Thickness of seed layers (nm)	33.0	61.0	88.2	158.7
Nanorod Diameter (nm)	63 ± 11	62 ± 12	76 ± 17	72 ± 16
Nanorod Length (nm)	481 ± 56	475 ± 56	510 ± 72	502 ± 44
Nanorod Density (rods μm^{-2})	141	138	108	122

The influence of heating conditions of seed layers on the morphology of nanorods was also investigated, as shown in Figure A.9. The nanorod diameter, length and areal density are quantified on the seed layers with 0.3 M concentration treated under conditions: (a) 110 ˚C, (b) 200 ˚C, (c) 300 ˚C, (d) 450 ˚C. The nanorods on 450 ˚C treated seed layer have the highest areal density and the ones with 110 ˚C have the lowest areal density. Compared with the seed layer preaheated at 110 ˚C, at which the vaporisation of solvents is at the initial stage and the decomposition of zinc acetate has not occurred, the seed layer of ZnO (450 ˚C) crystallised and the ions and atoms rearranged and orientated, which satisfies the columnar grain growth along the (002) direction due to the minimum free energy of the (002) plane. In the meantime, the defects were reduced as well. Therefore, the resulted better (002) orientation and the decrease in the defects enable a higher nucleation density for the growth of nanorods, corresponding to a higher density of nanorods. Also, less interaction and impingement of nanorods with more (002) oriented seed layers may occur during the competitive period, leading to a higher density as well[9]. Correspondingly, the nanorods are more aligned but with a shorter length for these dense nanorods. The morphology of nanorods on postheated seed layer is similar to that of nanorods with pulsed laser deposited seed layer that the seed layer is also highly (002) oriented, as shown in Figure A.10 and Table A.7.

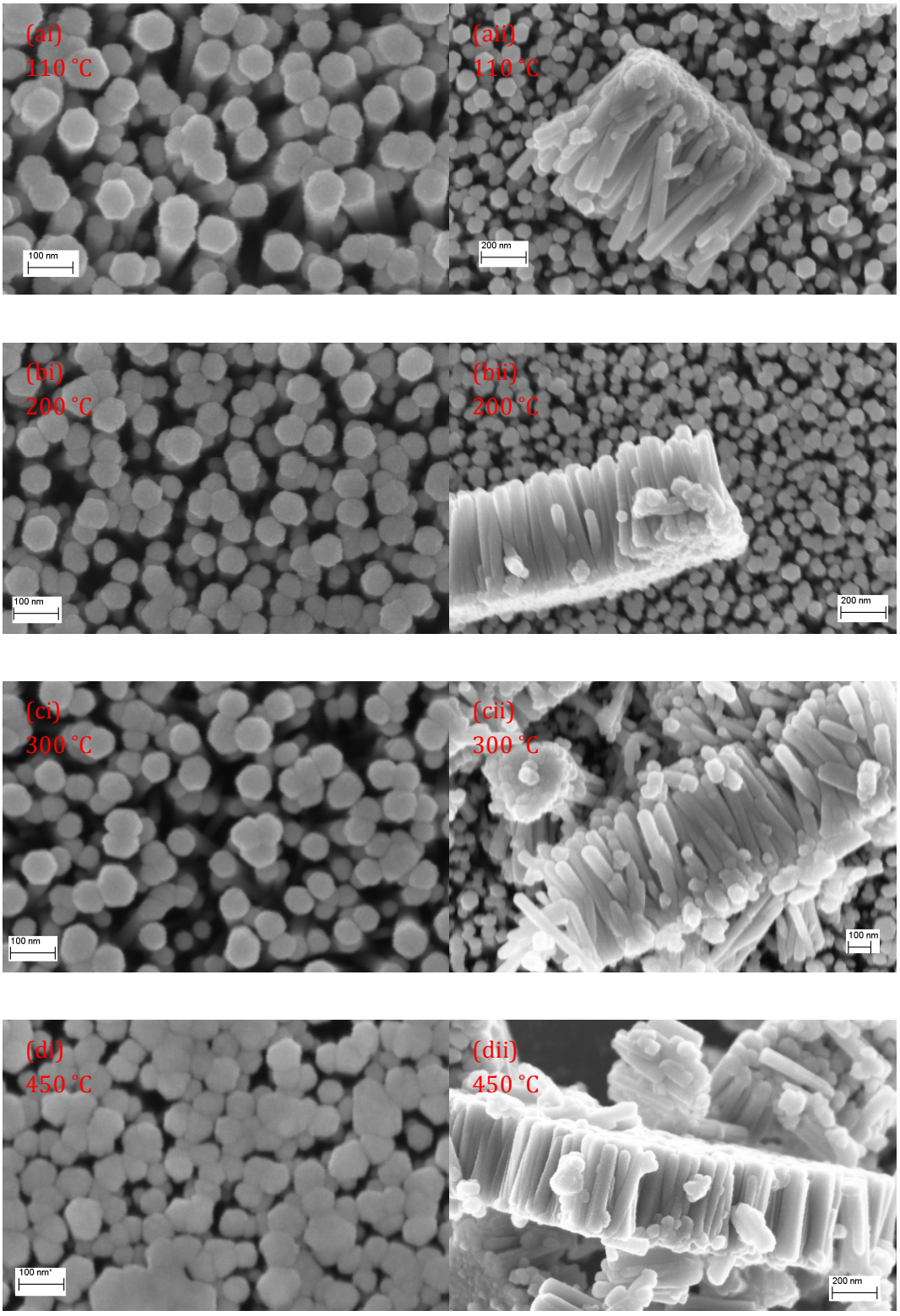


Figure A.9 SEM image of nanorods on the seed layers of different heating conditions, (a) 110 ˚C, (b) 200˚C, (c) 300˚C, (d) 450˚C.

Table A.6 The diameter, length and areal density of nanorods by variation of the seed layer heating conditions.

Heat conditions of seed layers	110 ˚C	200 ˚C	300 ˚C	450 ˚C
Diameter (nm)	77 ± 9	71 ± 10	71 ± 9	66 ± 10
Length (nm)	505 ± 40	467 ± 31	499 ± 36	410 ± 36
Density (rods μm^{-2})	157	180	174	200

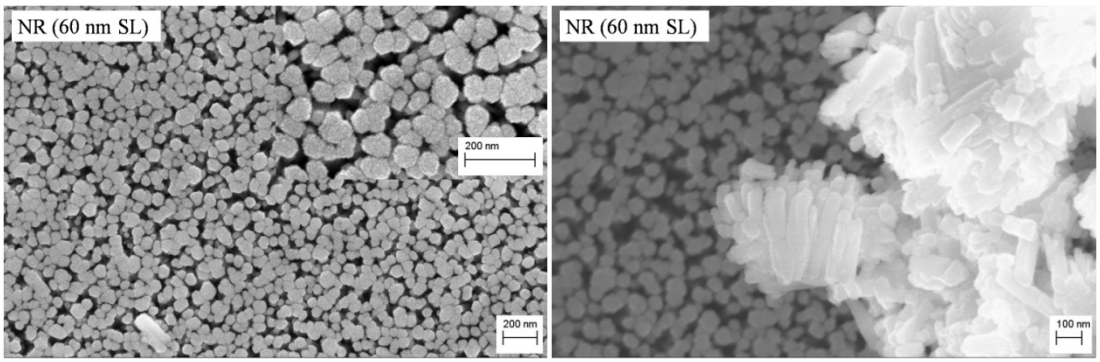


Figure A.10 SEM images of nanorods on 60nm-thick seed layers by pulsed laser deposition (PLD).

Table A.7 Nanorod parameters of nanorods on seed layers by PLD.

Thickness (nm)	30	60	85	155	190
Diameter (nm)	63 ± 20	68 ± 11	73 ± 15	72 ± 13	96 ± 14
Length (nm)	340 ± 8	360 ± 13	346 ± 13	396 ± 10	342 ± 12
Density (rods μm^{-2})	191 ± 16	207 ± 7	247 ±12	243 ± 16	258 ± 14

A.4.3 Dense layer and nanowalls

We also investigated ZnO dense planar layer and nanowalls by hydrothermal growth. For the aim of low temperature processed ZnO, sol-gel derived ZnO (110 ˚C) is used as seed layer. To get dense layer by hydrothermal growth, the nanorods are expected to closely coalesce with each other. The water bath temperature is therefore decreased from 95 ˚C for nanorods to 75 ˚C because higher temperature leads to higher growth rate along [002] direction while shows little influence on [101] and [100] directions[6]. The concentrations of zinc nitrate and HMT are increased from 25 mM to 100 mM because higher reactant concentration results in higher diameter of nanorods[5]. PEI is not used in dense layer growth because PEI can retard the growth in the lateral direction via adsorption on the non-polar surfaces[8]. The dense planar film is confirmed from the SEM images, Figure A.11.

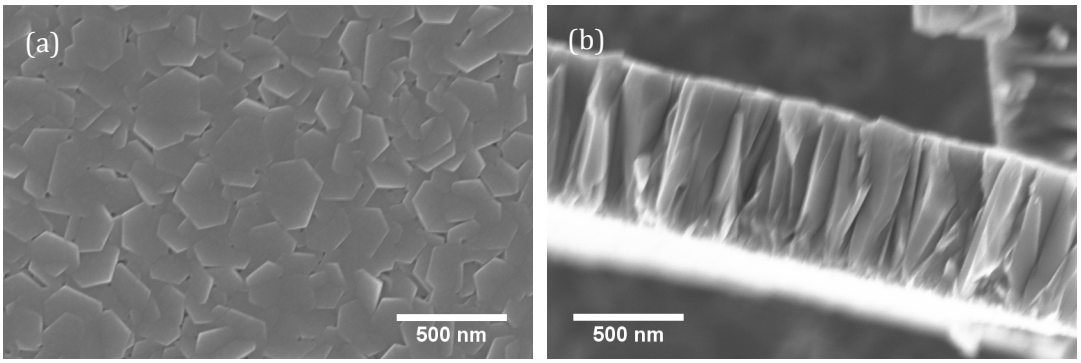


Figure A.11 SEM images of dense layer, (a) top-view and (b) cross section.

ZnO nanowalls were obtained by etching the aforementioned hydrothermal synthesised dense layer with KOH. The etching course was investigated. After 15 min etching the nanowall morphology has been acquired, showing that the etching starts from the center of hexagon, Figure A.12. The thickness of the walls is around 50 nm.

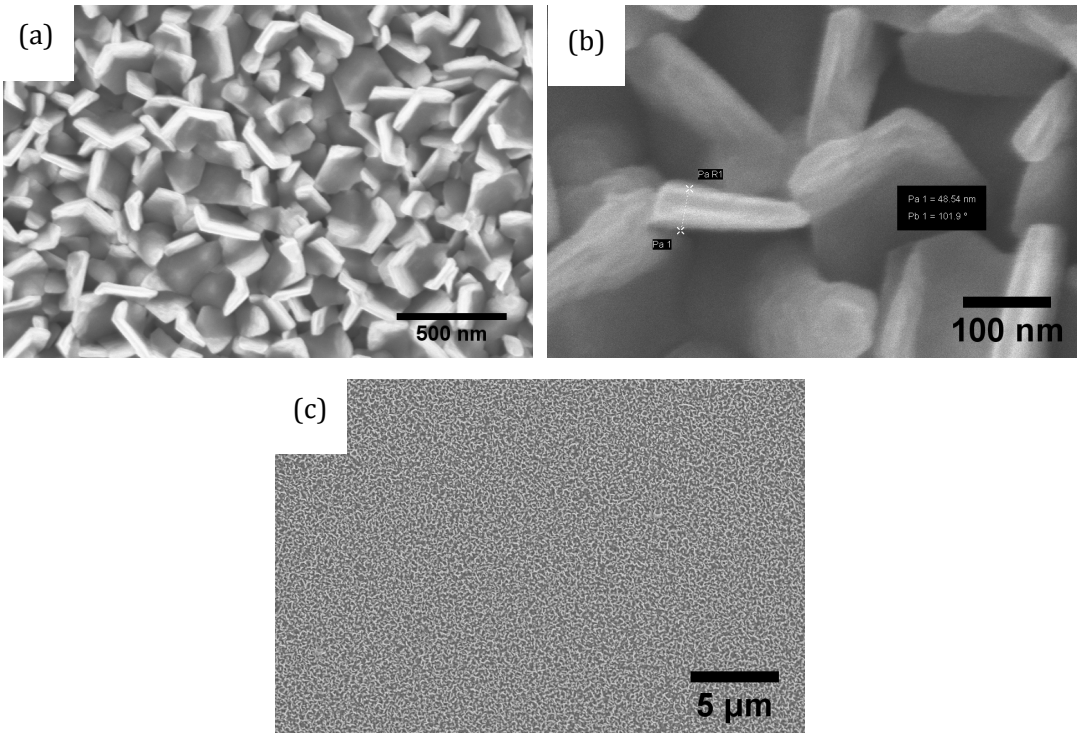


Figure A.12 ZnO nanowalls obtained by etching dense layer in KOH for 15 min, (a) nanowall morphology from top-view; (b) enlarged image shows the wall thickness around 50 nm; (c) uniform morphology is confirmed in large area.

After 30 min etching, the wall thickness is barely changed but the wall width is decreased, Figure A.13.

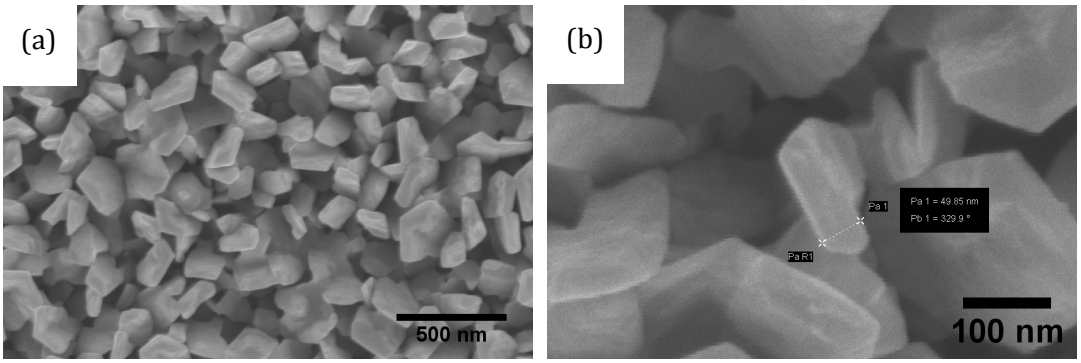


Figure A.13 Etching in KOH for 30 min, (a) nanowall morphology from top-view shows wall width is decreased; (b) enlarged image shows no change of wall thickness.

Finally, after 1 hour etching, all ZnO nanostructure is dissolved, Figure A.14.

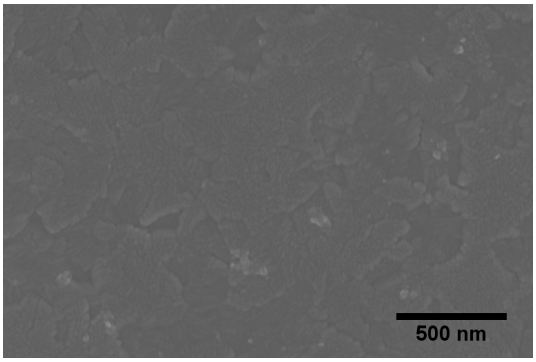


Figure A.14 Etching after 1h shows no ZnO nanostructure left.

In conclusion, ZnO nanostructures by hydrothermal growth based on seeded sol-gel derived ZnO planar film have been investigated, showing the successful synthesis of all-step low temperature (< 110 °C) processed ZnO nanorods, nanowalls and thick planar layer.

Appendix B - Sol-gel derived ZnO as Electron Transport Layers for Organic Solar cells

B.1 Starting materials

Table B.1 Starting materials

Materials	Formula	Purity	Supplier
Poly(3-hexylthiophene-2,5-diyl) (P3HT)	$(C_{10}H_{14}S)_n$	M_w~84,660Da M_n~54,500 PDI~1.553	De Mello group, Imperial College
Indene-C60 bisadduct (ICBA)	$C_{78}H_{16}$	Not specified	Nano-C
Poly[[4,8-bis[(2-ethylhexyl)oxy]benzo[1,2-b:4,5-b']dithiophene-2,6-diyl][3-fluoro-2-[(2-ethylhexyl)carbonyl]thieno[3,4-b]thiophenediyl]] (PTB7)	$(C_{41}H_{53}FO_4S_4)_n$	M_w>40,000 PDI~2.0	Ossila
[6,6]-Phenyl-C71-butyric acid methyl ester ($PC_{71}BM$)	$C_{82}H_{14}O_2$	>99%	Ossila
Poly(9,9-dioctylfluorene-*alt*-benzothiadiazole) (F8BT)	$(C_{35}H_{42}N_2S)_n$	M_w~115K PDI~3.2	American Dye Source
Chlorobenzene	C_6H_5Cl	99%	Sigma-Aldrich
1,8-diiodooctane	$I(CH_2)_8I$	98%	Sigma-Aldrich
Acetone	C_3H_6O	~100.0%	VWR Chemicals
Isopropanol	C_3H_8O	99.9%	VWR Chemicals

B.2 ZnO thickness dependent OPVs

The influence of film thickness of sol-gel derived ZnO on P3HT:ICBA based solar cell performance was investigated, as shown in Figure B.1-4.

It can be seen that V_{OC} is not particularly sensitive to ZnO thickness for all processing temperatures. ZnO layers with precursor concentration of 0.1 M show slightly decreased V_{OC} compared with 0.3 M and 0.5 M, which is possibly too thin to fully avoid the contact between ITO and photoactive layer, thus the recombination might occur at the interface.

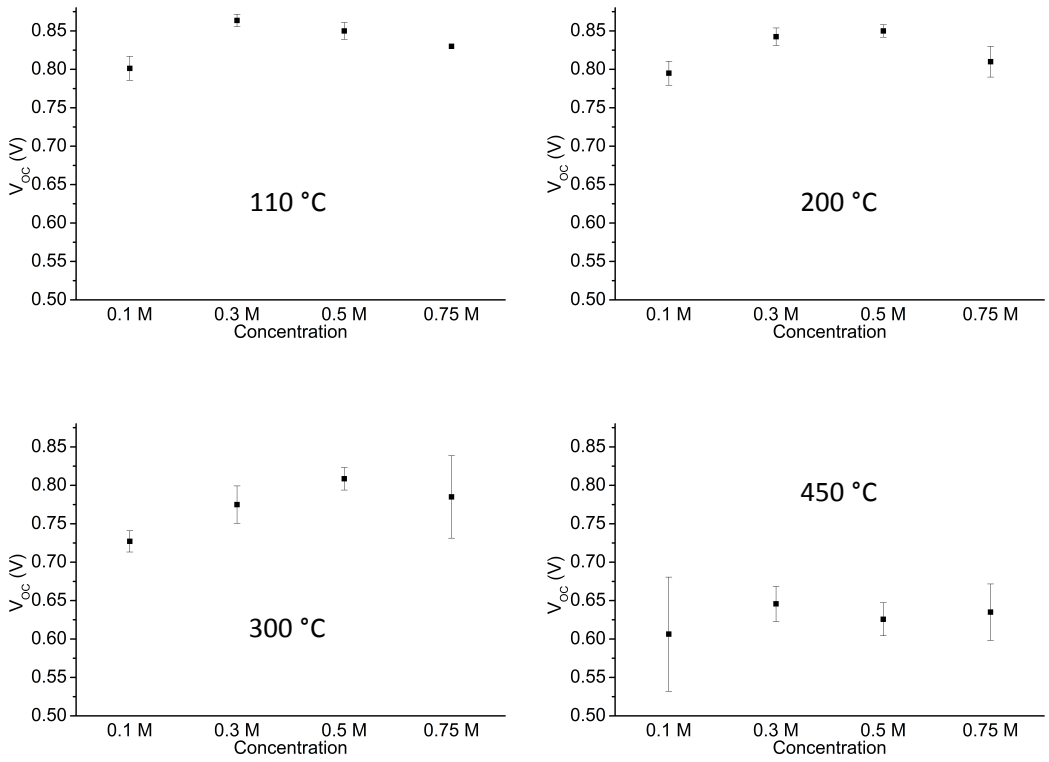


Figure B.1 Open-circuit voltage (V_{OC}) changing with ZnO film thickness (controlled by precursor concentration) under different ZnO processing temperatures.

The J_{SC} of ZnO (110 ˚C) is very sensitive to the film thickness, which may originate from the high resistivity of ZnO (110 ˚C) confirmed in Chapter 3. ZnO (200 ˚C) shows less sensitivity of thickness on J_{SC}. As for 300 and 450 ˚C, 0.1 M shows decreased J_{SC} compared with higher thickness, which may result from photogenerated carrier recombination due to cracks formed during solvent evaporation and crystallisation. The similar J_{SC} of ZnO at 450 ˚C among 0.3 to 0.75 M may benefit from the highly (002) oriented polycrystalline films in which the fast electron transport is expected in the direction vertical to the substrates.

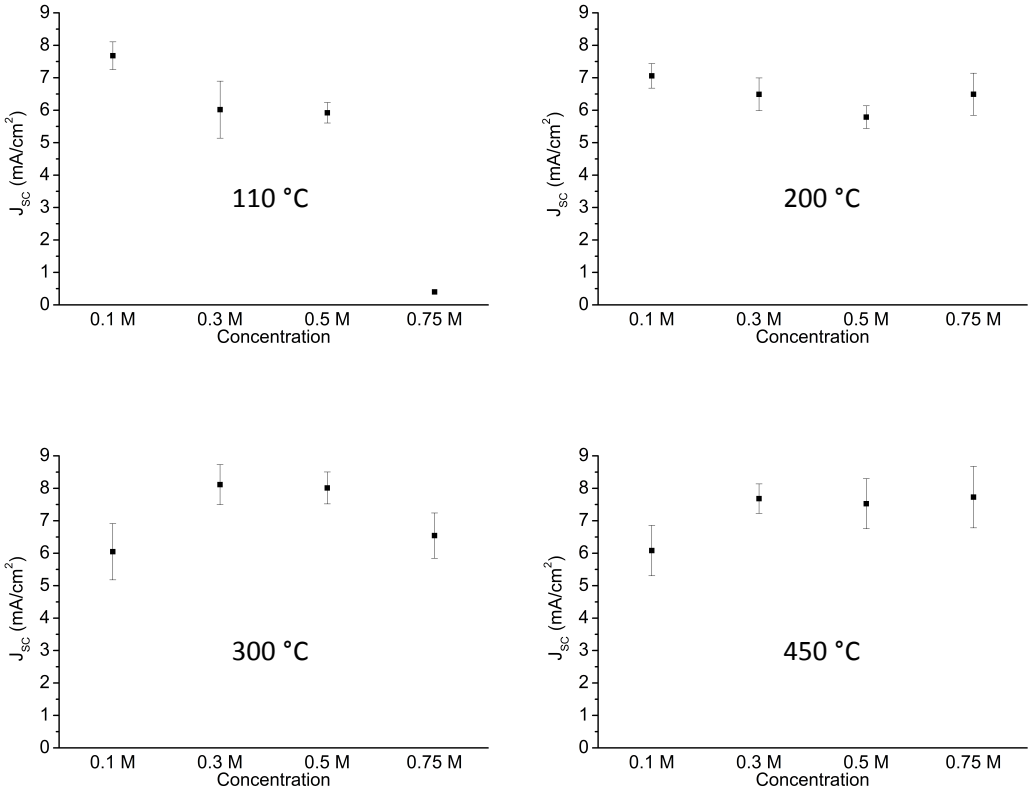


Figure B.2 Short-circuit current density (J_{SC}) changing with ZnO film thickness under different ZnO processing temperatures.

0.1 M shows decreased FF compared with 0.3 M for all ZnO processing temperature, indicating 0.1 M is too thin. For ZnO 110 – 300 ˚C, FF decreases with film thickness increasing from 0.3 M to 0.75 M. For ZnO at 450 ˚C, FF keeps similar within 0.3 M to 0.75 M.

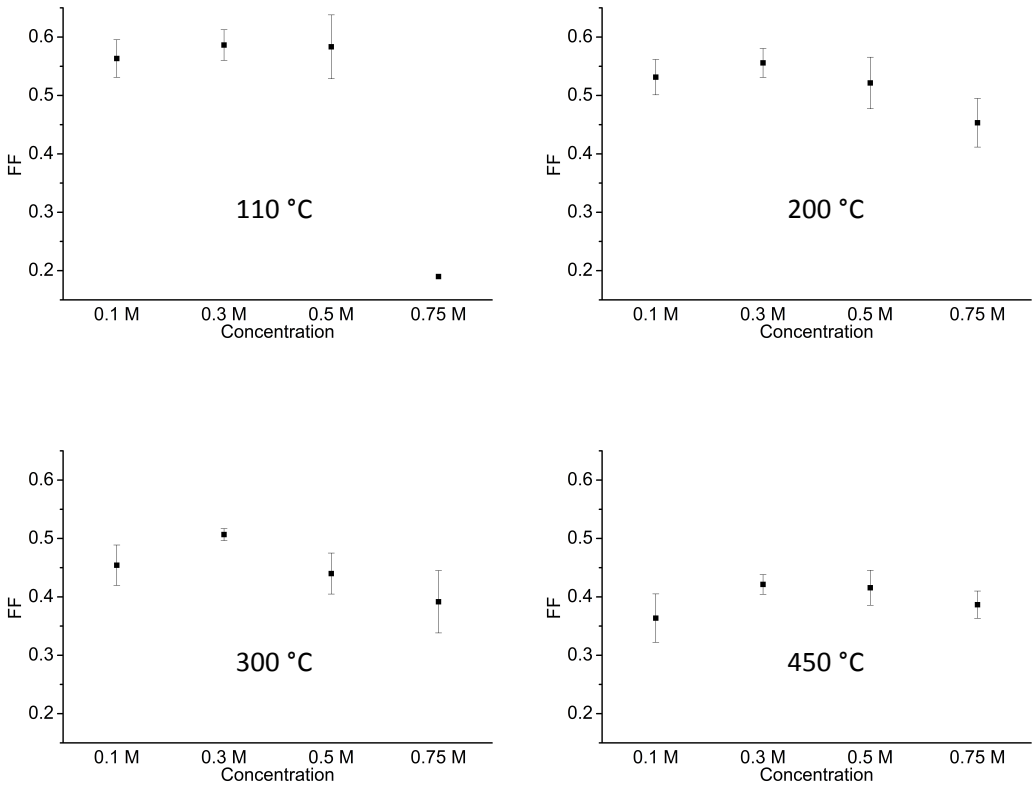


Figure B.3 Fill factor (FF) changing with ZnO film thickness under different ZnO processing temperatures.

PCE is the overall overcome of the V_{OC}, J_{SC} and FF changing. For ZnO (110 ˚C), 0.1 M to 0.5 M all works well. For ZnO (200 ˚C), 0.5 M and 0.75 M show a slight decrease of PCE compared with 0.1 M and 0.3 M. For ZnO (300 ˚C), 0.3 M and 0.5 M works better than 0.1 M and 0.75 M. For ZnO (450 ˚C), 0.3 – 0.75 M keeps similar with a drop on 0.1 M.

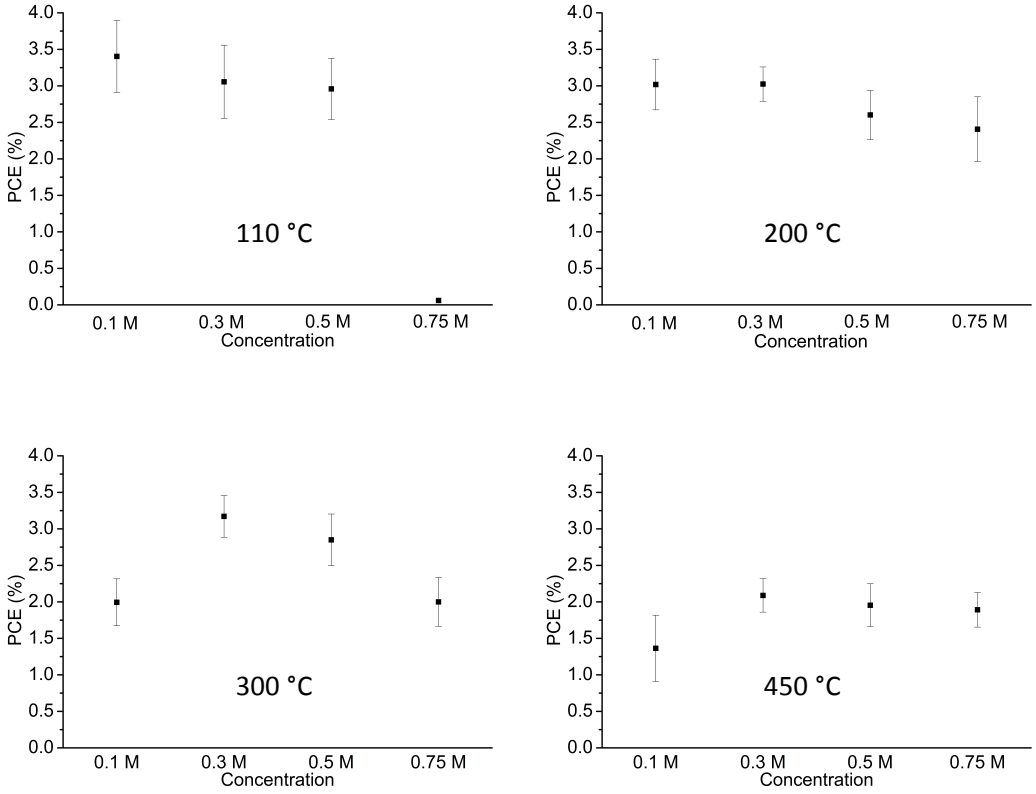


Figure B.4 Power conversion efficiency (PCE) changing with ZnO film thickness under different ZnO processing temperatures.

B.3 Statistical data of OPV performance

Table B.2 Statistical data of P3HT:ICBA based OPV devices

	V_{oc} (V)	J_{sc} (mA/cm²)	FF (%)	PCE (%)	R_s (Ω cm²)	R_{sh} (Ω cm²)
no ZnO	0.32 ± 0.06	2.85 ± 1.81	27.5 ± 2.2	0.27 ± 0.24	171.5 ± 55.4	234.2 ± 98.6
ZnO (25 ˚C)	0.57 ± 0.07	1.17 ± 0.50	14.8 ± 2.8	0.10 ± 0.05	2452.8 ± 1393.5	289.0 ± 73.4
ZnO (110 ˚C)	0.86 ± 0.01	6.02 ± 0.88	58.6 ± 2.6	3.05 ± 0.50	16.9 ± 2.9	1953.5 ± 626.5
ZnO (200 ˚C)	0.84 ± 0.01	6.49 ± 0.50	55.6 ± 2.5	3.03 ± 0.23	21.1 ± 1.1	1044.5 ± 269.1
ZnO (300 ˚C)	0.78 ± 0.02	8.11 ± 0.62	50.7 ± 1.0	3.17 ± 0.29	25.8 ± 2.1	500.6 ± 114.5
ZnO (450 ˚C)	0.65 ± 0.02	7.68 ± 0.45	42.1 ± 1.7	2.09 ± 0.23	30.1 ± 1.8	233.7 ± 42.0

Table B.3 Statistical data of PTB7:$PC_{71}BM$ based OPV devices

	V_{oc} (V)	J_{sc} (mA/cm²)	FF (%)	PCE (%)	R_s (Ω cm²)	R_{sh} (Ω cm²)
no ZnO	0.473 ± 0.023	16.02 ± 0.85	39.6 ± 6.4	3.06 ± 0.70	13.2 ± 4.1	94.3 ± 42.5
ZnO (25 ˚C)	0.666 ± 0.046	12.94 ± 1.918	35.1 ± 4.2	2.97 ± 0.37	39.9 ± 14.4	191.7 ± 92.4
ZnO (110 ˚C)	0.728 ± 0.008	17.30 ± 0.89	56.9 ± 2.2	7.01 ± 0.42	7.6 ± 0.6	416.7 ± 127.6
ZnO (200 ˚C)	0.722± 0.008	17.30 ± 1.77	56.3 ± 2.4	6.76 ± 0.55	7.6 ± 1.3	316.8 ± 82.9
ZnO (300 ˚C)	0.714 ± 0.007	19.02 ± 2.57	53.1 ± 1.6	6.90 ± 0.79	8.4 ± 0.8	268.7 ± 96.8
ZnO (450 ˚C)	0.618± 0.066	17.70 ± 0.71	42.0 ± 3.8	4.62 ± 0.83	13.9 ± 1.5	160.1 ± 68.1

B.4 Sol-gel derived ZnO for OLED

Sol-gel derived ZnO was also applied in organic light emitting diodes (OLEDs). F8BT was used as the light emitter. The device structure is glass/ITO/ZnO (30 nm)/F8BT (100 nm)/ MoO_3 (10 nm)/Au (100 nm)[10][11].

B.4.1 Experimental

Sol-gel derived ZnO thin films were fabricated on glass ITO substrates under same conditions as those employed for OPVs. The F8BT solution was prepared by mixing F8BT with toluene (15 mg/mL) and stirred overnight at room temperature. The F8BT layers were spun-cast at a speed of 2000 rpm for 30 s, acquiring a ~100 nm film. Then the as-cast F8BT films were put on a 90 °C hotplate for 20 min. 10 nm MoO_x hole transport layer and 100 nm Au electrode were then deposited by vacuum thermal evaporation.

The OLED characteristics were obtained using a computer-controlled Source Measure Unit (Keithley 236) and a luminance meter (Minolta) under ambient conditions.

B.4.2 Results and discussion

We investigated the influence of ZnO processing temperature on OLED performance. Unlike in OPVs, high processing temperature gives better performance in OLEDs.

The light turn-on voltages of OLEDs with ZnO processing temperatures are shown in Figure B.5. The 450 °C processed ZnO exhibits the lowest light turn-on voltage, 2.7 V.

And the 200 °C processed ZnO exhibits the highest light turn-on voltage, almost twice of that with 450 °C processed ZnO.

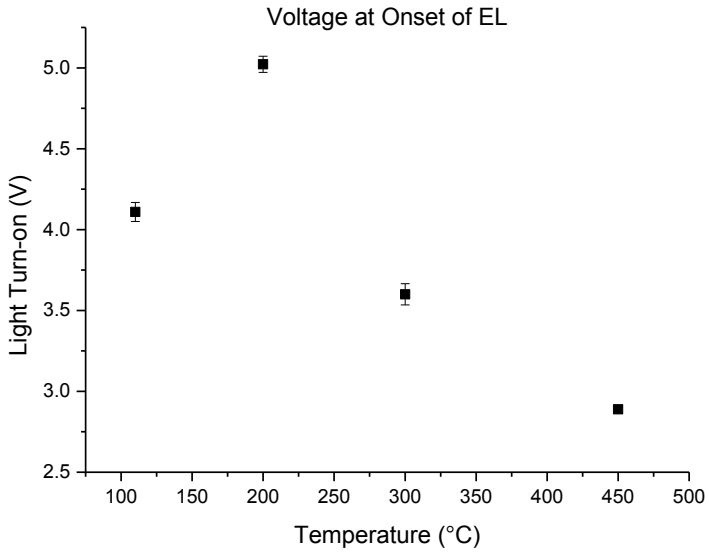


Figure B.5 Light turn-on voltage (V) of PLEDs with different ZnO processing temperatures.

Figure B.6 shows current density and current efficiency at 1000 cd/m^2 which is the brightness for general lightning application. 450 °C processed ZnO shows the lowest current density and corresponding the highest current efficiency. Compared with 200 °C and 300 °C, 110 °C ZnO exhibits higher current efficiency.

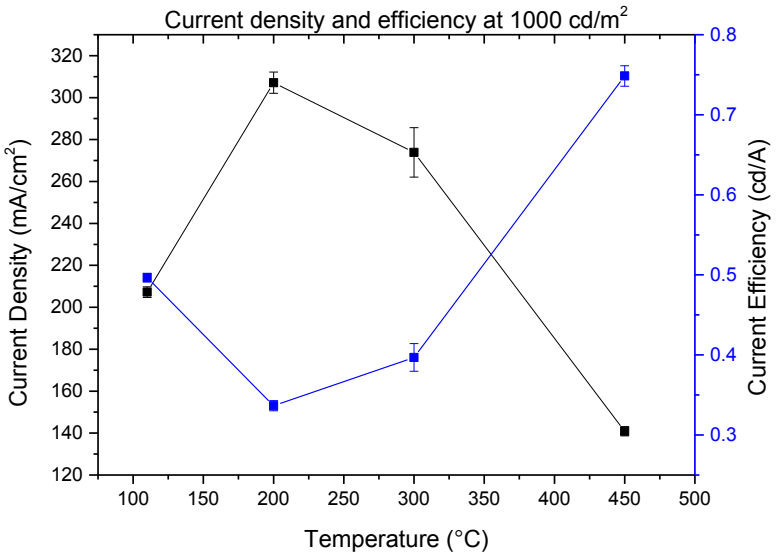


Figure B.6 Current density and current efficiency at 1000 cd/m^2 with different ZnO processing temperatures.

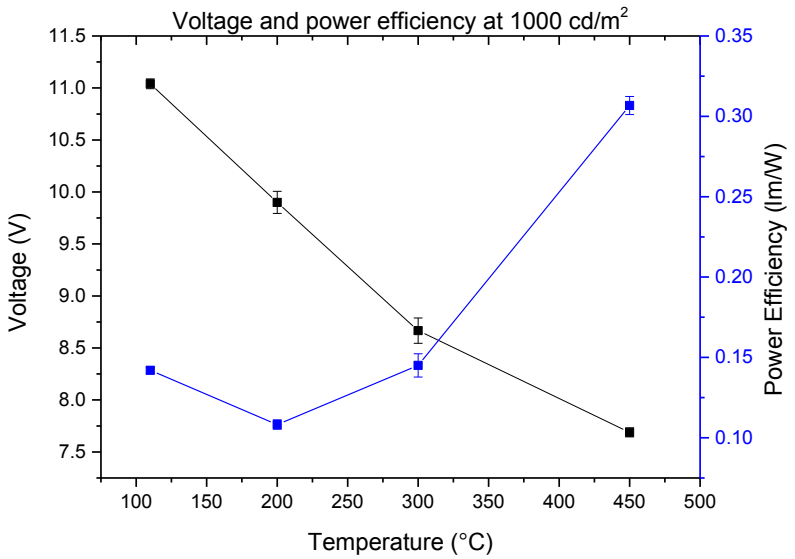


Figure B.7 Voltage and power efficiency at 1000 cd/m² with different ZnO processing temperatures.

Figure B.7 shows the voltage and power efficiency at 1000 cd/m². The operating voltages at 1000 cd/m² decrease with the ZnO processing temperature increase. For the power efficiency, ZnO at 110 – 300 °C shows similar value. While ZnO (450 °C) based device shows 0.31 lm/W which is more than twice of those with ZnO (110 – 300 °C).

In conclusion, OLEDs with sol-gel derived ZnO (110 – 450 °C) as electron injection layers all work well. But compared with ZnO (110 – 300 °C), highly oriented polycrystalline 450 °C ZnO performs much better.

Appendix C - Sol-gel derived ZnO as Electron Transport Layers for Perovskite Solar Cells

C.1 Starting materials

Materials	Formula	Purity	Supplier
2,2',7,7'-tetrakis[N,N-di(4-methoxyphenyl)amino]-9,9'-spirobifluorene (spiro-OMeTAD)	$C_{81}H_{68}N_4O_8$	99.5%	Borun Chemicals
bis(trifluoromethane)sulfonimide lithium salt (Li-TFSI)	$CF_3SO_2NLiSO_2CF_3$	99.0%	Sigma-Aldrich
Acetonitrile	CH_3CN	99.8%	Sigma-Aldrich
4-tert-butylpyridine	$C_9H_{13}N$	96%	Sigma-Aldrich
[6,6]-Phenyl-C61-butyric acid methyl ester (PCBM)	$C_{72}H_{14}O_2$	99.5%	Alfa Aesar
Lead iodide	PbI_2	99%	Sigma-Aldrich
Methylammonium iodide (MAI)	CH_3NH_3I	N/A	Solaronix
Gamma-butyrolactone (GBL)	$C_4H_6O_2$	99%	Sigma-Aldrich
Dimethyl sulfoxide (DMSO)	$(CH_3)_2SO$	99.9%	Sigma-Aldrich
Toluene	$C_6H_5CH_3$	99.5%	VWR Chemicals

Appendix D - Aqueous processed ZnO as Electron Transport Layers for Organic and Perovskite Solar Cells

D.1 Starting materials

Table D.1 Starting materials

Materials	Formula	Parameter	Supplier
Zinc oxide powders	ZnO	99.99%	Sigma-Aldrich
Ammonium hydroxide solution	NH_4OH	5.0 M	Sigma-Aldrich
Poly[N-9′-heptadecanyl-2,7-carbazole-alt-5,5-(4′,7′-di-2-thienyl-2′,1′,3′-benzothiadiazole)] (PCDTBT)	$(C_{43}H_{47}N_3S_3)_nC_{12}H_{10}$	M_w 65KDa PDI 2.4	1-Material

D.2 ZnO films by aqueous processing

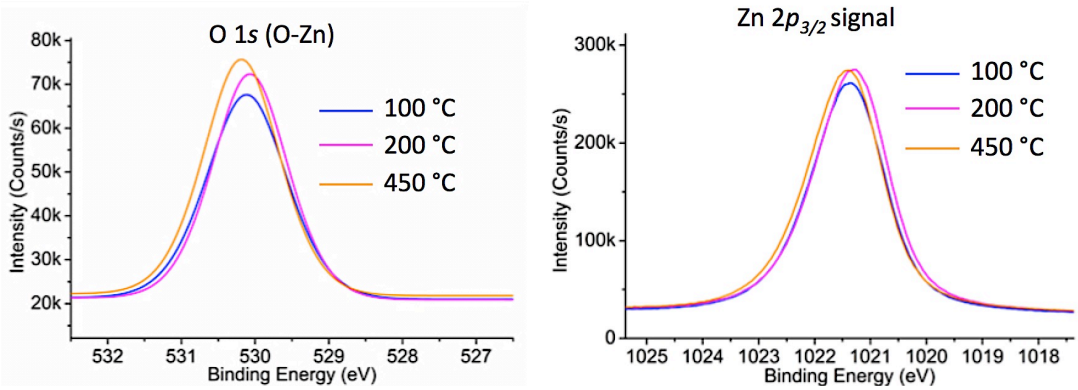


Figure D.1 ZnO XPS spectra of O 1*s* (O-Zn) and Zn $2p_{3/2}$, with different processing temperatures, indicating the E_F shift of ZnO films.

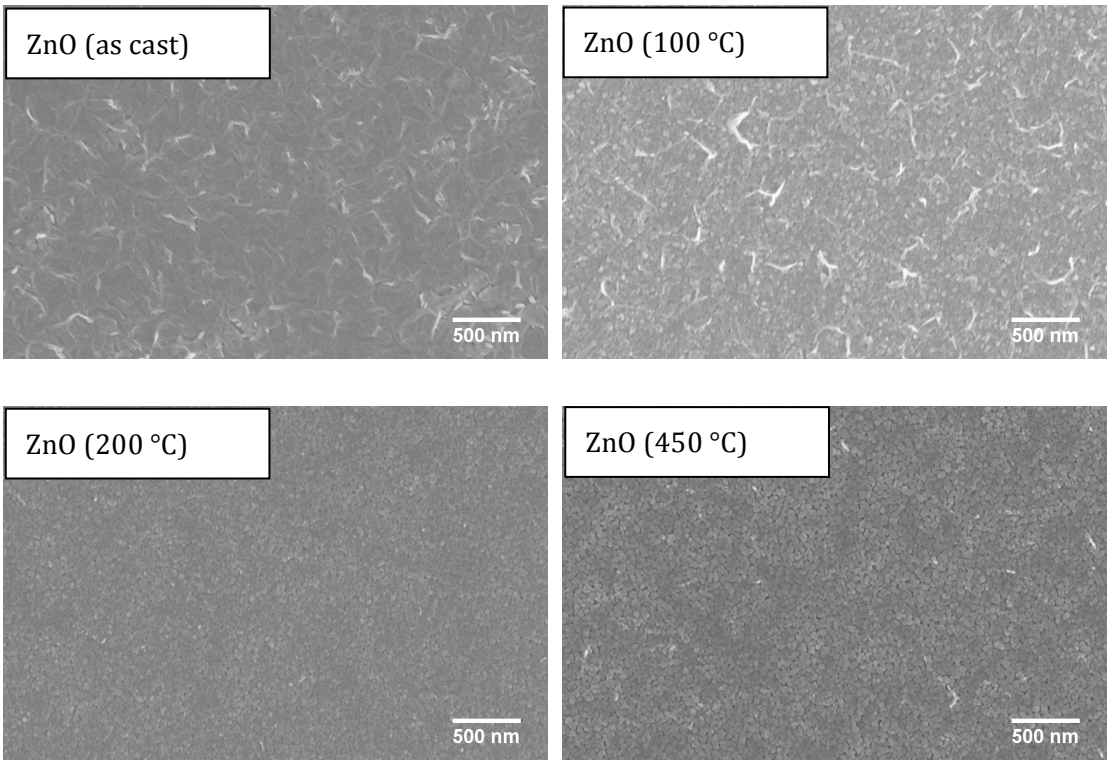


Figure D.2 Large area SEM images of ZnO films by ammonia methods.

D.3 Aqueous processed ZnO films for OLEDs

D.3.1 Experimental methods

For OLED fabrication, a green derivative of p-PPV obtained from Merck was dissolved in toluene in a 10 mg/ml concentration and stirred overnight at 60 °C. The solution was then spun dynamically at 1500 rpm for 40 s, which resulted in 70 nm thick films. The top electrode was deposited in the same way as that of OPV devices. OLED devices were characterized using a Kethley 2400 sourcemeter and a Minolta luminance meter, operated through a custom-written LabView script.

D.3.2 Results and discussion

OLED devices were fabricated, incorporating ZnO films as ETLs. The results are shown in Table D.2, while J-V-L data of representative devices for each temperature are presented in Figure D.3. The trends observed in OPV devices as shown in Chapter 6 are replicated, with films annealed at 100 °C and 200 °C showing similar, efficient behavior, and films treated at 450 °C showing higher performances than devices without any ETL but lower performances than the other two films. In particular, the higher turn-on voltage shown when 450 °C ZnO was used confirmed what already speculated for OPV devices, that the deep work function affects the energy level alignment at the interface.

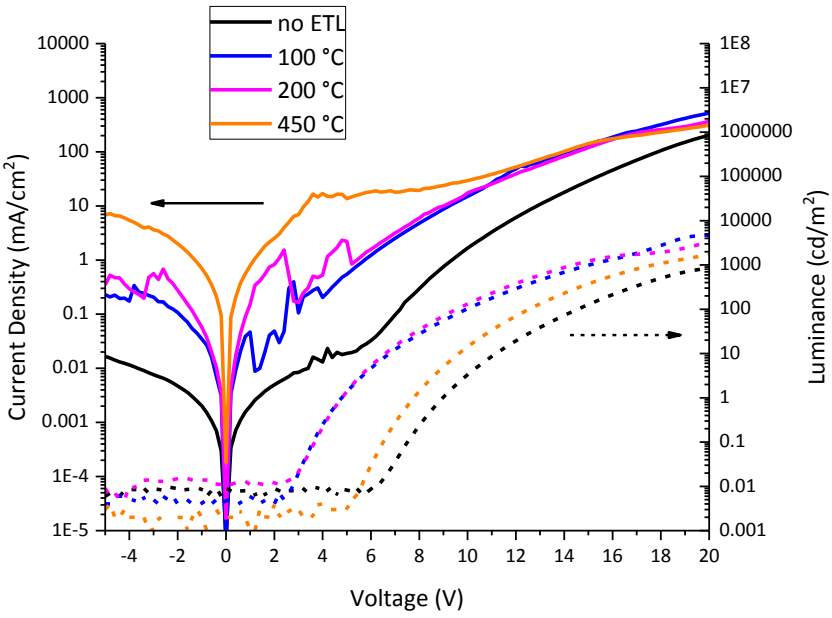


Figure D.3 J-V-L data of representative OLED devices with various ZnO layers.

Table D.2 OLED performance with various ZnO layers

Sample	Maximum current efficiency	Voltage at maximum current efficiency	Power efficiency at maximum current efficiency	Luminance at maximum current efficiency	Current density at maximum current efficiency	Turn-on voltage
	Cd/A	V	Lm/W	Cd/m²	mA/cm²	V
no ZnO	0.45	17.8	0.08	470	105.21	6.4
ZnO (100 ˚C)	1.00	19.0	0.17	4160	414.00	2.6
ZnO (200 ˚C)	1.03	13.2	0.25	640	62.10	2.6
ZnO (450 ˚C)	0.67	21.4	0.10	2970	443.00	5.4

D.4 Extrinsic dopants

For the carbon-free aqueous processed ZnO, few efforts have been made on doping. Alkali metal doping was investigated and did not show strong modulation on the electrical properties[12]. For donor group III elements, only Al doping was reported[13]. Here, a preliminary work of Ga-doped ZnO has been studied. The ionic radius of Ga^{3+} (0.62 Å) is smaller than that of Zn^{2+} (0.74 Å), which allows easy substitution of Ga^{3+} for

Zn^{2+}; in addition, the covalent band length of Ga–O (1.92 Å) is slightly shorter than that of Zn–O (1.97 Å), which reduces lattice distortion in ZnO thin film[14].

$Ga(NO_3)_3xH_2O$ was first chosen as the dopant, which was simply added into the pristine zinc precursor solution. The value of x of $Ga(NO_3)_3xH_2O$ is not given by the supplier (Sigma Aldrich). I conducted an initial measurement using a furnace. The $Ga(NO_3)_3xH_2O$ powder is annealed under 600 °C for 2 h to make sure it has been completely transferred to Ga_2O_3. The calculated x value is around 8-9 which is similar to the value in the reference[15]. However, $Ga(NO_3)_3xH_2O$ as the dopant presents phase separation in the film, Figure D.4a, probably because of the involvement of NO_3^- ion.

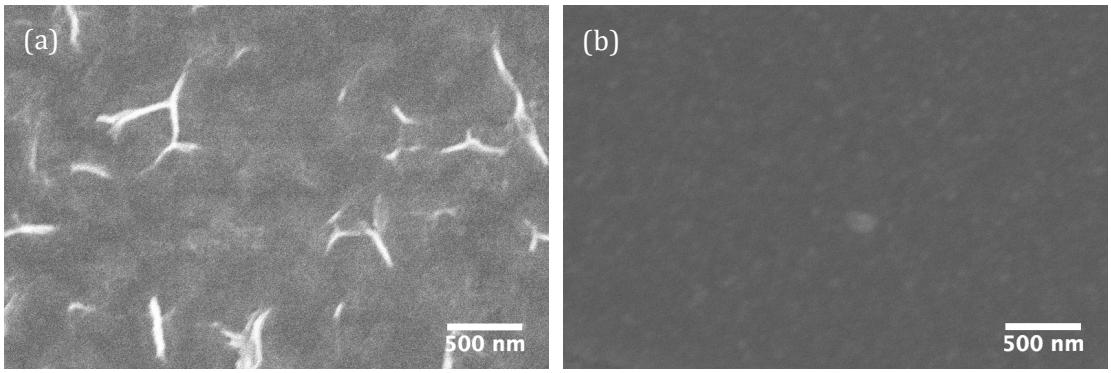


Figure D.4 SEM images of Ga-doped ZnO films by aqueous processing with 3 at% doping: (a) $Ga(NO_3)_3xH_2O$ as dopant; (b) $Ga(OH)_3$ as dopant.

Then, the gallium hydroxide was chosen as the dopant, which was synthesised via the addition of NaOH into $Ga(NO_3)_3$ solution. Smooth surface was obtained, as shown in Figure D.4b. TFTs were fabricated to assess the electron mobility, with the Ga doping in the range of 1 – 5 at%. Then the calculated field effect mobilities from saturation region are shown in Table D.3 with 25 V of V_D. 1 at% Ga doping presents increased mobility but further doping of 3-5 at% doping decreases the mobility, which trend is similar to sol-gel derived high temperature processed films[16].

Table D.3 Field effect mobilities of ZnO films calculated from transfer curves in saturation region.

Doping (at%)	Mobility ($cm^2 V^{-1}S^{-1}$)
0	0.09729
1	0.11209
3	0.04771
5	1.30E-05

References

[1] D. E. Bornside, C. W. Macosko, L. E. Scriven, *J. imaging Technol.* **1987**, *13*, 122.

[2] J. M. Downing, M. P. Ryan, M. A. McLachlan, *Thin Solid Films* **2013**, *539*, 18.

[3] K. Govender, D. S. Boyle, P. B. Kenway, P. O'Brien, *J. Mater. Chem.* **2004**, *14*, 2575.

[4] J. M. Downing, Control and Characterisation of Metal Oxide / Polymer Morphologies for Hybrid Photovoltaic Devices, Imperial College London, **2013**.

[5] L. Vayssieres, *Adv. Mater.* **2003**, *15*, 464.

[6] M. Guo, P. Diao, S. Cai, *J. Solid State Chem.* **2005**, *178*, 1864.

[7] J. H. Tian, J. Hu, S. S. Li, F. Zhang, J. Liu, J. Shi, X. Li, Z. Q. Tian, Y. Chen, *Nanotechnology* **2011**, *22*, 245601.

[8] M. Law, L. E. Greene, J. C. Johnson, R. Saykally, P. Yang, *Nat. Mater.* **2005**, *4*, 455.

[9] T. Y. Olson, A. A. Chernov, B. A. Drabek, J. H. Satcher, T. Y. Han, **2013**.

[10] L. K. Jagadamma, M. Al-Senani, A. El-Labban, I. Gereige, G. O. Ngongang Ndjawa, J. C. D. Faria, T. Kim, K. Zhao, F. Cruciani, D. H. Anjum, M. A. McLachlan, P. M. Beaujuge, A. Amassian, *Adv. Energy Mater.* **2015**, 1500204.

[11] J. Costa Dantas Faria, A. J. Campbell, M. A. McLachlan, *J. Mater. Chem. C* **2015**, *3*, 4945.

[12] S. Y. Park, B. J. Kim, K. Kim, M. S. Kang, K. H. Lim, T. Il Lee, J. M. Myoung, H. K. Baik, J. H. Cho, Y. S. Kim, *Adv. Mater.* **2012**, *24*, 834.

[13] Y. H. Lin, S. R. Thomas, H. Faber, R. Li, M. A. McLachlan, P. A. Patsalas, T. D. Anthopoulos, *Adv. Electron. Mater.* **2016**, *2*, 1.

[14] C. Y. Tsay, K. S. Fan, C. M. Lei, *J. Alloys Compd.* **2012**, *512*, 216.

[15] V. Berbenni, C. Milanese, *J. Therm. Anal. Calorim.* **2005**, *82*, 401.

[16] W. J. Park, H. S. Shin, B. Du Ahn, G. H. Kim, S. M. Lee, K. H. Kim, H. J. Kim, *Appl. Phys. Lett.* **2008**, *93*, 83508.